Optimal Control in the High Resolution NMR-Spectroscopy: Transfer Elements and their Application for Structure Elucidation

Zur Erlangung des akademischen Grades eines

DOKTORS DER NATURWISSENSCHAFTEN

(Dr. rer. nat.)

Fakultät für Chemie und Biowissenschaften

Karlsruher Institut für Technologie (KIT) - Universitätsbereich genehmigte

DISSERTATION

von

Dipl.-Chem. Sebastian Ehni

aus

Göppingen

Dekan: Prof. Dr. M. Bastmeyer

Referent: Prof. Dr. B. Luy

Korreferent: PD Dr. G. Guthausen

Tag der mündlichen Prüfung: 19.07.2013

Eidesstattliche Versicherung

Ich versichere, dass ich die von mir vorgelegte Dissertation selbstständig angefertigt, die benutzten Quellen vollständig angegeben und die Stellen der Arbeit, die anderen Werken im Wortlaut oder Sinn nach entnommen sind, in jedem Einzelfall kenntlich gemacht habe; dass diese - abgesehen von unten angegebenen Teilpublikationen - noch nicht veröffentlicht worden ist sowie, dass ich eine solche Veröffentlichung vor Abschluss des Promotionsverfahrens nicht vornehmen werde. Die von mir vorgelegte Dissertation ist von Herrn Prof. Dr. B. Luy betreut worden.

Publikationsliste

- S. Ehni, B. Luy, A systematic approach for optimizing the robustness of pulse sequence elements with respect to couplings, offsets, and B_1-field inhomogeneities (COB), Magn. Reson. Chem. 50, 63-72 (2012).

  DOI: http://dx.doi.org/10.1002/mrc.3846

- K. Kobzar*, S. Ehni*, T. E. Skinner, S. J. Glaser, B. Luy, Exploring the Limits of Broadband 90° and 180° Universal Rotation Pulses, J. Magn. Reson. 225, 142-160 (2012).

  DOI: http://dx.doi.org/10.1016/j.jmr.2012.09.013

- S. Ehni, B. Luy, BEBE^{tr} and BUBI: J-compensated concurrent shaped pulses for ^{1}H-^{13}C experiments, J. Magn. Reson. 232, 7-17 (2013).

  DOI: http://dx.doi.org/10.1016/j.jmr.2013.04.007

*Authors contributed equally to this work.

Contents

Contents

Spin dynamics are beautiful.

Offset selective track sequence

Nuclear spins are controlled by radio frequency irradiation.
Representation of the effect of a selective decoupling sequence, which is
numerically derived by optimal control methods (Chap. 10).

The transfer $S_z \rightarrow S_z$ is depicted for 1900 increments (left figure) and 1150
increments (right figure).
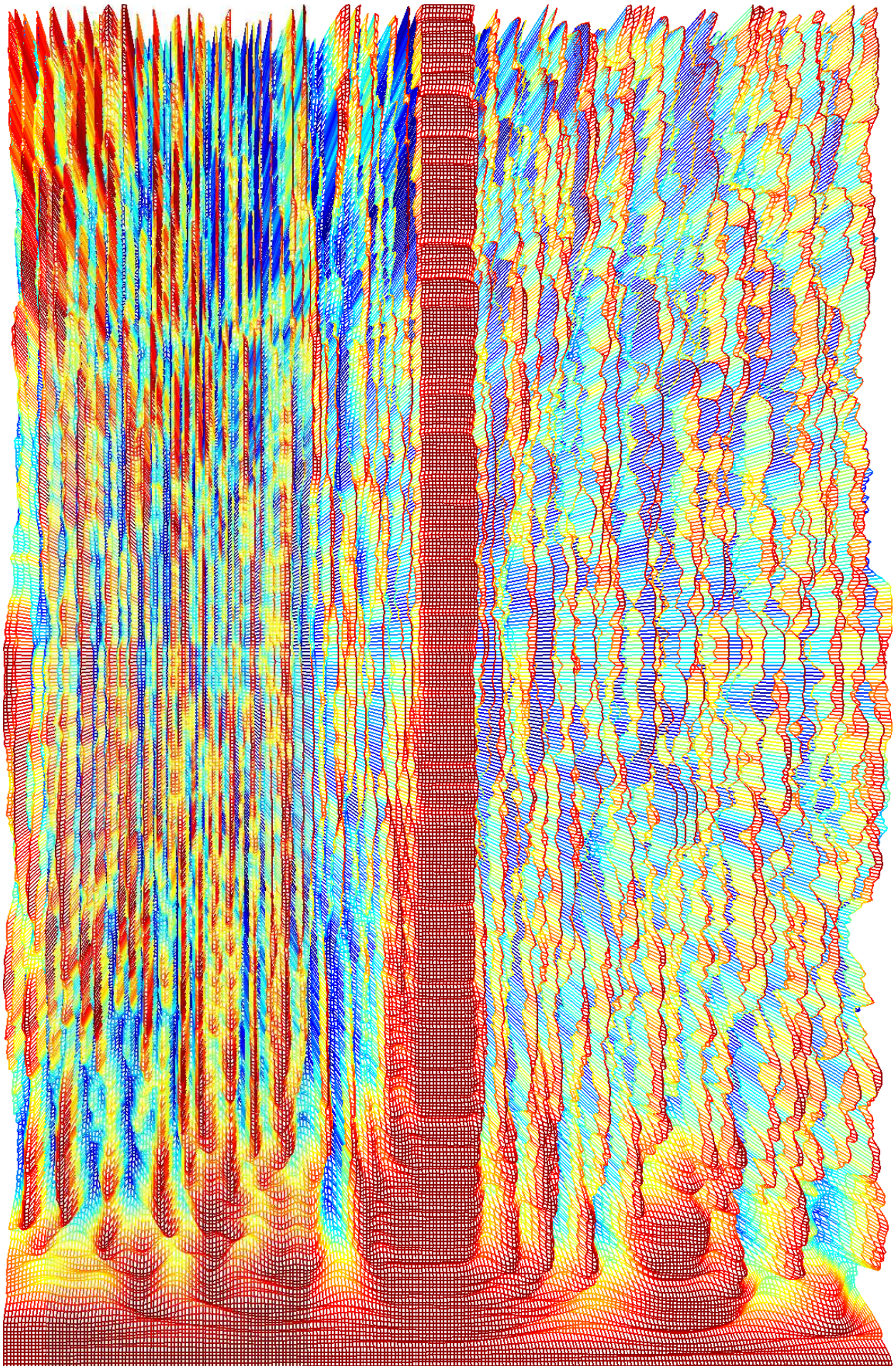
1. Scope of the Work

Nuclear magnetic resonance (NMR) spectroscopy is one of the most important analytical methods in organic chemistry. It is used for structure elucidation, purity and reaction control.

Experiments in modern Fourier transform NMR spectroscopy require the execution of radio frequency (rf) pulses. A wide variety of them is used for one- (1D) dimensional and multi-dimensional (nD) NMR techniques.

NMR Spectroscopy is a method that provides atomic resolution. This is due to the fact that most of the relevant properties are short-ranged and originate from closed quantum systems. For example, chemical shifts are usually determined by the first and second sphere of surrounding atoms. Scalar couplings ($^{n}J_{\mathrm{HH}}$) are typically active over a few bonds, while NOE interactions are used to correlate atoms that are closer than 5 Å directly over space.

The so called anisotropic parameters are introduced upon the use of alignment media (for example RDCs and RCSAs). As they depend on the angle to the external magnetic field, they introduce an external reference that can be used to correlate independent parts of a molecule, even if they are far apart. These parameters are complementary to the above mentioned short-ranged parameters but firstly, they introduce a new level of complexity to the spectral data and second, they provide long-range information.

The design of optimal pulses and NMR experiments is a vivid field of NMR spectroscopy. It is indispensable to provide access to high quality spectral data. Beside that, new methods are needed in order to control the spectral complexity, encountered when alignment media are used. Failing to comply with it leads to loss of atomic resolution, which is required for the extraction of long-range data. This thesis is focused on the development of optimal pulses and pulse sequences using optimal control theory (OCT) and their application in the analysis of organic compounds.

At present time, it is possible to derive shaped pulses, which are robust against radio frequency inhomogeneities and offset deviations by optimal control methods. Typical shaped pulses consist of several thousands of increments with variable rf phase and amplitude. Simple pulses are derived from single spin systems and can be tailored to meet the requirements in variety of applications.

This thesis describes the pulse development for multi spin systems. A new class of concurrent shaped pulses accounts for J-couplings, offset deviations and rf inhomogeneities. These pulses are referred to as "BUBI" and discussed in Chap. 8. They are designated

for the application in heteronuclear two and more spin systems and as a replacement for conventional single spin shaped pulses.

An equally robust class of shaped pulses are the so called *J*-evolution pulses that are presented in Chap. 9. These pulses are defined to accomplish a fraction of the heteronuclear coherence transfer while they are applied. Such pulse characteristics reduce the duration of the pulse sequence significantly.

The main focus of this thesis is the systematic study of coherence transfer elements (CTE) by means of OCT, i.e. the development of transfer elements for the following experiments: INEPT (heteronuclear inphase to antiphase, Chap. 4), BIRD (heteronuclear inphase to inphase selecting ^{13}C bound nuclei, Chap. 5), refocused INEPT (heteronuclear inphase to inphase on the second nucleus, Chap. 6) and INADEQUATE (homonuclear inphase to antiphase, Chap. 7). The transfer elements are examined by evaluating the transfer fidelity according to the physical limit. Optimal transfer elements are targeted, i.e. transfer elements that perform close to the best possible transfer element. Thereby, this thesis is based on considerations found for shaped pulses (Chap. 3.5) and continues it for coherence transfer elements. In this respect, OCT is applied as a tool to explore the physical limits of coherence transfer elements.

Decoupling sequences are of interest in a number of analytical questions to avoid spectral overlap and to increase the signal to noise ratio. They are crucial to obtain high quality spectral data. Chap. 10 is dedicated to the optimization of selective decoupling sequences that retain homonuclear and heteronuclear couplings within a narrow range of offsets.

In Chapters 11 and 12 the unambiguous assignment of racemic mixtures and the corresponding *meso*-isomers by means of NMR spectroscopy is described. For this purpose, the use of chiral liquid crystals and chiral solvents is discussed.

The discrimination of the absolute configuration of stereo isomers can be accomplished by the use of the chiral liquid crystal poly(γ-benzyl-*L*-glutamate). The examination of the interaction mechanisms between the analyte and the liquid crystals requires short-chained analogues. The synthesis of these is described in Chap. 13.

2. Ziel der Arbeit

Die Kernresonanzspektroskopie (NMR) gehört zu den wichtigsten Analysemethoden in der Organischen Chemie. Sie wird zur Strukturaufklärung und zur Reaktionskontrolle benutzt.

Unverzichtbare Bausteine der modernen Fourier-Transformations (FT) NMR Spektroskopie sind Radiofrequenz (rf) Pulse. Sie werden in unterschiedlichsten Arten für die ein- (1D) und mehrdimensionale (nD) NMR Spektroskopie verwendet.

NMR Spektroskopie ist eine Untersuchungsmethode mit atomarer Auflösung. Das beruht darauf, dass die meisten NMR relevanten Wechselwirkungen von kurzer Reichweite sind und aus geschlossenen Quantensystemen herrühren. Beispielsweise wird die chemische Verschiebung nur von der ersten und zweiten Hemisphäre von umgebenden Atomen bestimmt. Die häufig anzutreffenden skalaren Kopplungen ($^{n}J_{HH}$) reichen typischerweise über einige Bindungen, und NOE Interaktionen können Atome direkt über den Raum bis zu einer Entfernung von 5 Å korrelieren.

Ergänzend zu diesen Parametern können anisotrope experimentelle Parameter durch den Einsatz von Orientierungsmedien erhalten werden (z.B. RDCs und RCSAs). Da diese vom Winkel zum externen Magnetfeld abhängen, führen sie eine externe Referenz ein, die auch in großen Molekülen dazu verwendet werden kann, weit entfernte Zentren miteinander zu korrelieren. Damit unterscheiden sich diese signifikant von den bereits diskutierten Parametern mit kurzer Reichweite, führen jedoch auch eine neue Ebene der Komplexität in die Spektren ein.

Das Design von optimalen Pulsen und NMR Experimenten ist ein lebhaftes Feld der NMR Spektroskopie, das in vielen Anwendungsbereichen die sehr hohen Anforderungen an die Spektrenqualität überhaupt erst ermöglicht. Der Einsatz von modernen Pulsen und NMR Experimentenen ist unverzichtbar, um die Komplexität, eingeführt durch anisotrope Parameter, zu kontrollieren. Nur so kann die atomare Auflösung erhalten bleiben. Und diese ist die notwendige Bedingung zur Extraktion von langreichweitigen Informationen. Diese Arbeit befasst sich mit der Entwicklung von Pulsen und Pulssequenzen mit Hilfe der Optimal Control Theory (OCT) und deren Anwendung auf analytische Fragestellungen.

Mit OCT können heutzutage geformte Pulse erhalten werden, die robust gegen Radiofrequenzinhomogenität und Offsetabweichungen sind. Geformte Pulse bestehen typischerweise aus einigen tausend Pulsinkrementen mit variabler rf Phase und Amplitude. Mittlerweile können einfache Pulse, ohne große Probleme und direkt zugeschnitten auf die gewünschte Anwendung, aus Einspinoptimierungen erhalten werden.

Diese Arbeit führt die Pulsentwicklung für Mehrspinsysteme fort. Eine neue Klasse von gleichzeitig eingestrahlten Pulsen berücksichtigt J-Kopplung, Offset und Radiofrequenzinhomogenität und wird im Folgenden als "BUBI" bezeichnet (Kapitel 8). Dieses Pulspaar zielt auf die Anwendung in heteronuklearen Zwei- und Mehrspinsystemen ab, um herkömmliche geformte Pulse zu ersetzen.

Eine ebenso robuste Klasse von geformten Pulsen sind die sogenannten J-Evolution-Pulse, die in Kapitel 9 vorgestellt werden und für heteronukleare Mehrspinsysteme bestimmt sind. Diese Pulse zeichnen sich dadurch aus, dass ein Anteil des heteronuklearen Kohärenztransfers bereits während der Einstrahlung stattfindet. Dadurch wird die Gesamtzeit einer Pulssequenz signifikant reduziert.

Der Schwerpunkt dieser Arbeit liegt auf der systematischen Untersuchung von Kohärenztransferelementen (CTE) mit Hilfe von OCT. Im Einzelnen werden die Kohärenztransferelemente der folgenden Experimente untersucht: INEPT (heteronukleare Inphase nach Antiphase, Kapitel 4), BIRD (heteronukleare Inphase nach Inphase unter Selekton ^{13}C-gebundener Kerne, Kapitel 5), refokussiertes INEPT (heteronukleare Inphase nach Inphase des zweiten Kerns, Kapitel 6) und INADEQUATE (homonukleare Inphase zu Antiphase, Kapitel 7). Die Physik bestimmt den maximalen Transfer, anhand dessen die Güte eines Transferelements gemessen wird. Es werden optimale Transferelemente gesucht, d.h. Transferelemente, deren Eigenschaften so nahe wie möglich am bestmöglichen Transferelement liegen. Dabei beruft sich diese Arbeit auf Prinzipien, die für geformte Pulse (Kapitel 3.5) gefunden wurden und führt diese für Kohärenztransferelemente fort. In diesem Zusammenhang ist OCT das Werkzeug, das eingesetzt wird, um die physikalischen Grenzen zu erforschen.

Entkopplungssequenzen sind für eine Vielzahl analytischer Fragestellungen von Bedeutung, da sie spektrale Überlappungen vermeiden und das Signal zu Rausch-Verhältnis erhöhen. Damit tragen sie maßgeblich zur Qualität der Spektren bei. In Kapitel 10 wird die Optimierung selektiver Entkopplungssequenzen beschrieben, die gezielt homonukleare und heteronukleare Kopplungen in einem schmalen, definierten Offsetbereich erhalten.

Die Kapitel 11 und 12 befassen sich mit der Unterscheidung von racemischen Gemischen von den zugehörigen *Meso*-Isomeren mit Hilfe von NMR-Spektroskopie. Zu diesem Zweck wird der Einsatz von chiralen Flüssigkristallen und chiralen Lösemitteln beschrieben.

Die Unterscheidung der absoluten Konfiguration von Stereoisomeren ist beispielsweise mit Hilfe des chiralen Flüssigkristalls Poly(γ-benzyl-L-Glutamat) möglich. Zur Untersuchung der Interaktionsmechanismen von Analyt und Flüssigkristall werden dessen kurzkettige Analoga benötigt, deren Synthese in Kapitel 13 beschrieben wird.

3. Optimal Control Theory (OCT)

Optimal control theory is especially useful for the optimization of trajectories. The result of such an optimization is an optimal set of controls $\mathbf{u}$ that manipulates a state in order to suffice a given optimality criterion.

Optimal control theory is based on the classical Euler-Lagrange formalism, developed by Leonhard Euler and Joseph-Louis Lagrange in the 1750s. It uses the concept of Lagrange multipliers λ to minimize a functional in the presence of a number of equality constraints f_i that can be equations of motion and any other constraints that are given as a function of the controls $\mathbf{u}$.

The idea behind the Lagrange multipliers λ can be summarized by the following problem statement: Find local extreme values of $f(x, y)$ subjected to $g(x, y) = c$, for a given constant c. $f(x, y)$ and $g(x, y)$ may have continuous first partial derivates. Or with other words: $g(x, y)$ limits the domain of allowed x, y-coordinates for the minimization of $f(x, y)$. The allowed x, y-coordinates may be plotted (Fig. 3.1, dotted line) together with the graph of $f(x, y)$ (Fig. 3.1, shaded gray). If $g(x, y) = c$ is fulfilled, a Lagrange multiplier λ is introduced that connects $f(x, y)$ and $g(x, y)$ to result in the Lagrange equation:

$$\Lambda(x, y, \lambda) = f(x, y) + \lambda\Big(g(x, y) - c\Big) \tag{3.1}$$

The calculation of $\nabla_\lambda \Lambda(x, y, \lambda) = 0$ is a necessary requirement to find a maximum (Fig. 3.1, labelled by an arrow).

In contrast to the given example, optimal control theory is applied to time dependent problems. $\mathbf{u}$ is the control vector of the control Hamiltonian H_k.

$$\mathbf{u} = \begin{pmatrix} u_1(t) \\ \vdots \\ u_k(t) \\ \vdots \\ u_m(t) \end{pmatrix} \tag{3.2}$$

x_j is a state vector, for example a density matrix with the number of elements s determined
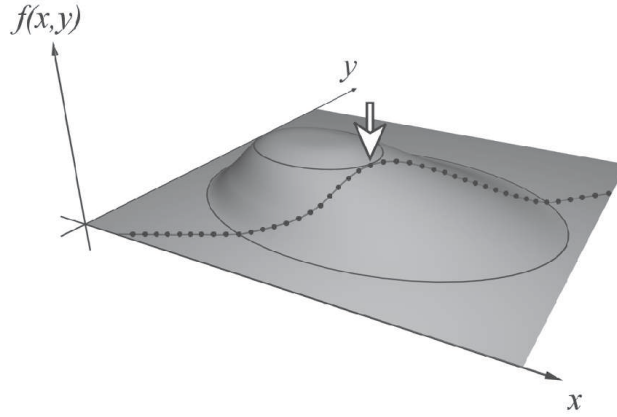
Figure 3.1: Maximization of the function $f(x, y)$ with respect to a function $g(x, y) = c$ that restricts the allowed x, y-combinations to distinct values (dotted line). The local maximum (indicated by an arrow) is found upon the introduction of Lagrange multipliers. Graphic taken from [1].

by the spin system and the nuclear spin quantum number.

$$x_j = \begin{pmatrix} x_1 \\ \vdots \\ x_s \end{pmatrix} \tag{3.3}$$

$\boldsymbol{x}$ is the trajectory of state vectors given by the number of time steps N.

$$\boldsymbol{x} = \begin{pmatrix} x(0) = x(t = t_0) \\ \vdots \\ x(j) = x(t = t_j) \\ \vdots \\ x(N) = x(t = t_N) \end{pmatrix} \tag{3.4}$$

$\boldsymbol{\lambda}$ are the Lagrange multipliers

$$\boldsymbol{\lambda} = \begin{pmatrix} \lambda_1 \\ \vdots \\ \lambda_\kappa \end{pmatrix}. \tag{3.5}$$

There are κ equality constraints, for example f_1 may be the systems equation of motion, f_2 may be some arbitrary function of $\mathbf{u}$ to constrain $\mathbf{u}$. f_ι is connected with the cost functional L by the Lagrange multiplier λ_ι.

$$\begin{aligned} H(\mathbf{x}, \mathbf{u}, \lambda) &= L(\boldsymbol{x}, \boldsymbol{u}) + \sum_{\iota=1}^{\kappa} \lambda_\iota f_\iota(\boldsymbol{x}, \boldsymbol{u}) \\ &= L(\boldsymbol{x}, \boldsymbol{u}) + \boldsymbol{\lambda}^t \mathbf{f}(\boldsymbol{x}, \boldsymbol{u}) \end{aligned} \tag{3.6}$$

with $\boldsymbol{\lambda}^t$ denoting the transpose of $\boldsymbol{\lambda}$. If the κ equality constraints are fulfilled, $\boldsymbol{\lambda}$ disappears from Eq. (3.6) to result in

$$\Phi = \phi(x_N, t_N = T) + \int_{t_0}^{T} L\left(\boldsymbol{x}, \boldsymbol{u}, t\right) dt. \tag{3.7}$$

Where Φ is a scalar objective functional. It depends on ϕ that depends only on the final state at the time $t_N = T$. The integral represents a running cost. It is dispensable if only the final state is of interest. A more detailed introduction into optimal control is given in [2].

So far no statement is made on the computation of the final state $x(N)$. Especially not how it is obtained according to the equation of motion. It was just assumed that a somehow obtained trajectory $\boldsymbol{x}$ is evaluated according to $\phi[\boldsymbol{x}, t]$. The GRAPE algorithm [3] is a very effective way to calculate $\boldsymbol{x}$ from the functional $L[\boldsymbol{x}, \boldsymbol{u}, t]$ and the gradients of ϕ with respect to the control Hamiltonians H_k.

3.1 Spin Dynamics

3.1.1 Universal Rotations (UR) Φ_3

A closed quantum system is defined by the drift Hamiltonian H_0 and the control Hamiltonians H_k. The coefficient of the control Hamiltonians H_k are the real-valued control amplitudes $u(t) = (u_1(t), u_2(t), \ldots, u_m(t))$. During each time step, the system is influenced by m control Hamiltonians. For example the first control Hamiltonian H_1 would be $H_1 = 2\pi I_x$. The Hamiltonian is defined for a n spin system. Accordingly, the drift Hamiltonian is influenced by n offset amplitudes $\nu_{l,\text{off}}$. Each of the nuclei may be coupled by J-couplings J_{lo} to other nuclei. $I_{x,y,z}$ are the spin operators as defined in [4].

$$\begin{aligned} H &= H_0 + H_{\text{ctrl}} \\ &= \sum_{l=1}^{n} \left(2\pi \nu_{l,\text{off}} I_{z,l}\right) + \sum_{l>o}^{n} \pi J_{l,o}\left(2I_{lx}I_{ox} + 2I_{ly}I_{oy} + 2I_{lz}I_{oz}\right) \\ &\quad + \sum_{k=1}^{m} u_k(t) H_k \end{aligned} \tag{3.8}$$

Resulting in a bilinear controlled system that can be influenced externally by choosing $u_k(t)$ and that is governed by the Schrödinger equation.

$$|\dot{\psi}(t)\rangle = -iH(t)|\psi(t)\rangle \tag{3.9}$$

If dissipative effects and unobservable global phase factors are neglected this leads to the Liouville von Neumann equation.

$$\dot{\rho}(t) = -i\left[H(t), \rho(t)\right] \tag{3.10}$$

It is the basis for spin dynamics of large ensembles of spins that is used for the description of macroscopic samples as discussed in Section 3.1.3.

Using $U(t) = \exp(-iH(t)t)$ and $|\psi(t)\rangle = U(t)|\psi(0)\rangle$, Eq. (3.9) can be lifted to the operator level. Thus, Eq. (3.11) is independent from the initial and final state $|\psi(0)\rangle$ and $|\psi(T)\rangle$.

$$\dot{U}(t) = -iH(t)U(t) = -i\left(H_0 + \sum_{k=1}^{m} u_k(t)H_k\right)U, \qquad (3.11)$$

where U is the propagator of the spin system and the initial propagator is $U(0) = \mathbb{1}$. In the following it is assumed that the chosen pulse duration t_p is discretized in N equal steps of duration $\Delta t = t_p/N$ (Fig. 3.2) and during each step the control amplitudes u_k are constant, e.g. during the jth step the amplitude $u_k(t)$ of the kth control Hamiltonian is given by $u_k(j)$. The time-evolution of the spin system during a time step j is then given by the propagator

$$U_j = \exp\left\{-i\Delta t\left(H_0 + \sum_{k=1}^{m} u_k(j)H_k\right)\right\} \qquad (3.12)$$

and the total propagator is given by

$$U(T) = U_{\text{eff}} = \prod_{j=1}^{N} U_j. \qquad (3.13)$$

For a general system consisting of n spins $1/2$, the fidelity with which U_{eff} approaches a desired propagator U_F can be quantified by the quality factor or cost function Φ_3

$$\Phi_3 = \frac{1}{2^n}\,\mathfrak{Re}\langle U_F|U_{\text{eff}}\rangle, \qquad (3.14)$$

which is identical to the definition given in [3] up to the normalization constant $1/2^n$. The common form of Eq. 3.14 is Eq. 3.15. The evaluation of Eq. 3.15 results in a complex value

$$\Phi_3 = \frac{1}{2}\,\langle U_F|U_{\text{eff}}\rangle. \qquad (3.15)$$

As shown in [3], to first order in Δt the gradient $\delta\Phi_3/\delta u_k(j)$ is given by

$$\frac{\delta\Phi_3}{\delta u_k(j)} = -\frac{1}{2}\mathfrak{Re}\langle P_j|i\Delta t H_k X_j\rangle \qquad (3.16)$$

with $X_j = U_j\cdots U_1$ and $P_j = U_{j+1}^{\dagger}\cdots U_N^{\dagger}U_F$.

A final state $\rho(t) = U\rho_0 U^{\dagger}$ does not depend on the global phase ϕ of the propagator. All propagators of the form $U' = e^{i\phi}U$ produce the same $\rho(t)$. An alternative possibility for the quality factor which explicitly eliminates this seemingly irrelevant global phase is

$$\Phi_4 = \frac{1}{4^n}|\langle U_F|U(t_p)\rangle|^2 \qquad (3.17)$$

which is identical according to the definition given in [3] up to the normalization constant $1/4^n$. In the special case of a single spin $1/2$, Eq. (3.18) reduces to

$$\Phi_1 = \Phi_3^2 = \frac{1}{4}\,\langle U_F|U(t_p)\rangle^2. \qquad (3.18)$$

The corresponding gradient $\delta\Phi_3/\delta u_k(j)$ to first order in Δt is given by [3]

$$
\begin{aligned}
\frac{\delta\Phi_1}{\delta u_k(j)} &= -\frac{1}{4}\left\{\langle P_j|X_j\rangle\langle i\Delta t H_k X_j|P_j\rangle\right.\\
&\qquad\left.+\langle P_j|i\Delta t H_k X_j\rangle\langle X_j|P_j\rangle\right\}\\
&= -\frac{1}{2}\,\mathrm{Re}\{\langle P_j|i\Delta H_k t X_j\rangle\langle X_j|P_j\rangle\}.
\end{aligned}
\tag{3.19}
$$

As discussed in [5], other definitions of the quality factor of UR pulses based on the match between the actual and desired (real orthogonal) rotation operators or the point-to-point (PP) transformation properties of three orthogonal magnetization vectors [5,6] which are equivalent to Φ_1 and hence are also insensitive to any global phase factors.

The quality factors $\Phi_3(\nu_{\mathrm{off}}, \nu_{\mathrm{rf}})$ and $\Phi_1(\nu_{\mathrm{off}}, \nu_{\mathrm{rf}})$ are local in the sense that they are defined for a specific offset ν_{off} and a specifically scaled maximum rf amplitude ν_{rf}. The corresponding global quality factor Φ_p with $p \in \{0, 1, 3\}$ for a pulse sequence that is broadband with respect to offset and robust with respect to scaling of the rf amplitude is defined by

$$
\Phi_p = \frac{1}{n_{\mathrm{off}} n_{\mathrm{rf}} n_{\mathrm{J}}} \sum_{i=1}^{n_{\mathrm{off}}} \sum_{\ell=1}^{n_{\mathrm{rf}}} \sum_{h=1}^{n_{\mathrm{J}}} \Phi_p(\nu_{\mathrm{off}}^i, \nu_{\mathrm{rf}}^\ell, J^h),
\tag{3.20}
$$

i.e. by the average of the local quality factor over a set of n_{off} equally spaced offsets ν_{off} and n_{rf} equally spaced scaled maximum rf amplitudes ν_{rf} and n_J equally spaced J-couplings in the desired range of offset, rf scaling and J-coupling [3].

3.1.2 The GRAPE Algorithm

Equipped with all necessary equations it is possible to formulate the basic GRAPE algorithm to perform optimizations of broadband universal rotations [3]:

1. Guess initial controls $u_k(j)$.

2. Starting from $U_0 = U(t=0) = \mathbb{1}$, calculate $X_j = U_j U_{j-1} \cdots U_1 U_0$ for all $j \leq N$.

3. Starting from the desired propagator U_F, calculate $P_j = U_{j+1}^\dagger \cdots U_N^\dagger U_F$ for all $j \leq N$.

4. Evaluate individual local gradients $\Gamma_k(j) = \delta\Phi_3/\delta u_k(j)$ according to Eq. (3.19) or $\Gamma_k(j) = \delta\Phi_1/\delta u_k(j)$, respectively.

5. Repeat steps 2.-4. for all n_{off} offsets ν_{off} and all n_{rf} rf amplitudes ν_{rf}. Then calculate the gradient of the global quality factor Φ_3 or Φ_1, which is given by the average gradient $\overline{\Gamma_k(j)} = \frac{1}{n_{\mathrm{off}} n_{\mathrm{rf}}} \sum_{i=1}^{n_{\mathrm{off}}} \sum_{\ell=1}^{n_{\mathrm{rf}}} \Gamma_k(j, \nu_{\mathrm{off}}^i, \nu_{\mathrm{rf}}^\ell)$ and update the $m \times N$ control amplitudes according to $u_k(j) \to u_k(j) + \epsilon \overline{\Gamma_k(j)}$.

6. If desired, restrict controls to a maximum rf amplitude [7–9] or enforce any other restrictions.

7. With these new controls, go to step 2 until convergence is reached.

The basic steepest ascent algorithm can be improved by using conjugate gradient methods [3] or second order methods and exact gradients [10–12].

3.1.3 Point-to-Point (PP) Transfers Φ_0

Another approach to deal with spin dynamics is the description of the samples macroscopic magnetization instead of the effective field that is caused by an rf pulse that was discussed in the last two Sections. First of all, the magnetization is subjected to relaxtion. Relaxation results in the build-up of a macroscopic magnetization parallel to the external field B_0, which provides the initial density operator ρ_0. Apart from that, longitudinal and transverse relaxation is neglected in good approximation since the relaxation time of small molecules normally exceeds the duration of considered shaped pulses and transfer elements.

The macroscopic magnetization emerges from the large number of spins that are present in a sample tube and may be described using density matrices ρ.

$$\rho = |\psi(t)\rangle\langle\psi(t)| \tag{3.21}$$

Using the definition of ρ, and starting from the Schrödinger equation (3.9), the Liouville von Neumann equation (3.10) is obtained. The solution of this first order differential equation with respect to the time propagation for a piecewise constant Hamiltonian H (3.8) is the matrix exponential that is also referred to as the propagator $U(t)$ (3.12).

For a time increment Δt, it propagates an initial density matrix $\rho(t_0) = \rho_0$ forward or backward in time

$$\rho(T) = U_N \cdots U_1 \rho_0 U_1^\dagger \cdots U_N^\dagger \tag{3.22}$$

while the norm of ρ is invariant under the action of the unitary propagator U. The performance function to be maximized is referred to as Φ_0. The problem to find optimal amplitudes $u_k(t)$ that propagate an initial density operator $\rho(t=0) = \rho_0$ in a given time T to a density operator $\rho(T)$ with a maximum overlap to some desired target operator C is given by

$$\begin{aligned}\Phi_0 &= \mathfrak{Re}\langle C|\rho(T)\rangle \\ &= \mathfrak{Re}\langle C|U_N \cdots U_1 \rho_0 U_1^\dagger \cdots U_N^\dagger\rangle.\end{aligned} \tag{3.23}$$

In analogy to Eq. (3.20) the cost function Φ_0 can be calculated in a local sense as it depends on offsets, B_1 field inhomogeneities and J-couplings as given by the total Hamiltonian (Eq. (3.8)). A pulse that is robust against a range of offsets is obtained by the average of the local quality factors over a set of n_{off} equally spaced offsets ν_{off} in the desired range of offsets.

For Hermitian operators ρ_0 and C, this overlap is measured by the inner product [3]

$$\langle C|\rho(T)\rangle = tr\{C^\dagger \rho(T)\}. \tag{3.24}$$

The chosen transfer time T is discretized in N equal steps of duration $\Delta t = T/N$ (Fig. 3.2). During each step the control amplitudes $u_k(t)$ are constant. Using Eq. (3.24) and the invariance of a product under cyclic permutations of the factors, the cost function Φ_0 can be written as:

$$\Phi_0 = \mathfrak{Re}\langle\underbrace{U_{j+1}^\dagger \cdots U_N^\dagger C U_N \cdots U_{j+1}}_{\lambda_j}|\underbrace{U_j \cdots U_1 \rho_0 U_1^\dagger \cdots U_j^\dagger}_{\rho_j}\rangle. \tag{3.25}$$
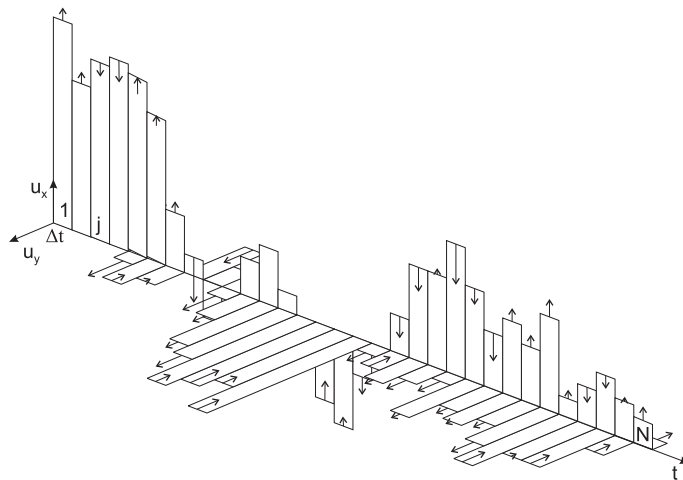
Figure 3.2: Schematic representation of a shaped pulse that is given by the control vector $u_k(t)$ for $k = 2$ (x and y controls), consisting of N steps of with duration $\Delta t = T/N$. During each step, the control amplitude $u_k(j)$ is constant. So that the total Hamiltonian H is piecewise constant. The arrows represent gradients $\partial\Phi/\partial u_k(j)$ that indicate in which direction each amplitude must be updated in order to result in an improved pulse shape. Graphic adapted from [13].

ρ_j is the density operator at time $t = j\Delta t$ and λ_j is the backward propagated target operator C at the identical time.

The response of Φ_0 according to a small variation ϵ in the control amplitudes $u_k(j)$ is given by Eq. (3.12) in first order approximation by

$$\partial U_j = -i\Delta t \partial u_k(j) H_k U_j. \tag{3.26}$$

If Δt and $|H|^{-1}$ fulfill the inequality

$$\Delta t \ll ||H_0 + \sum_{k=1}^{m} u_k(j)H_k||^{-1} \tag{3.27}$$

the first order derivative of Φ_0 is obtained as [3]

$$\frac{\partial\Phi_0}{\partial u_k(j)} = -\mathfrak{Re}\langle\lambda_j|i\Delta t[H_k, \rho_j]\rangle. \tag{3.28}$$

This gradient is used for the optimization of PP transfers by the GRAPE algorithm. The GRAPE algorithm is conducted in analogy to the description given in Chapter 3.1.2.

By assuming the dominant amplitude in the Hamiltonian H to not exceed 18.75 kHz, which may be a realistic assumption for a number of heteronuclei at a B_0 field strength of 600 MHz and a digitization Δt of typically 0.5 μs, the inequality (Eq. (3.27)) becomes equal to 8.5 μs, so that the inverse of the Hamiltonian is separated by approximately one order of magnitude from the desired timestep Δt.

This separation is often not sufficient to appropriately fulfill inequality (3.28). As a result the first order gradients deviate from the exact solution. This can lead to imperfect convergence properties of the GRAPE algorithm. The overall performance of a pulse

optimization is often limited by the update method (see Chapter 3.4), complex update methods often suffer from inaccurate gradients. As a result the cost function will not continuously improve. Instead it can perform chaotic jumps with no apparent tendency to approach to an optimal point.

3.2 Exact Gradients

As summarized in the Section 3.1.1 and 3.1.3 the first order derivatives of the cost functions may differ from the exact solution. Therefore the following is dedicated to the description of exact derivatives. Apart from other methods [12], the calculation of exact derivatives may be accomplished using the diagonalization of H. This strategy is advantageously chosen since the considered Hamiltonians are either constant or in case of a shaped pulse piecewise constant (see Fig. 3.2). These Hamiltonians are diagonalized reasonably quickly.

They key step to obtain exact gradients is the calculation of the derivatives of U with respect to the control amplitudes $u_k(t)$. Once they are known, exact gradients for Φ_3 and Φ_0 can be deduced.

For simplicity, the number of controls m (Eq. (3.8)) is assumed to be $m = 2$ in the following. This results in a control vector $(u_x(t), u_y(t))$. In general the derivative of U

$$\nabla_{x,y}U = \left(\frac{\partial \exp(-iHt)}{\partial u_x}, \frac{\partial \exp(-iHt)}{\partial u_y} \right) \tag{3.29}$$

with respect to the controls is unknown and non trivial, since the control Hamiltonians H_k do not commute with the drift Hamiltonian H_0.

$$[(Ix + Iy), Iz] \neq 0 \tag{3.30}$$

Therefore the calculation of $\nabla_{x,y}U$ includes a diagonalization of the Hamiltonian H. Apart from other methods (e.g. the Padé approximation), the diagonalization may be carried out by the use of transformation matrices that are derived from an eigenvector decomposition of H: For the considered cases, i.e. excluding relaxation and any kind of non-hermitian transfers, H is always hermitian. For each hermitian matrix exists a matrix of eigenvectors V and a matrix of eigenvalues D of the same dimension. Eigenvectors and eigenvalues may be calculated by third party software, for example by the routine ZHEEV that is included in LAPACK. It is optimized for the decomposition of triangular, symmetrical and complex eigendecompositions. For small spin systems it is comparable in speed to the diagonalization by the means of Padé approximation.

For the transformation matrices and universal propagators, the following relations are valid:

$$\begin{aligned} V^\dagger V = VV^\dagger &= \mathbb{1} \\ U^\dagger U = UU^\dagger &= \mathbb{1} \\ U^\dagger &= U^{-1} \end{aligned} \tag{3.31}$$

Where U^{-1} denotes the inverse matrix of U and $\mathbb{1}$ is the identity matrix.

V transforms H in a diagonal matrix of eigenvalues D

$$D = V^\dagger HV. \tag{3.32}$$

The exponential of D collapses to a scalar exponential

$$V^\dagger U V = \varsigma = \exp(-iV^\dagger HVt). \tag{3.33}$$

that is equivalent to the calculation of the propagator U in the eigenbasis of H. Using a second transformation

$$U = V\exp(-iV^\dagger HVt)V^\dagger, \tag{3.34}$$

the diagonal U is transformed out of the eigenbasis of H to result in the non-diagonal form that is equivalent to U obtained according to Eq. (3.12). The derivative of $\nabla_{x,y}U$ is available from the derivative of the scalar exponential function

$$\nabla_{x,y}U = \left(\frac{V\partial(\varsigma)V^\dagger}{\partial(u_x)}, \frac{V\partial(\varsigma)V^\dagger}{\partial(u_y)} \right). \tag{3.35}$$

The transformation matrices V are applicable to all species (e.g. density matrices) occurring in the context of the discussed spin dynamics. An arbitrary matrix A is transformed in the basis of H by

$$A_H = V^\dagger A V \tag{3.36}$$

and back by the operation

$$A = V A_H V^\dagger. \tag{3.37}$$

Therefore, it is principally possible to carry out the calculation of gradients either in the basis of the spin matrices I_x, I_y, I_z or in the basis of the Hamiltonian H since there is a transformation matrix for each piecewise constant Hamiltonian of duration Δt (see Fig. 3.2) the propagation (Eq. 3.13 and 3.25) is advantageously carried out independently of the actual Hamiltonian. More details on derivatives of spin dynamics are given in [12, 14, 15].

3.2.1 $\partial\Phi_3/u_{x,y}$

Starting from Eq. (3.14) and using Eq. (3.13) the derivative of Φ_3 is obtained by

$$\begin{aligned}
\nabla_{x,y}\Phi_3 &= \frac{1}{2^n} \frac{\partial\Re\langle U_F | U_{\text{eff}}\rangle}{\partial u_{x,y}(j)} \\
&= \frac{1}{2^n} \frac{\Re\langle U_F | \partial(U_N \ldots U_j \ldots U_1)\rangle}{\partial u_{x,y}(j)} \\
&= \frac{1}{2^n}\Re\langle U_F | (\underbrace{U_N'}_{=0} \ldots U_j \ldots U_1) + (U_N \ldots U_j' \ldots U_1) + (U_N \ldots U_j \ldots \underbrace{U_1'}_{=0})\rangle \\
&= \frac{1}{2^n}\Re\langle U_F | (U_N \ldots U_j' \ldots U_1)\rangle
\end{aligned} \tag{3.38}$$

Using the product rule, the only non-zero element is $U_N \ldots U_j' \ldots U_1$. U_j' is the derivative according to Eq. (3.35).

As the gradient and the quality factor Φ_3 are evaluated for a distinct offset ν_{off}, B_1 field and J-coupling, they are local. As described by Eq. (3.20) the arithmetic average of cost and gradient functions is taken in order to obtain pulses that are robust against deviations in the respective dimensions.

3.2.2 $\partial\Phi_0/u_{x,y}$

Starting from Eq. (3.23) and using Eq. (3.25) the derivative of Φ_0 is obtained by

$$
\begin{aligned}
\nabla_{x,y}\Phi_0 &= \frac{1}{2^n}\frac{\partial\mathfrak{Re}\langle C|\rho(T)\rangle}{\partial u_{x,y}(j)} \\
&= \frac{1}{2^n}\frac{\partial\mathfrak{Re}\langle U_{j+1}^\dagger\ldots U_N^\dagger CU_N\ldots U_{j+1}|U_j\ldots U_1\rho_0 U_1^\dagger\ldots U_j^\dagger\rangle}{\partial u_{x,y}(j)} \\
&= \frac{1}{2^n}\frac{\mathfrak{Re}\langle U_{j+1}^\dagger\ldots U_N^\dagger CU_N\ldots U_{j+1}|\partial(U_j\rho_{-1}U_j^\dagger)\rangle}{\partial u_{x,y}(j)}
\end{aligned}
\tag{3.39}
$$

Using the product rule and Eq. (3.39) yields

$$
\nabla_{x,y}\Phi_0 = \frac{1}{2^n}\mathfrak{Re}\langle U_{j+1}^\dagger\ldots U_N^\dagger CU_N\ldots U_{j+1}|(U_j\rho_{-1}U_j^\dagger)'\rangle.
\tag{3.40}
$$

To obtain the derivative $(U_j\rho_{j-1}U_j^\dagger)'$ the product rule is applied again:

$$
(U_j\rho_{j-1}U_j^\dagger)' = U_j'\rho_{j-1}U_j^\dagger + U_j\underbrace{\rho_{j-1}'}_{=0}U_j^\dagger + U_j\rho_{j-1}U_j^{\dagger\prime}
\tag{3.41}
$$

U_j' is known according to Eq. (3.35), $U_j\rho_{j-1}'U_j^\dagger = 0$ and $U_j^{\dagger\prime}$ is obtained starting from

$$
\begin{aligned}
(\mathbb{1})' &= (U_jU_j^\dagger)' \\
U_jU_j^{\dagger\prime} &= -U_j'U_j^\dagger
\end{aligned}
\tag{3.42}
$$

and multiplying from the left with $U_j^\dagger$ yields

$$
U_j^{\dagger\prime} = -U_j^\dagger U_j'U_j^\dagger.
\tag{3.43}
$$

As the gradient and the quality factor Φ_0 are evaluated for a distinct offset ν_{off}, B_1 field and J-coupling, they are local. As described by Eq. (3.20) the arithmetic average of cost and gradient functions is taken in order to obtain pulses that are robust against deviations in the respective dimensions.

3.2.3 $\partial\Phi_3/\partial t$

Beside from optimizing shaped pulses according to a piecewise time-constant Hamiltonian H it is possible to choose the duration Δt of the N control increments to be the variable of the optimization. Variable pulse increments or delays can be obtained by setting the rf amplitude to a distinct value or to zero-amplitude, respectively.

The time derivative is calculated trivially since the derivative of the exponent commutes with the exponential function.

$$
[-iH_j, \exp(-\mathrm{i}H_j\Delta t_j)] = 0
\tag{3.44}
$$

Starting from Eq. (3.15) the time derivative of Φ_3 is written as

$$
\frac{\partial\Phi_3}{\partial\Delta t_j} = \frac{1}{2^n}\frac{\mathfrak{Re}\langle U_F|\partial(U_N\ldots U_j\ldots U_1)\rangle}{\partial\Delta t_j}
\tag{3.45}
$$
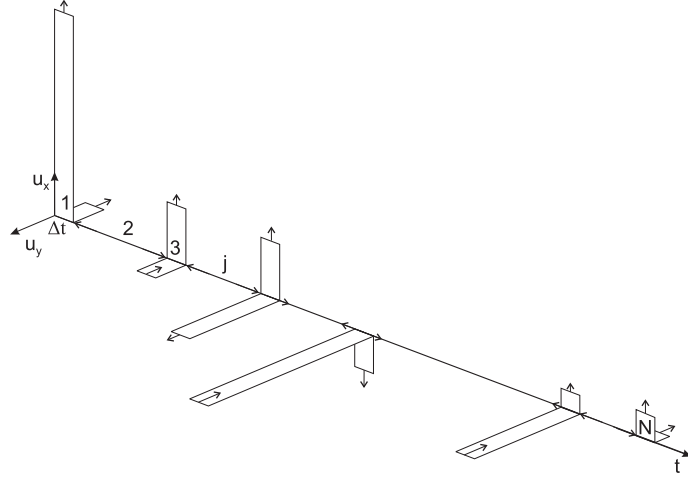
Figure 3.3: Schematic representation of a shaped pulse that is given by the control vector $u_k(j)$ for $k = 2$ (x and y controls) and $t(j)$, consisting of N steps. Odd numbered increments are chosen to have x, y rf amplitudes and x, y-gradients according to Eq. (3.38) and fixed duration. The even increments are delays of variable duration Δt_j and have zero x, y-amplitudes; the gradients with respect to time can be calculated according to Eq. (3.46 or 3.47). The arrows represent gradients $\partial\Phi/\partial u_k(j)$ and $\partial\Phi/\partial\Delta t_j$ that indicate in which direction each amplitude or delay must be updated in order to result in an improved pulse sequence. Using this scheme it is possible to optimize hard pulse-delay sequences that are especially useful for the successive optimization of coherence transfer elements: First a hard pulse-delay sequence is optimized that is time-optimal for a range of J-couplings and a desired coherence transfer. Second, hard pulses are exchanged by robust shaped pulses in order to obtain a sequence that is robust according to the total Hamiltonian H.

Using the product rule, the $N-1$ time derivatives from Eq. (3.45) vanish to result in

$$
\begin{aligned}
\frac{\partial\Phi_3}{\partial\Delta t_j} &= \frac{1}{2^n}\mathfrak{Re}\langle U_F|U_N\ldots U_j'\ldots U_1)\rangle \\
&= -\frac{1}{2^n}\mathfrak{Re}\langle U_F|U_N\ldots iH_jU_j\ldots U_1)\rangle
\end{aligned}
\tag{3.46}
$$

3.2.4 $\partial\Phi_0/\partial t$

The derivative of the cost function Φ_0 with respect to the time is obtained starting from Eq. (3.23) using the product rule and Eq. (3.42)

$$
\begin{aligned}
\frac{\partial\Phi_0}{\partial\Delta t_j} &= \frac{1}{2^n}\frac{\partial\mathfrak{Re}\langle U_{j+1}^\dagger\ldots U_N^\dagger CU_N\ldots U_{j+1}|U_j\ldots U_1\rho_0 U_1^\dagger\ldots U_j^\dagger\rangle}{\partial\Delta t_j} \\
&= \frac{1}{2^n}\frac{\mathfrak{Re}\langle U_{j+1}^\dagger\ldots U_N^\dagger CU_N\ldots U_{j+1}|\partial(U_j\rho_{j-1}U_j^\dagger)\rangle}{\partial\Delta t_j} \\
&= \frac{1}{2^n}\mathfrak{Re}\langle U_{j+1}^\dagger\ldots U_N^\dagger CU_N\ldots U_{j+1}|(U_j\rho_{j-1}U_j^\dagger)'\rangle.
\end{aligned}
\tag{3.47}
$$
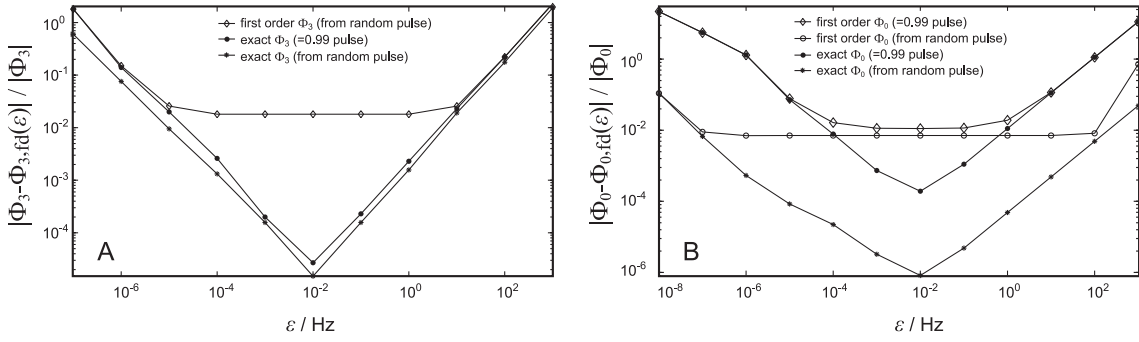
Figure 3.4: Φ_3 and Φ_0 Gradient accuracy in correlation to $\Phi_{3,\text{fd}}$ and $\Phi_{0,\text{fd}}$ finite difference gradients as a function of ϵ. ϵ is the finite difference by which the control amplitudes u are changed in order to obtain finite difference gradients. For the optimal ϵ, finite difference gradients are considered to be precise to machine precision. First order gradients ($\diamond$, $\bullet$) show higher deviations from finite difference gradients than exact derivatives for (A) Φ_3 and (B) Φ_0 cost functions. As the fidelity of random pulse is usually less perfect in comparison with a $\Phi = 0.99$ pulse, the scale of the gradients depends also on the actual fidelity and it vanishes for optimal pulses. The effect on the gradient precision is exemplarily shown for a random pulses (A, $\diamond$, $*$) and (B, $\circ$, $*$) and $\Phi = 0.99$ pulses (A, $\bullet$) and (B, $\diamond$, $\bullet$). Imperfection, noise and the dependence on the actual fidelity is more pronounced in case of $\nabla\Phi_0$ (B) as the calculation involves U and $U^\dagger$, while U is sufficient for the calculation of $\nabla\Phi_3$ (A).

$(U_j\rho_{j-1}U_j^\dagger)'$ is obtained using the product rule:

$$(U_j\rho_{j-1}U_j^\dagger)' = U_j'\rho_{j-1}U_j^\dagger + U_j\underbrace{\rho_{j-1}'}_{=0}U_j^\dagger + U_j\rho_{j-1}U_j^{\dagger\prime} \tag{3.48}$$

And $U_j^{\dagger\prime}$ is calculated according to Eq. (3.42 and 3.43) and U_j' is obtained from Eq. (3.35).

3.2.5 $\partial\Phi_{3,0}/\partial(u_{x,y}, t)$ Finite Difference Gradients

The derivative of an arbitrary function Φ can be calculated by the finite difference method. It is advantageously used if for some reason exact derivatives are not possible. Further they are used for verification and debugging: Often the design of a conceptually new shaped pulse requires the definition of a new cost function and its derivative. Whether it is possible to obtain a certain shaped pulse often uncovers first if the cost function reflects the actual question and if the derivative is correct. In this case a corresponding optimization might converge and the resulting shaped pulse gives evidence about the question whether the desired transfer properties are physically possible.

Optimizations based on the steepest ascent algorithm do not rely on the cost information. Convergence may be present even in case the gradient does not reflect the actual derivative of the cost function. In this case the pulse may not exhibit the demanded properties. The efficiency of update methods that rely on both, the cost and the gradient information can be decreased if the gradient is not the direct descendant of the cost. In the simplest case such an inconsistency can be a scalar factor. Since inconsistencies are sometimes hard to find, finite difference gradients unambiguously answer the question whether first order

and exact gradients are implemented correctly. Most of the exact gradients discussed throughout this thesis are checked by the comparison to finite difference gradients

$$\frac{\partial \Phi}{\partial u_k(t)} = \lim_{\epsilon \to 0} \frac{\Phi(u_k(t) + \epsilon) - \Phi(u_k(t))}{\epsilon}. \tag{3.49}$$

Setting ϵ to a sufficiently small positive value, this derivative can be considered exact to machine precision. In practice, the gradient becomes instable if ϵ falls below a certain value.

In principle, the calculation of one gradient $\nabla_k(j)$ requires two evaluations of the cost function. Since $\Phi(u_k(j))$ is not depending on ϵ, the calculation of the x, y-gradients is found to need $2N + 1$ full time propagations. On the first sight this seems numerically more expensive as compared to the calculation of first order and exact derivatives that only need two full-time propagations (one forward propagation and one backward propagation that is sufficient to obtain all gradients, for example x, y, z and t gradients).

But the calculation of finite difference gradients can be speeded up in the context of the GRAPE algorithm. This is due to the stepwise multiplication of unitary propagators (Φ_3) or the stepwise propagation of density matrices (Φ_0). Therefore each step of the forward propagation that yields $\Phi(\mathbf{u})$ can be stored. The numerical effort for this operation is one full time propagation. Next, an additional matrix exponential for every $u_k(j) + \epsilon$ is computed that is multiplied with each corresponding stage of the forward propagation in order to compute the gradients. The numerical effort for this step is $k * N$ matrix exponentials that corresponds approximately to k full time propagations.

Therefore, the overall numerical effort for the calculation of finite difference gradients is proportional to $k + 1$ full time evolutions ($k + 1 = 3$ full time evolutions for the calculation of x, y-gradients). Whereas the calculation of first order and exact derivatives takes 2 full time evolutions. Therefore it is concluded that the finite difference method is an efficient alternative for the numerical calculation of gradients, especially for small values of k.

Apart from that, the exact gradient contains roughly 10 matrix multiplications more than the finite difference gradient. For the calculation of complex gradients, the fraction of time spent with matrix multiplications, can be a worth considering percentage of the time of the matrix exponential. This may be surprising but is plausible when considering how easily eigenvectors and values of small, hermitian matrices are computed.

3.3 Parallel Computing

Though OCT enabled the possibility to obtain shaped pulses with thousands of independent variables computational resources are still an issue. Therefore the following briefly summarizes the key issues that define the numerical ballast. In a second step the parallelization strategy is outlined that is used throughout this thesis.

3.3.1 Motivation and Introduction

Shaped pulses that are usually obtained for one spin systems may be robust against offset and B_1 deviations. In order to accomplish the desired properties, arithmetic averages over the cost and gradient function are computed that are intended to drive the optimization towards an optimal state for a demanded robustness.

Practically, the majority of CPU-time is spent during the evaluation of the cost and gradient function. Therefore their number of executions is preferably kept as small as possible.
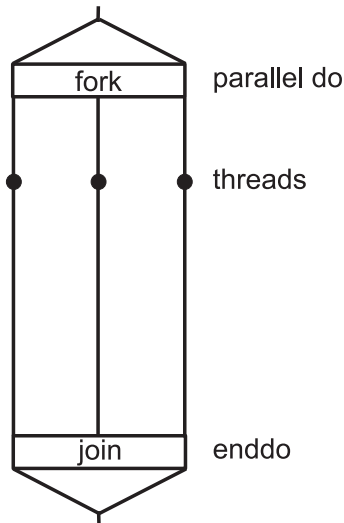
Figure 3.5: OpenMP parallelization scheme. Loops are ideally suited to create threads of sequential code by the use of compiler statements. The threads are distributed to the available CPU cores. Since the individual loops, employed in spin dynamics calculations, never rely on other loops they can be computed in parallel. The outcome of each loop is used for the calculation of an average value (denoted here as join).

It is a crucial step for the performance of the algorithm since the cost and gradient function need to be evaluated for all distinct combinations of drift and control Hamiltonians.

In practice, a grid of variables (offsets ν and B_1 deviations) define explicit points for the evaluation of the cost and gradient function. The grid with the largest mesh can be estimated by dividing the demanded range of offsets ν into v_i equidistant parts to result in ν/v_i evaluations of the cost and gradient function for each dimension i. The smallest number of v_i that results in the fastest optimization, is given by the selectivity s_i.

$$s_i = 1/t_p \tag{3.50}$$

Assuming a given pulse length t_p, the smallest value of v_i is given by

$$v_i = \nu/s_i. \tag{3.51}$$

As a shaped pulse must be robust against all possible combinations of the n_i different offset and B_1 dimensions, the number of cost and gradient evaluations v is given by the product:

$$v = \prod_{i=1}^{n_{i,\mathrm{max}}} v_i \tag{3.52}$$

As a result, single spin pulses with $n_i = 2$ are readily obtained using present PCs. Whereas optimizations based on two spin systems with $n_i \geq 3$ already pose severe numerical demands to the hardware that are only met adequately by the usage of parallelization techniques.

3.3.2 Parallelization Strategy

The most obvious way to convert a sequential code in a form that can be executed in parallel is illustrated by the fork-join model (Fig. 3.5). The single cycles of a loop construct make up a fork. Each cycle is distributed to one of the available CPU cores and is called a thread. The number of threads equals the number of CPU cores and the most efficient setup is obtained if each core has to perform the same number of cycles.

As discussed in the context of spin dynamics, the crucial numerical ballast is created within the loops of the cost and gradient function. Furthermore, each cycle is entirely independent from all others, e.g. there are no functions that depend on variables of another thread. Only the final cost or gradient obtained at the very end of each thread is used for the calculation of an average value. The formation of this value is considered to be the "join" of the parallel region that is depicted in Fig. 3.5.

The most common methods used for parallezation are MPI (Message Passing Interface) and OpenMP (Open Multi-Processing). MPI is a standard for message-passing that is explicitly used within the source code in order to obtain processes that cooperatively solve a problem. In contrast the paradigm of OpenMP is the creation of threads from loops. It is introduced via compiler statements that are assigned to the sequential source code. OpenMP is chosen for the parallelization of the discussed spin dynamics calculation because it is ideally suited for the execution on shared memory systems (processors that share the same RAM). It is expected to provide very robust performance and good scaling properties (linear speedup) on contemporary multi-core processors. Further, supercomputers combine the complementary advantages of MPI and OpenMP. MPI is used for the communication between the nodes, while OpenMP is used for the parallelization within the nodes. Another frequently applied strategy for the parallelization of nodes is the use of virtual shared memory protocols (SMP), which extents the application of OpenMP to a larger number of nodes.

The numerical character of spin dynamics is ideally suited for parallelization. Assuming that approximately all CPU time is spent in the parallel region the first guess according to Amdahl's law would be that the speedup S increases linearly until a maximum. The maximum is reached if the number of processors equals the number of threads and the number of cycles.

$$S = t_{\mathrm{seq}}/t_{\mathrm{parallel}} \tag{3.53}$$

The speedup S is defined as the quotient of the sequential execution time and the parallel execution time. The speedup S can be plotted against the number of cores that are used in the parallel region to obtain a graph that is constrained by the theoretical limit that is the bisecting line. Using the calculation of the speedup as a concept, different computers and architectures can be judged in terms of their parallel performance.

The characteristic of the speedup-plot is to eliminate any absolute performance measure of the considered systems. It is therefore useful for the scientific study of parallel computing but less useful in order to determine the system with the highest overall performance. Therefore, the correlation of the number of iterations as a function of the number of cores is preferred (Fig. 3.6). It allows the measure of the absolute performance that is defined as the number of iterations that are performed in a given time and secondly, gives evidence about the speedup. An efficient speedup is identified if the graph approaches a linear ascent.

For the current study a two spin system is used and a PP is defined by the transfer $I_z \to I_y$. The pulse length is $t_p = 500\ \mu$s with 1000 increments. 241 distinct offsets of the first spin
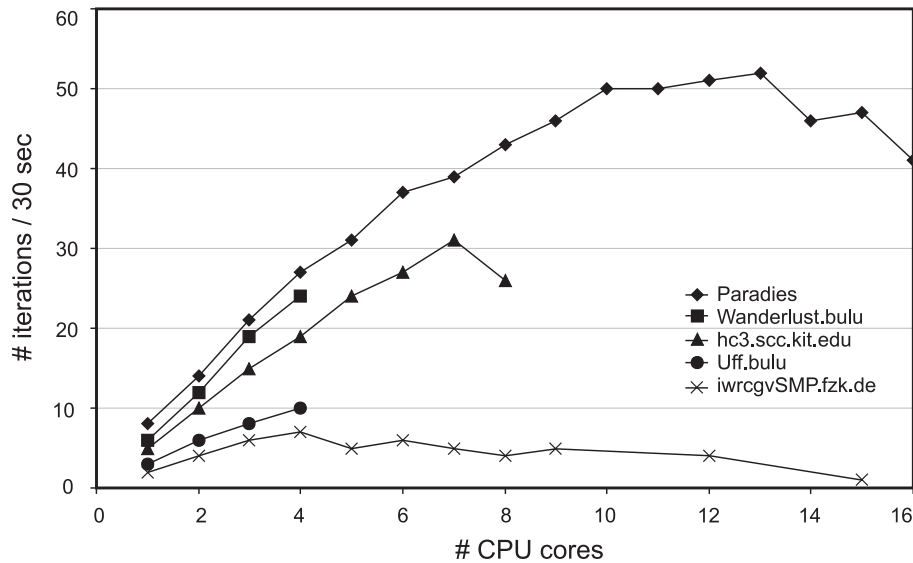
Figure 3.6: Performance obtained for OCT optimization using self written Fortran code. The number of iterations that are performed within 30 seconds is plotted as a function of the used CPU cores. A two spin calculation is carried out for the desired Φ_0-transfer ($I_z \rightarrow I_y$). The pulse length is $t_p = 500$ μs with a increment duration of $\Delta = 0.5$ μs resulting in $2*1000$ independent variables (x and y amplitudes). The loop over the offsets contained 241 cycles. The update method is steepest ascent. 5 linux based systems with details given in Table 3.1 are benchmarked: 16 cores ($\blacklozenge$), 4 cores ($\blacksquare$), 8 cores ($\blacktriangle$), 4 cores ($\bullet$ and 32 cores ($\times$). For all computers, the number of iterations increases almost linearly. A threshold is found for 12 cores ($\blacklozenge$). Only the virtual shared memory system (SMP) ($\times$) delivers less than the expected gain. Therefore it is concluded that shared memory systems, for example common desktop PCs equipped with multi core CPUs, reliably deliver the expected parallel performance and are ideally suited for the intended calculations. I like to thank PD Dr. J. Paradies from Karlsruhe for the possibility to use the *Paradies*-parallel computer.

are considered for 241 evaluations of the cost and gradient function. The update method is steepest ascent. The number of iterations carried out during 30 seconds of optimization is plotted against the number of cores (Fig. 3.6). The described setup is performed on the computers listed in Table 3.1.

Fig. 3.6 indicates speedups that are close to linearity for $n_{\mathrm{cores}} < 12$. Especially the performance increase for common quad or eight cores has always been observed to be very close to the theoretical limit, regardless of the architecture, operation system, release version of libraries and any other parameter. For example the overall performance is independent of the specific version of lapack and whether libraries are linked dynamically or statically (data not shown).

Considering the 16 core system (Fig. 3.6, $\blacklozenge$) it is observed that the parallelization procedure works for $n_{\mathrm{cores}} < 12$. According to Amdahl's law the fraction of time spent during the sequential execution of code would be $1/12 = 0.083$, which corresponds to 8.3%. Indeed 8.3% is not negligible and somewhat higher than the primarily expected value. Further, the performance plot is expected to asymptotically approach the maximal speedup, this is not exclusively observed: While there is a flattening in the linear part ($n_{\mathrm{cores}} < 12$) that could lead to an asymptotical behaviour, the graph becomes chaotic, once n_{cores} ex-

Table 3.1: Computers Used for the Parallelization Benchmark (Fig. 3.6)

Name	CPU # cores	Clock /MHz	Bit	Operating System	Age /Years
♦ Paradies	16	2.3	64	Ubuntu 3.5.0-252	1
■ Wanderlust.bulu	4	3.07	64	Centos 6.18-348.1.1.el5	2
▲ hc3.scc.kit.edu	8	>2.6	64	SUSE 3.0.42-0.7	-
• Uff.bulu	4	2.33	32	SUSE 2.6.25.18-0.2-pae	7
× iwrcgvSMP.fzk.de	32	2.0	64	Red Hat 2.6.21.7-5.vSMP	-

ceeds 12. This behaviour might be due to instabilities so that it is assumed that other factors than the ratio of sequential to parallel code, limits the maximal speedup. This is also supported by the fact that the maximum speedup does not increase if the number of pulse increments are increased, which increases the parallel allotment (data not shown). Further, the tendency to omit chaotic behaviour is found to be somewhat higher for the case of the SMP system (Fig. 3.6, ×) that is the more complex system.

More detailed studies on the parallelization properties would require the measure of the load balance that can be deduced from the CPU-time of the individual threads and the use of parallel debugging tools like the intel-inspector or scalasca to examine cache contentions and bandwidth contentions. However, this exceeds the scope of this chapter and is not pursued further.

Therefore it is summarized that speedups < 12 are reliably obtained for standard shared memory systems, which reduces the time demands by approximately one order of magnitude as compared to the sequential execution; enabling the efficient calculation of shapes with approximately $2 * 2000$ variables. As outlined in Chapter 8, this is sufficient for the optimization of the 600 μs BUBI-pulse. Further, longer shapes can be obtained by combining parallelization with z-controls, which allow to increase the duration of a time step to approximately some 10 μs. Finally, the achieved computational performance is still not sufficient to tackle the optimization of entire coherence transfer elements in higher spin systems. This problem is especially hard to tackle because it is not known whether the computational resources are the limiting factor or whether the convergence properties, according to the more complex hyper surface, is the bottle neck.

3.4 Update Methods and Convergence Properties

The update method is used to compute the control vector for the next iteration. The right setup of the update method limits the convergence and is therefore decisive for the speed of the OCT algorithm (see Fig. 3.7). Close to the global maximum the convergence is also determined by the gradients precision (see Section 3.2.5).

3.4.1 Steepest Ascent

As outlined in Section 3.1.1, steepest ascent is the easiest method to obtain the control vector $u_m^r(t_k)$ for the next iteration $u_m^{r+1}(t_k)$. It uses only the gradient information for the computation of the new controls according to

$$u_k^{r+1}(j) = u_k^r(j) + \epsilon^{(r)} \nabla_k \Phi(j), \tag{3.54}$$

k denotes the control Hamiltonian, r the iteration and j the control. $\epsilon^{(r)}$ is the step size parameter that is chosen to be a small, positive number, or is determined by a line search. Therefore it may be not identical for consecutive iterations.

Practically, steepest ascent shows slow convergence properties in many cases. If $\epsilon^{(r)}$ is to small, a single iteration of the algorithm is like a tiny, craven step on a long and shallow hyper surface. If $\epsilon^{(r)}$ is too large, it can not be expected that the way towards the global maximum is still pursued. Often, a chaotic behaviour of the cost is therefore observed close to the maximum if $\epsilon^{(r)}$ is chosen wrong. This is the motivation on the use of line search algorithms that can be used to determine the optimal step size.

3.4.2 BFGS and l-BFGS

Second derivatives as provided by the Hessian matrix can improve the convergence properties when being close to the global maximum. As the computation is expensive, methods for the approximation of the Hessian information are advantageous. The Broyden-Fletcher-Goldfarb-Shanno (BFGS) method uses only first-order gradient information for the approximation of the Hessian.

Further, the limited-memory variant of the BFGS (l-BFGS) is especially useful for large scale problems, since it requires the Hessian actually never to be calculated or stored. Instead, a short history of gradients is sufficient (e.g. the last 10 or 20 gradients). More detail about BFGS-methods is given in [16].

In the context of this thesis, Ipopt [17] is used. Ipopt is an Interior Point OPTimizer for the computation of large scale non-linear problems that uses an l-BFGS implementation. It is available for C++, C and Fortran. The cost and the gradient function, the control vector and the boundary conditions are provided to the solver that maximizes the cost under the given conditions. Second order methods demand exact gradients. Otherwise they are known to become instable. In the current work they are found to run instable for a number of advanced cost functions. This might be an intrinsic problem of the l-BFGS approximation procedure or due to technical reasons, e.g. an instable release. As a result they are reported to be fast throughout the work presented in this thesis but less reliable to obtain convergence in comparison to the other two update methods.

3.4.3 Conjugated Gradients

The idea behind conjugated gradients (CG) is to combine the advantages of a first-order method with that of a second-order method. Being far away from the optimum, it behaves like a first-order method. Close to the optimum it behaves like a second-order method without actually computing any Hessian information. CG is available in the FRPRMn (Fletscher Reeves Polak Ribiere Minimization) routine that is available for Fortran.

An exhaustive discussion of the algorithm is beyond the scope of this introduction. More details are found in [18]. Main steps of the algorithm are the following issues:

- At the current point, a sequence of orthogonal directions for every control j and control Hamiltonian k is created $d_1, \ldots d_{j \cdot k}$.

- The maximum for each direction d is computed and it is used for the search in the next direction

$$u_k^{r+1}(j) = u_k^r(j) - \alpha_i d_i \tag{3.55}$$

with $\alpha_i = arg\ min\Phi(u_k^r(j) - \alpha_i d_i$ being a scalar that is to be determined by a one-dimensional search [15]. Supposing that $\{d_i\}$ forms an orthogonal basis, we obtain

$$u_k^{r+1}(j) = u_k^1(j) - \sum_{i=1}^{j \cdot k} \alpha_i d_i. \tag{3.56}$$

More details on conjugated gradients are given in [18].

3.4.4 Line Search

The discussed update methods share the need to find an optimal scalar parameter (ϵ or α). This problem is referred to as line search [15]. Many approaches for the calculation of these parameters exist. But a detailed study is beyond the scope of this work. Therefore, the line search algorithms included in the described software packages are used with default settings.

3.4.5 Numerical Evaluation of Update Methods

The numerical performance of an OCT algorithm can be defined by the difference between desired and the actual fidelity that is obtained after a given number of steps or time.

As a benchmark scenario a not coupled two spin system is considered and the desired transfer is defined by Φ_0 to accomplish $(I_z + S_z) \rightarrow -(I_z + S_z)$. For each nucleus an offset range of 5 kHz is considered that is discretized by 6 explicit, equidistant points. A pulse with duration $t_p = 300$ μs and a timestep of $\Delta = 0.5$ μs is chosen. The rf amplitude for both nuclei is truncated to 20 kHz and the B$_1$ field inhomogeneity is switched off.

10 optimizations starting from random controls (max. random amplitude: 20 kHz) are performed for each of the update methods.

- Constant ϵ denotes the steepest ascent. ϵ is set to $1 * 10^9$.

- CG denotes conjugated gradients according to the FRPRMn (Fletscher Reeves Polak Ribiere Minimization) implementation. The tolerance level is set to 0.1.

- l-BFGS-30 denotes the limited memory BFGS implementation as provided by the Ipopt implementation that uses a history of 30 gradients for the approximation of the Hessian. Ipopt is ran with default parameters.

The difference of the fidelity function to one is given in correlation to the CPU wall time in logarithmic scale for first order gradients (Fig. 3.7A) and exact gradients (Fig. 3.7B).

According to Fig. (Fig. 3.7) the first thing that attracts attention is that optimizations performed with the identical update method clearly cluster around a well defined convergence trajectory. The vertical width of trajectories spans 1-2 orders of magnitudes and seems to be a result of the initial conditions. Accordingly, it is concluded that the optimization of a single pulse is not sufficient if the objective is to find an optimal pulse. A procedure that is pursued throughout this thesis is to optimize an ensemble of pulses, starting from random controls, while only the best is chosen for further considerations.

The smallest distribution within the convergence trajectory is found for the constant ϵ optimizations that also exhibit the smoothest graphs. The more efficient update methods (CG and Ipopt) tend to result in increasingly unsteady graphs. While CG normally reliably converges towards higher fidelities, the used Ipopt solver can get stuck as indicated by the horizontal lines in Fig. 3.7 (red).
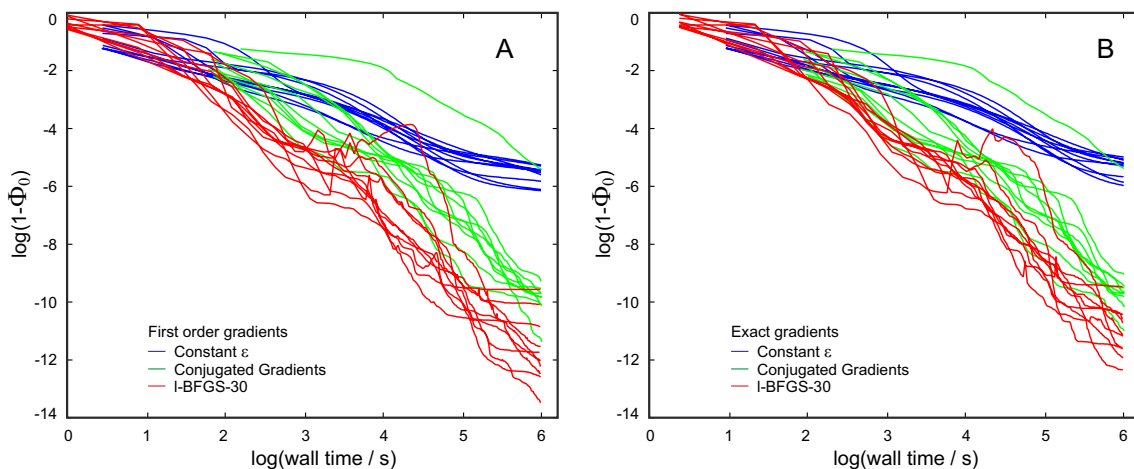
Figure 3.7: Convergence benchmark of OCT optimizations using different update methods. Update methods are: Constant ϵ (blue), conjugated gradients (green) and l-BFGS (red). For each update method, the convergence progress of 10 pulses, starting from random controls, is given for Φ_0 first order gradients (A) and Φ_0 exact gradients (B). Details on the numerical setup are given in the main text.

Nonetheless, BFGS assisted OCT is hardly outperformed by other update methods. More details on the performance of different update methods are given in [15]. As this kind of numerical studies normally focuses on the range of $1 - \Phi = 10^0 - 10^{-4}$ they give detailed insight in numerous pros and cons of the computational details but are less insightful in the context of practical pulse optimizations since the mentioned range of benchmarked fidelities corresponds to $\Phi = 0 - 0.999$ while a commonly used shaped pulse should have a minimum fidelity of at least 0.999. For practical considerations, studies should therefore focus on the range $1 - \Phi < 10^{-4}$, e.g. as depicted in Fig. 3.7.

Comparing 3.7 A and B it is worth noting that for the discussed setup, first order and exact gradients results in relatively identical convergence-profiles. This might be also owing to the fact that the fidelity is plotted as a function of the wall time and not as a function of the number of steps.

3.5 Exploring Physical Limits of Spin Dynamics

This section is intended to summarize some aspects of spin dynamic optimizations by OCT that is concerned with physical limits. For example whether a desired transfer is physically possible given a certain amount of time and peak rf power. Or with other words: How to set reasonable optimization parameters without guessing.

Apart from the advantages, discussed so far, OCT of spin dynamics has some more blessings, when compared to other quantum chemical methods (e.g. DFT-calculations). E.g.: What is the minimum energy electron density? The intrinsic problem about that kind of questions is that there may be always a lower energy state, not obtained in the calculation.

In contrast, OCT has a good starting condition because it is not concerned about minimum energies. Or with other words: While the problem of finding a minimum energy structure is the problem of finding an unknown structure, OCT is concerned about finding the optimal trajectory between two known states: The initial and the final state. Known initial and final states imply that there can be the calculation of a cost at each point of the trajectory, and the maximum of that cost may never exceed 1. Once, the fidelity

of the obtained shaped pulse approaches that value, it is assured that the transfer will be accomplished. Shaped pulses obtained throughout this thesis usually report a quality factor Φ of at least $\Phi = 0.999$.

This, however, does not answer the question whether there are other pulses, which facilitate the same fidelity but consuming less rf power, time or whatsoever. Such a pulse that performs close to the physical limit, regarding a certain property, is referred to as an *optimal pulse*. Exploring the limits of OCT spin dynamic simulations is a tool to evaluate estimates on physical bounds and is described in the following.

3.5.1 Optimization Procedure

A systematic study of pulse performance, similar to the one performed previously for PP and inversion pulses [7, 8], is performed for UR pulses using the described algorithm based on optimal control theory. Sets of 90° and 180° rotations are calculated for different bandwidths ranging from 10 kHz to 50 kHz with the rf amplitude limited to 10 kHz in all cases. Optimizations are performed using the performance function Φ_3 (Eq. (3.14)) with the two target propagators $\pm U_F$ for the case of 90° UR pulses, corresponding to U_F and $-U_F = e^{i\pi} U_F$ corresponding to 90°_y and 270°_{-y} rotations. In the case of 180°_y UR pulses, only the optimization of a single target propagator U_F is necessary because the quality criterion for a broadband 180°_y pulse is identical to the quality criterion for a broadband 180°_{-y} pulse. This is a direct result of the fact that a 180°_y pulse can be transformed into an equivalent 180°_{-y} pulse simply by shifting all pulse phases by π. Generally, pulse durations are incremented until the corresponding quality factor exceeded a value of 0.995. For the optimization, each chosen bandwidth is divided into equal increments, with $n_{\text{off}} = 100$. The time digitization for the optimized shapes is 0.5 μs in all cases.

The results of the optimizations of 90° and 180° rotations are depicted in Fig. 3.8 where the corresponding performance functions are given with respect to the pulse length. As previously found for PP excitation and inversion pulses [7,8] UR pulses show a performance that is step-wise increasing with increasing pulse lengths.

UR pulses have been used for decades and it is important to evaluate the performance of previously published composite and shaped pulses in the context of the systematic study presented here. We therefore compare in Fig. 3.9 all 90° and 180° UR pulses we could find in the literature with corresponding BURBOP performance. For this comparison, we scaled all pulses to the maximum allowed rf amplitude of 10 kHz and looked for the maximum bandwidth with the overall quality factor $\Phi_3 = 0.99$. We chose this value as it confines a relatively good performance which is covered by most conventional published pulses. Many of the simulated pulse shapes are too long to be represented in Fig. 3.9. For some of the UR pulses, which are for example optimized for bandselectivity like the pulses reported in [21,25], the quality factor might not be adequate because of the different goal of the original optimization. The result of the comparison, however, is surprising: For UR 90° pulses none of the previously published pulses is shorter than the corresponding BURBOP-90 shapes and only few composite 180° UR pulses for very short durations [22, 26] and a very recent pulse shape optimized by optimal control [27] get near the BURBOP-180 performance. Many of the previously published pulses have twice the pulse length of time-optimal BURBOP pulses with the same overall performance, leaving ample room for improvement.

3.5.2 Discussion

In spin systems where the theoretical limits of quantum evolution are known [29–35], numerical algorithms based on principles of optimal control theory provide pulse sequences
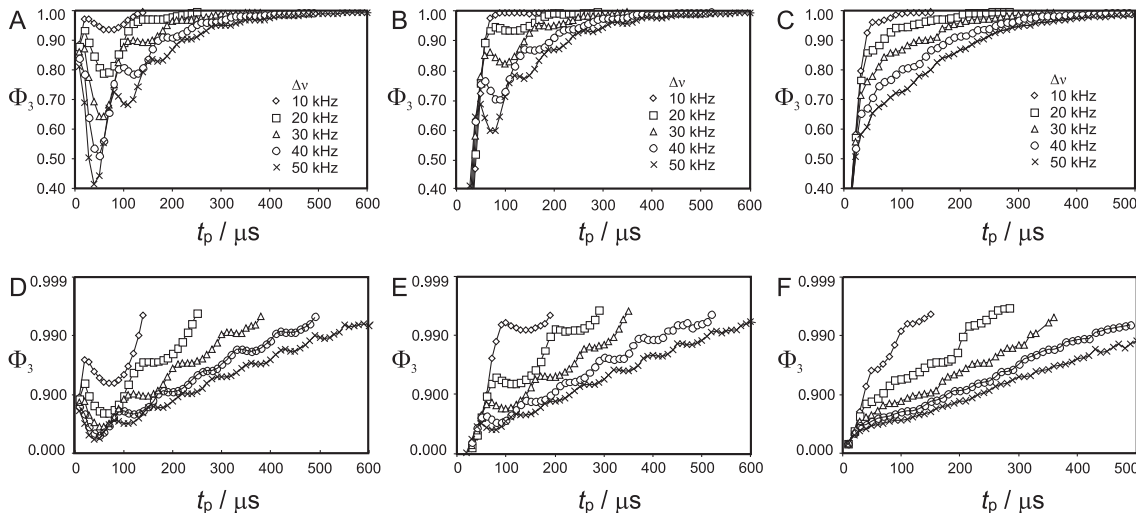
Figure 3.8: Maximum quality factors reached for broadband universal 90° and 180° rotations. Optimum performances are shown for offset bandwidths ranging from 10 kHz to 50 kHz. Rf amplitudes are generally limited to 10 kHz and rf variations are not taken into account. The absolute value of optimal performances for 90° rotation pulses are given for the quality factor Φ_3 with target propagator U_F (A, D) and $-U_F$ (B, E). The corresponding curves for 180° rotations for the target function Φ_3 are depicted in (C, F). Plots in (D-F) show data identical to (A-C) using a semilogarithmic scale.

which approach the physical limits [36, 37]. An optimal control theory based numerical algorithm therefore appears to be a well-suited tool to explore the physical limits for robust broadband excitation, inversion and universal rotations. Using *exploring the limits* as a concept this results may be expanded to other pulse families, since the search for limits is expected to pretend on some generality to provide the estimates for physical boundaries [38]. This should also apply for the systematic study of coherence transfer elements that are the main subject of the current thesis. *Exploring the limits* is used to find the most efficient sequence. Accordingly, the found sequences should perform close to the *best possible* sequence.

It is emphasized that the pulses presented for a given set of parameters establish lower bounds for the physical limits of pulse performance, since there is no guarantee that the ultimate upper bounds are actually reached. For example the GRAPE optimizations for BURBOP pulses (Fig. 3.8) show very good convergence, but might represent only local optimal solutions rather than the global optimum. The results presented in this thesis provide high performance quality factors for a given set of parameters such as pulse duration, maximum rf amplitude, and compensation for B_1-inhomogeneity that are readily attainable. One needs not settle for pulses with significantly lower performance. Whether a more efficient pulse is possible remains an open question.

The hypothesis that OCT derived pulses are likely to approach the actual physical limit is also supported by the fact that pulses of higher efficiency (e.g. less time consumption while retaining an certain fidelity for a given robustness) are, so far, never reported in literature. This is exemplarily shown for our OCT-derived UR pulses (Fig. 3.9) that are compared to all known UR pulses that are accessible to us at the present time. Not even analytically derived pulses exceed the performance of the proposed OCT-pulses [9].
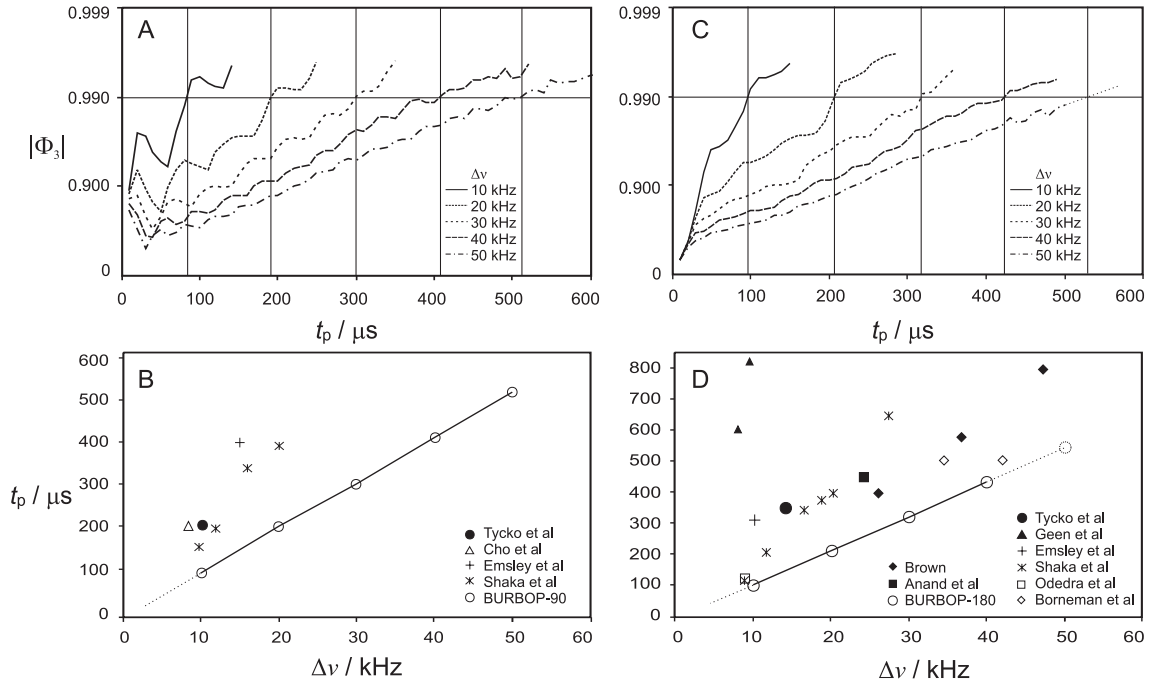
Figure 3.9: Comparison of BURBOP-90 and BURBOP-180 pulses with previously published UR pulses. The maxima of so-called TOP curves from Fig. 3.8 are used to define time-optimal pulse shapes with $\Phi_3 = 0.99$ (indicated by grid lines as guide to the eyes) for BURBOP-90 (A) and BURBOP-180 pulses (C). Previously published UR pulses are scaled to 10 kHz maximum rf amplitude and the largest bandwidth with $\Phi_3 = 0.99$ determined (B and D). 90° UR pulses are taken from (B): Tycko et al. [19], Cho et al. [20], Emsley et al. [21], Shaka et al. [22]. 180° UR pulses are from (D): Brown [23], Anand et al. [24], Tycko et al. [19], Geen et al. [25], Emsley et al. [21], Shaka et al. [22], Odedra et al. [26], Borneman et al. [27]. Additional pulses from [6, 28] are considered but result in values outside the plots. None of the previously existing UR pulses achieve the optimal performance limits of the BURBOP pulses. Dotted lines indicate extrapolation.

4. COB-INEPT

4.1 Introduction and Motivation

Modern NMR spectroscopy is based on complex radio frequency pulse sequences designed to enable efficient magnetization transfer via specific pathways and the corresponding evolution of desired spin densities. The pulse sequences usually can be divided into several well-known basic elements, developed e.g. for coherence transfer via J-couplings or the evolution of chemical shifts with effective suppression of such couplings. It is essential that these elements are very robust with respect to all types of experimental imperfections and that they adequately address expected variations of spin systems under study.

Today's availability of high magnetic fields, the extension of NMR spectroscopy to new types of samples, and novel applications with ever higher demands on reproducibility and spectral comparability require improved technologies, including robust pulse sequence elements. In this context, several fundamental aspects affect the quality of practically every high resolution NMR experiment: the coverage of involved resonance offsets and couplings, the compensation of unavoidable imperfections like B_1-field inhomogeneities, and the adequate consideration of dynamic effects like relaxation or exchange. Our goal here is to present a viable approach to systematically optimize such pulse sequence elements to the desired needs for applications regarding small to medium-sized organic molecules. The procedure for the example of INEPT-type transfer in spin systems with a relatively large variation of heteronuclear one-bond coupling constants as observed in small molecules containing acetylene-type groups or partially aligned molecules with the presence of residual dipolar couplings (RDCs) is demonstrated.

The INEPT transfer element was introduced in 1979 [39, 40] and since then has been the central element for heteronuclear inphase-to-antiphase transfers in a vast number of applications, including for example the HSQC [41] and all types of triple resonance experiments (see e.g. [42]). Very early, attempts were made to improve the robustness of the pulse sequence element. It became evident that the most critical pulse of the sequence is the 180° pulse on the heteronucleus, which has been replaced by offset-compensated inversion pulses [43, 44]. Furthermore, small improvements have been achieved by replacing all pulses of the element by broadband shaped pulses [45, 46]. Compensation against variations in J-couplings was introduced in a series of publications, either based on direct optimization of the transfer element using known composite pulses in the so-called broadband-INEPT [47], by the ACCORDION approach, in which several scans with different transfer delays are added [48], or by an empirical relation found for chemical shifts and J-couplings [49, 50],

which, however, only works for sp^3 and sp^2 hybridized carbon moieties in isotropic samples. The occurrence of dynamic effects, finally, led to a multitude of different approaches. For the refocussing of exchange effects, for example, HEHAHA-type transfer elements [51], and CPMG-based elements [52–54] have been introduced, which create homonuclear effective isotropic mixing conditions for the exchanging nuclei; and loss due to relaxation has been minimized in transfer elements like the ROPE sequences, which provide maximum coherence transfer in the presence of autorelaxation [33], and a multitude of elements has been designed for the presence of significant cross-correlated relaxation [34, 55–57].

In the following, the specific needs of a robust INEPT-type transfer element for small molecules are outlined and provide a viable optimization strategy for the desired task.

4.1.1 Experimental Requirements

For an effective optimization, it is necessary to specifically define the goal of the desired transfer. As a first step, a compilation of the required properties of the transfer element is provided, which will be the ^{1}H,^{13}C-INEPT with wide-spread use in natural abundance, small molecule samples.

Especially in heteronuclear NMR spectroscopy, offset effects arise from the mismatch between the possible radio frequency strength and the broad range of spins that need to be excited. If one wants to cover all diamagnetic carbon spins directly attached to a proton, including methyl groups as well as aldehydes, an effective chemical shift range of roughly 250 ppm must be addressed. Considering a 600 MHz spectrometer as a typical high-field instrument in use for small molecule applications, this results in a required carbon bandwidth of 37.5 kHz. On the proton side, a chemical shift range of only 12 ppm is needed. However, to be on the safe side, optimization for a 10 kHz bandwidth are done, corresponding to 16.6 ppm on a 600 MHz spectrometer.

Regarding the range of couplings over which effective coherence transfer has to be achieved, two applications are considered: on one hand routine applications on isotropic samples with J-couplings ranging from 120 Hz in sp^3 hybridized groups to 250 Hz in sp hybrids; and on the other hand applications comprising weakly oriented samples with residual dipolar couplings (RDCs) spanning typically ±30 Hz on top of one-bond J-couplings. With these applications in mind, it was decided to define the optimization range from $J_{\min}$ to $2.2J_{\min}$, corresponding to approximately the 120-250 Hz range of isotropic samples and the (RDC+J)-coupling range of aliphatic and aromatic moieties.

For the available RF-amplitude, safe upper limits of 20 kHz for protons (corresponding to a 12.5 μs 90° pulse) and 10 kHz for carbons (corresponding to a 25 μs 90° pulse) have been used that should easily be accomplished by the vast majority of modern inverse probeheads designed for the acquisition of proton signals. After having significant experience with a number of different probeheads, it was decided to take a compensation against B_1-field inhomogeneties of $\pm5\%$ for the carbon channel into account as well as a corresponding compensation of $\pm20\%$ for the proton channel, where the latter one was motivated by the B_1-field variety of high Q cryoprobes.

As the application of the transfer element focusses on small molecules, effects like cross-correlated relaxation and differences in T_1 and T_2 can be neglected to a good approximation. In this case, an explicit treatment of relaxation is not necessary and it is sufficient to look for a time-optimal solution [29, 58]. Exchange effects are not taken into account in our optimization procedure, but as will be discussed later, their compensation can in principle be accomplished by the addition of CPMG-type elements.

4.2 Optimization strategy

In a first attempt to optimze the INEPT-type transfer element, optimizations for inphase-to-antiphase transfer were started, including all combinations of offset bandwidths and scalings of B_1-fields on both nuclei and the defined range of couplings using a heteronuclear two-spin system represented by spin density operators. The algorithm used is based on the GRAPE approach [3] with calculated spin density after the pulse sequence ρ_N and desired density operator ρ_F, imposing hard limits on maximum RF-amplitude and using the cost function

$$\Phi_0(\nu, \vartheta, J) = Re\langle\rho_F|\rho_N\rangle \tag{4.1}$$

averaged over all combinations of offsets ν, B_1-scalings $(1 \pm \vartheta)$, and coupling constants J in the desired ranges for the evaluation of transfer. Optimal control based algorithms like GRAPE are known to provide very good convergence properties for a wide range of spectroscopic problems [59–62] that usually outperform classical approaches when optimizing trajectories. However, with the multitude of conditions related to the INEPT-type optimization problem, the algorithm did not converge after two months of calculations on a quad-core PC for a fixed transfer duration of 8 ms and piecewise constant timesteps of 5 μs length. Most likely, the algorithm cannot escape local minima with the boundary conditions applied.

As the problem appears to be too demanding for a direct optimization with currently available computational setups, it was decided to focussed on a stepwise strategy in which it was tried to separate individual requirements to reduce the hypersurface for calculations and allow better convergence. A general strategy that worked very efficiently in our case is based on two independent optimization steps with relatively fast convergence, the time-optimal compensation of a range of couplings on the one hand and the improvement of robustness with respect to offset and B_1-field variations on the other hand. The strategy consists of a number of individual techniques that have been successfully applied in the past and can be summarized as follows:

1. Systematically optimize coherence transfer with respect to the range of desired coupling constants for a variety of transfer times and no restrictions on RF-amplitude assuming that coupled spins are on-resonance. Approximate these ideal solutions in a DANTE-type approach by a hard pulse-delay sequence as preparation for the robustness introduced in step 2.

2. After picking out the best solution with respect to coherence transfer, insert 180° pulses in the centers of all delays and replace hard pulses by offset- and B_1-compensated pulse shapes.

With this general approach, it should be possible to obtain robust pulse sequence elements for all types of coherence transfer as long as relaxation properties are not expected to dominate transfer efficiencies. In the following sections detailed steps towards the COB-INEPT sequence are given using the derived optimization strategy and different flavors of the GRAPE algorithm for individual optimizations.

4.2.1 *J*-compensation

Efficient coherence transfer in the presence of a range of coupling constants has been of interest since the invention of the INEPT transfer element [47, 63–66]. *J*-compensated experiments like the broadband-INEPT [47] were derived using existing phase-alternating composite pulses via a simple geometric relation of coupling and offset evolution in the
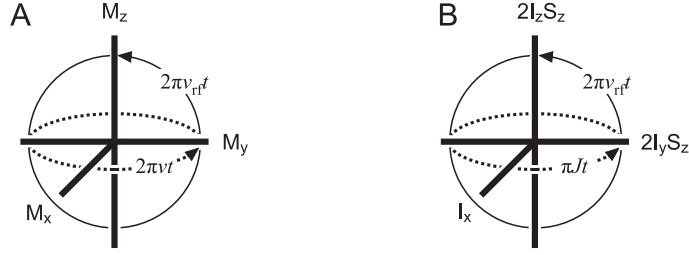
Figure 4.1: Equivalence of magnetization components of a single spin 1/2 (A) and the evolution of J-coupling in a two-spin system (B). Both frames allow the description of RF-pulses with the effective rotational axis along x.

Bloch picture: While coherence transfer via J-couplings in the weak coupling limit is described by the relation

$$I_x \xrightarrow{2\pi J I_z S_z t} I_x \cos(\pi J t) + 2I_y S_z \sin(\pi J t), \tag{4.2}$$

the evolution of offset ν in the Bloch picture is represented by

$$M_x \xrightarrow{2\pi \nu M_z t} M_x \cos(2\pi \nu t) + M_y \sin(2\pi \nu t). \tag{4.3}$$

Within their coordinate systems, as is visualized in Fig. 4.1, $2I_z S_z$ and M_z are rotated by identical angles around the z-axis for $\nu = J/2$. Similarly, rf pulses applied along the x-axis with amplitude $\nu_{\rm rf}$ give the corresponding transfers

$$2I_z S_z \xrightarrow{2\pi \nu_{\rm rf} I_x t} 2I_z S_z \cos(2\pi \nu_{\rm rf} t) - 2I_y S_z \sin(2\pi \nu_{\rm rf} t) \tag{4.4}$$

and

$$M_z \xrightarrow{2\pi \nu_{\rm rf} M_x t} M_z \cos(2\pi \nu_{\rm rf} t) - M_y \sin(2\pi \nu_{\rm rf} t), \tag{4.5}$$

respectively. However, the transformation obtained using rf pulses applied along the y-axis cannot be expressed within the coordinated system shown in Fig. 4.1B. As a consequence of the correspondence shown in Figs 4.1A and 4.1B, results obtained for purely phase-alternating offset-compensated composite pulses applied along x can directly be transferred to heteronuclear coherence transfer experiments. However, it should be noted that the equivalence of the Bloch picture implies that the transfer is only optimized for the on-resonant case, without possibility to optimize offset and coupling variations simultaneously.

For the first step in our optimization strategy, equivalence to explore the physical limits of on-resonant coherence transfer in the Bloch picture is used as previously reported for broadband excitation and inversion pulses [7, 8]. Using the same quality factor as in [7] ($\Phi = \mathbf{M}(t_p) \cdot \mathbf{F}$), a shape consisting of x-pulses with overall durations t_s of 4.0 to 16.0 ms and individual pulse lengths of 100 μs were optimized to cover a frequency offset equivalent to J-couplings in the range of 120 to 250 Hz. The corresponding TOP (time optimal pulses) curve is shown in Fig. 4.2 with open circles. Clearly, a step-like behavior of the coherence transfer efficiency is seen and an ideal candidate with good performance and tolerable sequence length t_s can be found at an overall duration around $t_s \approx 0.84/J_{\min} = 7$ ms (the pulse shape is shown in Fig. 4.3C).

As it is needed to approximate the continuous pulse train by a hard pulse-delay sequence for further steps in the overall strategy (i.e., including tolerance to resonance offset and
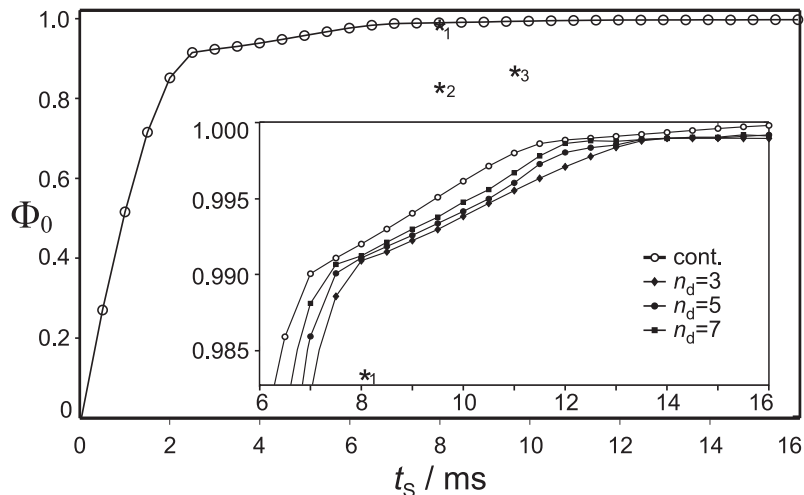
Figure 4.2: Time optimal (TOP) curves for the on-resonant transfer of inphase to antiphase coherence in a two-spin system averaged over the J-coupling range 100 Hz $< J < 250$ Hz. The unrestricted, continuous shape provides highest performance at each overall duration t_s (open circle). Optimal hard pulse-delay sequences with n_d delays intersected by $n_d - 1$ pulses show slightly decreased transfer efficiencies. TOP curves for $n_d = 3$ (filled diamonds), $n_d = 5$ (filled dots), $n_d = 7$ (filled squares) are depicted. Transfer of the literature known sequences J45+90A (*1) and J45+90B (*2) [65] and the broadband INEPT $90_0 - \tau - 120_{90} - 2\tau - 30_{90}$ (*3) [47] are shown for comparison.

B_1-inhomogeneity), the optimization of TOP curves restricting ourselves to n_d delays with (n_d-1) intersecting hard pulses along x is repeated. However, the advantage of convergence of the optimal control based algorithm for such a small amount of independent parameters is only marginal and other optimization methods could have been used as well. As can be seen in Fig. 4.2, achievable performance is never as good as with the continuous pulse train and decreases further with decreasing n_d, but by only slightly increasing the pulse sequence duration to $t_s = 8$ ms, more than 99% transfer over the entire coupling range is obtained with $n_d = 3$. As the number of pulses should be as low as possible, it was decided to continue our optimization with this transfer element, for which the resulting on-resonant pulse sequence is given in Fig. 4.3D.

For completeness, it should be mentioned that the optimal solution for $n_d = 1$ is the INEPT sequence itself (Fig. 4.3A), which performs as good as the best sequences for $n_d = 2$. A comparison of the $n_d = 3$ sequence with known J-compensated INEPT sequences ([47,65], Fig. 4.2), shows that all sequences are of roughly equal duration with the newly optimized one having a slightly better peformance for the desired conditions. The J45+90A-INEPT as the best previously reported J-compensated element can be seen as a $n_d = 3$ sequence with vanishing initial delay (Fig. 4.3B).

It should also be mentioned that in principle the limitation to x-pulses could lead to non-optimal sequences that might be improved by additional y-pulses. However, the optimization of a corresponding TOP curve based on spin density operators of a coupled two spin system without any restrictions on the pulse shape shows numerically that the Bloch approach leads to solutions with identical performance.

The actual theoretical transfer efficiencies with respect to coupling constants are given in Fig. 4.4A for the sequences of Fig. 4.3A,B,E,F. While INEPT performs well only in the
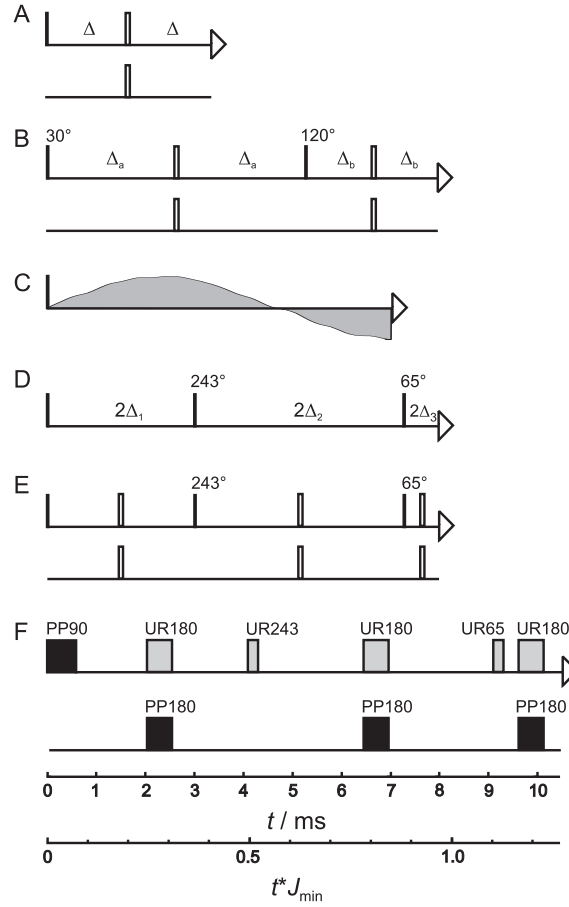
Figure 4.3: Pulse sequences for the transfer $I_z \to 2I_yS_z$. (A) INEPT, (B) J-compensated J45+90A-INEPT (derived from [65]), (C) on-resonant shape solution for optimal J-compensated transfer, (D) on-resonant hard pulse-delay solution with n_d =3, (E) hard pulse broadband version for the n_d =3 sequence, (F) COB-INEPT derived from the n_d =3 sequence using shaped pulses from Table 4.1. All pulse sequences are drawn to timescale with the overall sequence length t_s given in multiples of J (bottom) and in ms for J-compensation over the range 120 Hz < J < 250Hz. Pulse phases are x unless indicated otherwise. For hard pulse sequences narrow bars indicate 90° pulses or pulses with the flip angles indicated and wide open bars indicate 180° pulses. In (F) filled black boxes indicate shaped pulses for point-to-point transformation and grey boxes universal rotation pulses (for details see also Fig. 4.5 and Table 4.1). Delays correspond to $\Delta = 1/(4J_{\text{del}})$, $\Delta_a = 2.68/J_{\text{min}}$, $\Delta_b = 1.34/J_{\text{min}}$, $\Delta_1 = 1.469/J_{\text{min}}$, $\Delta_2 = 2.134/J_{\text{min}}$, $\Delta_3 = 0.394/J_{\text{min}}$, where J_{del} =145 Hz and J_{min} =120 Hz are used for the specific timescale shown.
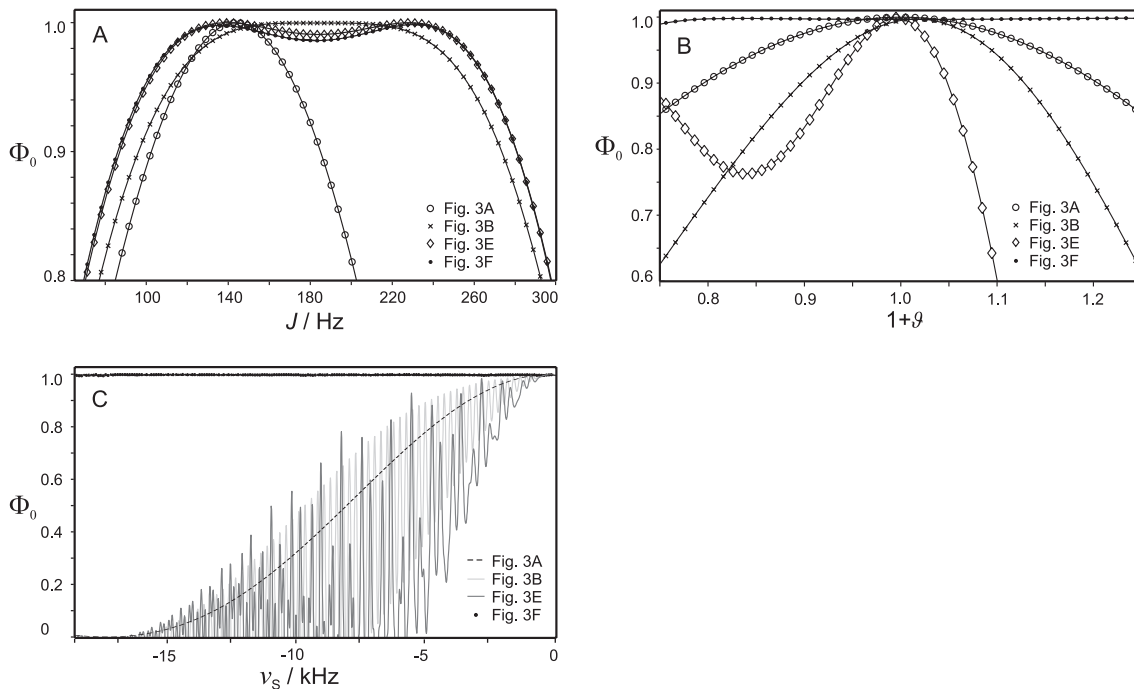
Figure 4.4: Simulations of inphase to antiphase transfer efficiencies for the sequences depicted in Fig. 4.3A,B,E,F as a function of J-couplings with on-resonant RF-irradiation and ideal RF-amplitude (A); as a function of the RF-scaling ϑ for the on-resonant case and $J =145$ Hz (B); and as a function of the carbon offset ν_s for -18.75 kHz $< \nu_s <$ 0 kHz with ideal RF-amplitudes and $J =145$ Hz (the cost function is symmetric around $\nu_s = 0$ Hz for all sequences) (C). The INEPT (circles, dashed), the J-compensated J45+90A-INEPT (crosses, light gray), the hard pulse version of the $n_d = 3$ sequence (diamonds, dark gray), and the COB-INEPT (filled dots) are compared.

region of J-couplings close to the matching condition $\Delta = 1/(4J)$, the J-compensated sequences show a good performance over the entire coupling range of interest. When comparing the J45+90A-INEPT sequence with the newly optimized sequences (Fig. 4.3E,F) in more detail, only slight differences can be found: while the J45+90A-INEPT has better transfer efficiency close to 100% in the central coupling region but drops to 97% at the edges of the desired coupling range, the transfer of the newly optimized sequences is reduced in the central region but reaches 99% over the entire range of 120 Hz $< J <$ 250 Hz. An experimental verification at this stage of the optimization strategy would not yet be successful, as resulting J-compensated sequences appear to be too fragile with respect to offset and B_1 variations, which will be addressed in the following section.

4.2.2 Offset and B_1 Compensation

Having a hard pulse-delay sequence with desired on-resonance performance, it is common practice to insert a pair of 180° pulses in the center of the delays as a Hahn echo [67] to achieve broadband performance, as has been done with the original INEPT and broadband-INEPT sequences [47]. Also continuous pulse shapes have previously been reduced to hard pulse-delay sequences in a DANTE-like [39] approach with further addition of 180° pulses [33] or more complex methods like the star echo in relaxation optimized sequences [56]. However, the more pulses are added the more important become corresponding pulse imperfections.

In Fig. 4.4B,C the dependence of transfer efficiencies with respect to scaling of the RF-amplitude ϑ and offset of the heteronucleus ν_S is shown for the sequences of Fig. 4.3A,B,E,F. Clearly, the robustness of the INEPT transfer is remarkable, making it one of the most widely used building blocks today. With increasing number of hard pulses in the J-compensated transfer steps, however, the performance with respect to offset and B_1 robustness drops down considerably. Only a narrow range of variations in RF-amplitudes is tolerated by the hard pulse-delay sequences and the offset dependence with increasing number of 180° pulses shows vigorous oscillations, making such pulse elements useless for the majority of applications. The approach is therefore extended by using optimized broadband shaped pulses with the desired offset and B_1 robustness to replace all hard pulses of the $n_d = 3$ sequence.

For the pulse sequence, three types of broadband pulses need to be optimized. Most easily obtained are so-called point-to-point (PP) pulses, which are designed to transfer a single initial state to a defined final state. Examples for PP pulses are excitation pulses flanking the INEPT-type transfer with desired transfer $I_z \rightarrow -I_y$ and inversion pulses for the transfer $I_z \rightarrow -I_z$. Especially excitation and inversion pulses are very well studied with corresponding TOP curves for most applicational ranges [7,8]. It should be noted that PP pulses do not lead to any defined transfer besides the one specific component they are optimized for. When the inverse transfer is desired, e.g. $-I_y \rightarrow -I_z$ as inverse excitation, the time-reversed PP pulse has to be applied (indicated by superscript tr). With respect to the desired robustness it was decided to use BEBOP(10kHz, 20kHz, 600μs, ±20%) pulses for proton and BEBOP(37.5kHz, 10kHz, 600μs, ±5%) pulses for carbon excitation.

The second class of pulses needed for the $n_d = 3$ sequence are so-called universal rotation (UR) pulses, designed to transfer all three components of Euclidian space like an ideal hard pulse. UR pulses can be directly optimized [3] or constructed out of PP pulses of half the effective flip angle [68]. The requirements for UR pulses are more demanding than for PP pulses and therefore corresponding pulse lengths are significantly longer. However, refocussing, i.e. UR 180°, pulses are needed, as the defined transformation of all magnetization components is necessary. Specifically optimized BURBOP-243(10kHz, 20kHz, 200μs, ±20%) and BURBOP-65(10kHz, 20kHz, 200μs, ±20%) pulses are applied for protons and a BURBOP-180(37.5kHz, 10kHz, 1.1ms, ±5%) pulse for carbon.

The third type of broadband pulses concerns the pair of 180° pulses applied in the center of corresponding delays. Here, a refocussing pulse on protons and an inversion pulse on carbons have to be applied simultaneously. Since there can be crosstalk based on coupling evolution or heteronuclear Hartmann-Hahn conditions with coupled spins, ideally a pulse sandwich optimized with offsets and B_1-field inhomogeneities on both nuclei and the heteronuclear coupling taken into account is applied. The optimization of such a pulse sandwich, which is called BUBI (Broadband Universal rotation and Broadband Inversion) [69], turned out to be complex with the necessity to mathematically derive a novel quality factor. The derivation of the BUBI pulse is discusssed in chapter 8, its use in the current work turned out to be essential, as only the J-compensated concurrent pulse shape allowed a full quantitative experimental treatment (see experimental section). A list of all broadband pulses used in the final COB-INEPT sequence is given in Table 4.1 with the corresponding nomenclature used in Fig. 4.3F and 4.5.

The theoretical performance of the COB-INEPT with respect to offset and B_1-field inhomogeneities is exceptional, with general transfer efficiencies of $\approx 99\%$ in the desired ranges (Fig. 4.4B,C).

Table 4.1: Shaped Pulses for COB-INEPT

	name[a]	transfer	t_p [μs][b]	ν [kHz][c]	ϑ[d]
^{1}H	PP90	z $\rightarrow$ -y	600	10	$\pm 20\%$
	PP90^{tr}	-y $\rightarrow$ z	600	10	$\pm 20\%$
	PP180	z $\rightarrow$ -z	100	10	$\pm 20\%$
	UR243	243°_x	200	10	$\pm 20\%$
	UR65	65°_x	200	10	$\pm 20\%$
^{13}C	PP90	z $\rightarrow$ -y	600	37.5	$\pm 5\%$
	UR180	180°_y	1100	37.5	$\pm 5\%$
	PP90^{tr}	-y $\rightarrow$ z	600	37.5	$\pm 5\%$
BUBI[e]	UR180	180°_x	550	10	$\pm 20\%$
	PP180	z $\rightarrow$ -z	550	37.5	$\pm 5\%$

[a] Abbreviations used as in Figs. 4.3F and 4.5: PP for point-to-point or state transfer pulses for a single magnetization component (e.g. excitation and inversion pulses); UR for universal rotation pulses for defined rotations around a specific axis (e.g. refocussing pulses); *tr* for time reversed pulse shapes;
[b] pulse length;
[c] offset range of pulses for which corresponding pulses are compensated for;
[d] variation of RF-amplitude for which corresponding pulses are compensated for;
[e] combined pulse sandwich for ^{1}H refocussing and ^{13}C inversion.

4.3 Experiments

To confirm the theoretical results experimentally, it was started with a detailed quantitative analysis on a well-defined sample, ^{13}C-labeled sodium formate in deuterated glycerol as a heteronuclear two spin system.

All contributions to the Hamiltonian have been checked or set meticulously on a Bruker 600 MHz Avance III spectrometer equipped with an inverse H,C,N-triple resonance probehead: the offsets are set to $\nu_I = 0$, $\nu_S = 0$, the *J*-coupling experimentally determined to be $J_{\exp} = 193.0$ Hz and the RF-amplitude calibrated to be 20 kHz (10 kHz) for ^{1}H (^{13}C), respectively. The proton T_1 and T_2 relaxation times are determined to be 1.3 s and 0.2 s, respectively, at 298 K. As a reference experiment, a simple ^{1}H 1D experiment with a single scan and a 90° pulse for excitation is recorded to obtain the maximum possible signal intensity. This reference allows a reliable and highly reproducible evaluation unbiased by the experiment used for comparison. As the sample is ^{13}C-labeled, signal intensities can directly be compared with carbon-correlated spectra.

The COB-INEPT is then incorporated in a standard gradient enhanced and phase cycled HSQC-experiment for $J_{\min} = 120$ Hz and without decoupling during acquisition. The resulting COB-HSQC pulse sequence is shown in Fig. 4.5C (note that the second COB-INEPT for the back-transfer is mirrored and the phase cycle adapted). A conventional HSQC experiment with INEPT transfer elements set to delays matching $1/(2 J_{\rm del})$ with $J_{\rm del} = 145$ Hz is implemented. All pulses in the two experiments are implemented as shaped pulses according to Table 4.1. As coherence order selection is used for carbon selection, 50% loss of signal intensity as compared to the ^{1}H 1D experiment is taken into account.

In Fig. 4.6, a comparison with respect to the effective coupling range of the two types of HSQC experiments has been performed. Multiple experiments have been conducted varying the delay time Δ in order to obtain experiments as applied to molecules with
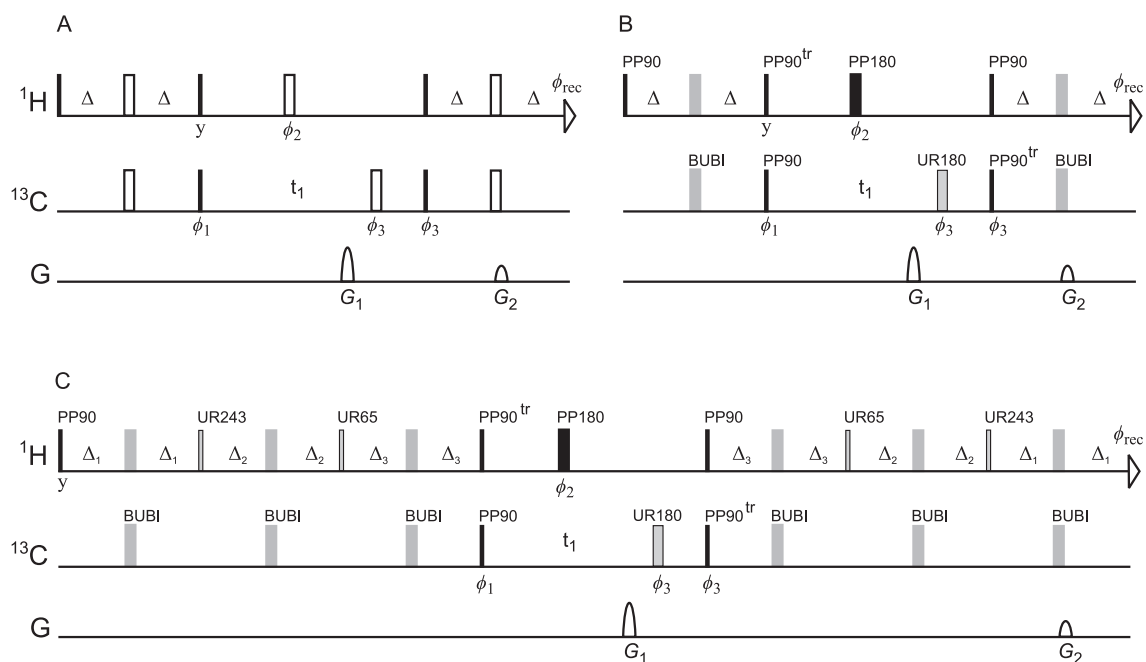
Figure 4.5: Pulse sequences of a standard HSQC (A), a conventional shaped pulse HSQC with compensation for offset and B_1-field inhomogeneity (B), and the COB-HSQC using COB-INEPT elements from Fig. 4.3F for coherence transfer steps. The phase cycle is $\phi_1 = x, -x$, $\phi_2 = 4(x), 4(-x)$, $\phi_3 = x, x, -x, -x$, $\phi_{\mathrm{rec}} = x, -x, -x, x$, (C). In (B) and (C), all applied pulses are broadband pulses described in detail in Table 4.1. Gradients G_1 and G_2 are applied with the ratio 80:20.1 for coherence order selection. The phase-sensitive echo/antiecho recording scheme is achieved via changing the sign of G_1 every other increment. Heteronuclear decoupling is not applied in the experiments shown here to avoid a potential source of error in quantification or to be able to measure corresponding $^1T_{\mathrm{CH}}$ couplings.
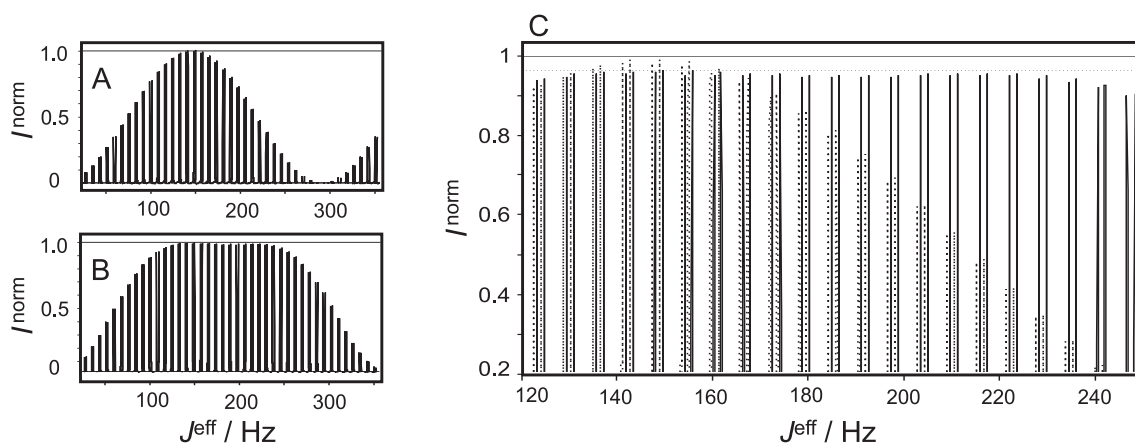
Figure 4.6: Multiple conventional shaped pulse HSQC (A) and COB-HSQC (B) spectra of the ^{1}H-^{13}C moiety of ^{13}C-labeled sodium formate in glycerol-d_8 with scaled transfer delays allow the comparison of overall transfer efficiencies. A direct comparison of results in the optimized region of 120 Hz $< J^{\text{eff}} <$ 250 Hz is shown in (C) with dashed lines for the HSQC and solid lines for the COB-HSQC. Signal intensities I^{norm} have been normalized to the 50% intensity of a corresponding 90° ^{1}H 1D-experiment to allow an unbiased comparison of performances. The signal intensities of the COB-HSQC for central J-coupling values are only approximately 4% lower than the theoretical maximum (dotted line). Spectra are given with respect to the effective coupling constant J^{eff} as described in the main text. Spectra have not been edited in any way, i.e. relaxation has not been accounted for.

effective J-couplings J^{eff} in the range of 25-350 Hz. For the standard HSQC and the COB-HSQC the delays have been altered in the way that $\Delta = \frac{J^{\text{eff}}}{2J_{\text{del}}J_{\text{exp}}}$ and $\Delta = \frac{J^{\text{eff}}}{2J_{\text{min}}J_{\text{exp}}}$, respectively. The resulting signal intensities with respect to J^{eff} (Fig. 4.6A,B) resembles the theoretically expected transfer efficiencies within the experimental error.

For a quantitative look at the results, signal intensities normalized to the 50% intensity of the ^{1}H 1D experiment are shown for the two HSQCs in Fig. 4.6C. For J^{eff} =145 Hz the conventional shaped pulse HSQC approaches 99% transfer. The maximum transfer for the COB-HSQC is approximately 96%, for which the loss can be attributed to remaining pulse imperfections and relaxation effects. For larger values of J^{eff}, the superiority of COB-HSQC is evident. The experimental results are consistent with the theoretical predictions within an error of approximately $\pm 2\%$.

In a second experimental approach the COB-HSQC is evaluated on realistic molecules covering the extremes with respect to offset and coupling compensation. Therefore a sample containing ethylvanillin, methylpropiolate and orthoethylformate in DMSO-d_6 is prepared; with coupling constants in the range of 125 - 258 Hz and chemical shifts spanning almost 200 ppm and acquired a 2D-COB-HSQC (Fig. 4.7B). For a fair evaluation a series of ideal conventional HSQC experiments are recorded using the shaped pulses as before and setting J_{del} always to the experimentally determined coupling constant in order to obtain maximum possible signal intensities (corresponding to 100% coherence transfer for each signal within the experimental error). Please note that all shaped pulses used accomplish a theoretical transfer efficiency of $\overline{\Phi} \geq 99.9\%$ and are tested intensively with regard to their outstanding experimental performance where they generally perform as good or better than previously reported pulses. As can be seen in Fig. 4.7A, experimental signal intensities for the COB-HSQC and the conventional HSQCs with ideal settings are identical within a few percents error, demonstrating the achieved robustness of the COB-approach close to the physical limits.

A conventional hard pulse HSQC is acquired with delays matching J_{del} =145 Hz. The comparison of the COB-INEPT with this original-type HSQC gives a clear statement: the best signal intensities of the spectrum acquired for the test sample using the hard pulse HSQC hardly reach half the intensity of the COB-HSQC and the majority of signals shows strong phase distortions. The reduced performance can thereby be attributed to offset and B_1 effects for couplings close to 145 Hz, which usually result in inphase cross peaks with reduced intensities, and non-matching coupling constants with corresponding incomplete transfer and dispersive antiphase contributions even in the case of close-to-resonant carbon chemical shifts (see e.g. signals with $J = 186$ Hz and 258 Hz), showing nicely the generally positive effects of both J-compensation and broadband pulses.

Finally, an experimental evaluation concerning the use of the COB-HSQC for the measurement of RDCs has been attempted. For this purpose, it was decided to use sucrose in gelatin/D$_2$O within a rubber-based stretching apparatus [70, 71] as a test sample. ω_2-coupled HSQC experiments are frequently used to determine heteronuclear one-bond RDCs in organic molecules, but phase distortions due to incomplete back-transfer from unmatched couplings during the second INEPT step lead to phase distortions that have to be corrected in a tedious way in order to accurately determine coupling constants [72]. Clean phase spectra can be obtained by the so-called CLIP/CLAP-HSQC approach [46], but corresponding signals with incomplete transfer will have signal intensities reduced by $\sin^2(\pi J_{\text{exp}}/2J_{\text{del}})$. The COB-INEPT with close to 100% coherence transfer, instead, does not result in any residual dispersive antiphase coherence responsible for the phase distortions and clean cross peaks with maximum signal intensities should be reached without the need of additional modifications of the HSQC sequence. The corresponding COB-HSQC spectrum for the sucrose in stretched gelatin/D$_2$O sam-
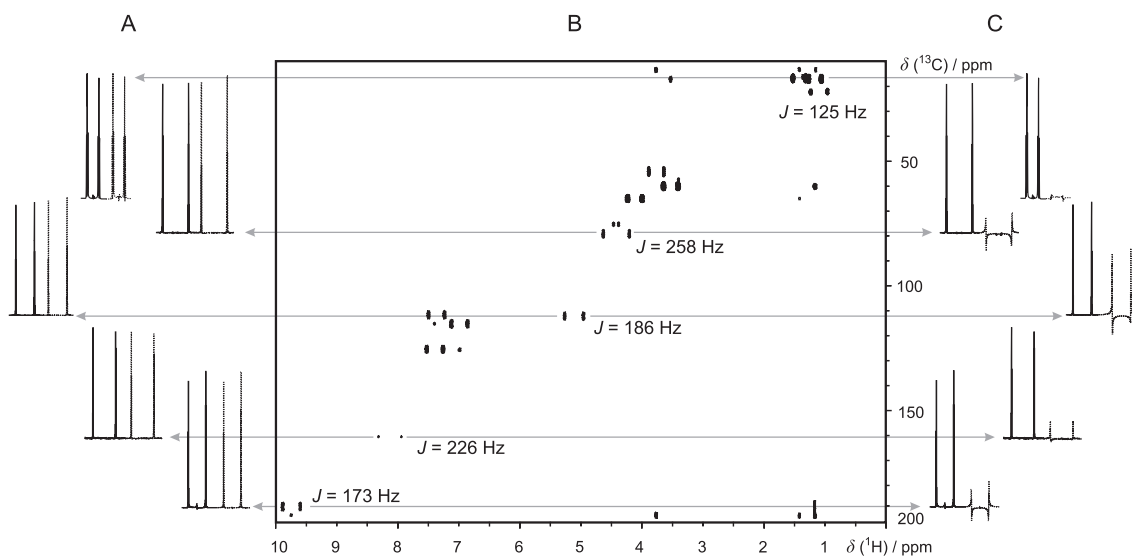
Figure 4.7: Evaluation of the experimental performance of the COB-HSQC using a mixture of ethylvanillin, methylpropiolate and orthoethylformate in DMSO-d_6 as a natural abundance test sample covering most of the desired offset and *J*-coupling ranges. The resulting 2D spectrum of the COB-HSQC is shown in B. Slices out of the 2D spectrum (A and C, solid lines) are compared to slices from ideal and conventional spectra: a series of shaped pulse HSQC spectra recorded using the sequence of Fig. 4.5B with ideal delays set individually for each experimentally determined coupling according to $\Delta = 1/(2J_{\mathrm{exp}})$ (A, dashed lines), marking the maximum possible transfer efficiency for each cross peak; and slices from a hard pulse HSQC using the pulse sequence shown in Fig. 4.5A with $\Delta = 1/(2 \cdot 145 \text{ Hz})$ (C, dashed lines), demonstrating the overall gain obtained by the various compensations.
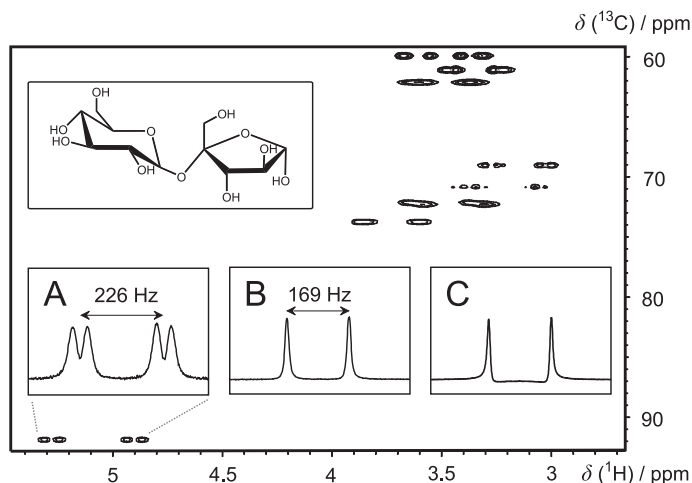
Figure 4.8: Measurement of residual dipolar couplings (RDCs) from ω_2-coupled COB-HSQC spectra on the model compound sucrose in 40% (w/v) gelatin/D_2O [73]. Stretching of the gel is achieved using a rubber-based stretching device [70]. The 2D spectrum of the sample stretched to a quadrupolar splitting of the deuterated solvent of $\Delta\nu_Q =437$ Hz is shown with the corresponding 1D slice of the anomeric center as the cross peak with the largest RDC as insert (A). The same slice is shown for the unstretched sample for the COB-HSQC (B) and a shaped pulse standard HSQC (C). Clearly, the COB-HSQC provides clean inphase signal due to complete transfer via the COB-INEPT steps, while the standard HSQC shows significant dispersive antiphase contributions to the signal, affecting the accuracy of coupling extraction.

ple is shown in Fig. 4.8 with a slice through the most critical case, the anomeric cross peak with $^1T_{CH} =^1 J_{CH} +^1 D_{CH} = 226$ Hz, given as an insert (Fig. 4.8A). Two more slices of the same cross peak (Fig. 4.8B,C) provide a comparison with the COB-HSQC and a conventional shaped pulse HSQC ($J_{del} =145$ Hz) on the unstretched sample with $^1J_{CH} = 169$ Hz. Clearly, the COB-HSQC provides clean phases for the wide range of heteronuclear couplings and eases the determination of coupling constants.

4.4 Discussion

With the COB-INEPT it is possible to provide an INEPT-type transfer element with exceptional robustness which can be implemented on any state-of-the-art NMR spectrometer equipped with an inverse probehead designed for ^1H detection. The RF-power requirements especially on carbon are sufficiently low to even accomodate older probehead designs with 90° pulses as long as 25 μs. The pulse sequence element is designed to provide the best possible robustness for the multitude of real life applications and has been tested vigorously.

Before discussing benefits in potential applications, it should be focused on general aspects of the presented approach: The robustness against variations of couplings, offsets, and B_1-fields (COB) has been achieved by a two step optimization procedure using a DANTE-like hard pulse-delay approximation in between steps. Individual optimizations have been characterized using highly efficient algorithms based on principles of optimal control.

In all cases, either systematically TOP curves have been performed or previous studies with respect to physical limits were considered [7–9] to provide elements close to time-

optimality. We can therefore be certain that the COB-INEPT performs very close to the *best* possible pulse sequence for the desired robustness.

Nevertheless, the approximation with a hard pulse-delay sequence inherently does not fully represent the global optimum of the desired transfer in terms of time efficiency. The coherence transfer averaged over all optimzed conditions reaches 99% neglecting relaxation and the hard pulse-delay approximation optimized in the initial optimization step provides a very short sequence which is only ≈15 % longer than the optimal shape solution on resonance for practically identical transfer efficiency. The replacement of hard pulses by robust shaped pulses in the second optimization step leads to an additional increase in the overall pulse sequence duration which adds up to a total factor of ≈ 1.5 compared to the time-optimal shaped pulse on resonance solution. In general, the increased robustness with respect to chemical shift offsets will inevitably come with an increase of sequence duration and the presented sequence is close to a theoretical limit, but even with the optimization approach pursuit a small window of potential further improvement seems possible: While the increase in transfer time due to the DANTE-like approximation cannot be avoided with the optimization strategy, the additional time needed for the shaped pulses can in principle be reduced by ICEBERG-type pulses [74], that allow defined heteronuclear coherence transfer during the pulse shape. Unfortunately, the described ICEBERG-approach so far only works with Point-to-Point transformation pulses and the universal rotation pulses as the majority of pulse shapes of the COB-INEPT cannot be replaced accordingly. In the future, however, delays and therefore the overall duration of the sequence might be further reduced by the introduction of universal rotation pulses with inherent heteronuclear coupling evolution.

The DANTE approach comes with an increased overall duration of the transfer elements and in principle better solutions might exist based, for example, on continuous, robust pulse shapes applied to the heteronuclei. However, the approach also increases the compatibility of the sequence with other building blocks like coherence order selection or potential water suppression. Both elements can easily be inferred into delays of the hard pulse approximation (see e.g. Fig. 4.5), but would be very difficult to implement within a full shaped pulse solution. The two-step optimization strategy with the DANTE-type approach also allows the partial adaptation to other problems. The COB-INEPT step optimized for ^{1}H,^{13}C-transfer can be transferred to ^{1}H,^{15}N-transfer elements by only replacing corresponding offset and B_1-field compensated shaped pulses with the ones optimized for the specific needs of the heteronucleus. The time-optimal J-compensated element for coherence transfer can be kept. Vice versa, the shaped pulses optimized for ^{1}H,^{13}C-correlation experiments might be used to make other proton-carbon correlation pulse sequence elements more robust.

The hard pulse-delay sequence element also offers the possibility to reduce losses due to conformational or chemical exchange processes. It is well-known that trains of 180° pulses applied simultaneously on both nuclei involved in the heteronuclear transfer create homonuclear isotropic mixing conditions [54, 75, 76], which bring the effective chemical shift differences of exchanging nuclei close to zero and avoid loss of magnetization. To keep the robustness against offset and B_1-field variations high, CPMG-trains of compensated shaped pulses, as e.g. pulses published in [6], could be used. A pulse with even better performance for the CPMG-type sequence would be the BUBI pulse or sophisticated supercycles [77], which would also be compensated for heteronuclear coherence transfer. However, it remains to be proven how the overall COB-INEPT would perform in the presence of exchange processes and with the addtional pulses, as the application of CPMG-type sequences usually reduces the effective bandwidth of the experiment.

It should be mentioned that the COB-INEPT does not take homonuclear coupling evolution into account. Typical artifacts like dispersive antiphase contributions from homonu-

clear couplings are most likely increased due to the increased overall duration of the transfer element. In acquired example spectra, however, none of the inspected cross peaks showed intolerable distortions and the effect seems to be of minor interest.

Regarding practical implications of the COB-INEPT, a multitude of applications come to mind. One example are routine applications like HSQC/HMQC-type experiments for synthetic or natural products. In such compounds, acetylene-type, sp hybridized groups are rarely found, but they do exist and most synthetic chemists do not understand why there are no cross peaks for their acetylene ^{1}H,^{13}C-correlation spectra. One of the authors experienced several such occasions which once even led to a severe structural misinterpretation. These misunderstandings could easily be overcome by J-compensated experiments like the COB-HSQC, which will provide correlations for the full bandwidth of $^1J_{CH}$ coupling constants. The COB-HSQC in addition allows to cover the full 250 ppm chemical shift bandwidth of carbon on a 600 MHz spectrometer and would still apply for all aliphatic and aromatic carbons on a 1 GHz instrument with no variation in signal intensity, so that no potential correlation is missed.

The COB-approach might also have an even stronger impact on routine heteronuclear long-range correlation experiments like the HMBC. The presence of acetylene-type moieties will lead to ghost peaks with conventional low pass filters and the carbon chemical shift range needed cannot be covered adequately with hard pulses on high field spectrometers.

The second type of applications was our original motivation to start the development of the COB-INEPT transfer element. With modern equipment, ^{1}H,^{13}C-RDCs on small organic molecules can be scaled to a convenient range of approximately $\pm$ 20-30 Hz [70, 71]. In the presence of aliphatic and aromatic protons, this inevitably results in a coupling range of $^1T_{CH} = {}^1J_{CH} + {}^1D_{CH}$ = 100-200 Hz or larger, which usually cannot be covered adequately in a single HSQC experiment. With the COB-HSQC introduced here, instead, corresponding correlations are easily measurable, even without phase distortions that occur with a conventional ω_2-coupled HSQC if couplings do not match the ideal transfer conditions [46, 72].

Finally, applications are seen in the field of quantitative NMR spectroscopy, as the transfer efficiency over the entire range of compensated experimental conditions only varies within a couple of percents neglecting dynamic effects. To our knowledge, this is far better than most quantitative heteronuclear correlation experiments, especially regarding high field instruments. Relaxation and exchange effects are, of course, not taken into account and the applicability to quantitative NMR should be tested in a separate systematic study.

4.5 Summary

In summary, a viable two-step optimization strategy for robust transfer elements dedicated to small molecules is introduced which generally should provide performance close to physical limits. Within this COB-approach, the pulse sequence element is directly optimized with respect to ranges of Coupling constants, Offsets, and B_1-field inhomogeneities. Dynamic effects are indirectly considered by the optimization of TOP-curves which provide the time-optimal solutions for corresponding transfer and pulse durations.

The approach has been demonstrated in theory and experiment using the probably most intensely studied heteronuclear transfer element: the ^{1}H,^{13}C-INEPT. For this transfer element a multitude of modifications does exist that either provides J-compensation or offset and B_1-compensation. The goal of the work presented here was not to improve existing building blocks - the INEPT has been optimized for several decades now and only small gains for extreme conditions can be expected - but to provide the best sequence element possible for a range of corresponding experimental variations.

Indeed, the comparison of cross peaks from COB-INEPT and COB-HSQC experiments with cross peaks from individually optimized conventional INEPT and HSQC experiments with ideal experimental settings shows practically equal performance of the transfer elements, demonstrating that the best possible performance is reached over the entire range of variations within the experimental error.

With the optimization strategy in hand, optimal solutions might now be found for other transfer elements like transfer via long-range couplings, low-pass or X-filter, spin-state selective, and BIRD-type building blocks. The presented ^{1}H,^{13}C-COB-INEPT, on the other hand, has been demonstrated to be beneficial for a variety of applications where the full bandwidth of compensation might occur, as e.g. in routine NMR service or when dealing with partially oriented samples.

Some of the pulse sequence elements have been developed within this thesis and will be discussed in the following chapters.

5. COB-BIRD

5.1 Introduction and Motivation

Since the early days of NMR spectroscopy it has been a longstanding goal to remove the effect of scalar J-couplings from ^{1}H-NMR spectra (Fig. 5.1A vs. B and C). Resolution could be drastically improved and spectral overlap avoided. Decoupling is principally achieved by the selective sign inversion of one spin in a bilinear term of coupled spin pairs (while the other spin stays untouched), so that the coupling evolution is refocused. This conceptually simple task is readily achieved for coupled heteronuclei (e.g. ^{1}H, ^{13}C), which can be addressed separately by distinct Larmor frequencies, while the same is very challenging for homonuclear coupled spin pairs. Indeed it is impossible to do a selective sign inversion at a given resonance offset ν for *all* offsets ν in the spectral region, without losing a significant amount auf S/N.

Various methods have been proposed to obtain broadband homonuclear decoupling, which have to be classified according to the following two techniques: (i) The first technique uses rf fields to achieve the decoupling, while the second uses the local field of a dilute natural abundance nuclei, such as ^{13}C, and is denoted as bilinear rotation decoupling (BIRD) [79] (see Section 5.2.1 for details).
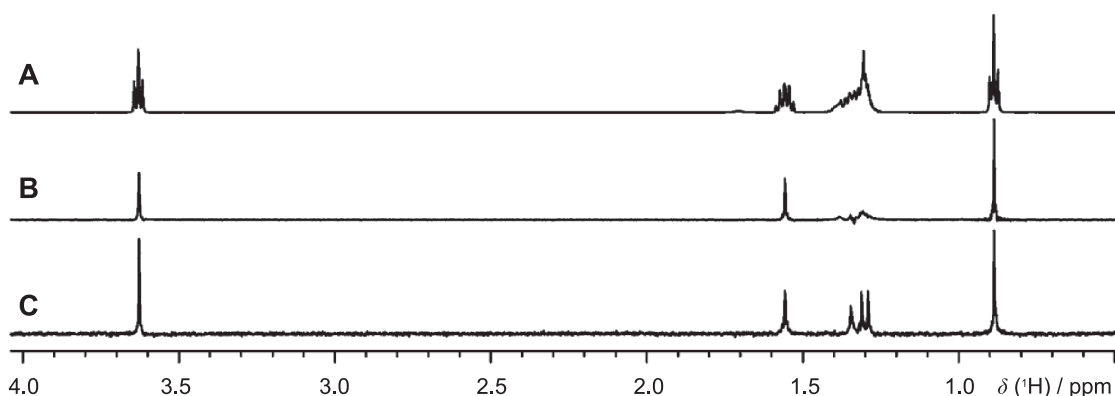
Figure 5.1: (A) Normal ^{1}H spectrum, (B) Zangger-Sterk pure shift spectrum measured in 1.25 min, (C) BIRD pure shift spectrum measured in 1.5 min, for a solution of n-hexanol (127 mM) in CDCl$_3$. Graphic adapted from [78].

Although, BIRD originally was proposed as a pure shift method, it seems to never have been used as such. Instead it became a standard building block in heteronuclear multidimensional NMR spectroscopy. Only very recently it is more widely applied in a pure shift HSQC experiment [80].

5.1.1 BIRD Decoupling

The beauty of BIRD decoupling is revealed by the comparison with the technique proposed by Zangger and Sterck [81], which is a standard method for homonuclear decoupling (Fig. 5.1B). In a pictorial way, the spectral region can be imagined as divided, by a weak z-gradient, in thin slices over the whole sample volume. Each slice is addressed by a selective 180° pulse. On the cost of S/N the need to shift the filter in the offset dimension is eliminated.

In case of BIRD, it is also a dilute sub-ensemble of spins which can be addressed in terms of a sign inversion, while the majority of spins, which are considered to be the coupling partners, stay untouched. Even in the notoriously difficult case of strongly coupled CH_2 groups in an alkyl chain, homonuclear J-decoupling can be obtained (see Fig. 5.1C at 1.3 ppm, in comparison to Fig. 5.1B at 1.3 ppm). But leading to the same conceptual loss in S/N unless ^{13}C is not selected anyway by the experiment (as for example in a natural abundance $^1H,^{13}C$-HSQC). Since this is often the case in multidimensional NMR spectroscopy, there is no additional attenuation when applying BIRD, as it would be in the case of the Zangger and Sterck method.

In addition to existing building blocks, the naturally occurring coupling constant in the range of 120-250 Hz should be addressed by BIRD to assure good decoupling properties. This poses the requirement of J-compensated BIRD sequences.

5.1.2 BIRD as Building Block in Multidimensional NMR Spectroscopy

Using BIRD on protons in a ^{13}C moiety results in a sign inversion of the ^1H product operators involved, which can be used as a labelling procedure for $^1J_{CH}$ spin systems. One potential application is the decoupling of $^1J_{CH}$ spin systems in the indirect dimension while retaining $^nJ_{CH}$-couplings. This poses divergent requirements: An optimal sequence would have to have perfect transfer in the range of $^1J_{CH} = 120 - 250$ Hz and no transfer in the range of $^nJ_{CH} = 0 - 30$ Hz. According to the product operator formalism this can not be obtained by simple spin echo sandwiches, since the evolution of ^nJ-couplings will always follow the sine-function in its region of steepest ascent, if the BIRD block is calibrated for $^1J_{CH}$-couplings. As this leads to severe experimental drawbacks the need of J-selective BIRD filters is imposed

5.1.3 BIRD Objectives

While there was a J-robust BIRD sequence suggested in the initial publication [79] already, no attempts have been made to elucidate time optimal sequences so far. The following will be therefore dedicated to the search of time optimal sequences by OCT, which are expected to approach the physical limit for BIRD decoupling sequences.

A second step is concerned about J-selective BIRD filters, which are conceptually new to the field of multidimensional NMR spectroscopy. This aims to provide insights into the requirements that need to be fulfilled in order to obtain J-selectivity. Further, time optimal J-selective BIRD sequences are derived by the use of OCT.

A

^{1}H τ*3.448 τ*3.448
y y

^{13}C

B

^{1}H τ*1.310 τ*1.310 τ*2.620 τ*2.620 τ*1.310 τ*1.310
y -x -x y

^{13}C

C

-47.454° -85.092° 135.546°

^{1}H τ*2.522 τ*2.522 τ*2.522 τ*2.522

^{13}C

D

81.257° -115.117° 36.249°

^{1}H τ*2.629 τ*2.629 τ*5.252 τ*5.252

^{13}C
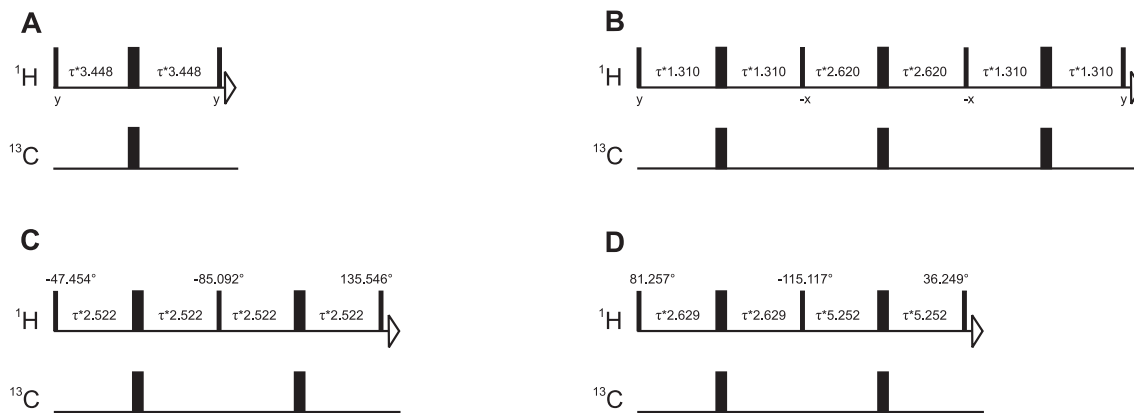
Figure 5.2: Pulse sequences for the transfer $I_z \rightarrow I_z$ (via antiphase) (A and B) derived from [79]. Pulse sequences for the transfer $I_z \rightarrow -I_z$ (via antiphase) derived by OCT (C and D). (A) BIRD transfer with $t_s = 6.896$ ms, (B) J-compensated BIRD with $t_s = 10.6$ ms, (C) J-compensated pulse-delay sequence obtained from OCT with $n_d = 2$ and $t_s = 10.5$ ms, (D) J-selective pulse-delay sequence obtained from OCT with $n_d = 2$ and $t_s = 15.76$ ms. Wide bars indicate 180° pulses and narrow bars 90° pulses, or pulses with the annotated flip angles. Pulse phases are x unless indicated otherwise. The duration of delays is given in ms and can be scaled by τ in order to obtain sequences optimal for an arbitrary range of J-couplings. Setting $\tau = 1$ results in the "standard" sequence that performs optimal for $^1J_{CH} = 120 - 250$ Hz.

5.2 Theory

5.2.1 Known BIRD Sequences

In the following, an ABX three spin system ($I_1I_2S_3$, i.e. ^{1}H^{1}H^{13}C) with coupling constant $^nJ_{12} = 5$ Hz, $^1J_{13} = 145$ Hz and $^nJ_{23} = 0$ Hz and $\Delta = 1/(2 * J_{13})$ is considered.

Regarding heteronuclear coupling evolution, two scenarios have to be distinguished when applying the BIRD sequence (Fig. 5.2A): (i) Starting from spin B (I_2) there is excitation, followed by chemical shift evolution that is refocused, followed by a second 90° pulse.

$$I_{2z} \xrightarrow{\frac{\pi}{2}I_y} I_{2x} \xrightarrow{\omega I_z \Delta/2 + \pi(I_x + S_x) + \omega I_z \Delta/2} I_{2x} \xrightarrow{\frac{\pi}{2}I_y} -I_{2z}$$

The overall effect of the BIRD sequence on spin B (I_2) resembles an 180° pulse. (ii) Turning to spin A (I_1), the transfer is:

$$I_{1z} \xrightarrow{\frac{\pi}{2}I_y} I_{1x} \xrightarrow{(\omega I_z + 2\pi J I_{1z}S_{3z})\Delta/2} \xrightarrow{\frac{\pi}{2}(I_x + S_x)} \xrightarrow{(\omega I_z + 2\pi J I_{1z}S_{3z})\Delta/2} -I_{1x} \xrightarrow{\frac{\pi}{2}I_y} I_{1z}$$

The overall effect of the BIRD sequence on spin A (I_1) that is coupled to ^{13}C resembles a 360° pulse. The local field of ^{13}C inverts the sign of the I_1 operator. By this, decoupling can be accomplished, even in the strong coupling limit, when there is no difference in the chemical shifts of spin A and B.

The J-compensated BIRD sequence [79] could be deduced in analogy to composite pulses, which compensate for offset or B_1 inhomogeneity. Likewise an 180° pulse is more susceptible to mismatching offsets than a 90° pulse, the BIRD sequence suffers the same drawback, while the INEPT, being an equivalent to a 90° pulse, is more tolerant to mismatching coupling constants. As could be taken from Fig. 5.4A (solid line), the standard BIRD performs well within a small range of coupling constants, while the compensated sequence is more robust (Fig. 5.4A, dotted line).
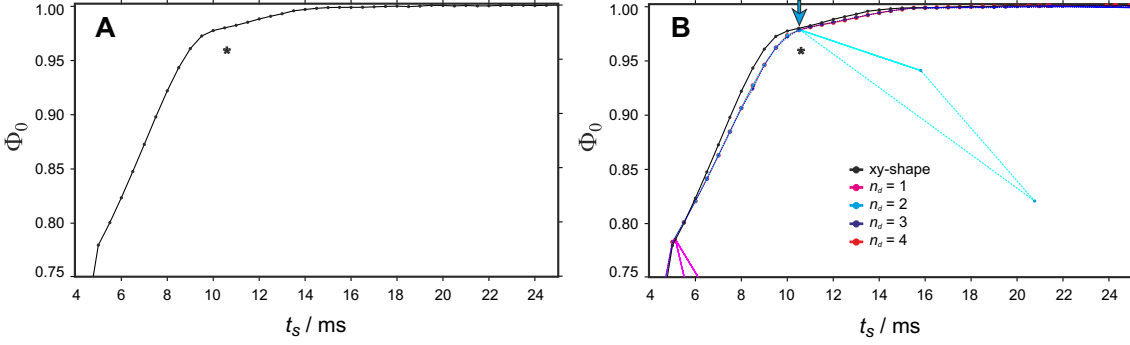
Figure 5.3: Time-optimal (TOP) curve for J-compensated BIRD transfers as obtained by OCT. For the on-resonant transfer of $I_z \to -I_z$ (via antiphase) in a 2 spin system averaged over the J-coupling range $120 < J < 250$ Hz. The continuous x, y-shape (A, black), provides the highest performance at each overall sequence duration t_s. Optimal hard pulse-delay sequences with n_d delays intersected by $n_d + 1$ pulses show slightly decreased transfer efficiency (B). TOP curves for $n_d = 1$ (solid line, magenta), $n_d = 2$ (dashed line, cyan), $n_d = 3$ (dotted line, blue) and $n_d = 4$ (solid line, red) are depicted. The pulse sequences depicted in Fig. 5.1C originates from $n_d = 2$ and $t_s = 10.5$ ms (highlighted by an arrow).

5.3 Broadband J-Compensated BIRD Sequences from OCT

OCT can be used to derive BIRD sequences. A heteronuclear coupled two spin system is considered and a cost function Φ_0 (according to Eq. (3.23)) is defined that is the overlap of the transfer $I_{1z} \to -I_{1z}$ with the target density operator $-I_{1z}$ (note that this implies a sign inversion for moieties containing ^{13}C, while there is no sign inversion in case of the standard BIRD [79]). The full two spin Hamiltonian is considered (Eq. (3.8)). The offset of the first and second spin is set to zero, B_1 field inhomogeneity is not considered and controls on spin S are disabled. The cost and gradient function is evaluated for 11 explicit points in the range of $J_{CH} = 120 - 250$ Hz.

Applying an $180°$ pulse would be the trivial solution that satisfies Φ_0. To avoid that, the cost and gradient function are evaluation at $J_{CH} = 0$ Hz and weighted by a factor of 11 before averaging over the remaining points.

The first step is to optimize x, y-shaped sequences with durations $t_s = 0.5$-25 ms and a digitization of 100 μs. Conjugated gradients are used for update. For a given sequence length t_s, 10 optimizations, starting from random controls, are carried out and the ones with best fidelity form the TOP curve depicted in Fig. 5.3A. As expected, the fidelity of the TOP curve increases with increasing sequence lengths t_s and the smooth shape is interpreted in the way that good convergence is obtained. If convergence is assured, OCT optimizations usually converge close to the physical limit (see [7–9]).

As it is needed to approximate the continuous pulse shape by a hard pulse-delay sequences to make it robust against offset and B_1 inhomogeneity, the optimization of the TOP-curves is repeated, with the restriction to n_d delays and n_d+1 surrounding hard pulses. Delays are defined by zero-controls and the gradient with respect to the time is evaluated. Pulses are defined by a duration of 0.5 μs and the gradient with respect to x, y-controls is calculated for the I-spin while no controls are allowed on the S-Spin. The update method is steepest ascent with $\epsilon_{delay} = 5 * 10^{-7}$ and $\epsilon_{pulse} = 50 * 10^{12}$. While there is no restriction for the rf strength, the duration of delays is scaled down, proportionately, once t_s exceeds $t_{s,max}$, while there is no penalty for sequences shorter than $t_{s,max}$. For a given sequence length

t_s, 10 optimizations, starting from random durations and controls, are carried out and the ones with best fidelity form the TOP curves depicted in Fig. 5.3B.

5.3.1 Interpretation of TOP Curves

The first thing that attracts attention when comparing the TOP curves of the hard pulse-delay sequences among each other (Fig. 5.3B, colored), is that there is no convergence observed, once a certain sequence length t_s is exceeded. The limit for that increases with the number of increments in the hard pulse-delay sequence and is clearly seen for $n_d = 1$ and 2. The first sequence that shows convergence over the whole range from $t_s = 0.5 - 25$ ms has 3 delays. If the TOP curve increases that can be explained by the fact that if a sequence ends with $t_s = t_{s,max}$ it has to accommodate with $t_s * J$ coupling evolution that necessarily needs to be involved in the inphase→antiphase→inphase-transfer. If the number of intersecting pulses is restricted, t_s will at one point not match the range of present coupling constant any longer and the corresponding sequence is designated to not converge.

The second result that attracts attention when comparing the TOP curves of the hard pulse-delay sequences (Fig. 5.3B, colored) with the TOP curve of the x, y-shape (Fig. 5.3B, black) is that there is only a small difference in fidelity. Therefore it is concluded that pulse-delay sequences can be used to approximate the x, y-shape.

The third result that attracts attention when comparing the TOP curves of the hard pulse-delay sequences among each other (Fig. 5.3B, colored) is that there are only very small differences in fidelity. So that it is possible to select a sequence with $n_d = 2$ and 10.5 ms for further evaluation.

5.3.2 Simulation of BIRD Sequences

The in Fig. 5.1C depicted sequence with duration of 10.5 ms originates from the $n_d = 2$ delay TOP curve (Fig. 5.3B). The simulated transfer is shown in Fig. 5.4A (dashed line). The OCT BIRD sequence fulfills the demanded robustness according to $^1J_{CH}$ coupling in the range of 120-250 Hz. Applying the cost function Φ_0 with identical simulation parameters to the originally proposed compensated BIRD sequence [79], results in a fidelity of 0.957, which is plotted against the sequence lengths (10.6 ms) in Fig. Fig. 5.3A and B (asterisk). The sequence is a good trade-off, however it is concluded that a 1.3 ms shorter OCT sequence could have reached the same fidelity.

As seen from Fig. 5.4A, the transfer efficiency of the BIRD and the J-compensated BIRD sequence increase around $J_{CH} = 0$ Hz. Following the sine function, smaller $^nJ_{CH}$-couplings give rise to a steep ascent of the transfer efficiency in that region. This is an unwanted property when using BIRD as a high pass J-filter in multidimensional NMR spectroscopy as will be discussed in the following.

5.3.3 High-Pass *J*-Compensated BIRD Sequences from OCT

This conceptually new type of sequences can be directly obtained from the conclusions drawn in Chap. 5.3. The identical optimization setup is chosen except that a second region is introduced, starting from $J_{CH} = 0$ Hz and ranging to $J_{CH} = 30$ Hz, which is evaluated at 11 explicit points (instead of weighting the point at $J_{CH} = 0$ Hz by a factor of 11). The transfer within that region is defined to be maximal if $I_{1z} \rightarrow I_{1z}$ is fulfilled. While the transfer within the region $J_{CH} = 120 - 250$ Hz is maximal if $I_{1z} \rightarrow -I_{1z}$ is fulfilled.
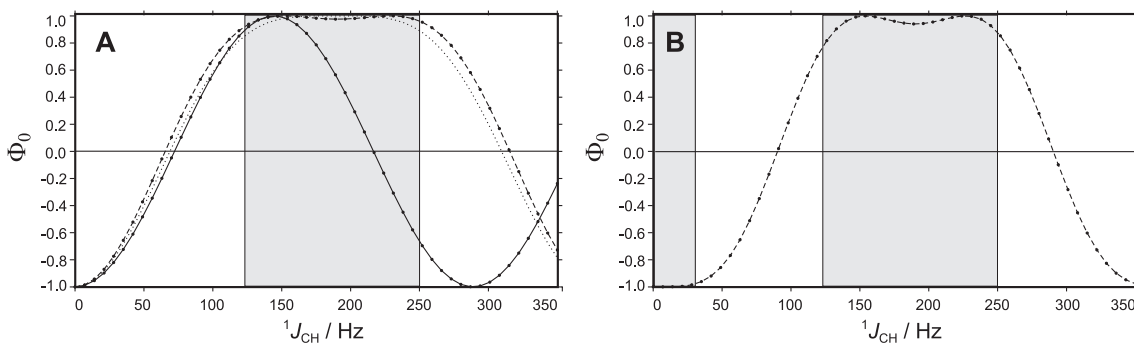
Figure 5.4: Simulations of transfer efficiencies (see text for details) for BIRD sequences depicted in Fig. 5.2 as a function of the J-coupling with on resonant rf irradiation and ideal rf amplitude. (A) BIRD sequence (solid line) [79], (A) J-compensated BIRD (dotted line) [79], (A) J-compensated pulse-delay sequence obtained from OCT with $n_d = 2$ and $t_s = 10.5$ ms (dashed line), (B) J-selective pulse-delay sequence obtained from OCT with $n_d = 2$ and $t_s = 15.76$ ms (dashed line).

By this, a "stop" and a "pass" band are defined, which are separated by a transition of $J_{CH} = 90$ Hz. In order to obtain a selectivity, which meets the demanded transition region, sequences are expected to not be shorter than $t_{s,\text{min}} = 1/\Delta_{J\text{trans}} = 11.1$ ms.

The first step is to optimize x, y-shaped sequences with durations $t_s = 0.5$-25 ms and a digitization of 100 μs. Conjugated gradients are for the update of the pulse sequence. For a given length t_s, 10 optimizations, starting from random controls, are carried out and the ones with best fidelity form the TOP curve depicted in Fig. 5.5A. As expected, the fidelity of the TOP curve increases with increasing sequence lengths t_s and the smooth shape is interpreted in the way that good convergence is obtained.

As it is needed to approximate the continuous pulse shape by a hard pulse-delay sequences to make it robust against offset and B_1 inhomogeneity, the optimization of the TOP-curves is repeated, with the restriction to n_d delays and $n_d + 1$ surrounding hard pulses. Parameters as described in Section 5.3 are used. The TOP curves are depicted in Fig. 5.5B.

5.3.4 Interpretation of High-Pass J-Compensated BIRD Sequences

The Interpretation of the high-pass J-compensated BIRD sequences follows the interpretation of broadband BIRD sequences. The x, y-TOP curve (Fig. 5.5A) forms a smooth envelope and it is concluded that good convergence according to the physical limit is reached (see Chapter 3.5). The vertical line at 11.1 ms assigns the lower limit of sequence lengths t_s, imposed by the chosen transition region.

Comparing pulse-delay sequence (Fig. 5.5B) among each other results in larger differences as compared to the broadband TOP curves (Fig. 5.3B). Also sequences with smaller number of delays are more distinct to not converge, once a critical sequence length t_s is exceeded. Nonetheless the $n_d = 4$ TOP curve approaches the x, y-TOP curve well. Among sequences with fewer delays, the sequence with $n_d = 2$ and $t_s = 15.76$ ms has a fidelity of 0.964 and is depicted in Fig 5.1D. The simulated transfer is given in Fig. 5.4B (dashed line) and it is concluded that the J-high-pass properties are adhered.

Finally, the TOP curves of x, y-shaped broadband BIRD (Fig. 5.6 magenta line) and high-pass BIRD sequences (Fig. 5.4 red line) are compared on the basis of Φ_0. Surprisingly, for
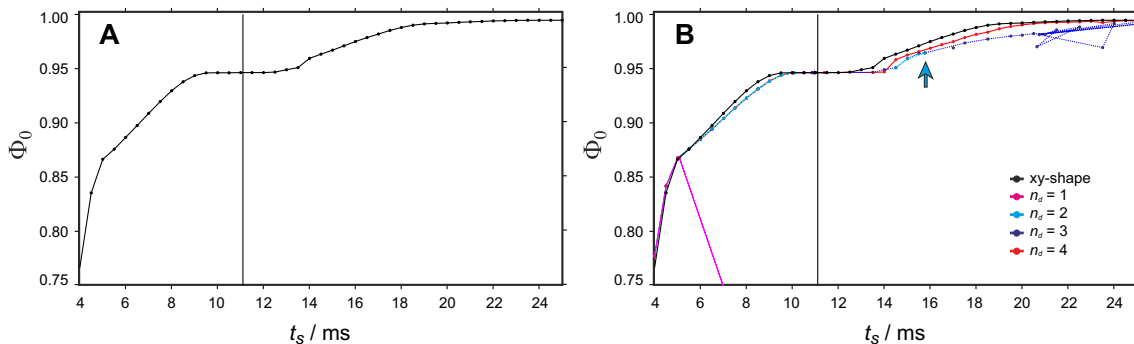
Figure 5.5: Time-optimal (TOP) curve for high-pass J-compensated BIRD filters as obtained by OCT for the on-resonant transfer of $I_z \rightarrow -I_z$ (via antiphase) in a 2 spin system. The combined cost function Φ_0 is averaged over the stop J-coupling range $0 < J < 30$ Hz and the pass J-coupling range $120 < J < 250$ Hz. The continuous x, y-shape (A, black), provides the highest performance at each overall sequence duration t_s. Optimal hard pulse-delay sequences with n_d delays surrounded by $n_d + 1$ pulses show decreased transfer efficiencies (B). TOP curves for $n_d = 1$ (solid line, magenta), $n_d = 2$ (dashed line, cyan), $n_d = 3$ (dotted line, blue) and $n_d = 4$ (solid line, red) are depicted. The pulse sequences depicted in Fig. 5.1D originates from $n_d = 2$ and $t_s = 15.76$ ms (highlighted by an arrow).

values shorter than $t_{s,\min}$, the fidelity of the high pass BIRD seems superior as compared to the broadband BIRD. While this relation is numerically correct for the defined cost function Φ_0 it may be counter intuitive according to what is expected for the mentioned sequences. This apparent discrepancy is explained by the fact that the stop band of the high-pass BIRD filter is easily fulfilled by short sequences while there is no stop band in the broadband BIRD, leading to the distorted picture that high-pass sequences seem to be superior in the region < 11.1 ms.

For sequences with durations larger than 8.33 ms, higher transfer efficiency are found for the broadband BIRDs. This can be understood from the fact that they are readily obtained from optimization.

5.4 Summary

As an 180° pulse is more sensitive to offset deviations as compared to a 90° pulse it has been shown that BIRD transfers suffer the equivalent problem when comparing them to the INEPT sequence with respect to J-robustness. J-compensated sequences are therefore highly desirable but the originally proposed broadband BIRD [79] does not meet sufficient performance.

As was pointed out, TOP curves are used to determine optimal sequences. It is concluded [7–9] that obtained sequences perform very close to optimal sequences for the desired robustness.

Second, conceptually new high pass BIRD filters are obtained by OCT methods. According to the TOP curves it is shown that the sequences perform very close to the best possible sequences for the desired robustness, making them potentially ideal for the application as building blocks in the multidimensional NMR spectroscopy, such as the suppression of $^1J_{CH}$-couplings in the presence of $^nJ_{CH}$-couplings.
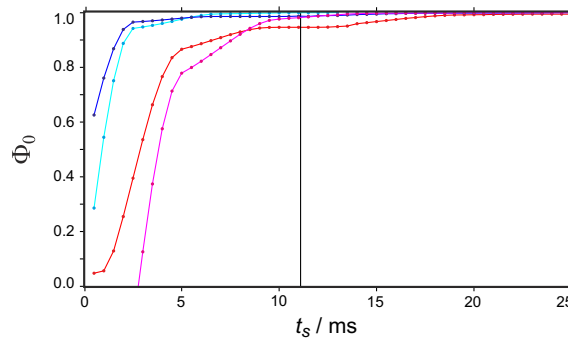
Figure 5.6: Time-optimal (TOP) curves for continuous x, y-J-compensated INEPT and BIRD sequences. All considered sequences have a duration of timesteps of 100 μs. BIRD sequences ($I_z \rightarrow I_z$, reddish colored liens) are compared to INEPT sequences ($I_x \rightarrow 2I_yS_z$, bluish colored lines). Broadband sequences are robust for J-couplings in the range of $120 < J < 250$ Hz (cyan and magenta line). High-pass sequences providing robust transfer for $120 < J < 250$ Hz and no transfer for $0 < J < 30$ Hz (blue and red line). As indicated by the intersection, observed at approximately 5 and 8 ms, high-pass sequences seem to be more efficient for short durations. This is misleading and arises from the evaluation points being evenly spread over the stopp and the pass-band. As a result of the selectivety being the reciprocal of the duration, selective sequences also need to be longer than 11 ms (vertical line). See main text for details. Larger transfer efficiencies obtained for the INEPT sequences (bluish lines) indicated that this transfer is more easily accomplished compared to the BIRD sequence.

It should be pointed out that, apart from the wanted transfer, there can be additional transfer in coupled spin systems. This is due to homonuclear couplings in the presence of the pulse-delay sequence. The discussed BIRD sequences are not robust against this couplings. But the effects are expected to be small as the $^1J_{\text{CH}}$-couplings are larger by approximately on order of magnitude.

Pulse sequences shown so far are only optimized for the on-resonant case. With the optimization of BURBOP pulses for corresponding hard-pulse rotations as described for the COB-INEPT (Chap. 4), the sequences become robust against offset and B_1-field inhomogeneities. Note also that the literature known J-compensated BIRD sequence [79] as well as the BIRD sequences described in this thesis transfer only one magnetization component (e.g. I_z), accordingly they do not possess universal rotation abilities.

6. Refocused COB-INEPT

6.1 Introduction and Motivation

The direct acquisition of natural abundance hetero nuclei, such as ^{13}C, has several advantages: a larger dispersion and longer coherence life times, compared to ^{1}H detection. This is enabled by proton decoupling, which avoids linebroadening due to scalar and dipolar CH-couplings.

Usually INEPT is used to enhance the sensitivity by transferring magnetization from ^{1}H to the low γ nucleus. However, it is not feasible to decouple the INEPT-enhanced signals because they are antiphase with respect to ^{1}H. The decoupling field would collapse the multiplet and the positive and negative parts would cancel out. Only the not enhanced inphase magnetization survives the decoupling.

In order to decouple, it is needed to refocus the enhanced antiphase signals. In the simplest case this is done by adding another spin echo sandwich. Turning towards CH, CH_2 and CH_3 groups, this is impossible because the optimal delays Δ of the refocusing sequence are different for all three spin systems (see Fig. 6.2A). Even for the optimal delay, the theoretical transfer limit of a CH_3 group can not be reached by a simple spin echo sandwich. Therefore, the following is dedicated to the question how efficient refocused INEPT sequences can be obtained by OCT-methods, which approach the physical limit for the mentioned spin systems.

6.2 Theory and Physical Limits

Applying pulse sequences with delays set to a standard value always poses the problem of non-uniform coupling evolution, since a single delay Δ can not match more than one coupling constant. Essentially the same is expected for refocusing, but the consequences are even more severe since the effect increases with the number of directly coupled spins.

Apart from mismatching $^1J_{\mathrm{CH}}$ couplings there is the question of the theoretical transfer limits for weakly coupled two, three and four spin systems (CH, CH_2 and CH_3). Surely an enhancement of γ_H/γ_C, $2\gamma_H/\gamma_C$ and $3\gamma_H/\gamma_C$ when starting from 1, 2 or 3 protons will not be exceeded. But a simple simulation reveals that these values are never reached for CH_2 and CH_3 groups. Starting on ^{13}C as the I-spin, which is antiphase with respect to one of the directly coupled ^{1}H-spins, the wanted transfer can be written as: $I_x S_{2z} \rightarrow I_y$ (since S_2, S_3 and S_4 commute). The simulation of this transfer, for the refocusing sandwich (Fig.
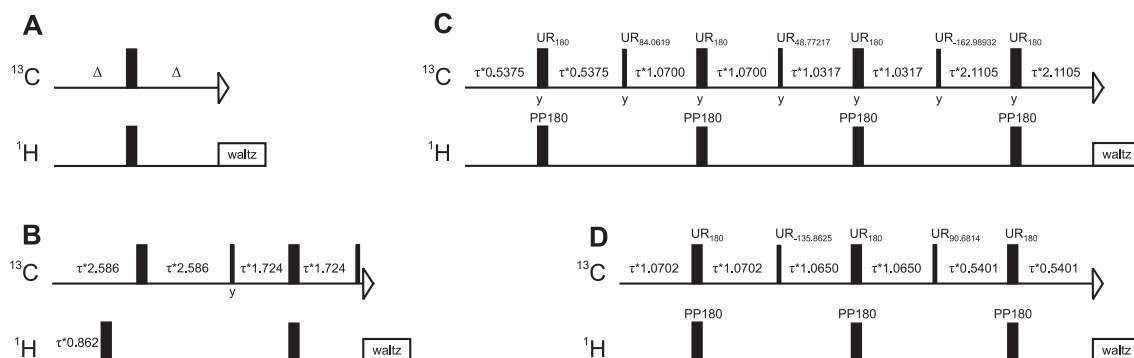
Figure 6.1: Pulse sequences for refocusing INEPT (antiphase to inphase): (A) Spin echo sandwich, (B) INEPT CR (derived from [82]) with $t_s = 8.62$ ms, (C) pulse-delay sequence obtained from OCT with $n_d = 4$ and $t_s = 9.5$ ms, (D) pulse-delay sequence obtained from OCT with $n_d = 3$ and $t_s = 5.5$ ms. Wide bars indicate 180° pulses and narrow bars 90° pulses, or pulses with the annotated flip angles. Shaped pulses according to Table 6.1. Pulse phases are x unless indicated otherwise. $\Delta = 1/(4 * 145$ Hz$)$. The duration of delays is given in ms and can be scaled by τ in order to obtain sequences optimal for an arbitrary range of J-couplings. By setting $\tau = 1$ results in the "standard" sequence that performs optimal for $^1J_{\mathrm{CH}} = 120 - 250$ Hz in CH, CH$_2$ and CH$_3$ spin systems.

6.1A), approaches the enhancement factor 1 for the CH spin system at $\Delta = 1/(2 *^1 J_{\mathrm{CH}})$ (Fig 6.2A, red, solid line). In this case the number of protons and the enhancement factor is identical, while this is not the case in the three spin system (CH$_2$) that has a maximal enhancement factor of 1 (Fig. 6.2A, blue, dotted line) at $\Delta = 1/(4 *^1 J_{\mathrm{CH}})$. The maximum enhancement factor in the four spin system (CH$_3$) is 1.155 (Fig. 6.2A, green, dashed line).

The problem of finding the theoretical limit for the refocusing boils down to finding the theoretical bound for Hermitian operator transfers in two, three and four spin systems that is discussed elsewhere [83]. But considering only weak heteronuclear coupling evolution, transfer properties can be imagined in a more pictorial way by assuming a number of two spin systems. As already seen by simulation (Fig 6.2A, red, solid line), the transfer in the two spin system (CH) is 100%. This would correspond to the hypothetical inversion of the negative part of the multiplet and thereby lead to an enhancement factor of 1.

The CH$_2$ system can be imagined as a two spin system in presence of a third spin, which may be up or down (Fig. 6.3D, E). Consequently there are two antiphase doublets with an overall displacement of J, leading to a cancellation of signal in the centre of the multiplet (Fig. 6.3B). As a result, the Hermitian bound is decreased by a factor of 2 and the enhancement factor for CH$_2$ groups is 1, and the effective heteronuclear coupling constant corresponds to $2 *^1 J_{\mathrm{CH}}$.

The theoretical bound of the enhancement factor of the CH$_3$ group is 1.5 and can be obtained in the same way, but starting from the CH$_2$ group. The multiplet patterns are therefore summarized to be (1:-1), (1:0:-1) and (1:1:-1:-1) for CH, CH$_2$ and CH$_3$ groups, respectively (Fig. 6.3A-C).

6.2.1 Known Refocusing Sequence

First steps towards the solution of the refocusing problem were made by Wimperis and Bodenhausen [47], who suggested a longer refocusing sequence, with improved sensitivity for CH$_3$ groups.
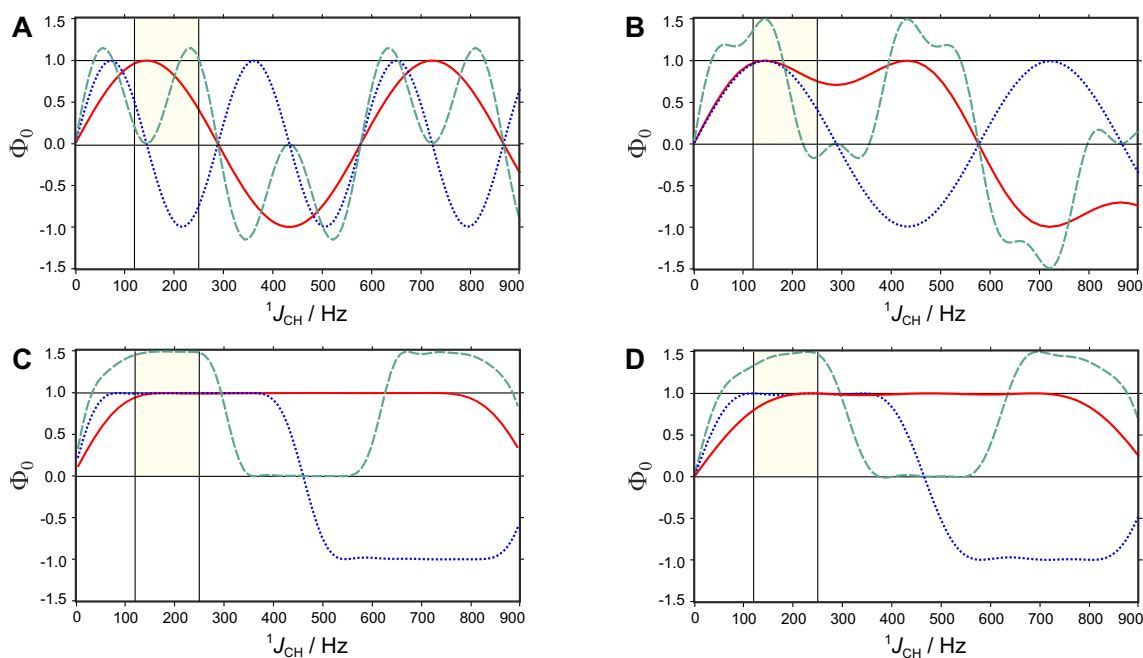
Figure 6.2: Transfer efficiencies for refocusing antiphase to inphase $(2I_xS_z \to I_y)$ for sequences depicted in Fig. 6.1A, B, C and D as a function of J-couplings with on-resonant rf irradiation and ideal rf amplitude. (A) Spin echo sandwich, (B) INEPT CR [82], (C) pulse-delay sequence obtained from OCT with $n_d = 4$, (D) pulse-delay sequence obtained from OCT with $n_d = 3$. Transfers depicted for CH_3 (red, solid line), CH_2 (blue, dotted line) and CH (green, dashed line) with physical transfer efficiency limits at 1, 1 and 1.5 (horizontal lines). Note that there is a $45°$ phase change for CH_2 groups (blue, dotted line) relative to CH and CH_3 groups for the INEPT CR (B) (that is compensated by the target operator of the simulation, but would lead experimentally to dispersive spectral artifacts. See text for details).

Figure 6.3: (A-C) ^{13}C antiphase multiplets, as obtained by INEPT, for CH, CH_2 and CH_3 groups. Three spin system can be imagined as two spin system with a third spin being either up (D) or down (E). Four spin system can be explained by three spin systems in the same way. Note that there is cancelation of signal for the CH_2 and CH_3 group (B, C), which decreases the bound of the enhancement factor.

In 1988 Soerensen et al. [82] derived the INEPT CR (Composite Refocusing) sequence (Fig. 6.1A), which approaches the theoretical limits for CH, CH$_2$ and CH$_3$ groups for a single coupling constant (Fig. 6.2B, close to $J = 145$ Hz). It is based on an analogy to the $(\beta)_x(2\beta)_y$ composite pulse for refocusing rf inhomogeneity. The simulation from antiphase to inphase results in enhancement factors of 1, 1 and 1.5 for CH, CH$_2$ and CH$_3$ groups for $^1J_{CH} = 145$ Hz and a given sequence length of 8.62 ms. Since coupling constants may be in the range of 120-250 Hz (vertical lines, Fig. 6.2) a severe effect on the enhancement factor is calculated. A further drawback of the INEPT CR is, that CH$_2$ groups are subject to a 45° phase change relative to CH and CH$_3$ groups, so that the resulting spectrum is not purely absorptive.

6.3 Refocusing Sequences from OCT

In principle, refocusing sequences could be optimized according to the needs by OCT in an interleaved fashion to suffice two, three and four spin systems. But considering the operators involved, a more efficient strategy can be applied.

$$2I_xS_{3z} \xrightarrow{\pi J_{13}\tau\pi J_{13}\tau} I_y sin(\pi J_{13}\tau) \xrightarrow{\pi J_{12}\tau} I_y sin(\pi J_{13}\tau)cos(\pi J_{23}\tau) = I_y sin(2\pi J_{13}\tau)$$

Considering a three spin system with I, S_1 and S_2 and starting from an enhanced antiphase signal $2I_xS_{3z}$, only the transfer into inphase operators is of interest. Other operators are neglected since they do not lead to detectable signals or are extinguished by the decoupling field. In this case, the closest inphase operator is I_y; that is modulated in a second step by J_{12}. The resulting term has a sine and cosine modulation and can be combined to a sine-amplitude at $2*J$, if $J = J_{13} = J_{12}$ is assumed.

Or with other words: The (1:0:-1) multiplet Fig. 6.3B can be lead back to a (1:-1) doublet of a two spin system with coupling constants J scaled by a factor of 2. As a result the J_{max} increases for the two spin system to 2*250 Hz.

This assumption holds true as long as there is no coherence transfer between different doublets. This transfer is avoided if there are no pulses other than 180° on ^{1}H that would just interchange coherence between the two transitions within the doublets.

Essentially the same holds for the 4 spin system that can be understood as the combination of a second one spin doublet with coupling constant J, and a one spin doublet with coupling constant $3J$ Fig. 6.3C. Allowing for that, the J_{max} of the corresponding one spin system increases to $J_{max} = 3*250 = 750$ Hz.

Obtaining the optimal operator transformation from antiphase to inphase in a two spin system with coupling constant spanning $J = 120-750$ Hz should approach the theoretical bound for operator transformations in three and four spin systems. Consequently, two spin OCT-optimizations should be sufficient to explore refocusing sequences that meet the theoretical bounds.

6.3.1 Exploring the Limits of Refocusing Sequences

The first step is to optimize x, y-shaped sequences in the Liouville van Neumann space with durations $t_s = 0.5$-40 ms and a digitization of 100 μs, which transform $2I_xS_z \rightarrow I_y$ according to a two spin system. The rf controls for the I-spin never approached the limit of 10 kHz and controls on the S-Spin are disabled. The cost and gradient function are evaluated for 31 explicit points in the range of $J = 120-750$ Hz and the offset of both spins are set to zero and no B_1 deviations are assumed. Conjugated gradients are used to update the sequence. For a given length t_s, 10 optimizations, starting from random
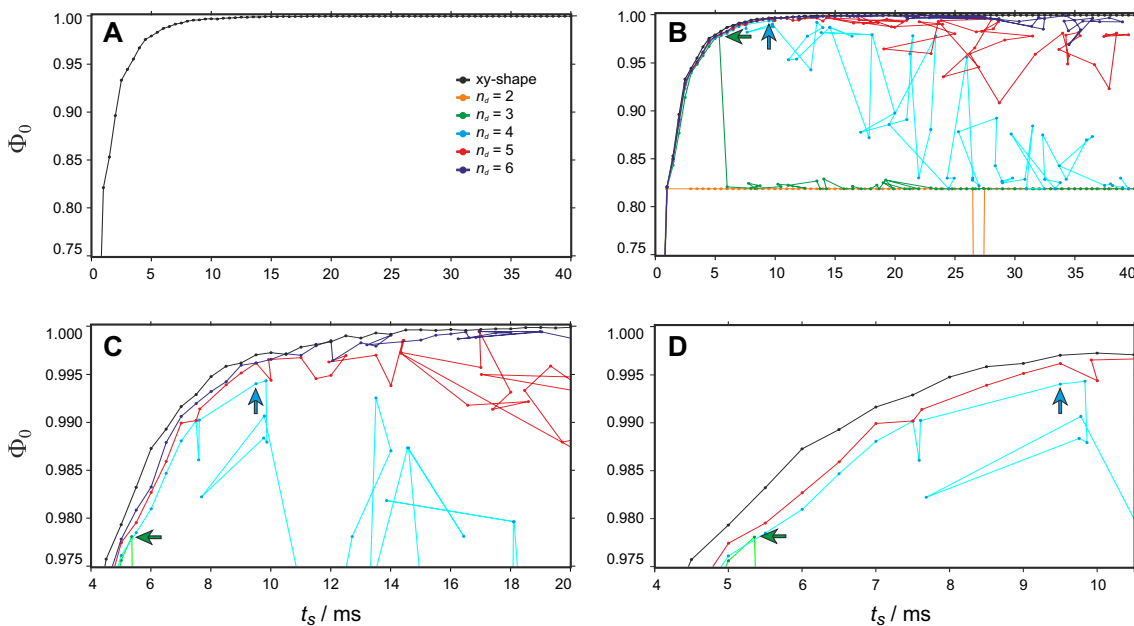
Figure 6.4: Time-optimal (TOP) curve for the on-resonant transfer of antiphase to inphase coherence $(2I_xS_z \rightarrow I_y)$ in a two spin system averaged over the J-coupling range $120 < J < 750$ Hz. The continuous x, y-shape (A, B, C and D, black), provides the highest performance at each overall sequence duration t_s. Optimal hard pulse-delay sequences with n_d delays intersected by $n_d - 1$ pulses show slightly decreased transfer efficiency (B, C and D). TOP curves for $n_d = 2$ (orange), $n_d = 3$ (green), $n_d = 4$ (cyan), $n_d = 5$ (red) and $n_d = 6$ (blue) are depicted. Sequences depicted in Fig. 6.1C, D and simulated in Fig. 6.2C, D originate from $n_d = 4$ and $n_d = 3$ (highlighted by arrows).

controls, are carried out and the ones with best fidelity form the top curve depicted in Fig. 6.4A. As expected, the fidelity of the top curve increases with increasing sequence lengths t_s and the smooth and continuous shape is interpreted in the way that good convergence seems to be obtained.

As it is needed to approximate the continuous pulse shape by a hard pulse-delay sequences to make it robust against offset and B_1 inhomogeneity, the calculation of the TOP curves are repeated, with the restriction to n_d delays and $n_d - 1$ intersecting hard pulses. Delays are defined by zero-controls and the gradient with respect to the time is evaluated. Pulses are defined by a duration of 0.5 μs and the gradient with respect to x, y-controls is calculated for the I-spin while no controls are allowed on the S-Spin. The update method is steepest ascent with two different update prefactors $\epsilon_{\text{delay}} = 10^{-7}$ and $\epsilon_{\text{pulse}} = 10^{12}$. While there is no restriction for the rf strength, the duration of delays is scaled down proportionately once t_s exceeds $t_{s,\text{max}}$, while there is no penalty for sequences shorter than $t_{s,\text{max}}$. For a given length t_s, 50 optimizations, starting from random durations and controls, are carried out and the ones with best fidelity yield the TOP curves depicted in Fig. 6.4B, C, and D.

The first thing that attracts attention when comparing the top curves of the hard pulse-delay sequences among each other (Fig. 6.4B, colored graphs), is that there is no convergence observed, once a certain sequence length t_s is exceeded. The limit for that observation increases with the number of increments in the hard pulse-delay sequence. The first sequence that would show convergence over the whole range from $t_s = 0.5 - 40$ ms has 7 delays (not depicted). If the number of intersecting pulses is restricted, t_s will at one

point not match the range of present coupling constant any more and the corresponding sequence is designated to not converge.

Looking closer into the hard pulse-delay top curve (Fig. 6.4C) reveals that: (i) The curves are not as continuous as the one derived from the x, y-shape. This might be due to incomplete convergence and by this gives an estimate of the "error" of the optimization. (ii) The top curves are very similar in fidelity. There is a small difference in fidelity as compared to the x, y-shape that is just large enough to be significant within the optimization-error. Leading to the interpretation that the simplest sequences with $n_d = 3$ and 4 delays and sequence lengths of $t_s = 5.5$ ms and $t_s = 9.5$ ms can be chosen for the experimental evaluation, with an expected performance of 97.81% and 99.40%, close to the physical limit.

6.3.2 Evaluating the Chosen Sequences and Theoretical Bounds

The chosen hard pulse-delay sequences (3 delays, 5.5 ms and 4 delays, 9.5 ms) are in each case the longest ones with highest fidelity, out of their top curve-families (see Fig. 6.4D). The pulse sequences are given in Fig. 6.1C,D. Actually, a number of optimizations clusters around that values, which seems to be the optimum for this combinations of length vs. increment number. Without putting any constraints, both sequences have uniform pulse phases, such as pure x or pure y-pulses and the evaluation with respect to the CH, CH_2 and CH_3 spin system reveals anti-symmetric and symmetric response on J when exceeding the optimized range for CH_2 and CH_3, respectively (Fig. 6.2C and D).

The 3 and 4-delay sequences also approach the enhancement factors 1, 1, and 1.5 for CH, CH_2, and CH_3 groups, respectively that is close to the theoretical bounds (Fig. 6.2C and D).

6.4 Experimental Setup

To confirm the theoretical results experimentally, a Bruker Avance II spectrometer (Rhe-instetten, Germany), equipped with a room temperature BBI inverse broadband probehead is used. A natural abundance sample containing a one molar solutions of dimethoxymethane (CH_2 and CH_3 spin system) and trimethoxymethane (CH spin system) in $CDCl_3$ at 298° K is used as the test system. The chemical shift on ^{13}C and the $^1J_{CH}$ coupling are: CH (112.3 ppm, $^1J_{CH,exp} = 187$ Hz), CH_2 (97.4 ppm, $^1J_{CH,exp} = 162$ Hz) and CH_3 (54.7 ppm, $^1J_{CH,exp} = 142$ Hz).

To cover the chemical shift on ^{13}C and avoid artifacts due to B_1-field inhomogeneity, pulses according to Table 6.1, obtained from single spin optimizations, are used. COB-INEPT (Chp. 4) is used to create the enhanced $^1H,^{13}C$ antiphase operators that are subjected to the discussed refocusing procedure, either by the adherence of the 5.5 ms or the 9.5 ms refocusing sequence.

6.4.1 The Three-Delay, 5.5 ms Sequence

Experiments are done with the sequence depicted in Fig. 6.5. ^{13}C magnetization is dephased and antiphase signals are created, starting from ^1H (Fig. 6.5A). The 5.5 ms refocusing sequence is used to bring the antiphase to inphase and the ^{13}C signal is recorded while decoupling is applied on protons. For robustness with respect to offsets and B_1-variations, pulses listed in Table 6.1 are optimized and used at the appropriate position in the pulse sequence instead of the hard pulses. The enhanced ^{13}C signals are compared to the reference experiment (Fig. 6.5B). The enhancement factors relative to the factor four expected from the ratio of ^1H and ^{13}C gyromagnetic ratios found, are 0.93, 0.91 and 1.28 for CH, CH_2 and CH_3 groups, respectively.

Table 6.1: Shaped Pulses for Refocused INEPT

	name[a]	transfer	t_p $[\mu s]$[b]	ν [kHz][c]	ν_{rf} [kHz]	ϑ[d]
^{1}H	PP180	z → -z	100	10	20	±20%
	PP90	z → x	550	10	20	±20%
	PP90^{tr}	x → z	550	10	20	±20%
^{13}C	UR180	180°_x	1000	37.5	10	±5%
	UR84	84.0619°_x	700	37.5	10	±5%
	UR48	48.77217°_x	700	37.5	10	±5%
	UR-162	-162.98932°_x	700	37.5	10	±5%
	UR-135	-135.8624°_x	700	37.5	10	±5%
	UR90	90.6814°_x	700	37.5	10	±5%
	PP90	z → x	550	37.5	10	±5%

[a] Abbreviations used as in Fig. 6.1: PP for point-to-point; UR for universal rotation pulses (e.g. refocussing pulses); [b] pulse length; [c] offset range of pulses for which corresponding pulses are compensated for; [d] variation of rf amplitude for which corresponding pulses are compensated for; [e] combined pulse sandwich for ^{1}H refocussing and ^{13}C inversion.
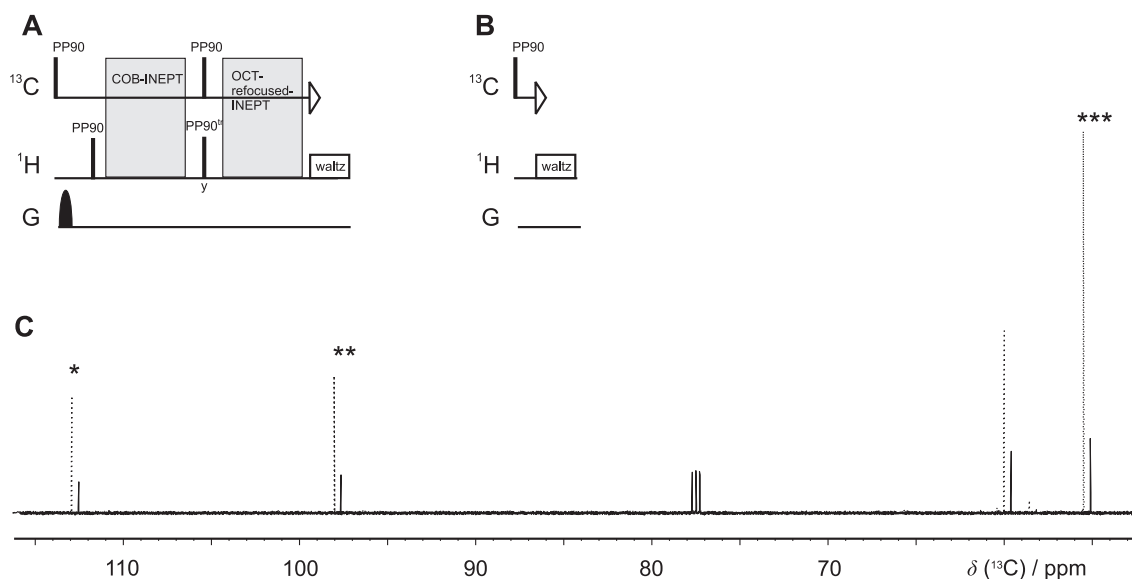
Figure 6.5: (A, B) Pulse sequences for the experimental determination of enhancement factors for CH, CH$_2$ and CH$_3$ groups. COB-INEPT is used for antiphase creation and the $n_d = 3$ sequence with $t_s = 5.5$ ms (Fig. 6.1D) for refocusing. ^{13}C spectrum (C, solid line), obtained by sequence (B) is compared to the enhanced ^{13}C spectrum (C, dotted line), which is obtained by sequence (A). Enhancement factors taking into account the expected gain of a factor 4 due to the gyromagnetic ratios of the initial magnetization are found for CH: 0.93 (C*), CH$_2$: 0.91 (C**) and CH$_3$: 1.28 (C***).

In order to map out the transfer efficiency as a function of the coupling, which can be directly compared to the simulation, given in Fig. 6.2D, the coefficient τ scales the delays in order to obtain experiments as applied to molecules with different effective J-couplings J^{eff}. Multiple experiments with $10 < J^{\mathrm{eff}} < 900$ Hz are acquired. The relaxation delay is 15 s. The scaling factor τ is calculated from $J^{\mathrm{eff}} = 10$ Hz until $J^{\mathrm{eff}} = 900$ Hz in increments of 5 Hz by $\tau = J^{\mathrm{eff}} / {}^1 J_{\mathrm{CH,exp}}$.

Figure 6.6 depicts the response of the CH group. Clearly, for shaped pulses applied to sp^3 hybridized moieties, only coupling constants $120 < J^{\mathrm{eff}} < 250$ Hz are expected, but as demanded by the theoretical considerations, the transfer would be optimal until $J^{\mathrm{eff}} = 750$ Hz.

Essentially the same behaviour is observed for the CH_2 group. There is robust transfer in the range of $120 < J^{\mathrm{eff}} < 250$ Hz. Again, the compensated region exceeds the necessary range.

The behaviour of the CH_3 group is given in Fig. 6.6. There is a robust transfer in the range of $120 < J^{\mathrm{eff}} < 250$ Hz. By this it can be stated that the experimental results for the simplest sequence (5.5 ms) are in good accordance with the theory (Fig. 6.2D).

6.4.2 The Four-Delay, 9.5 ms Sequence

To explore the experimental fidelity of the longer 9.5 ms sequence that has a superior overall transfer efficiency of 99.4%, the identical procedure is carried out.

Figure 6.7 depicts the results for the CH, CH_2 and CH_3 group, respectively. The result can be directly compared to Fig. 6.2C and Fig. 6.6. The first difference in the experimental performance is a dip at $J^{\mathrm{eff}} = 230$ Hz. Since the experimental setup (probehead, sample, experimental scheme, temperature) is identical, it is expected that the more complex sequence may be likely to be less pardoning to combinations of offsets and B_1 fields, which may be at the edge of the tolerated ranges. Another problem might be the concurrent shaped pulse design. In principle, the same kind of coupling evolution as in the BUBI pulse is expected for the present pulses, since shaped pulses are obtained from single spin optimizations. But the effects should be kept small, since the concurrent shaped pulse in the refocusing sequences consist of a combination of long (1 ms) ^{13}C and short (100 μs) ^{1}H pulses. So that the effective time with concurrent controls is short. But on the other hand, coupling constants in the CH_3 group reach the equivalent of $3*J$. As a result, sequences with a larger number of concurrent shaped pulses are expected to perform worse in combination with higher spin systems. This might be an explanation for the imperfect envelope observed for CH_3 groups (Fig. 6.7, CH_3). Note that the simulation (Fig. 6.2) considers only concurrent hard pulses, while experiments are performed with concurrent shaped pulses.

Under the assumption, that the artifact creation depends on the product of coupling and pulse length ($^1 J_{\mathrm{eff}} * t_p$), even the worst case scenario ($^1 J_{\mathrm{eff}} * t_p = 3 * {}^1 J_{\mathrm{CH_3}} = 3*145*100$ μs) yields a product, which is smaller by approx. a factor of 2, as compared to the BUBI pulse ($^1 J_{\mathrm{eff}} * t_p = 1 * {}^1 J_{\mathrm{CH}} = 1*145*600$ μs). Therefore it is concluded that the short concurrent pulses are an effective trade-off but small artifacts, as in the envelope of Fig. 6.7, CH_3, might be due to coupling evolution.

6.5 Conclusion

It has been shown that known refocused INEPT experiments [82] can reach the theoretical bound for CH, CH_2 and CH_3 groups just for a single $^1 J_{\mathrm{CH}}$-coupling and produce a phase shift for CH_2 groups so that the resulting spectra are not of pure absorptive phase.
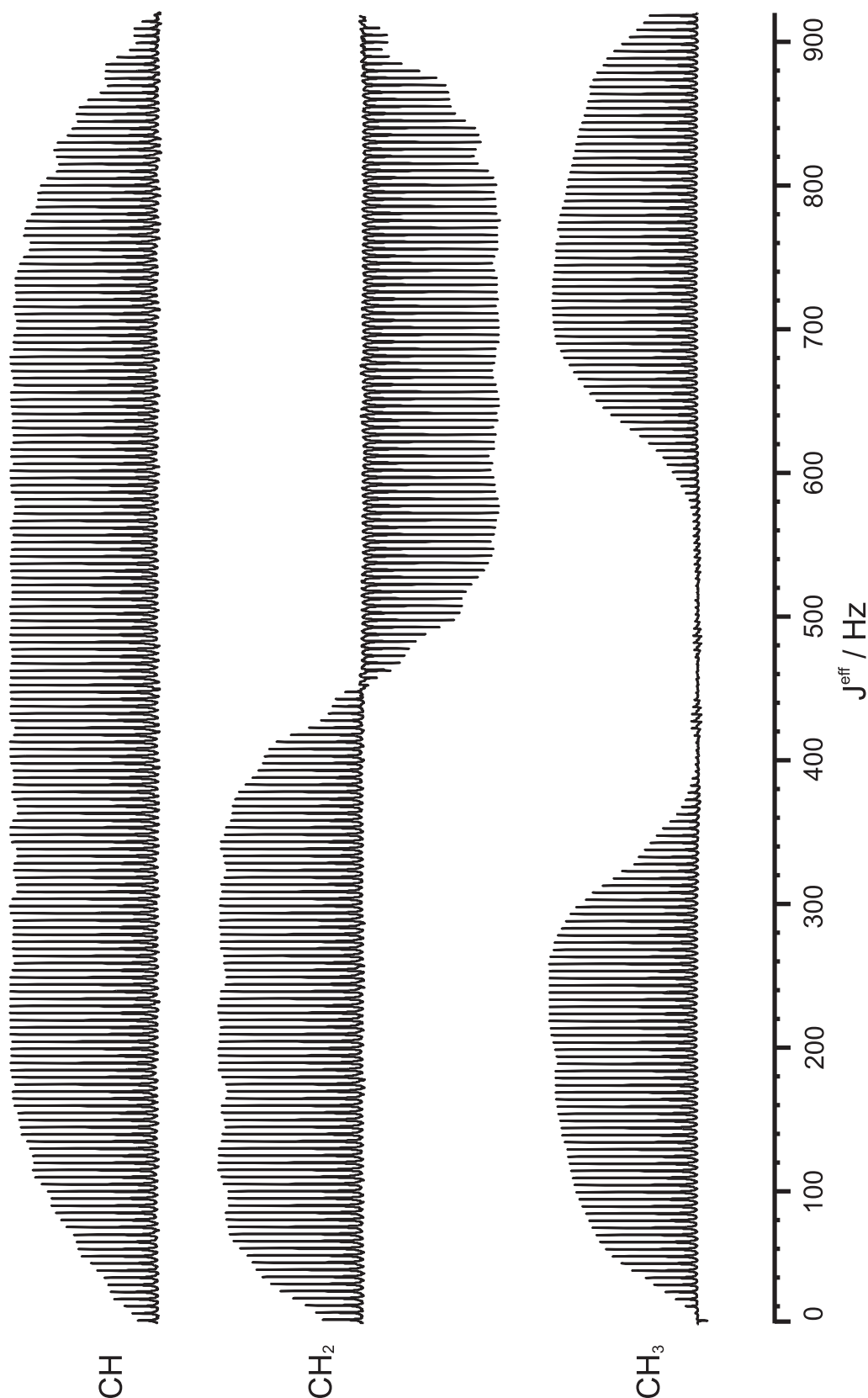
Figure 6.6: Multiple refocused INEPT experiments using the $n_d = 3$, $t_s = 5.5$ ms sequence (Fig. 6.1D), performed on CH, CH$_2$ and CH$_3$ groups of the compounds dimethoxymethane (CH$_2$ and CH$_3$) and trimethoxymethane (CH). Resulting transfer efficiencies are compared to theoretical results (Fig. 6.2D). Spectra are given according to J^{eff} as described in the main text.
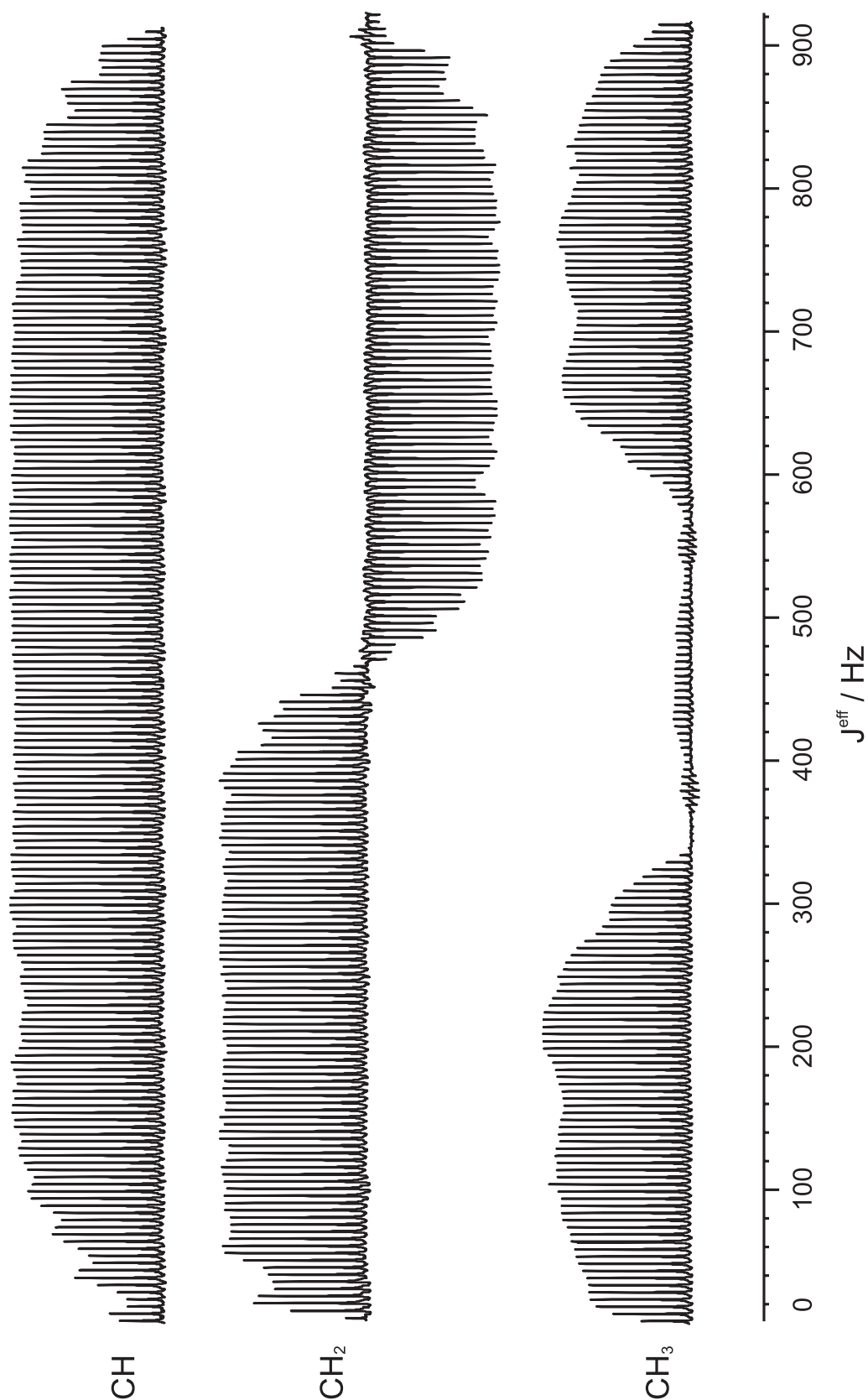
Figure 6.7: Multiple refocused INEPT experiments using the $n_d = 4$, $t_s = 9.5$ ms sequence (Fig. 6.1C), performed on CH, CH$_2$ and CH$_3$ of the compounds dimethoxymethane (CH$_2$ and CH$_3$) and trimethoxymethane (CH). Resulting transfer efficiencies are compared to theoretical results (Fig. 6.2C). Spectra are given according to J^{eff} as described in the main text.

Beside that, it was demonstrated that the theoretical framework of two, three and four spin systems can be boiled down to two spins, enabling efficient OCT optimizations of the refocusing problem.

Optimized pulse sequences approach the theoretical bound for the mentioned spin systems. According to the calculated TOP curves, sequences are provided, which are close to time-optimality. Therefore it is concluded [7–9], that the found OCT-refocusing sequences perform very close to the best possible sequences for the desired robustness.

The found sequences do not create phase deviations so that the resulting spectra are of pure, absorptive phase.

Experimentally, it is shown, that pulse-delay sequences as short as 5.5 ms can be used to acquire refocused INEPT experiments, which in essence meet the simulated transfers and the theoretical limits within the experimental error.

72

7. COB-INADEQUATE

7.1 Introduction and Motivation

There is no doubt about that INADEQUATE [84] is maybe the most attractive NMR experiment, for structure determination of organic molecules and natural products via ^{13}C,^{13}C-correlation. But there is also consensus about its main drawback, namely low sensitivity. At natural abundance, only one molecule out of 8734 contributes to the spectrum. This is very low, even by NMR standards and it is not uncommon that a structural problem can not be solved by INADEQUATE, simply because there is not enough material available or soluble to record a spectrum.

According to the INADEQUATE pulse sequence, given in Fig. 7.1, all potential aspects of signal loss have been analyzed:

- robust pulses (especially robust refocusing pulses) [84]

- optimal relaxation delay (=1.26*T_1) [84]

- Ernst excitation (is counter-productive. A 90° pulse not only excites the spectrum, but also suppresses single quantum artifacts) [84]

- optimal read pulse (that puts DQ coherence most efficiently back into SQ coherence) [84]

- optimal delays for the most common J_{CC} couplings [85]

- J_{CC}-compensated transfer elements [85]

- optimal coherence pathways selection (so that no signal is lost during PFG-echo, antiecho-selection) [86]

Of course, none of these improvements could have tackled the central issue, namely the given sensitivity at natural abundance level. It is emphasized that also OCT-techniques are not going to change the conceptual problem.

Nonetheless, OCT will be used in the following to obtain J_{CC}-compensated transfer elements that can span the whole range of naturally occurring coupling constants and perform well in regions where conventional sequences fail, opening for example the possibility to record ^{13}C,^{13}C-RDCs from INADEQUATE experiments.
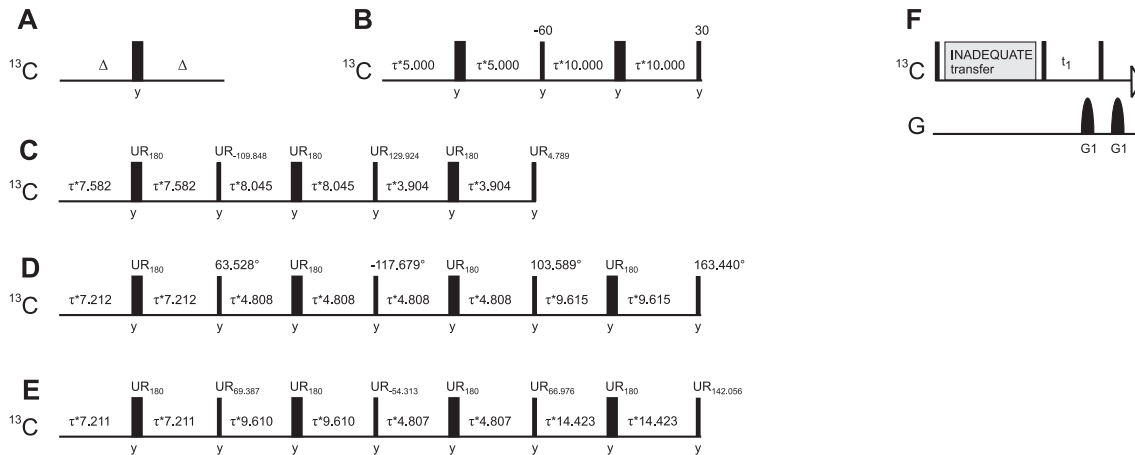
Figure 7.1: Pulse sequences for the INADEQUATE experiment. A two spin transfer element (A-E) is inserted in a standard, gradient enhanced INADEQUATE experiment (F). Transfer elements are: (A) a spin echo building block as suggested in [84], (B) J-compensated INADEQUATE as suggested in [85], (C) OCT derived J-compensated sequence with $n_d = 3$ and $t_s = 39.68$ ms for $30 \leq J \leq 100$ Hz, (D) OCT derived J-compensated sequence with $n_d = 4$ and $t_s = 52.88$ ms for $30 \leq J \leq 170$ Hz, (E) OCT derived J-compensated sequence with $n_d = 4$ and $t_s = 72.11$ ms for $20 \leq J \leq 188$ Hz. Wide bars indicate 180° pulses and narrow bars 90° pulses, or pulses with the annotated flip angles. Shaped pulses are listed in Table 7.2 accordingly. Pulse phases are x unless indicated otherwise. $\Delta = 1/(4 * 55$ Hz$)$. The duration of delays is given in ms and can be scaled by τ in order to obtain sequences optimal for an arbitrary range of J-couplings. Setting $\tau = 1$ results in the "standard" sequences that performs optimal for the range of naturally occuring $^1J_{\text{CC}}$ coupling constants.

7.2 Theory

According to Fig. 7.1F, the first 90° pulse converts z magnetization $(I_{1z}+I_{2z})$ to transverse magnetization $-(I_{1y}+I_{2y})$. During the following spin-echo, chemical shift is refocused, while J_{CC} puts $-(I_{1y}+I_{2y})$ into antiphase $(2I_{1x}I_{2z}+2I_{1z}I_{2x})$. The succeeding 90° pulse creates the desired double-quantum coherences $-(2I_{1x}I_{2y}+2I_{1y}I_{2x})$ that are modulated in f_1 according to the DQ frequency. Finally, magnetization is transferred back to detectable SQ $(2I_{1z}I_{2y}+2I_{1y}I_{2z})$ by a 90°_y read pulse. The resulting spectrum is antiphase with respect to the coupling partner.

Phase cycling can be used to select the DQ pathway and to reduce SQ artifacts. Usually phase cycling is capable of attenuating signals by approximately two orders of magnitude. Using phase cycling only, a first guess would be that artifacts and signals are on the same order of magnitude as a result of the naturally occuring isotope distribution. This may be the reason why most INADEQUATE experiments are acquired with gradient coherence order selection (COS), which is capable of suppressing unwanted coherence pathways by three orders of magnitudes, on top of the phase cycling. The price for the gradient enhanced signal to artifact (S/A) ratio is a reduction of S/N by a factor of two (since gradient selection applies either to the coherence order +1, or -1).

Gradient selection has become common practice, stressing the importance of artifact-suppressing experiments. The maybe most important innovation to INADEQUATE was only very recently a state selective version, which combines the benefits of gradient COS while retaining full S/N [87] [88] [86]. The sequence has good J_{CC} robustness (transfer efficiency 96.35 for J_{CC} 20% off and transfer efficiency 86.02 for J_{CC} 40% off (not taking into account the scaling of the excitation sequence by $sin(\pi J_{CC}\tau)$)) in addition artifacts created by mistuned J_{CC} have a coherence order which is gradient-suppressed, so that the S/A is not reduced.

Torres et al. [85] have proposed an analogy to B_1-field compensated composite pulses, which allows to derive J-compensated INADEQUATE sequences. They used Levitt's $90^\circ_\alpha 180^\circ_{\alpha+2\pi/3}$ [89] that is a short but efficient B_1-compensated 90° composite pulse. The correspondences of the Bloch picture with two spin coherences used in the approach are:

- $I_z \rightarrow (I_{1y}+I_{2y})$

- $I_x \rightarrow (2I_{1z}I_{2z}-2I_{1x}I_{2x})$

- $I_y \rightarrow (2I_{1x}I_{2z}+2I_{1z}I_{2x})$

With these relations, Levitt's composite pulse is transformed in the INADEQUATE transfer element shown in Fig. 7.1B, which is denoted in the following as JC-INADEQUATE. The fidelity of JC-INADEQUATE is obtained by simulation (Fig. 7.2A, solid line) and it is concluded that it covers most of the sp^3 and sp^2 coupling constants (indicated by the shaded regions in Fig. 7.2). There is a zero crossing in between the sp-carbons and the lower coupling constants, which in principle is not harmful, because there are only few functional groups resulting in a J_{CC}, in this region.

Essentially the same is also true for the simple spin-echo transfer element (Fig. 7.1A). As the simulation shows (Fig. 7.2A, dash dotted line), $\Delta = 1/55$ Hz seems to be a good compromise for most of the coupling constants. This might be the case because naturally occurring coupling constants of sp^3, sp^2 and sp moieties cluster nicely around some well defined values (as indicated by the shaded rectangular in Fig. 7.1). Signal attenuation is expected only for a few molecular sites (such as sp^3-sp^2 spin systems).
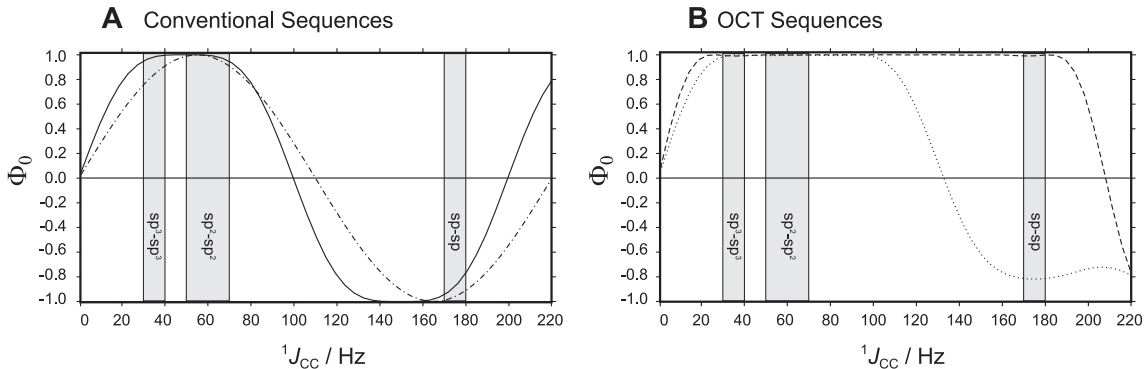
Figure 7.2: Simulations of transfer efficiencies for INADEQUATE transfer elements as depicted in Fig. 7.1A, B, D, E as a function of the J-coupling with on resonant rf irradiation and ideal rf amplitude. (A) Spin echo sandwich (dot dashed line), (A) JC-INADEQUATE (solid line) [85], (B) pulse-delay sequence obtained from OCT with $n_d = 3$ and $t_s = 39.68$ ms (dotted line), (B) pulse-delay sequence obtained from OCT with $n_d = 4$ and $t_s = 72.11$ ms (dashed line). Shaded rectangulars indicate the most common J-coupling ranges for sp^3, sp^2 and sp carbons. Note that the spin echo sandwich performs close to $\Phi_0 = -1$ for $J = 170$ Hz and by this performs well for most molecular sites in isotropic phase.

The situation changes if dipolar couplings are present, which are beneficially chosen to be in the order of ± 20 Hz to keep the experiment error small. They have to be counted on top of the $^1J_{CC}$ couplings, expanding the range of interest to approximately 20-190 Hz. As shown in Fig. 7.2A, neither the spin-echo transfer element (dash dotted line), nor the JC-INADEQUATE (solid line) are capable of covering this range. Therefore the following is dedicated to find OCT-sequences, which suffice this requirement.

7.3 Broadband J-Compensated INADEQUATE Sequences from OCT

Broadband J-compensated INADEQUATE sequences from OCT are derived in analogy to composite B$_1$-compensated 90° pulses using the analogy by Torres [85] as introduced in Section 7.2.

7.3.1 Antisymmetric x-Gradients

The derivation of B$_1$-compensated pulses by OCT poses, however, a number of challenges, when compared to other OCT-optimization protocols. This may be understood from the following conclusions: Lets assume x-pulses with arbitrary flip angle β. The effective flip angle β is given by the product of the rf amplitude ν_{rf} and the B$_1$-field scaling ϑ.

$$\beta = \nu_{\mathrm{rf}} * (1 \pm \vartheta) * 360° * t_p$$

If neglecting offset and spin-coupling, magnetization is restricted to a subspace, spanned by the operators $I_z \rightarrow -I_y \rightarrow -I_z \rightarrow I_y \rightarrow I_z$. By this, the state of the magnetization becomes directly dependent on the applied control and the corresponding hyper surface may be imagined as entirely symmetric and smooth, having maxima and minima at $-I_y$ and I_y. In order to obtain B$_1$ compensated pulses, a range of scaling factors ϑ is considered. However, $\partial\Phi/\partial u_x$-gradients at $\nu_{\mathrm{rf}=90+\epsilon}$ and $\nu_{\mathrm{rf}=90-\epsilon}$ are anti symmetric and therefore cancel out by the average that is computed in the gradient routine. In other words:
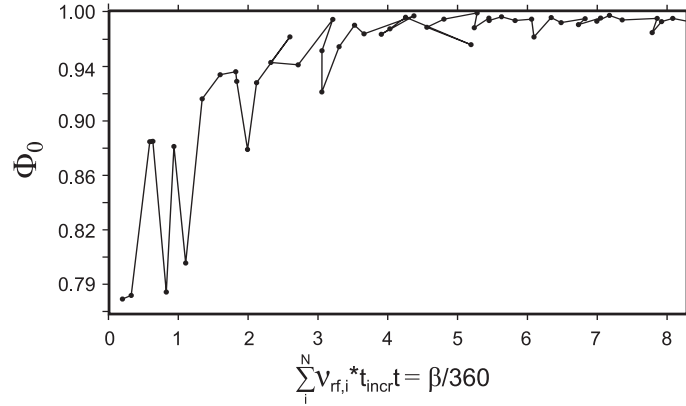
Figure 7.3: Time-optimal (TOP) curve for the on-resonant transfer of $I_z \rightarrow -I_y$ in a single spin system averaged over 31 distinct rf scaling factors spanning $\vartheta = \pm 80\%$. The pulse digitization is 1 μs and rf controls are truncated to not exceed 10 kHz. The actual rf amplitude ν_{rf} at each pulse increment i is multiplied with the increment duration ($t_{incr} = 1$ μs). The sum of the product is plotted against the fidelity Φ_0. The TOP curve shows an unsteady envelope that originates from incomplete convergence of the underlying optimizations (see main text for details).

Conventional, uncompensated 90° pulses are local maxima to OCT-optimizations, and are highly preferred due to the symmetry cancellation of gradients. This applies for both x, y-shaped pulses and composite pulses. This will result in optimizations that always converge towards the local maximum that is the not B_1-compensated pulse instead of the B_1-compensated pulse.

The symmetry is broken, either if additional terms in the Hamiltonian such as offset are considered, or if the initial rf fields ν_{rf} are very strong. Using a pulse with strong initial rf controls as starting point, OCT-optimizations can converge close to the global maximum for the demanded robustness. Because of the very restricted convergence, optimization success is almost exclusively restricted by the initial pulse; hence the calculation of TOP curves is much hindered.

Indeed it is not possible to obtain x, y-TOP curves in an appropriate optimization time. An unsteady TOP curve is exemplarily shown for $\vartheta = \pm 80\%$ in (Fig. 7.3).

7.3.2 B_1 Compensated Composite Pulses from OCT

Because of hindered convergence, TOP curves could not be used to review the physical boundaries of B_1-compensated pulses as a function of the overall flip angle β. Alternatively, three distinct sequences are optimized, which facilitate maximum rf tolerance, while not exceeding a maximum rf consumption of β_{max}.

To obtain B_1-compensated excitation composite pulses, a single spin is considered. A cost function Φ_0 is defined according to Eq. 3.23. The desired transfer is $I_z \rightarrow I_x$ that is measured by the overlap to the final density operator $\rho_F = I_x$.

A single spin Hamiltonian is considered (Eq. 3.8) and the offset is set to zero. The pulse shape is restricted to n_i increments with duration of 1 μs. The gradient according to the x and y amplitudes is calculated for 21 explicit points in the range of the present rf scalings ϑ. Starting from random controls, constant ε is used to update the pulse sequence. The overall rf consumption of the composite pulse is restricted to β_{max}. If β exceeds β_{max}, the

Table 7.1: B_1 Compensated Composite Pulses for the Creation of INADEQUATE Transfer Elements

n_i^a	β_{max}^b	$\pm\vartheta$	Φ_0^c	composite pulse	$\to t_s$ [ms]^d
3	1.25	0.54	0.99497	$174.69^\circ_{139.94}185.36^\circ_{359.63}89.95^\circ_{99.78}$	39.68
4	2.75	0.70	0.99532	$270.00^\circ_{155.88}180.00^\circ_{28.83}180.00^\circ_{264.18}360.00^\circ_{57.00}$	52.88
4	3.75	0.80	0.99626	$270.00^\circ_{179.18}360.00^\circ_{40.41}180.00^\circ_{149.03}540.00^\circ_{15.08}$	72.11

^{a} number of increments;
^{b} maximum number of rotations caused by the composite pulse that my not be exceeded;
^{c} fidelity for excitation (evaluated at 11 explicit points within the range of $(1 \pm \vartheta)$);
^{d} sequence length for corresponding INADEQUATE.

control vector is proportionally scaled down. In the following, composite pulses with the restriction to $\beta_{max} = 1.25$, 2.75 and 3.75 are optimized (Table 7.1).

Once the optimization converges close to an ordinary 90° pulse (that is the preferred local maximum) the corresponding value of the cost function triggers the reset of the pulse vector. The optimization is continued until convergence beyond the 90° threshold is reached. Random controls are on the order of several 360° rotations. An ensemble of composite pulses is collected. They are further optimized, while the update method, ε and the number of points for the evaluation of $(1 \pm \vartheta)$ is changed in order to escape local maxima. In total three B_1 compensated composite pulses with parameters listed in Table 7.1 are obtained. Consecutively, the pulses are transformed in pulse-delay sequences by the relation given in [85] and the resulting INADEQUATE sequences are depicted in Fig. 7.1.

7.3.3 Simulation of INADEQUATE Sequences

In the following, the properties of the INADEQUATE sequences are compared with the primarily obtained B_1-compensated composite pulses from Table 7.1.

A simulation of the transfer $I_z \to I_x$ for the B_1 compensated composite pulses is given in Fig. 7.4A-C that gives a detailed review on the transfer pattern in the range of $\Phi_0 = 0.95$ to 1. As expected by the B_1-J-equivalence, an identical envelope is found in Fig. 7.4D-F in the J-profile for the INADEQUATE sequences from Fig. 7.1C-E.

Note that the time and the J-coupling form a product in the Hamiltonian. Accordingly, the sequences depicted Fig. 7.1 are scaled in order to meet the desired J-coupling ranges. This is done for the chosen sequences, to result in overall durations of 39.68, 52.88 and 72.11 ms.

A simulation of the $n_d = 3$ ($t_s = 39.68$ ms) and the $n_d = 4$ ($t_s = 72.11$ ms) sequences are shown in Fig. 7.2B. The depicted frame ranges from $\Phi_0 =$ minus one to one and is compared to the simulation of the spin-echo and the JC-INADEQUATE (Fig. 7.2A). The $n_d = 3$ is concluded to be a short INADEQUATE transfer element that is ideal for the application with standard samples that have J-couplings in the range of $30 \leq J \leq 100$ Hz. On the other hand, the $n_d = 4$ ($t_s = 72.11$ ms) sequences covers the whole range of J-couplings. The transfer efficiency does not cross the zero-line as this is observed for the spin-echo or the JC-INADEQUATE and makes the sequence an ideal candidate for the measurement of $^1J_{CC}$-RDCs.
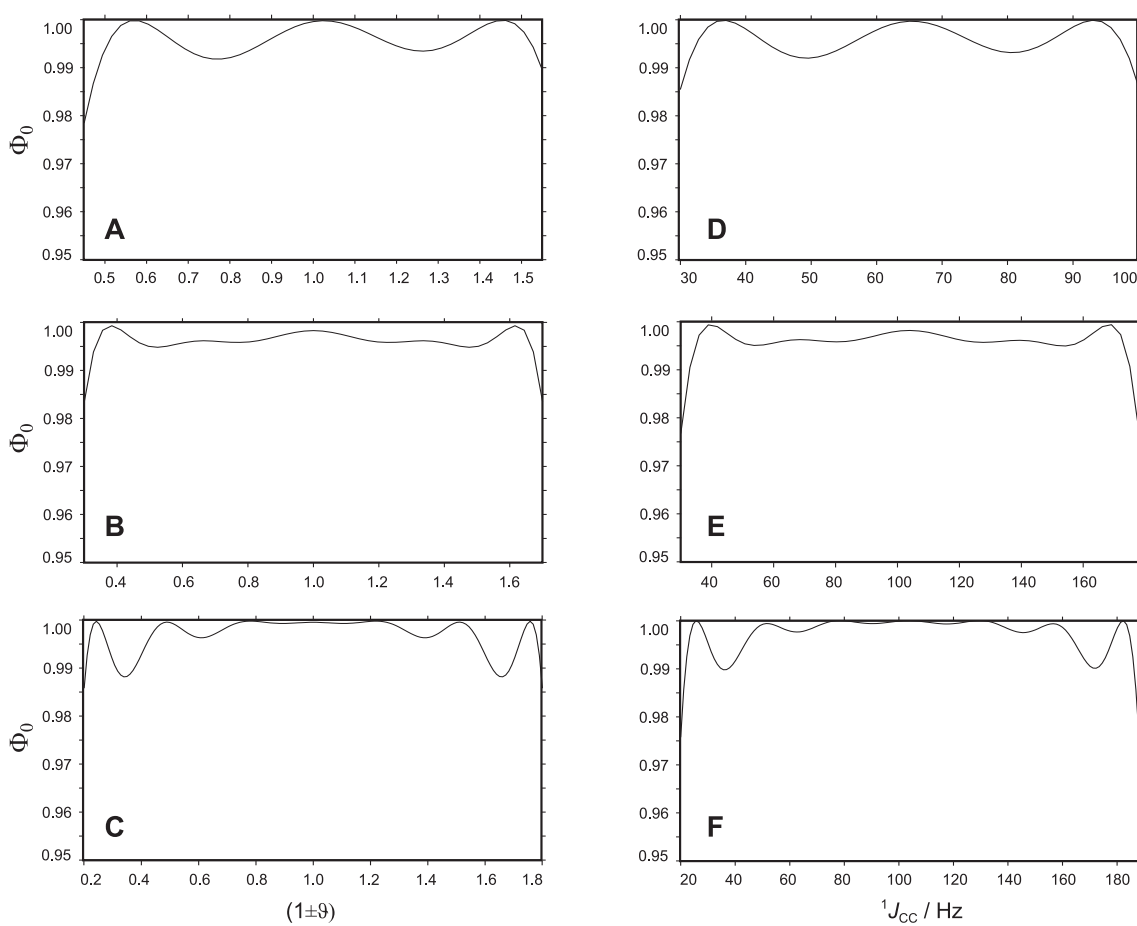
Figure 7.4: Simulation of transfer efficiencies for B_1 compensated composite pulses (A-C) (as summarized in Table 7.1) and the corresponding J-compensated INADE-QUATE sequences (D-F) (Fig. 7.1C-E). The offset is set to zero for all simulations. The INADEQUATE sequences are compensated for (D) $\vartheta = \pm 54\%$, (E) $\pm 70\%$ and (F) $\pm 80\%$. Because of the equivalence between rf scaling and J-coupling [85], profiles in a row resemble each other.

Table 7.2: Shaped Pulses INADEQUATE

name[a]	transfer	t_p [μs][b]	ν [kHz][c]	ν_{rf} [kHz]	ϑ[d]
PP90	z $\rightarrow$ -y	550	37.5	10	$\pm 5\%$
UR180	180°_x	1000	37.5	10	$\pm 5\%$
UR90	90°_x	700	37.5	10	$\pm 5\%$
UR-109	-109.848°_x	700	37.5	10	$\pm 5\%$
UR129	129.924°_x	700	37.5	10	$\pm 5\%$
UR4	4.789°_x	700	37.5	10	$\pm 5\%$
UR69	69.387°_x	700	37.5	10	$\pm 5\%$
UR-54	-54.313°_x	700	37.5	10	$\pm 5\%$
UR66	66.976°_x	700	37.5	10	$\pm 5\%$
UR142	142.056°_x	700	37.5	10	$\pm 5\%$

[a] Abbreviations used as in Fig. 7.1: PP for point-to-point; UR for universal rotation pulses;
[b] pulse length;
[c] offset range of pulses for which corresponding pulses are compensated for;
[d] variation of rf amplitude for which corresponding pulses are compensated for;

7.4 Experimental Evaluation of the INADEQUATE Sequences

7.4.1 Experimental Setup

The comprehensive theoretical framework of NMR spectroscopy gives access to very useful simulations. Despite, the experimental evaluation is still crucial. This might be due to the fact that the consequences of artifact creation on the resulting spectra are hard to calculate and may have severe consequences, as discussed in Chap. 8. For example ideal pulses are considered in the simulation. But in reality shaped pulses from single spin models are subjected to the full Hamiltonian. Homonuclear coupling evolution during shaped pulses may occur. This effect is estimated to be small, however, it needs to be shown whether the OCT-derived sequences, which employ a number of those pulses, perform the way they are intended to.

Accordingly, the following is dedicated to the experimental verification of the theoretical results, i.e. the reproduction of the simulated transfer profiles given in Fig. 7.2.

A very well arranged analyte is found in sodium 1,2-$^{13}C_2$ acetate that is purchased from Sigma Aldrich (99 atom %). A mixture of 400 μl DMSO-d_6 and 100 μl D$_2$O is prepared. The solvent composition is chosen to ensure good solubility for chromium acetylacetonate that is used as a relaxation enhancer and the sample is titrated with a saturated solution in DMSO-d_6 until relaxation times of $T_{1,^{13}C_{Me}} = 1.3$ s, $T_{2,^{13}C_{Me}} = 0.60$ s, $T_{1,^{13}C_{CO_2H}} = 2.3$ s and $T_{2,^{13}C_{CO_2H}} = 0.82$ s are obtained.

The experiments are performed using Brukers 600 MHz Avance III spectrometer (Rheinstetten, Germany), equipped with a H,C,N-triple resonance cryogenic probehead. They are performed at 300° K and the relaxation delay is set $> 5 * T_1$.

The chemical shift on ^{13}C and the $^1J_{CC}$ coupling are: CH$_3$ (25 ppm, $^1J_{CC,exp} = 52$ Hz), CO$_2$H (177 ppm, $^1J_{CC,exp} = 52$ Hz). To cover the chemical shift and to avoid artifacts due to B$_1$-field inhomogeneity, pulses according to Table 7.2, obtained from single spin optimizations, are used. The carbon rf irradiation frequency is set to 100 ppm.

During all experiments, waltz64 decoupling is applied on protons with a 180° pulse length of 100 μs.

7.4.2 The 39.68 ms INADEQUATE Transfer Element

The first OCT-derived sequence that is compared to the theoretical findings is the $n_d = 4$, $t_s = 39.68$ ms sequence (Fig. 7.1C).

The transfer element is inserted in a standard, gradient enhanced, INADEQUATE experiment (Fig. 7.1F). To compensate for B_1 field inhomogeneity and to cover the range of chemical shifts present on a 600 MHz spectrometer, shaped pulses listed in Table 7.2 are used. The shaped pulses are derived by OCT-methods using single spin models.

In order to map out the transfer properties of the OCT-derived sequence as a function of coupling strength, multiple experiments are performed, while changing the coefficient τ. τ is a scaling factor to all delays in the transfer element. Since the time and J_{exp} form a product in the Hamiltonian, changing τ is equivalent to employing spin systems with different J_{exp}. By changing τ from 0.03 to 2.5, multiplets as modulated by J^{eff} in the range of $1.6 \leq J^{\text{eff}} \leq 130$ Hz are calculated. The minimal and maximal values of τ are obtained by $\tau_{\text{min}} = J^{\text{eff}}_{\text{min}}/J_{\text{exp}}$ and $\tau_{\text{max}} = J^{\text{eff}}_{\text{max}}/J_{\text{exp}}$. The behaviour of the pulse sequence on J^{eff} is monitored by the concatenation of the antiphase multiplets resulting from the CO_2H group at 177 ppm and is depicted in Fig. 7.5B. The resulting envelope is of smooth shape and results in optimal transfer properties for the range of $30 \leq J^{\text{eff}} \leq 100$ Hz as expected from simulation (Fig. 7.2B, dotted line). A closer look at the experimental data reveals three maxima that are observed in the simulation given in (Fig. 7.4D) as well. Accordingly, it is assumed that the artifact contributions that could superimpose with wanted signals and interfere constructively or destructively is negligible small. It is concluded that the OCT-derived sequence can be used with the shaped pulses listed in Table 7.2, i.e. that the following two assumptions are fulfilled: (i) the number of shaped pulses and the effect of homonuclear coupling evolution during the shaped pulses is small, (ii) proton decoupling provides a setup that is compatible with the intended ^{13}C two spin system.

The same scaling procedure can be applied to the standard INADEQUATE sequence as well. In this case $\Delta = 1/(4 * 55$ Hz$)$ is subjected to the identical scaling factors τ. The response of the transfer efficiency follows the sine function and forms a smooth envelope (Fig. 7.5B). The maximum transfer is found at $J^{\text{eff}} = 55$ Hz.

Comparing the experimental data from Fig. 7.5A and B for couplings in the range of 0-30 Hz reveals a steeper ascent for the longer sequence (B). Generally, longer sequences result in better performance for small coupling constants. In other words: The lower transfer efficiency threshold ($J^{\text{eff}}_{\text{min}} = 30$ Hz) is defined by the maximum sequence length $t_{s,\text{max}}$. For the upper transfer efficiency threshold ($J^{\text{eff}}_{\text{min}} = 100$ Hz), the sequence length is not primarily critical. But the pulse-delay sequence must contain a minimum number of intersecting pulses to facilitate a transfer that can span an extended range of coupling constants, for example $20 \leq J^{\text{eff}} \leq 188$ Hz as discussed in the following for the $n_d = 4$, $t_s = 72.11$ ms sequence.

7.4.3 The 72.11 ms INADEQUATE Transfer Element

The $t_s = 72.11$ ms sequence (Fig. 7.1E) that should facilitate optimal transfer covering the whole range of naturally occurring $^{13}C,^{13}C$-coupling constant is evaluated experimentally using the same sample as in the foregoing section.

The transfer element is inserted in a gradient enhanced INADEQUATE sequence (Fig. 7.1F). To compensate for B_1 field inhomogeneity and to cover the range of chemical shifts present on a 600 MHz spectrometer shaped pulses listed in Table 7.2 are used. The shaped pulses are derived by OCT-methods using single spin models.

Multiple INADEQUATE experiments are performed, while changing the coefficient τ. By changing τ from 0.03 to 4.0 multiplets as modulated by J^{eff} in the range of $1.6 \leq$
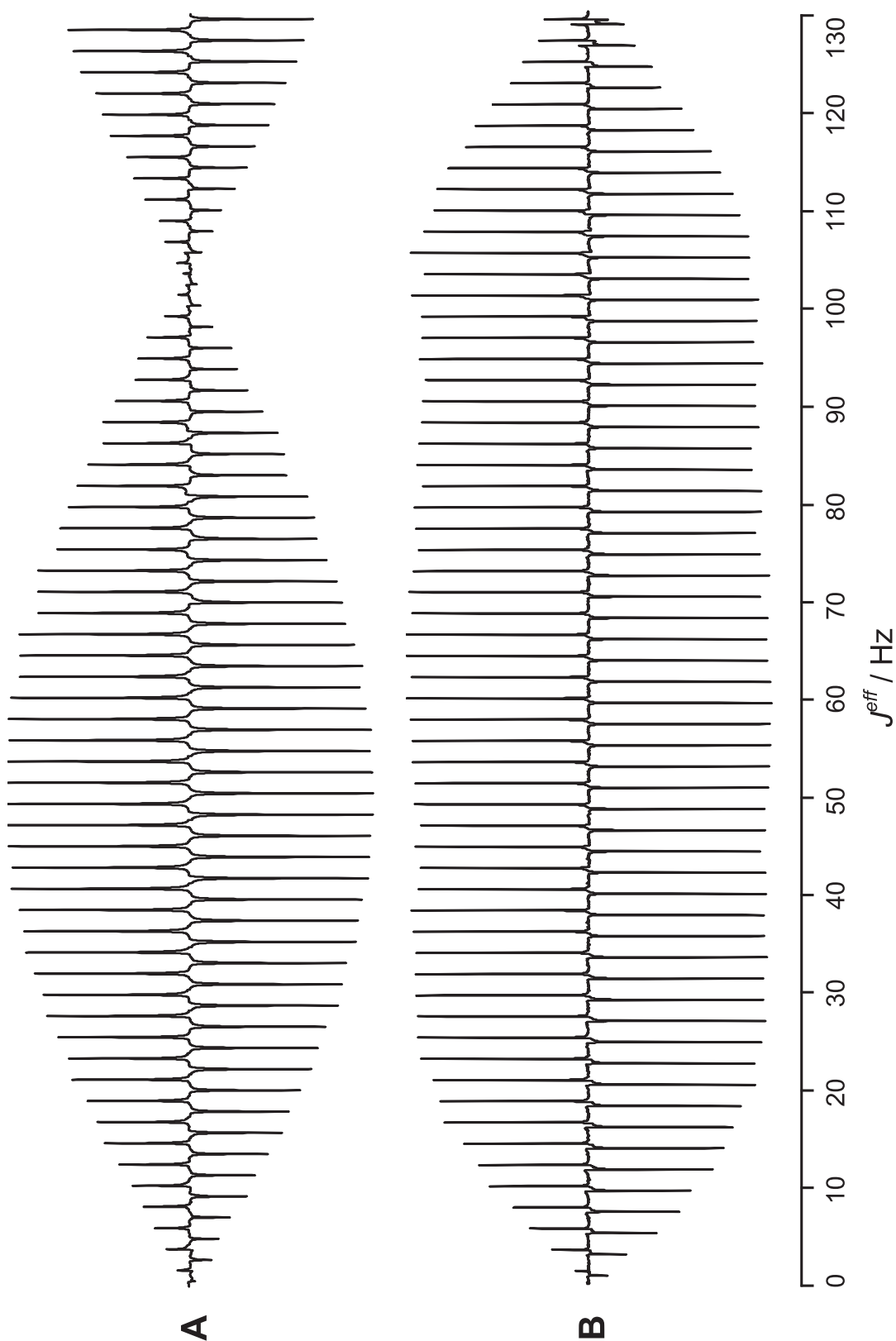
Figure 7.5: Multiple INADEQUATE experiments with the (A) spin echo transfer element (Fig. 7.1A) or (B) the $n_d = 3$, $t_s = 39.68$ ms sequence (Fig. 7.1C) performed on a uniformly ^{13}C enriched sodium acetate sample in DMSO-d_6, D$_2$O that serves as a homonuclear ^{13}C two spin system. Experiments result in 60 antiphase doublets that are depicted in a row. The pattern is modulated by J^{eff} (see main text for details). The envelopes are compared with the simulations given in Fig. 7.2A (dot dashed line and B, dotted line).

$J^{\mathrm{eff}} \leq 208$ Hz are obtained. The minimal and maximal values of τ are calculated by $\tau_{\min} = J^{\mathrm{eff}}_{\min}/J_{\exp}$ and $\tau_{\max} = J^{\mathrm{eff}}_{\max}/J_{\exp}$. The performance of the pulse sequence on J^{eff} is monitored by the concatenation of the antiphase multiplets resulting from the CO_2H group at 177 ppm and is depicted in Fig. 7.6B.

The obtained envelope is of smooth shape and depicts the transfer properties within the range of $20 \leq J^{\mathrm{eff}} \leq 188$ Hz that is in accordance with the simulation (Fig. 7.2B dashed line). A closer look at the experimental data reveals a characteristic modulation of the envelope (i.e. the dips at $J^{\mathrm{eff}} = 30$ Hz and $J^{\mathrm{eff}} = 170$ Hz) that are also recognized in the simulation given in Fig. 7.2B (dashed line).

Therefore it is assumed that the artifact contributions that could superimpose with wanted signals and interfere constructively or destructively is negligible small. It is concluded that the OCT-derived sequence in combination with the shaped pulses given in Table 7.2 is applicable to standard samples, i.e. that the following two assumptions are fulfilled: (i) the number of shaped pulses and the effect of homonuclear coupling evolution during this shaped pulses is small, (ii) proton decoupling provides a setup that is compatible with the intended ^{13}C two spin systems.

The scaling procedure is now applied to the standard INADEQUATE within the extended bounds of $1.6 \leq J^{\mathrm{eff}} \leq 208$ Hz and results are given in Fig. 7.6A. The response of the transfer efficiency follows the sine function and forms a smooth envelope Fig. 7.6B. As the magnetization is transferred it performs up to a full rotation ($-I_y \rightarrow 2I_xS_z \rightarrow I_y \rightarrow -2I_xS_z \rightarrow -I_y$) with zero transfer at $J^{\mathrm{eff}} = 110$ Hz. In contrast, the OCT derived sequence facilitates a robust transfer over the entire region.

7.5 Summary

Since its initial proposal [84] the INADEQUATE has been under continuous improvement. All aspects that are critical for optimal S/N are illuminated in several studies [90].

- robust pulses

- optimal relaxation delay

- optimal read pulse

- optimal coherence pathway selection

- optimal delays and J-compensated sequences [85]

According to that enumeration it can be stated that the present knowledge about INADEQUATE allows for experiments that perform very close to the theoretical transfer limit. However no J-compensated transfer elements are available that perform well over the whole range of naturally occurring coupling constants. The best known sequence [85] (simulation given in Fig. 7.2A, solid line) shows optimal transfer for $40 \leq J^{\mathrm{eff}} \leq 60$ Hz and $140 \leq J^{\mathrm{eff}} \leq 160$ Hz, which corresponds to approximately a quarter of the required bandwidth. The use of that sequence can result in signals with attenuated amplitude or the loss of the entire signal.

Therefore, in the present study, three OCT-derived INADEQUATE sequences are proposed. An analogy [85] to derive INADEQUATE sequences from B_1 compensated composite pulses is used and the optimization of B_1 compensated pulses is described. Guided by previous studies [7–9], it is concluded that sequences close to time-optimality are found.
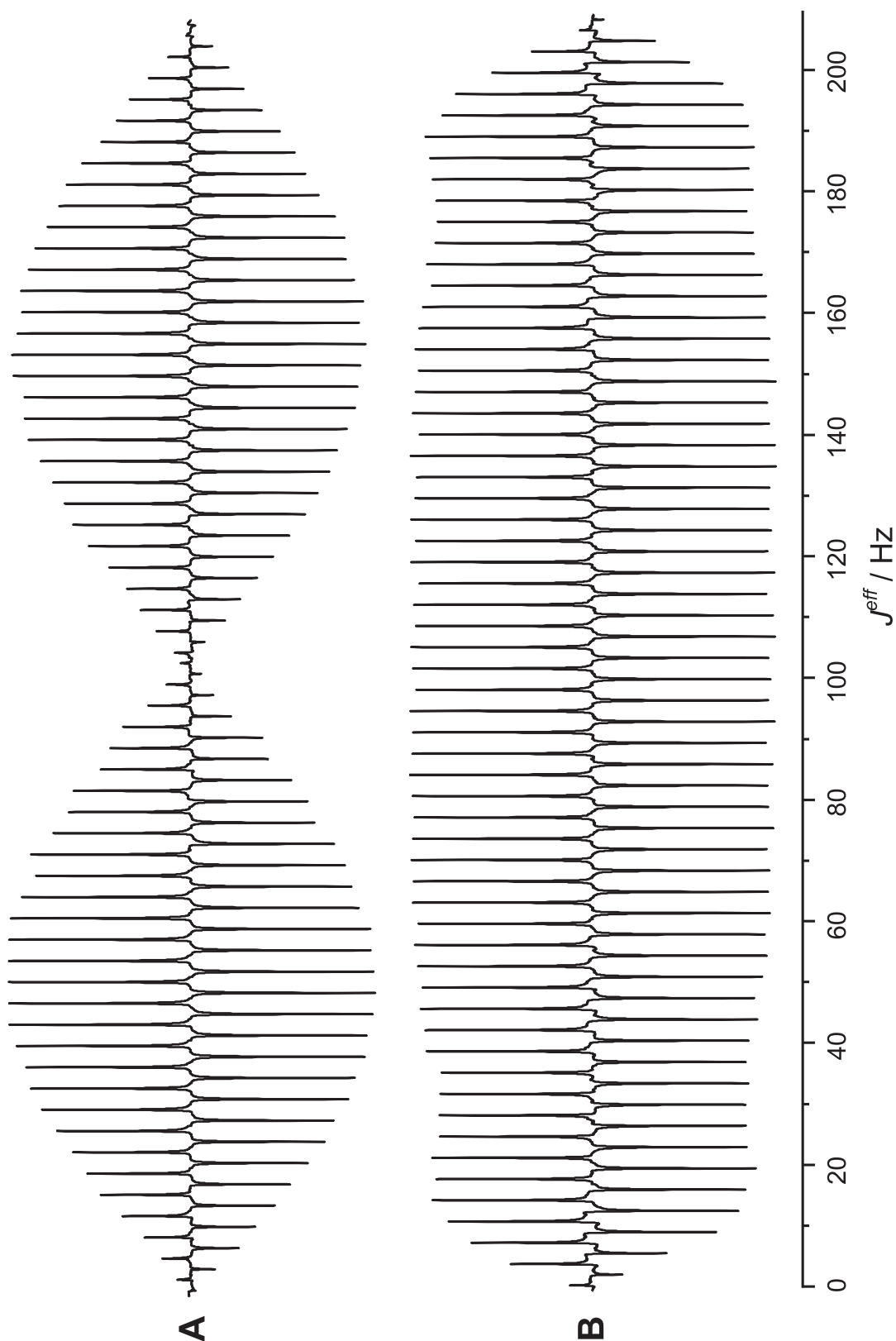
Figure 7.6: Multiple INADEQUATE experiments with the (A) spin echo transfer element
(Fig. 7.1A) or (B) the $n_d = 4$, $t_s = 72.11$ ms sequence (Fig. 7.1E) performed on
a uniformly ^{13}C enriched sodium acetate sample in DMSO-d_6, D$_2$O that serves
as a homonuclear ^{13}C two spin system. Experiments result in 60 antiphase
doublets that are depicted in a row. The pattern is modulated by J^{eff} (see
main text for details). The envelopes are compared with the simulations given
in Fig. 7.2A (dot dashed line and B, dashed line).

It is found that the on-resonant optimizations of B_1 compensated single spin pulses encounter gradient cancelation that is due to the antisymmetric behaviour that occurs when altering the flip angle $\beta = 90°$ by a small increment $\pm\varepsilon$.

Corresponding, optimizations are found to most likely converge to that local maximum that corresponds to a non-B_1-compensated excitation pulse. Using a large number of optimizations starting from random initial pulses, composite pulses are obtained that exceed the local maximum. The rf consumption of the B_1 compensated pulses is constraint to an overall flip angle β_{max} to later on ensure INADEQUATE experiments with sequence lengths shorter than $t_{s,\mathrm{max}}$.

Three Sequences are obtained that either span the entire range of naturally occurring coupling constants (Fig. 7.1E) or certain selected ranges (Fig. 7.1C and D). Making them good candidates for the acquisition of ^{13}C,^{13}C-RDCs.

Because the chemical shift on ^{13}C spans a range of approximately 250 ppm (37.5 kHz at 150.79 MHz) hard pulse-delay sequences would lead to serious offset defects. B_1 and offset compensated shaped pulses (Table 7.2) are tailored for the flip angles demanded by the OCT-derived INADEQUATE sequences.

The obtained sequences are evaluated experimentally as a function of J^{eff} and it is found that the theoretical predictions are affirmed. Especially it is confirmed that the supposed approximations are appropriate. For example that homonuclear coupling evolution during shaped pulses is negligible small. This holds for all proposed multi pulse sequences in this chapter.

Finally, it is concluded that time efficient INADEQUATE sequences are obtained that are robust against the whole range of naturally occurring coupling constants. The use of shaped pulses ensures stability against the most important variations found for the Hamiltonian of standard samples and it is concluded that the experiments performs close to the maximum transfer possible for the desired robustness.

8. The BUBI Pulse Sandwich

8.1 Introduction and Motivation

In modern NMR spectroscopy available field strengths for many nuclei lead to spectral widths which can barely be covered by the bandwidths of achievable hard pulses. It was early on recognized that the accessible bandwidth can be significantly increased by the use of composite pulses [19, 91–95], which led to computer optimization of corresponding pulses for diverse applications [22, 28, 96–100]. Today, a large variety of composite and shaped pulses are available which allow broadband excitation [7, 8, 101–109], inversion [7, 8, 110–112], and refocusing [6, 9, 23, 24, 26, 27, 68, 113–120] as the basis for robust correlation experiments. With the advent of optimal control derived computer algorithms [3, 10, 11, 121–124], the optimization of shaped pulses [125–127] and transfer elements [128–131] has been taken to a further level of complexity, as such methods allow the efficient optimization with several thousand independent parameters like rf amplitudes and pulse phases, which even led to the calculation of time optimality [29] to explore the physical limits of corresponding pulses [7–9] and transfer elements [33, 34].

In ^{1}H,^{13}C correlation experiments broadband shaped pulses have a long history, especially concerning inversion and refocusing pulses on carbon [113, 116], which are used routinely in corresponding pulse sequences today. Corresponding proton pulses are still applied as hard pulses as available rf amplitudes more or less cover the necessary bandwidth. However, B_1-inhomogeneities and large variations of ^{1}H pulse lengths with respect to salt concentrations in especially cryogenically cooled probeheads make the use of robust shaped pulses also desirable for this nucleus.

First attempts of using broadband and especially B_1-compensated shaped pulses for protons are promising, but sometimes unexpected losses of magnetizations or phase distortions have been observed (unpublished data), which so far cannot be attributed to a specific cause. One explanation is J-coupling evolution during pulse shapes. We therefore started the optimization of J-compensated pulse shapes to theoretically and experimentally study potential differences in performance compared to conventionally derived broadband pulses that are not compensated for coupling evolution. In the following, corresponding results for two concurrently applied pulse pairs are described. After a detailed derivation of optimization procedures for J-compensated pulses using optimal control derived algorithms, an experimental comparison of the performance of such pulses with respect to uncompensated time optimal pulse shapes is given.
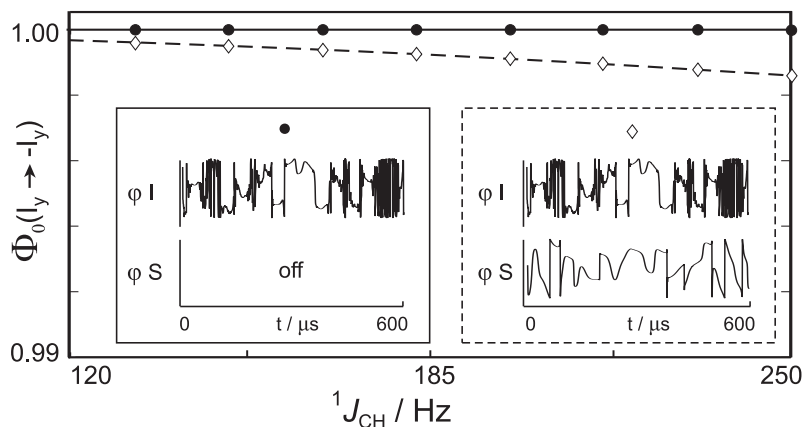
Figure 8.1: Theoretical on-resonant proton transfer efficiency $\Phi(I_y \rightarrow -I_y)$ of a conventional universal rotation 180° or refocusing pulse (BURBOP-180, [6,9]) with respect to the J-coupling of a heteronuclear two spin system. While the pulse refocuses coupling evolution with close to 100% transfer if no pulse is applied to the heteronucleus (•, dashed line), the concurrent application of an inversion pulse (BIBOP, [7,8]) leads to reduced transfer efficiencies ($\diamond$, solid line).

8.2 Theory

Modern shaped pulses for broadband applications are usually derived using a single spin $\frac{1}{2}$, generally neglecting spin-spin couplings. In many especially heteronuclear experiments, however, coupling evolution may significantly affect the pulse performance. The effect thereby depends not only on the spin system being present, but also on the particular use within a pulse sequence or pulse sequence element. In Fig. 8.1, for example, the simulated transfer efficiency for $I_y \rightarrow -I_y$ of a refocusing or universal rotation (UR) 180° pulse is shown for the simplest and frequently occuring heteronuclear 2-spin system of a ^{1}H nucleus directly coupled to a covalently attached ^{13}C nucleus (a 600 μs BURBOP-180$_x$(11 kHz, 20 kHz, 600 μs, $\pm$20%, 1200) refocusing pulse, using the nomenclature defined in Ref. [9]). In the first case, when only the proton pulse is applied, the on-resonant performance is 0.999997, independent of the heteronuclear J-coupling (Fig. 8.1, dashed lines); the second case, involving the concurrent irradiation of an inversion pulse on the heteronucleus, results in a decreasing transfer efficiency for increasing $^1J_{\mathrm{CH}}$ coupling constants.

The cross talk during concurrently applied shaped pulses generally has two potential sources:

- conventional coupling evolution from inphase to antiphase and vice versa, and

- heteronuclear coherence transfer under double rotating frame Hartmann-Hahn matching conditions [132].

With few exceptions [74], broadband shaped pulses are usually phase-compensated to provide the same particular magnetization components throughout the optimized bandwidth. With this phase-compensation, any rotation in the x, y-plane, i.e. chemical shift evolution as well as heteronuclear J-coupling evolution, is inherently refocused when the pulse is applied to a single nucleus. In this case also the Hartmann-Hahn condition cannot be fulfilled, as rf fields do not match for the heteronuclear coupled spins, explaining the observed independence with respect to J-couplings (Fig. 8.1, dashed line). When a concurrent pulse shape is applied, instead, coupling evolution is no longer refocused and HEHAHA matching
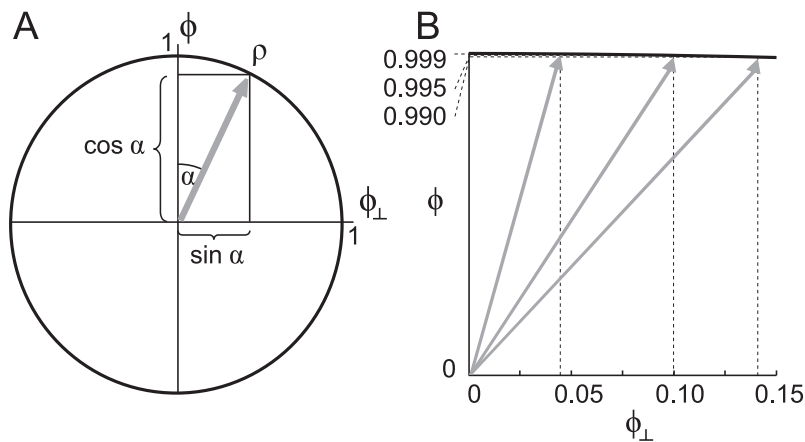
Figure 8.2: Visualization of the amount of expected undesired pulse properties for various values for quality factors or cost Φ. (A) Neglecting relaxation, the effect of any pulse sequence can be described by effective rotations, conserving the norm of the total spin density operator and the effective propagator; for any given quality factor Φ defined as the scalar product to a desired property, an angle $\alpha = \cos^{-1} \Phi$ can be derived and the amount of total unwanted magnetization results to $\Phi_\perp = \sin \alpha$. Quality factors as high as 0.999 still result in potentially undesired terms in the order of several percent (B).

conditions might be accidentally reached, eventually leading to reduced pulse performance (Fig. 8.1, solid line).

At first glance, the reduction of $\Phi(I_y \to -I_y)$ to values around 99.8% appears to be negligibly small for the desired transfer. For applications in complex pulse sequences, however, also the transfer to unwanted magnetization has to be considered, which eventually could lead to artifact signals and further signal reduction after undesired coherence transfer. If Φ represents a quality factor defined as the projection of the effective propagator U_{eff} or spin density ρ_{eff} to the desired target U_F or ρ_F, respectively, the term $\Phi_\perp$ might represent the corresponding maximum projection perpendicular to the desired property. As long as relaxation is neglected, the effective evolution under a pulse sequence can be described by rotations and Φ and $\Phi_\perp$ can be considered to be proportional to $\cos \alpha$ and $\sin \alpha$, respectively (Fig. 8.2). In this situation, already small deviations from perfect transfer properties are responsible for significant amounts of unwanted magnetization with quality factors of $\Phi = 99.9\%$ (99.5%; 99%) leading to angles $\alpha = 2.6°$ (5.7°t; 8.1°t), and artifact signals of $\Phi_\perp = 4.5\%$ (10%; 14.1%). Especially for UR pulses, which are typically used when spectral cleanup is difficult to achieve as more than one magnetization component has to be preserved, such amounts of undesired magnetization will result in severe limitations with respect to applications. Our aim in the following is therefore to reduce the amount of potential artifact magnetization by optimizing J-compensated concurrent pulse shapes using optimal control theory.

8.2.1 Spin Hamiltonian and Optimal Control Theory

Considering a heteronuclear two spin system, the total Hamiltonian $H(t)$ can be written as the sum of the spin Hamiltonians of spins I and S and a coupling term

$$H(t) = H_I(t) + H_S(t) + H_J, \tag{8.1}$$
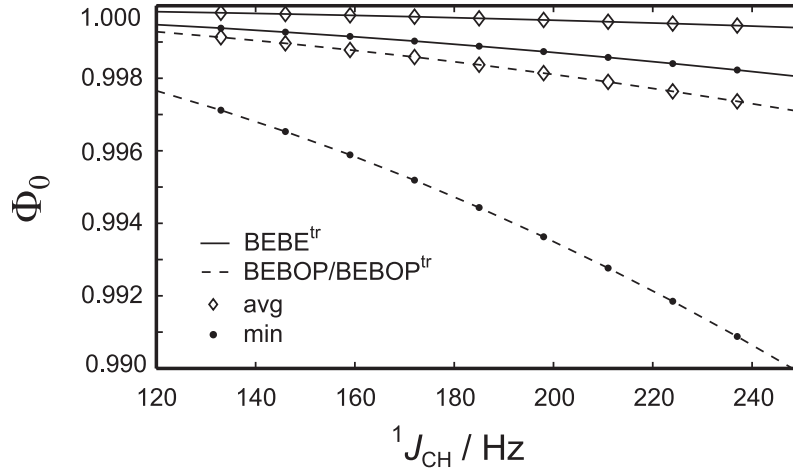
Figure 8.3: Simulation of the transfer efficiencies $I_z \rightarrow -I_y$ of the BEBE^{tr} pulse sandwich (solid lines) compared to the simultaneous application of a BEBOP(11 kHz, 20 kHz, 550 μs, $\pm$20%, 1100) on I and a time-reversed BEBOP(37.5 kHz, 10 kHz, 550 μs, $\pm$5%, 1100) on S (dashed lines) with respect to the J-coupling of a heteronuclear two spin system. For each pulse pair the average ($\diamond$) as well as the minimum performance ($\bullet$) over all specified offsets and rf amplitude ranges is given. The transfer of $I_x \rightarrow I_x$ and $I_y \rightarrow -I_y$ are qualitative and quantitative very similar (not shown)

with

$$H_I(t) = 2\pi\nu_I I_z + 2\pi u_{I_x}(t)I_x + 2\pi u_{I_y}(t)I_y, \qquad (8.2)$$

$$H_S(t) = 2\pi\nu_S S_z + 2\pi u_{S_x}(t)S_x + 2\pi u_{S_y}(t)S_y, \qquad (8.3)$$

$$H_J = \pi J 2 I_z S_z. \qquad (8.4)$$

where the spin Hamiltonians contain entries for the offsets ν_I and ν_S and for effective rf pulses at times t described by the control vector $u(t) = (u_{I_x}(t), u_{I_y}(t), u_{S_x}(t), u_{S_y}(t))$.

A cost function Φ, which specifies the fidelity of $u(t)$, can be defined in different ways. Following the nomenclature of the original GRAPE algorithm [3], two very intuitive and powerful basic types of cost functions, Φ_0 and Φ_3, are readily available for the optimization of shaped rf pulses.

8.3 Concurrent Shaped Pulses from OCT

8.3.1 Concurrent PP Excitation Pulses: The BEBE^{tr} Pulse Sandwich

A straightforward case for the optimization of concurrent shaped pulses are PP pulses, as for example the common case of an excitation pulse on one nucleus and a time-reversed excitation pulse on the second nucleus. Neglecting heteronuclear coupling, this task can for example be accomplished by a BEBOP and a time-reversed BEBOP pulse on ^{1}H and ^{13}C, respectively. Correspondingly, the concurrent pulse sandwich representing the same broadband excitations in a J-compensated way is refered to as BEBE^{tr}.

The extension of the cost function Φ_0 for a single point-to-point transformation according to Eq. (3.23) to n_{PP} individual transformations is simply the average of the corresponding individual cost functions as described by the sum

$$\Phi_{00} = \frac{1}{n_{\mathrm{PP}}} \sum_{i=1}^{n_{\mathrm{PP}}} \Phi_0^i \tag{8.5}$$

$$= \frac{1}{n_{\mathrm{PP}}} \sum_{i=1}^{n_{\mathrm{PP}}} \mathfrak{Re} \langle \rho_{\mathrm{F}}^i | U_N \cdots U_1 \rho_0^i U_1^\dagger \cdots U_N^\dagger \rangle$$

using the propagators of the full spin system $U = U(I, J, S)$. It should be noted that this average is not identical to simply applying Eq. (3.23) to the sum of the individual starting and target spin density functions $\sum_{i=1}^{n_{\mathrm{PP}}} \rho_0^i$ and $\sum_{i=1}^{n_{\mathrm{PP}}} \rho_{\mathrm{F}}^i$, respectively, as such an optimization setup still would allow the occurrence of cross talk between the individual spin density components, while Eq. (8.5) ensures complete decoupling of the individual point-to-point transformations. The gradient as the derivative of the cost function Φ_{00} follows directly as the sum of the gradients of the individual cost functions

$$\nabla_j \Phi_{00} = \frac{1}{n_{\mathrm{PP}}} \sum_{i=1}^{n_{\mathrm{PP}}} \nabla_j \Phi_0^i = \frac{1}{n_{\mathrm{PP}}} \sum_{i=1}^{n_{\mathrm{PP}}} \frac{\partial \Phi_0^i}{\partial u_j} \tag{8.6}$$

$$= \frac{1}{n_{\mathrm{PP}}} \sum_{i=1}^{n_{\mathrm{PP}}} \frac{\mathfrak{Re} \partial \langle \rho_{\mathrm{F}}^i | U_N \cdots U_1 \rho_0^i U_1^\dagger \cdots U_N^\dagger \rangle}{\partial u_j}.$$

In the case of the BEBE^{tr} pulse, the two transfers of interest are $I_z \rightarrow -I_y$ and $S_y \rightarrow S_z$ and corresponding initial and target density operators result to $\rho_0^1 = I_z$, $\rho_{\mathrm{F}}^1 = -I_y$, $\rho_0^2 = S_y$, and $\rho_{\mathrm{F}}^2 = S_z$. The Hamiltonians and propagators comprise the two spin system as described in section 8.2.1.

Regarding numerical optimizations, only the J-coupling Hamiltonian H_J can interchange magnetization from one spin to the other or create bilinear terms. Maximizing the BEBE^{tr} cost function Φ_{00} minimizes the creation of bilinear terms and leads to concurrent excitation pulses, which perform in a coupled two spin system as close as possible to the way they would in two uncoupled spin systems.

The initial pulse $u^0(t)$ for the optimization of BEBE^{tr} pulses could be chosen as random controls. However, due to the high calculational effort of the optimization problem, it is decided to start the BEBE^{tr} optimization with a BEBOP(11 kHz, 20 kHz, 550 μs, $\pm 20\%$, 1100) pulse for ^{1}H and a time-reversed BEBOP(37.5 kHz, 10 kHz, 550 μs, $\pm 5\%$, 1100) for ^{13}C, that are both optimized to time-optimality using single spin systems as previously reported [7]. The parameters are chosen to accomodate the common bandwidths $\Delta\nu_I$ =11 kHz and $\Delta\nu_S$ =37.5 kHz and variations in rf amplitudes of $\vartheta_I = \pm 20\%$ and $\vartheta_S = \pm 5\%$ of typical inverse-detected probeheads on a 600 MHz NMR spectrometer. For the optimization, spin systems with heteronuclear coupling constants up to $^1J_{\mathrm{CH}} = 250$ Hz are considered. (for a summary of optimization parameters see Table 8.1). After 39 days of optimization on a quad core 2.4 GHz processor under Suse Linux 2.6.27.21-0.1-pae using self-written code, a BEBE^{tr} of 550 μs duration and overall performance of $\Phi_{\mathrm{PP}} = 0.99922$ are obtained.

To benchmark the performance of the BEBE^{tr} pulse sandwich, the simulation of the transfer $I_z \rightarrow -I_y$ is exemplarily shown in Fig. 8.3 for the heteronuclear two spin system. While both the single spin BEBOP and time-reversed BEBOP pulses (dashed lines) and

Table 8.1: Shaped Pulses optimization parameters

	name[a]	transfer	t_p [μs][b]	ν [kHz][c]	ϑ[d]
BE^{tr}BE[e]	PP90^{tr}	-y $\to$ z	550	10	$\pm20\%$
	PP90	z $\to$ -y	550	37.5	$\pm5\%$
BEBE^{tr}	PP90	z $\to$ -y	550	10	$\pm20\%$
	PP90^{tr}	-y $\to$ z	550	37.5	$\pm5\%$
BUBI[f]	UR180	180_x°	600	10	$\pm20\%$
	PP180	z $\to$ -z	600	37.5	$\pm5\%$

[a] Abbreviations used as in Figs. 8.7 and 8.8: PP for point-to-point or state transfer pulses for a single magnetization component (e.g. excitation and inversion pulses); UR for universal rotation pulses for defined rotations around a specific axis (e.g. refocusing pulses); tr for time reversed pulse shapes;
[b] pulse length;
[c] offset range of pulses for which corresponding pulses are compensated for;
[d] variation of rf amplitude for which corresponding pulses are compensated for;
[e] combined pulse sandwich for ^{1}H time-reversed excitation and ^{13}C excitation.
[f] combined pulse sandwich for ^{1}H refocusing and ^{13}C inversion.

the BEBE^{tr} pulse (solid lines) show decreased performance with increasing J-coupling constants, the newly optimized pulse pair performs significantly better on average ($\diamond$) and particularly for the worst case ($\bullet$) (cf. Fig. 8.3).

8.3.2 Concurrent Universal Rotation (UR) Pulses

Although no actual pulses have been optimized within the work presented here, the second class of concurrent shaped pulses to be discussed are concurrent UR pulse sandwiches, like e.g. two simultaneous refocusing pulses on spins I and S. In this case, the action of the two simultaneously applied pulses is fully described by the resulting effective propagator and the cost function Φ_{33} is identical to Φ_3 of Eq. (3.23) with the only difference that initial and target propagator include the full two spin propagation

$$\Phi_{33} = \mathfrak{Re}\langle U_F(I,J,S)|U_{\text{eff}}(I,J,S)\rangle. \tag{8.7}$$

According to Eq. (3.12), for example, the target propagator for a concurrent 180_x° UR pulse results in $U_{\text{F}}(I,J,S) = e^{-i\pi(I_x+S_x)}$. In order to perform a two spin optimization with respect to J-cross talk control Hamiltonians of both spins need to be involved in the formation of $U_{\text{eff}}(I,J,S)$. It turns out that the use of the highly demanding UR pulse sandwiches is not necessary in the most basic transfer elements. We therefore concentrated our efforts to the third class of concurrent pulse sandwiches, the simultaneous application of UR and PP pulses.

8.3.3 Concurrent UR and PP Pulses: the BUBI Pulse Sandwich

The refocusing of chemical shift during INEPT-type transfer elements requires a central refocusing pulse on ^{1}H, while the simultaneously applied 180° pulse on ^{13}C only has to invert the z-component of the S spin. The corresponding pulse sandwich consisting of a broadband UR-180°t pulse on ^{1}H and a broadband inversion pulse on ^{13}C, in the following called BUBI (broadband universal broadband inversion) pulse, is therefore highly desirable for a multitude of pulse sequences.
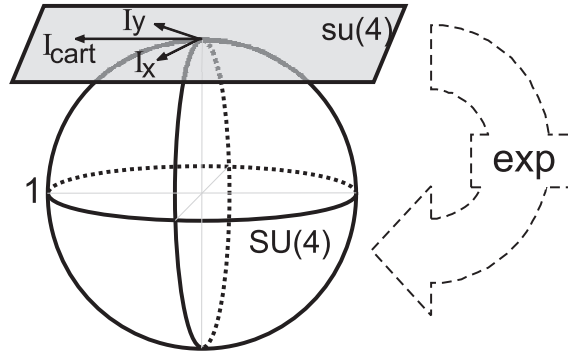
Figure 8.4: Scheme for the relation of cost functions with respect to su(4) and SU(4) of a spin system consisting of two spins $\frac{1}{2}$. The cost function Φ_0 is defined in the tangential space su(4) (depicted as a tangential plane), while the cost function Φ_3 is defined in the corresponding unitary group SU(4) (depicted as a sphere). The cost function Φ_{3b} is defined in both spaces (see text for details).

The optimization of such a pulse sandwich consisting of a UR pulse on one nucleus and a concurrent PP pulse on the second nucleus is by no means trivial and cannot be achieved directly by any of the quality factors Φ_3 or Φ_0. While an arbitrary number of individual point-to-point transformations can be added as shown for the BEBE$^{\text{tr}}$ pulse, the optimization of the UR part of the pulse sandwich usually describes the full propagator, including both participating spins I and S. Φ_3 therefore would unnecessarily restrict the freedom of S-magnetization, as the S_x and S_y components are not relevant for the transfer element and need not to be considered in the optimization. The separation of I and S spins can, however, be achieved by the special cost function

$$\Phi_{30} = \Phi_{3'} + \Phi_0, \tag{8.8}$$

where $\Phi_{3'}$ is described by

$$\Phi_{3'} = \mathfrak{Re}\langle U_F(I, J, S)\, U_{\text{eff}}(S) \mid U_{\text{eff}}(I, J, S)\rangle \tag{8.9}$$

with $U_{\text{eff}}(I, J, S) = U_{\text{eff}}$ being the total propagator as defined by Eq. (3.14), Eqs. (8.1 - 8.4), and Eq. (3.13) and

$$U_{\text{eff}}(S) = U_N(S) \cdots U_1(S) = e^{-iH_{S,N}\Delta t} \cdots e^{-iH_{S,1}\Delta t} \tag{8.10}$$

representing the part of the propagator that is solely determined by the S spin offset and rf controls. $\Phi_{3'}$ therefore represents a reduced propagator projection which retains all elements directly influencing the desired universal rotation on the I spin, i.e. H_I and H_J, while it eliminates all effects of the S spin on the quality factor, allowing any type of transformation to occur on this spin. In the way that $U_{\text{eff}}(S)$ applied in $\Phi_{3'}$ cancels out the not interpretable contributions of H_S to $U_{\text{eff}}(I, J, S)$, it retains at the same time the effects of J-crosstalk, which have arisen from the matrix exponential of the two spin Hamiltonian H. The gradient $\nabla\Phi_{30}$ follows Eqs. (3.38) and (3.40).

$\Phi_{3'}$ (Eq. (8.9)) can also be considered from a group theoretical point of view. 16 orthogonal basis vectors imply a scalar product and span up a two spin Liouville von Neumann space. This is a Hilbert space, containing the Hamiltonians, the spin density operators ρ and the
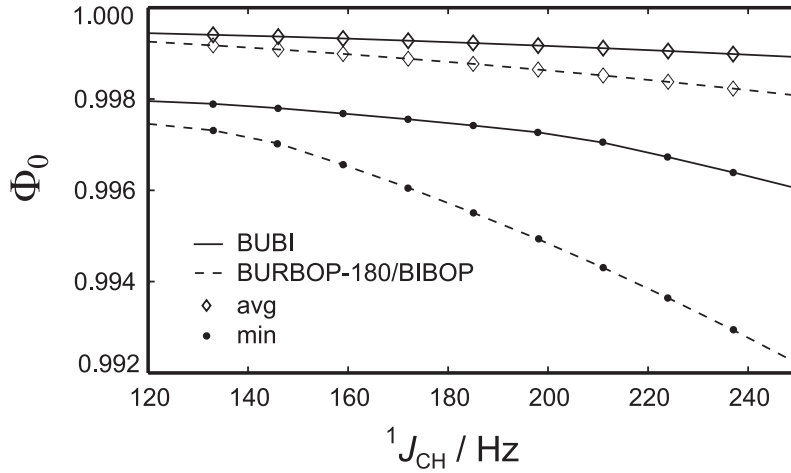
Figure 8.5: Simulation of transfer efficiencies $S_z \to -S_z$ of the BUBI pulse sandwich (solid
lines) compared to the simultaneous application of a BURBOP-180(11 kHz,
20 kHz, 600 μs, $\pm 20\%$, 1200) on I and a BIBOP(37.5 kHz, 10 kHz, 600 μs, $\pm 5\%$,
1200) inversion pulse on S with respect to the J-coupling of a heteronuclear
spin system. For each pulse pair the average ($\diamond$) as well as the minimum
performance ($\bullet$) over all specified offsets and rf amplitude ranges is given.
The corresponding transfers of $I_x \to I_x$ and $I_y \to -I_y$ are qualitatively and
quantitatively very similar (not shown).

cost function Φ_0 and Φ_{00}, and is referred to as the tangential space su(4) (see Fig. 8.4)
that is mapped to the special unitary group SU(4) by the matrix exponential (Eq. 3.12).

The cost functions Φ_3 and Φ_{33} are defined in the SU(4), which is the Lie-group that can
be depicted as a sphere of the unitary rotations of a two spin system (see Fig. 8.4). The
problem of separating the not interpretable contribution $U_{\mathrm{eff}}(S)$ from $U_{\mathrm{eff}}(I, J, S)$ (Eq.
(8.9)) arises, because the orthogonal basis in su(4) is not retained when transforming in
the corresponding SU(4). In other words, there is always the possibility to form a scalar
product onto 16 different basis vectors in su(4), allowing the definition of 16 subsystems
with independently defined quality factors Φ_0^i, while a scalar product in SU(4) may be only
defined by the overlap of U_{eff} to a *single* unitary propagator. Hence, the overall system
properties (in terms of the Hamiltonian) can not be separated from a subsystem by the
use of Φ_3 only. In this case, it is common practice [133] to lift the underlying problem to
the level of the corresponding algebra su(4), which is done by introducing $U_{\mathrm{eff}}(S)$ into Eq.
(8.9) according to Eq. (8.10).

Regarding the numerical optimization of the BUBI-(11/37.5 kHz, 20/10 kHz, 600 μs,
$\pm 20/5\%$, 1200) pulse, it is started from a single spin preoptimized BURBOP-180$_x$(11 kHz,
20 kHz, 600 μs, $\pm 20\%$, 1200) pulse for ^{1}H and a preoptimized BIBOP(37.5 kHz, 10 kHz,
600 μs, $\pm 5\%$, 1200) pulse for ^{13}C. The concurrent pulses are then subjected to an opti-
mization according to Φ_{30} with offset bandwidths $\Delta\nu_I$=11 kHz (7), $\Delta\nu_S = 37.5$ kHz (24),
B_1-compensations according to $\vartheta_I = \pm 20\%$ (5), $\vartheta_S = \pm 5\%$ (2), and a J-coupling up to
250 Hz (1). Number of explicit evaluations of the cost and gradient functions given in
parentheses.

To benchmark the performance of the BUBI pulse, the simulation of the transfer $S_z \to -S_z$
is carried out using a two spin system ($\Delta\nu_I = 10$ kHz (5), $\Delta\nu_S = 37.5$ kHz (21), $\vartheta_I = \pm 20\%$
(2), $\vartheta_S = \pm 5\%$ (2), $120 \leq J \leq 250$ Hz (11). Number of explicit evaluations of the cost
funtion given in parentheses. The other transfers ($I_x \to I_x$, $I_y \to -I_y$, etc.) perform

comparable (simulation data not shown). The single spin pulses (Fig. 8.5, dashed line) report losses as the $^1J_{CH}$ coupling constant increases. Minimal ($\bullet$) and average ($\diamond$) transfer values decrease with the $^1J_{CH}$ coupling, whereas the BUBI pulse sandwich (Fig. 8.5, solid line) is to some extend $^1J_{CH}$-compensated.

Starting from the performance benchmark in Fig. 8.5, it is difficult to directly evaluate the impact on a real multi-pulse experiment. Turning to the simulation of the full pulse sequence, several types of experimental imperfections and correlations, including for example the correlation of B_0 and B_1-field inhomogeneities in a probehead, lead to severe obstacles that cannot easily be realized in calculations. We therefore further evaluate the performance of BEBE^{tr} and BUBI pulse sandwiches in a number of experiments.

8.4 Experimental

Several experiments are performed for the evaluation of the pulse sandwiches on a highly controlled model system and on a sample covering the bandwidth of typically observed chemical shifts and coupling constants for small molecule natural abundance ^{1}H,^{13}C correlation spectroscopy. As the observed J-coupling effects are considerably stronger for the BUBI pulse compared to the BEBE^{tr} pulse, the following is mainly focused on relevant aspects of the combined refocusing and inversion pulse sandwich in pulse trains and HSQC-type experiments.

8.4.1 BUBI and Pulse Train Experiments

Pulse trains are frequently used in modern NMR spectroscopy. Especially CPMG-type pulse trains based on repetitive 180° pulses in spin echo sequences play an important role in many experiments, including for example refocusing of exchange-broadened resonances and the measurement of corresponding relaxation rates [134,135], as well as the suppression of chemical shift evolution in heteronuclear transfer elements in e.g. the CAGEBIRD [136] or long-range transfer elements [75, 76, 137]. Especially in the latter type of application, the fast refocusing of proton chemical shifts should be combined with a good coverage of the carbon chemical shift range, for which the application of robust broadband inversion pulses is highly desirable. Since the repetitive application of corresponding pulse shapes also allows the detailed examination of the J-coupling effects under controlled conditions, this scheme is used in the following for an experimental evaluation of pulse performance.

For highly defined experimental conditions a sample containing ^{13}C-labeled sodium formate in a mixture of DMSO-d_6 and D$_2$O with an experimentally determined $^1J_{CH}$ coupling constant of 184 Hz is used. The transmitter offsets for ^{1}H and ^{13}C are set on-resonant, and corresponding rf amplitudes are carefully calibrated to 20 and 10 kHz, respectively.

After exciting the I spin (^{1}H), $4n$ repetitions of spin echo elements $\Delta - 180° - \Delta$ and delays matched to the J-coupling constant according to $\Delta = 1/(4\ ^1J_{CH}) = 1.3587$ ms are applied. In the case that the 180° pulse is only applied on the I spin, effective heteronuclear decoupling is achieved; if, in addition, the S spin is inverted, magnetization evolves according to $I_x \rightarrow 2I_yS_z \rightarrow -I_x \rightarrow -2I_yS_z \rightarrow I_x$ and again pure inphase coherence will be detected for ideal 180° pulses every $4n$ spin echoes. This way, pulse performance of refocusing pulses on the I spin can be directly compared to pulse sandwiches applied to both I and S spins.

Using this experimental scheme, corresponding FIDs for experiments with $n = 0, ..., 5$ and four different 180° pulse shape combinations are recorded:

- a single BURBOP-180 pulse applied to ^{1}H (Fig. 8.6 A),
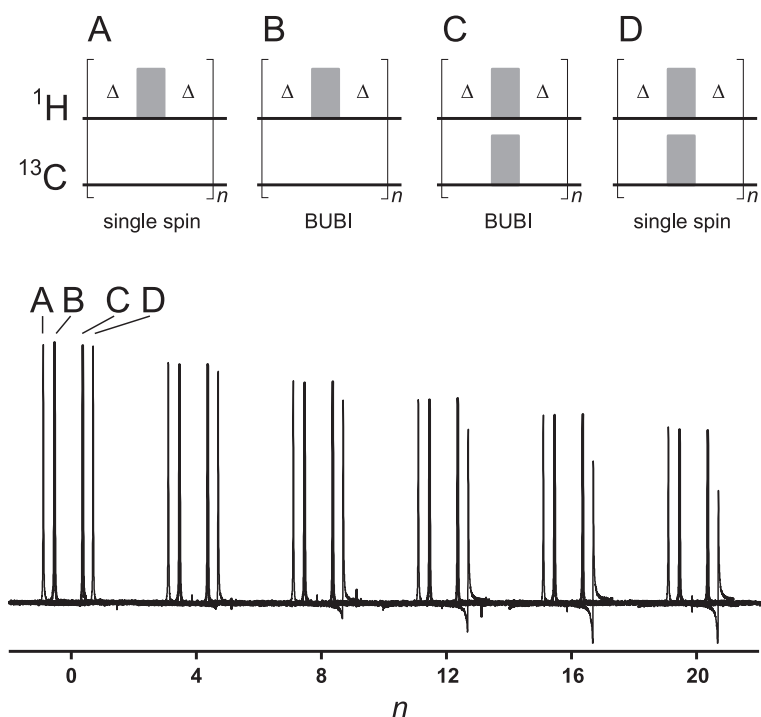
Figure 8.6: Experimental evaluation of J-evolution during pulse shapes using UR180 pulse trains of individual pulses and pulse pairs. Spectra according to (A-D) are acquired on a 600 MHz spectrometer at 300 K, being on-resonant on a multiplet component of the 184 Hz ^{1}H,^{13}C doublet of ^{13}C-labeled sodium formate in DMSO-d_6/D$_2$O. After excitation, 0, 4, 8, 12, 16 and 20 pulse shapes are applied with delays $\Delta = 1.3587$ ms, corresponding to $4n$ refocusing periods or n periods of $2/J$ with $n = 0, \ldots, 5$, for which pure inphase signals are expected for ideal pulses with no heteronuclear coupling evolution. Only the on-resonant parts of the doublets are shown. As long as a single pulse is applied, the single spin-optimized BURBOP-180 pulse (A) performs as good as the ^{1}H part of the BUBI pulse sandwich (B). The J-compensated full BUBI sandwich (C) shows equal performance while the simultaneous application of BURBOP-180 and BIBOP pulses leads to significant phase distortions due to heteronuclear J-coupling evolution (D).

- the UR part of the BUBI pulse sandwich applied to ^{1}H (Fig. 8.6 B),

- the concurrent BUBI pulse sandwich (Fig. 8.6 C), and

- concurrently applied BURBOP-180 and BIBOP pulses on ^{1}H and ^{13}C, respectively (Fig. 8.6 D).

Applying only ^{1}H BURBOP-180 and BUBI pulses (Fig. 8.6 A,B), experimentally defines the relative 100% transfer efficiency, including pulse imperfections and signal loss due to relaxation. The solely applied ^{1}H part of the BUBI pulse sandwich demonstrates that the individual BUBI pulses can also be applied alone, as the pulse sandwich is as well optimized for two uncoupled spins. A comparison with the signal obtained using the full BUBI pulse sandwich clearly indicates that no loss of performance is visible when the $^1J_{\mathrm{CH}}$ coupling is active (Fig. 8.6 C) as expected. The simultaneous application of BURBOP-180 and BIBOP pulses finally shows severe evolution of heteronuclear J-coupling with corresponding phase distortion and a decrease of transfer efficiency of the detected signal (Fig. 8.6 D). This result is a clear first experimental indication that the small effect of coupling evolution during concurrent pulse shapes can have significant impact and that the application of J-compensated BUBI pulse sandwiches might be beneficial.

8.4.2 Effects of BEBE^{tr} and BUBI Pulses in Standard HSQC Experiments

A wide spread variety of ^{1}H,^{13}C spin systems can be found in small molecule natural abundance samples. Typically the $^1J_{\mathrm{CH}}$ coupling constants differ from 120-250 Hz as a function of the hybridization, going from sp^3 to sp and the chemical shift range can easily reach 200 ppm and more. We therefore used a mixture of natural abundance ethylvanillin and methylpropiolate in DMSO-d_6 at 300 K as a realistic test sample that covers most of the corresponding coupling and chemical shift ranges. For the experimental setup, rf amplitudes are calibrated to be 20 and 10 kHz for ^{1}H and ^{13}C, respectively. A Bruker 600 MHz Avance III spectrometer (Rheinstetten, Germany) equipped with an inverse ^{1}H,^{13}C,^{15}N-triple resonance probehead is used. 16k complex data points are acquired in the directly detected dimension with 256 t_1-increments for the indirect dimension in corresponding HSQC experiments. Spectra are apodized using 90° phase shifted squared sine bell functions in both dimensions.

For a comparison of the effect of J-compensated BUBI pulse sandwiches in everyday experiments, a simple echo/antiecho HSQC experiment [41, 46] as depicted in Fig. 8.7 with either the original 600 μs long BURBOP-180 and BIBOP pulses with outstanding performance applied as the central refocusing step in the INEPT transfer periods (Fig. 8.7A) or the corresponding BUBI pulse sandwich with the same overall duration and rf consumption (Fig. 8.7B) is used. A BEBE^{tr} pulse and the corresponding time-reversed (BEBE^{tr})^{tr} = BE^{tr}BE pulse sandwich around the t_1 evolution period for best performance is used. To avoid additional artifacts over the wide chemical shift range, it is not decoupled during acquisition, resulting in signals split by the heteronuclear $^1J_{\mathrm{CH}}$ coupling.

The experimental results are shown in Fig. 8.7C-G. Almost all signals show a slight increase of 6-8% in sensitivity for the BUBI pulse sandwich experiment (Fig. 8.7 D,E,G) compared to the BURBOP-180/BIBOP sequence. Only a spin system of a sp hybridized methine group with $^1J_{\mathrm{CH}}$=258 Hz shows the inverse effect, which, however, can be contributed to the unmatched INEPT-delay for this coupling constant, which leads to almost vanishing inphase-to-antiphase transfer, as can be seen in the following section.

The size of the experimental gain observed for the BUBI HSQC corresponds roughly to the expected amount of undesired artifact magnetization being avoided by the J-compensation

Figure 8.7: Evaluation of the performance of J-compensated BEBE^{tr} and BUBI pulse sandwiches compared to corresponding conventually optimized broadband pulses of equal performance using a conventional HSQC. Pulse sequence with corresponding pulse shapes indicated are given with BEBE^{tr}, BE^{tr}BE, and BUBI pulse pairs (A) and corresponding BEBOP, time-reversed BEBOP, BURBOP-180, and BIBOP pulses (B). Delays and gradient strengths for the ^{1}H,^{13}C correlation experiments are $\Delta = 1.724$ ms, and $G_1 = 80\%$, $G_2 = 20.1\%$; phases are cycled according to $\phi_1 = x, -x$, $\phi_2 = 4(x), 4(-x)$, $\phi_3 = 2(x), 2(-x)$, $\phi_{\text{rec}} = x, -x, -x, x$. The spectrum of ethylvanillin and methylpropiolate dissolved in DMSO-d_6 at 300 K using sequence (A) is shown in (C) with splittings of cross peaks due to $^1J_{\text{CH}}$ coupling constants in the range of 126-258 Hz. For four of the cross peaks corresponding slices are shown (solid lines) together with annotation of their coupling constants of 126 Hz (D), 144 Hz (E), 258 Hz (F), and 173 Hz (G). Corresponding slices for the identical spectrum recorded using sequence (B) are shown with dashed lines in (D)-(G). Relative losses due to J-evolution during pulse shapes, defined as the difference of dotted signal amplitudes relative to the solid signal amplitudes of the fully J-compensated HSQC, are indicated for the traces. It should be noted that the cross peak with $^1J_{\text{CH}}=258$ Hz (F) has almost vanishing intensity, as the zeroing condition for the INEPT-transfer $\Delta = 1/J$ is almost fulfilled for this large coupling constant. For a fair quantitative comparison, heteronuclear decoupling is omitted during acquisition.

(Figs. 8.1 and 8.2). Considering that the individual BURBOP-180 and BIBOP pulses both are close to perfect performance and that their pulse length of 600 μs is rather short, the effect of J-compensation is surprisingly strong.

8.4.3 Effects of BEBE^{tr} and BUBI Pulses in the COB-HSQC Experiment

To avoid artifacts as observed in Fig. 8.7F for unmatched INEPT delays, we recently reported the COB-INEPT [131], which is optimized with respect to variations in couplings, offsets and B$_1$-inhomogeneity. The pulse sequence element with the desired performance is practically time-optimal and relies on the usage of J-compensated BUBI and BEBE^{tr} pulse sandwiches as it is seen in the following.

Using the same experimental setup as for the standard HSQC experiments, three different versions of the COB-HSQC involving two COB-INEPT periods (Fig. 8.8A) are acquired. Involving three refocusing periods per COB-INEPT, the overall sequence includes six BUBI pulse sandwiches and one BEBE^{tr} and one BE^{tr}BE pulse pair. Resulting spectra are shown in Fig. 8.8B-F:

- the fully J-compensated version with all pulse sandwiches as derived in this article (traces in Fig. 8.8C-F, solid lines);

- the COB-HSQC with all refocusing elements being equipped with BUBI pulse sandwiches but BEBE^{tr} and BE^{tr}BE pulses being replaced by corresponding BEBOP and BEBOP^{tr} pulses of equal duration (traces in Fig. 8.8C-F, dashed lines); and

- the COB-HSQC with BEBE^{tr}, BE^{tr}BE, and BUBI pulse sandwiches being replaced by BEBOP, BEBOP^{tr}, BURBOP-180, and BIBOP pulse shapes (traces in Fig. 8.8C-F, dotted lines).

A comparison of the first two spectra reveals the effect of the BEBE^{tr} on the overall transfer efficiency. Improvements are barely visible and only for the cross peak with the strongest $^1J_{CH}$ coupling (Fig. 8.8E) shows a difference of 2%. This effect is small, but adds up to the total performance of the pulse sequence.

A comparison to the third spectrum with only conventional, single-spin-derived pulses, instead, exhibits dramatic changes in sensitivity. sp^3 hybridized spins show a difference of $\approx$25% (Fig. 8.8C,D), sp^2 hybridized spins lead to a difference of $\approx$35% (Fig. 8.8F), and sp hybridized spins result in a difference of up to 68% (Fig. 8.8F).

8.5 Discussion

Composite or shaped pulses for broadband applications are usually optimized using the Bloch equation or the spin density formalism for a single spin 1/2. Effects due to coupling constants are neglected with the argument that pulse lengths are usually short compared to the characteristic times for efficient coupling evolution of larger spin systems. Heteronuclear couplings, however, can easily reach a couple of hundred Hertz and might lead to significant contributions. Following this insight, a set of Bloch-optimized PP and UR pulses with little effect on J-coupling evolution is very recently selected for the application in ^{1}H,^{13}C experiments [138].

Here, the effect of heteronuclear J-couplings for a typical two spin system consisting of a proton with a directly attached carbon nucleus and a $^1J_{CH}$ range of 120-250 Hz in very detail and specifically optimized two J-compensated pulse sandwiches for two very frequently simultaneously applied pulse combinations are studied. It can be shown that
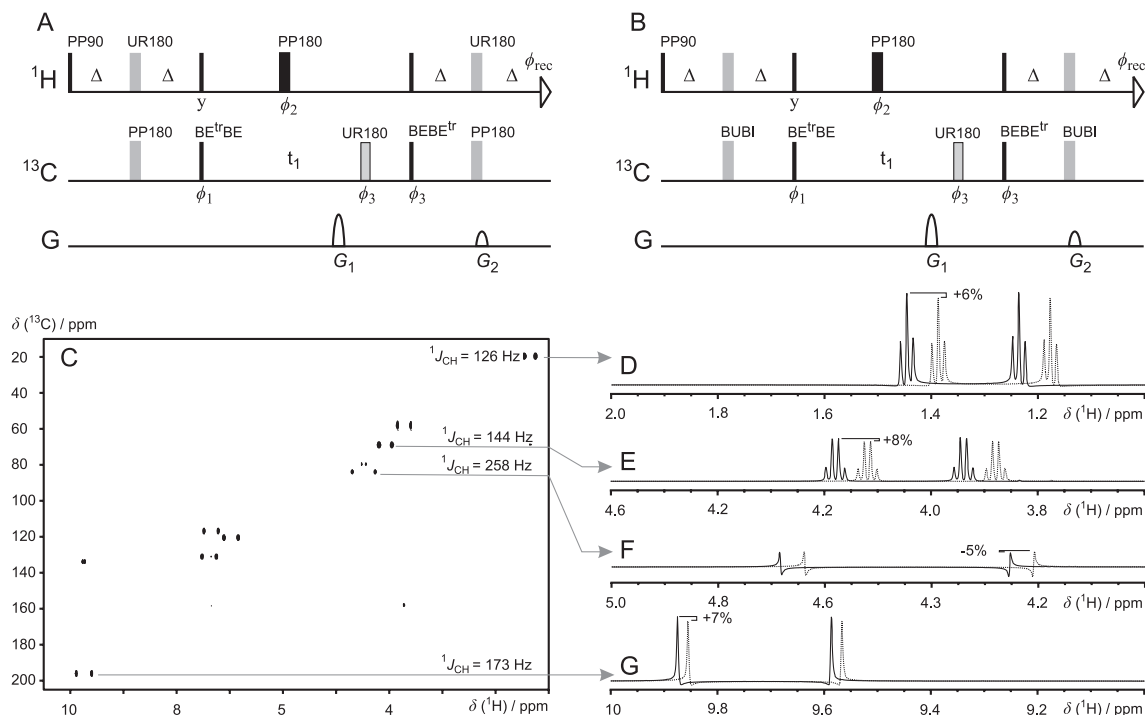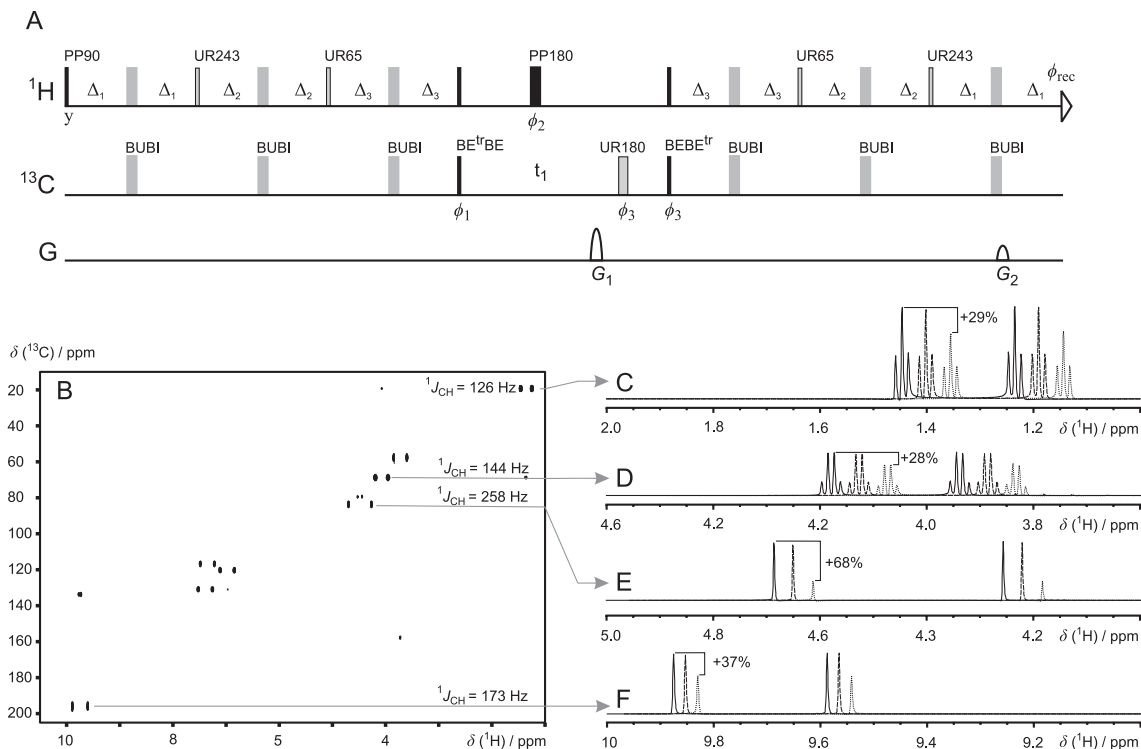
Figure 8.8: Evaluation of the performance of J-compensated BEBE^{tr} and BUBI pulse sandwiches compared to corresponding conventually optimized broadband pulses of equal performance using the COB-HSQC for highest robustness against variations in couplings (compensation for the range $^1J_{CH} = 120\text{-}250$ Hz), offsets and B$_1$-inhomogeneities [131]. (A) Pulse sequence with corresponding pulse shapes indicated. Delays and gradient strengths for ^{1}H,^{13}C experiments are $\Delta_1 = 1.469$ ms, $\Delta_2 = 2.135$ ms, $\Delta_3 = 0.394$ ms, and $G_1 = 80\%$, $G_2 = 20.1\%$; phases are cycled according to $\phi_1 = x, -x$, $\phi_2 = 4(x), 4(-x)$, $\phi_3 = 2(x), 2(-x)$, $\phi_{rec} = x, -x, -x, x$. (B) Spectrum of ethylvanillin and methylpropiolate dissolved in DMSO-d_6 at 300 K, showing splittings due to $^1J_{CH}$ coupling constants in the range of 126-258 Hz. For four of the cross peaks corresponding slices are shown (solid lines) together with annotation of their coupling constants of 126 Hz (C), 144 Hz (D), 258 Hz (E), and 173 Hz (F). Further spectra are recorded and corresponding traces shown with the pulse sequence from (A) being modified by replacing the BEBE^{tr} and the BE^{tr}BE pulse sandwiches by corresponding BEBOP and time reversed BEBOP pulses (dashed lines), and by replacing all BEBE^{tr}, BE^{tr}BE, and BUBI pulse pairs by corresponding BEBOP, time-reversed BEBOP, BURBOP-180, and BIBOP pulses (dotted lines). In addition, the significant relative losses due to J-evolution during pulse shapes, defined as the difference of dotted signal amplitudes relative to the solid signal amplitudes of the fully J-compensated COB-HSQC, are indicated for traces (C)-(F).

a single offset-compensated shape applied to one of the two coupled nuclei will lead to effective decoupling of the second spin, because chemical shift and coupling evolution is inherently refocused in such offset-compensated pulses. But the situation changes as soon as Bloch-optimized pulses are applied simultaneously on the two nuclei as it could be shown for the two pulse combinations, one consisting of a BEBOP [7, 105] and a time-reversed BEBOP broadband excitation pulse and one consisting of a BURBOP-180 [6,9] refocusing pulse on ^{1}H and a BIBOP inversion pulse [7] on ^{13}C. In both cases, quality factors are approximately reduced by only 0.001. While this reduction of desired transfer is of only minor interest, corresponding potential artifact magnetization will increase by roughly 5-10% per pulse pair (cf. Fig. 8.2). As a consequence, concurrent pulse shapes that are not compensated for heteronuclear J-coupling evolution can easily result in significant spectral distortions and reduced signal intensities when applied within a pulse sequence.

Experimental results corroborate theoretical findings. While two J-compensated BEBE^{tr} pulse sandwiches lead to negligible distortions compared to two pairs of corresponding BEBOP pulses in HSQC spectra, the application of two BUBI pulse sandwiches apparently avoids a loss of 6-8% signal intensity compared to concurrent BURBOP-180 and BIBOP pulses. In the COB-HSQC with six BUBI or BURBOP-180/BIBOP combinations, respectively, even losses of up to 68% have been recorded (Fig. 8.8) in accordance with large phase distortions observed in CPMG-type pulse train experiments (Fig. 8.6). The experimental findings surprisingly demonstrate that coupling evolution during concurrently applied pulses must be considered as an important contribution to the overall pulse sequence performance.

The J-compensated pulse sandwiches introduced in this article are both developed using typical full bandwidths, rf amplitudes, and B$_1$-compensations applicable to ^{1}H and ^{13}C nuclei in corresponding correlation experiments at a spectrometer frequency of 600 MHz. The pulse pairs in all cases are improved starting from single spin-optimized time-optimal pulse shapes and show outstanding performances. Taking into account previous systematic searches for physical limits of broadband excitation, inversion, and universal rotation pulses [7–9], as well as experimental comparisons under highly controlled conditions (this article and Ref. [131]), both pulse sandwiches must be considered to be very close to the global optimum for the chosen parameters of the pulse optimization.

The BEBE^{tr} pulse sandwich is an example of a PP/PP pulse pair, which can simply be optimized by adding the cost functions of the individual PP pulses in a combined gradient and combined cost function of a two spin system. The BUBI pulse sandwich, instead, represents a UR/PP pulse pair for which a novel cost function had to be derived prior to optimization. With this cost function in hand, any combination of individual pulses, PP/PP, UR/PP, or UR/UR can directly be optimized as derived in section 8.2 using optimal control-derived algorithms.

The pulse sandwiches are optimized in total using a coupled two spin system, but the individual pulses for each nucleus can also be applied separately as single pulse shapes or, equivalently, in uncoupled spin systems. As has been shown for CPMG-type experiments (Fig. 8.6), the performance in this case is as good as in the coupled case. The corresponding shapes therefore can directly be used for replacement of all corresponding excitation, time-reversed excitation, proton refocusing and carbon inversion pulses in a given sequence. It should also be noted that the phases of the individual pulse shapes can be varied without compromising the heteronuclear J-compensation, so that phase cycling can be achieved straightforwardly on each nucleus within a corresponding pulse pair.

The expected performance gain for a single pulse sandwich in ^{1}H,^{13}C-experiments compared to conventionally optimized concurrently applied time-optimal pulse shapes of equal duration is quite small, less than approximately 2% per BEBE^{tr} and less than 5% for BUBI.

In a single INEPT step the difference in performance therefore is of minor interest and even in conventional HSQC experiments the overall gain is only in the order of 5-10%. In more complex transfer elements with many concurrently applied pulses, as for example the COB-INEPT [131] with strongly improved robustness against couplings, offsets, and B_1-inhomogeneity, or generally J-compensated transfer steps [65, 66, 139] the effect is instead vital for the overall performance of the experiment. In fact, the lack of correspondingly robust pulse shapes has probably spoiled the success of such transfer elements so far, as their robustness is decisively reduced by the application of hard pulses or single-spin-optimized broadband pulses.

Conventional pulse shapes are easily scaled and half the rf amplitude will lead to twice the pulse length with half the effective bandwidth of the pulse. The same linear response is also valid for the BEBE^{tr} and BUBI pulse sandwiches, as long as both pulses are scaled identically. In this case also the effective J-compensation range will scale proportional to the rf amplitude. As soon as the individual pulse shapes are scaled differently, the J-compensation might be lost - at least to some extend. This scaling behavior reduces the usefulness of the pulse sandwiches for applications involving other spins like ^{15}N, for example. For this nucleus an rf amplitude of 10 kHz as specified for the carbon channel of BUBI and BEBE^{tr} pulse pairs would not be available on most modern probeheads, but a scaling to lower rf amplitudes could only be achieved by simultaneous reduction of the proton bandwidth and the effective J-compensation range. In this case it would probably be better to directly optimize corresponding pulse shapes for an adequate set of parameters. However, even in such cases the already derived pulse sandwiches within limits might perform better than uncompensated pulse sandwiches.

The pulse sandwiches introduced here are optimized as pure phase broadband pulses without coupling evolution during pulses. In many applications like the INEPT transfer step, however, the application of pulses with maximum heteronuclear J-evolution might be desirable instead. One such example is certainly the introduction of ICEBERG pulses [74] for the initial excitation in such refocused pulse sequence elements. The approach of defined coupling evolution can most likely also be extended to concurrent pulse shapes using slightly different cost functions from the ones derived here. Such pulses would shorten the overall length of transfer elements which would be of special interest for larger molecules with reduced relaxation times.

Finally, it should be noticed that none of the pulse shapes used in this article are compensated for homonuclear coupling evolution. The simultaneous compensation of homonuclear and heteronuclear couplings would imply the simulation of at least a coupled three spin system. Since the optimization for BUBI and BEBE^{tr} pulse sandwiches already required optimization runs of several weeks, the extension to additional dimensions of optimization parameters seems hardly achievable with reasonable computing time on today's personal computers. The direct optimization against homonuclear coupling evolution neglecting any heteronuclear coupling evolution might be feasible.

8.6 Summary

In summary, two J-compensated pulse sandwiches designed for ^{1}H,^{13}C-INEPT-type transfer elements to study the effect of heteronuclear coupling evolution in corresponding correlation experiments are optimized. A pulse pair for broadband refocusing on ^{1}H and inversion on ^{13}C, called BUBI, and a pair for excitation and time-reversed excitation on the two nuclei, called BEBE^{tr}, were optimized starting from time-optimal BURBOP-180, BIBOP, and BEBOP pulses. The improvement found in terms of the desired transfer efficiency for a coupled spin system relative to the original pulses is only on the order of 0.1%. It was therefore surprising to see significantly improved performance in resulting

experiments like an HSQC with reduced losses of approximately 5-10% and more advanced sequences like the COB-HSQC with avoided losses of up to 68%.

The results obtained lead to the conclusion that J-compensated pulses are essential for the design of robust pulse sequences of a certain complexity with a larger number of concurrently applied pulses. The achievable performance in such optimized pulse sequences can lead to a variety of highly interesting applications, as for example quantification of cross peaks of mixtures or of metabolomics-derived samples from heteronuclear correlation experiments with ensured coherence transfer close to the theoretical maximum in each scan irrespective of the actual J-coupling (see e.g. [131]).

9. The Concurrent J-Evolution Pulse

9.1 Introduction and Motivation

The steadily increasing field strengths in NMR spectroscopy and the emergence of cryogenically cooled probeheads poses new requirements to the implementation of NMR experiments. There is a demand for pulses, which meet a number of properties. Hard pulses can barely cover the bandwidths of typical hetero nuclei, such as ^{13}C, that spans approximately 37.5 kHz at a 600 MHz NMR spectrometers.

Therefore, from the early days of NMR spectroscopy, composite pulses have been proposed that improve the offset dependence drastically. Meanwhile a large number [19, 91–95] of composite pulses is known that compensate for resonance offset effects. The same is true for rf compensated pulses. They are advantageously used in combination with cryogenic probeheads that often bring an increased range of rf field strengths (typically $B_1 = \pm 20\%$) to the sample when compared with room temperature probeheads that have a narrow distribution of approximately $B_1 = \pm 10\%$.

Following the same objectives, namely offset and B_1 compensation, computer optimized pulses brought the field of NMR spectroscopy to the next level. A vivid era of pulse engineering began with the possibility to optimize pulse shapes containing as much as some thousand independent variables such as rf amplitudes and phases [3]. Finally OCT proved to be a very useful tool for the optimization of shaped pulses. At the present time, pulses are available for a variety of nuclei and bandwidths such as ^{1}H and ^{13}C but also for more specialised applications e.g. low-power MRI pulses and microwave pulses for the use in EPR spectroscopy. Meanwhile pulse engineering is conveniently accomplished by OCT-methods leading to the question whether optimal (e.g. time optimal, rf optimal...) pulses can be obtained that approach the physical limit for a demanded robustness. Systematic studies on the optimization of shaped pulses [7–9] and on quantum evolutions with known physical limits [30–35, 140] lead to time optimal (TOP) curves that are a versatile tool to find estimates for physical limits in spin dynamics. So that with some generality it may be assumed [38] that OCT-derived transfers approach the underlying physical limits.

The design of time optimal experiments for time efficient coherence transfer elements as described in the Chapters 4 and 7 is equally important. It is considered to be a crucial point since the majority of time should be spent during delays that are used for coherence transfer or chemical shift evolution, rather than for the application of rf pulses. The trivial conclusion would be to keep pulse durations as short as possible.

A better approach would even be the combination of delays and pulses. Ideally the sequence length t_s would not be increased by the duration of the shaped pulse t_p. This would be equivalent to the overall optimization of the NMR experiment with respect to all relevant interactions from the underlying Hamiltonian H. For example B_1 and offset deviations of all nuclei involved in the spin system, as well as the spin-spin couplings. Only very little is known about the convergence properties of such complex optimizations and the computational resources exceed the available possibilities by far. The direct optimization of complex NMR experiments must be considered to be currently infeasible.

An indirect way to obtain the "combination" of pulses and delays to result in a more efficient descendant is proposed by Gershenzon et al. [74] for the case of excitation pulses that are directly followed by a period of free precession. Such pulses are named ICEBERG pulses. Conventional broadband excitation pulses are defined by the transfer that results in magnetization with a unique and defined final phase. This transfer is accomplished for all resonance offsets within a given range. In contrast, the idea behind the ICEBERG pulses is to result in magnetization that has a phase that is determined by the current offset. The phase after excitation in this case resembles the phase that would is created upon a certain time of free precession under the actually given offset-term of the Hamiltonian.

Since the phase progress of magnetization is defined within the x, y-plane, it corresponds to a effective z-rotation. Assuming that rf controls can be applied on I_x and I_y that dominate the overall Hamiltonian H, then phase evolution can be mimicked in principle by controls. For example, a $180°$ pulse with phase perpendicular to the actual magnetization would result in a phase manipulation of $180°$. Because of the given relation between offset and rf controls, ICEBERG pulses can be considered the simplest class off "drift Hamiltonian mimicking" pulses.

Accordingly, the next step towards time optimal experiments should be the combination of shaped pulses with coherence transfer elements. This could be, for example, the combination of two concurrent UR-$180°$ pulses in heteronuclear spectroscopy that are often used in the center of delays to refocus chemical shift evolution during coherence transfer (e.g. in the COB-HSQC, Chap. 4).

This kind of pulses is denoted as J-evolution (J_{ev})-pulses in the following. J_{ev}-pulses are of special interest because UR pulses are longer by a factor of 2 compared to excitation pulses [9]. Accordingly, they are more important in terms of time consumption.

While the underlying motivation on ICEBERG and J_{ev}-pulses is the same, they are conceptually different in the way they are obtained. This is already foreseen by the fact that the J-coupling evolution is the property that needs to be resembled by the J_{ev}-pulse; and it can be imagined as a rotation around the $I_z S_z$ axis. Since this is a bilinear term, it can not be directly mediated by the rf Hamiltonian, i.e. by any user specified control, but must involve the drift Hamiltonian.

Therefore, the question that is to be answered in the following is whether it is possible to obtain such pulses and in a second step: Whether this kind of pulses are actually more efficient compared to shorter concurrent refocusing pulses that are flanked by delays to result in a pulse with identical overall time consumption.

9.2 Theory

Shaped pulses are usually derived using single spin models. In analogy, J-coupling evolution can be described by offset or B_1 compensated pulses (Chap. 4,7). This kind of workaround is usually applied on composite pulses since they result in pulse delay sequences that can be further improve by the incorporation of tailored shaped pulses. This
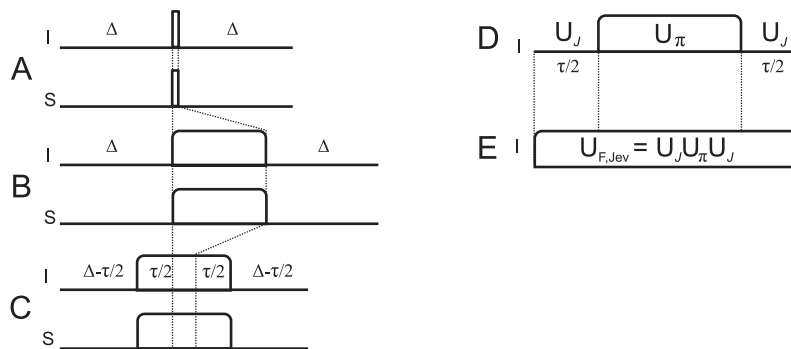
Figure 9.1: Spin-echo pulse sequences for the refocusing of chemical shift during heteronu-
clear coupling evolution with respect to coupled nuclei I and S. With (A)
concurrent hard pulses, (B) concurrent shaped pulses that increase the se-
quence duration to $t_s = 2\Delta + t_p$, (C) concurrent shaped pulses with sequence
duration decreased to $t_s = 2\Delta + t_p - \tau$ that can be imagined as a delay τ that
is moved inside the shaped pulse to result in a J_{ev}-pulse. (D) J_{ev}-pulses are
comparable to J_{ev}-building blocks that are composed from BUBU pulses and
delays τ. A J_{ev}-pulse (E) is made up of the product of unitary rotations. U_J
is the unitary propagator that results from a free precession period $\tau/2$. This
is combined with the effect of a refocusing pulse U_π to form $U_{F,Jev}$ that is the
final propagator of a J_{ev}-pulse.

approach is necessary because only a single property, e.g. B_1 robustness, of the com-
posite pulses can be "transformed" into another property of the resulting sequence, e.g.
J-robustness; resulting in sequences that are not robust against all other deviations of the
Hamiltonian H, e.g. B_1 and offset deviations of the first and second spin.

As a result, single spin models are inappropriate for the derivation of concurrent refocusing
pulses and the spin system must be described according to the two spin cost function Φ_{33} of
Eq. (8.7). A concurrent 180° broadband universal rotation pulse (abbreviated as BUBU-
pulse) is obtained by defining the target propagator U_π as

$$U_\pi = e^{-i\pi(I_x + S_x)}.$$

An effective propagator U_{eff} is derived from the single propagators

$$U_{\mathrm{eff}} = U_N \cdots U_j \cdots U_1$$

according to the matrix expotential of the Hamiltonian H

$$H = H_0 + H_{\mathrm{ctrl}}$$

And the scalar product of U_{eff} and U_F yields the cost function Φ_{33}

$$\Phi_{33} = \mathfrak{Re}\langle U_F | U_{\mathrm{eff}} \rangle.$$

Optimizations using Φ_{33} yield robust analogues (Fig. 9.1B) of concurrent hard 180° pulses.
These refocusing pulses are used in the center of delays whereupon the sequence length t_s

is increased by the length of the shaped pulse t_p (as indicated by the dotted line in Fig. 9.1).

In the next step it is assumed that shorter sequences could be obtained if the delays are partly moved into the shaped pulse (Fig. 9.1C). A fraction of time is defined by $\tau = q * t_p$ (with $0 \leq q \leq 1$). In this case, the overall time consumption t_s would be decreased by τ. This is equivalent to the idea that J-coupling evolution is mediated through the pulse. It is realized by a new cost function Φ_{jev}. Accordingly, pulses obtained by Φ_{jev} are denoted as J-evolution pulses.

$$\Phi_{\text{jev}} = \mathfrak{Re}\langle U_{F,\text{jev}}|U_{\text{eff}}\rangle \tag{9.1}$$

with

$$U_{F,\text{jev}} = U_J U_\pi U_J$$

and

$$U_J = e^{-i\pi J 2 I_z S_z * q * t_p / 2}$$

The target propagator $U_{F,\text{jev}}$ (Fig. 9.1E) can be written as the product of U_J and U_π. It can be imagined as a pulse that mediates the effect of a free precession period $\tau/2$ followed by an ideal $180°$ concurrent refocusing pulse followed by one more $\tau/2$ precession period as depicted in Fig. 9.1D. The OCT optimization needs to accommodate that in a shaped pulse.

9.2.1 Calculation of Gradients

The gradient needed for the optimization is calculated as the derivative of the cost function Φ_{jev} with respect to the x and y-controls.

$$\frac{\partial \Phi_3 3}{\partial u_k(j)} = \frac{\partial \mathfrak{R}\langle P_{j+1}|X_j\rangle}{\partial u_k(j)} = \frac{\partial \mathfrak{R}\langle U_{j+1}^\dagger \cdot\cdot U_N^\dagger U_F|U_j \cdot\cdot U_1\rangle}{\partial u_k(j)} = \mathfrak{R}\langle U_{j+1}^\dagger \cdot\cdot U_N^\dagger U_F|\frac{\partial U_j}{\partial u_k(j)} \cdot\cdot U_1\rangle$$

where the challenging task is to calculate the derivative of U,

$$U' = \frac{\partial U_j}{\partial u_k(j)},$$

which is given in a first order approximation by [3]

$$\frac{\partial \Phi_3 3}{\partial u_k(j)} = -\mathfrak{R}\langle P_{j+1}|i\Delta t H_k X_j\rangle.$$

For the present study, however, the exact derivative U' is used that can be obtained, apart from other methods, by an eigenbasis transformation into the basis of the time independent Hamiltonians H.

In the basis of H, the matrix exponential U and its derivative with respect to the controls u_k collapses to a scalar exponential and its ordinary derivatives. Using the product rule it is obtained by

$$U_j' = \frac{\partial U_j}{\partial u_k(j)} = \frac{\partial exp(-iH_j t)}{\partial u_k(j)} = \frac{\partial V exp(-iD_j t) V^\dagger}{\partial u_k(j)}$$

Table 9.1: Optimization and evaluation parameters for J_{ev}-pulses

	ν_I /kHz[a]	$\pm\text{B}_{1I}\%$[b]	ν_S /kHz[c]	$\pm\text{B}_{1S}\%$[d]	J /Hz
optimization	7 (8)	20 (3)	37.5 (42)	5 (2)	250 (1)
evaluation	7 (12)	20 (23)	37.5 (62)	5 (19)	given in text

[a] offset range of pulses for first nucleus;
[b] B_1 deviation of first nucleus;
[c] offset range of pulses for second nucleus;
[d] B_1 deviation of second nucleus;
number of explicit evaluations given in parantheses.

$$= \frac{\partial V}{\partial u_k(j)} exp(-iD_j t)V^\dagger + V\frac{\partial exp(-iD_j t)}{\partial u_k(j)}V^\dagger + V exp(-iD_j t)\frac{\partial V^\dagger}{\partial u_k(j)}$$

Only the derivative of the exponential function is non zero and the equation simplifies to

$$U'_j = V\frac{\partial exp(-iD_j t)}{\partial u_k(j)}V^\dagger.$$

9.3 Optimization of J_{ev}-Pulses

The initial pulse $u^0(t)$ is chosen as random controls. Conjugated gradients are used for update and rf controls are truncated once they exceed $\nu_{\text{rf}} = 20$ kHz for ^{1}H and $\nu_{\text{rf}} = 10$ kHz for ^{13}C.

The optimization parameters are chosen to accommodate the common bandwidths and B_1 field inhomogeneities for ^{1}H and ^{13}C spin systems, respectively by setting $\Delta\nu_I$=7 kHz (8), $\Delta\nu_S = 37.5$ kHz (42), B_1-compensations according to $\vartheta_I = \pm20\%$ (3), $\vartheta_S = \pm5\%$ (2), and a J-coupling up to 250 Hz (1). The number of explicit and equidistant evaluations of the cost and gradient functions are given in parentheses. This optimization parameters are summarized in Table 9.3 together with the parameters used for the evaluation. Optimization and evaluation parameters are identical except that the number of full time propagations in the respective dimension of the evaluation is somewhat higher to avoid any dependence of the cost function on the number of points used for evaluation.

Usually 1 ms concurrent BUBU or J_{ev}-pulse with digitization of $t_{\text{step}} = 10$ μs are obtained within 24h running in parallel on 4 nodes of a 2.4 GHz shared memory linux system (Suse Linux 2.6.27.21-0.1-pae). A series of J_{ev}-pulses are optimized with $q = 0.001$, 0.2, 0.4, 0.6, 0.8 and 0.999, resulting in pulses that should accomplish an increasing amount of heteronuclear J-coupling.

9.3.1 z-Controls

According to the parameters defined in Table 9.3, a single evaluation of the cost or gradient functions needs 8*3*42*2*1=2.016 full time evolutions of the spin system. Usually t_{step} is set to 0.5 μs which would lead to 2.016*1 ms/0.5 μs=4.032.000 complex eigenvalues decompositions of the Hamiltonian. Since this is the speed determining step it is decided to increase t_{step} to 10 μs resulting in 201.600 eigenvalue decompositions.

Assuming a maximum carbon bandwidth of 37.5 kHz there is a phase evolution of up to approximately 67.5° within an increment duration of $t_{\text{step}} = 10$ μs. This unnecessarily

brings a new constraint to the available rf controls that can limit the fidelity obtained by a Φ_{33}-optimization.

To avoid that, an additional set of controls, namely z-controls are introduced. z-controls are calculated in accordance to the formulas derived for x, y-controls. z-controls cause z-rotations. They can be imagined as the effect that occurs on changing the transmitter offset to a new value. Since any z-rotation can be mediated also by a phase sweep of x, y-controls, it is possible to transform x, y, z-pulses into x, y-pulses that can be realized by the available hardware. By this, the difference between high resolution x, y and lower resolution x, y, z pulses is reduced to a distinct incrementation of rf offset *changes*, while the whole range of possible rf offsets is not reduced.

After a pulse is obtained the z-controls are rendered with a resolution of 0.5 μs onto the $t_{\text{step}} = 10$ μs delays to obtain a pulse that can be used on the spectrometer.

Nonetheless, simulations given in the following directly use the obtained z-controls.

9.4 The Evaluation of J_{ev}-Pulses

This section is dedicated to the evaluation of the J_{ev}-pulses in order to find out whether

- J_{ev}-pulses accomplish heteronuclear J-coupling

- and whether they are more effective compared to their shorter BUBU equivalents (see Fig. 9.1D) flanked by appropriate delays to accomplish an equivalent J-evolution.

To answer that question, simple scalar products are employed, but it is also necessary to distinguish effects that originate either from J-coupling or from the 180° rotation from artifact contributions. Since UR pulses provide more general spin manipulations compared to PP pulses their analysis is less straight forward. See for example Chap. 8 for details on the Lie algebras and groups that Φ_0 and Φ_3-derived cost functions are defined in and the consequence that arise for the analysis of spin dynamics from that.

The obtained J_{ev}-pulses with q =0.001, 0.2, 0.4, 0.6, 0.8 and 0.999 are evaluated according to Eq. (9.1). The evaluation is done three times for the coupling constants J =145, 195 and 250 Hz. The number of checks for the remaining dimension is set according to Table 9.3 and the resulting graphs are plotted as a function of q (Fig. 9.2A-C, dashed lines). Because the selectivity of an arbitrary property depends on the reciprocal of the pulse length, it is on the order of 1/1 ms = 1000 Hz for the present J_{ev}-pulses. Because of that, Fig. 9.2A-C (dashed lines) shows a similar behaviour of the graphs because the selectivity spans the whole range of coupling constants ($J = 145$, 195 and 250 Hz). The discussed graphs differ in first approximation only linearly as a function of the actual J-coupling constants.

Since the cost function Φ_{jev} is intended to be a measure for both (i) 180° pulses and (ii) J-evolution, this two properties need to be resolved in order to judge the obtained pulses according to their J-evolution capability. Therefore an ideal effective propagator $U_{eff,\pi}$ is defined by

$$U_{eff,\pi} = e^{-i\pi(I_x + S_x)}$$

that is evaluated according to $U_{F,\text{jev}}$ as a function of q that is also used to obtain the J_{ev}-pulses

$$\Phi_{\text{jev},\pi} = \mathfrak{Re}\langle U_{F,\text{jev}} | U_{\text{eff},\pi}\rangle$$

Figure 9.2: Transfer efficiencies for concurrent 180° refocusing pulses, calculated for $J = 145$, 195 and 250 Hz and averaged over offsets and B$_1$ deviations according to Table 9.3. Six J_{ev}-pulses are evaluated as a function of the J-evolution constant q that demands a ratio of J-coupling that is based on the pulse length $t_p = 1$ ms. (A-C) Upper limit of transfer efficiency that can be reached by conventional, concurrent refocusing pulses is calculated by Φ_{Jev} (solid lines). (A-C) J_{ev}-pulses acquire heteronuclear J-coupling and exceed that limit (dashed lines). (A-C) The 180° performance of J_{ev}-pulses is obtained by the cost function Φ_{Jdistr} (dotted lines). (D-F) The J-coupling that has effectively been acquired upon a J_{ev}-pulse is given by q_{eff} (dashed lines). For $q \leq 0.6$ the linear behaviour and the shift according to the diagonal indicates that J-evolution performance depends on q.

The numerical values of this cost function are plotted in Fig. 9.2A-C (solid line). They assign the fidelity that would be reached upon Φ_{jev} by ideal concurrent 180° pulses, i.e. infinitely hard pulses without rf variation. This class of pulses are supposed to not evolve J-coupling, which is the reason for the declining transfer efficiency with increasing q and J as illustrated in Fig. 9.2A-C (solid lines). Such ideal pulses set up a maximum fidelity that can be reached with conventional refocusing pulses. Every pulse that reports a transfer efficiency higher than this threshold must evolve J-coupling according to Φ_{jev}. This is observed for the discussed J_{ev}-pulses.

Considering the threshold given by the ideal 180° pulses (Fig. 9.2A-C, solid line) it is concluded that the range of values given by Φ_{jev} is dominated by the refocusing property. Therefore the analysis of J-coupling properties is restricted to the range of $1 \leq \Phi_{\mathrm{jev},\pi}(q)$. The difference between Φ_{jev} and $\Phi_{\mathrm{jev},\pi}$ is divided by $\Phi_{\mathrm{jev},\pi}$ to result in the percentage of J-coupling that is acquired. This can be written as a function of q to result in a constant q_{eff} that is actually provided by the J_{ev}-pulse.

So far concurrent 180° pulses (BUBU) are not used in the argumentation. Only the effect of a perfect concurrent 180° pulse is considered as a measure, introduced by $\Phi_{\mathrm{jev},\pi}$.

$$q_{\mathrm{eff}} = q \frac{\Phi_{\mathrm{Jev}} - \Phi_{\mathrm{Jev},\pi}}{1 - \Phi_{Jev,\pi}}$$

The values of q_{eff} are plotted as a function of q (Fig. 9.2D-F). The graph of q_{eff} is nearly parallel to the diagonal in the range of $0 \leq q \leq 0.6$ indicating an increase of J-coupling capability as demanded by the coefficient q. The parallel displacement of q_{eff} to the diagonal is explained by the 180° property of the J_{ev}-pulse: While the magnetization must be in the x, y-plane to acquire J-coupling it must leave the x, y-plane to facilitate a 180° rotation. The shift is caused by the fraction of time within the shaped pulse that is used for the 180° rotation. The parallel slope of the graph of q_{eff} to the diagonal indicates that there are unused "resources" for $q \leq 0.6$, which can be used for J-coupling evolution.

$0.6 \leq q \leq 1$ assigns the region, which can not bring additional J-evolution because of the opposing requirements needed for J-evolution and 180° rotations. Since J-coupling is only acquired for transversal magnetization, it needs to leave the x, y-plane for the 180° rotation. Because of that and for the demanded robustness and the given pulse length t_p, it is concluded that the found J_{ev}-pulses can acquire up to $q = 0.6$ J-evolution. This corresponds to 60% of t_p and allows to reduce the duration of flanked delays by 600 μs. Or in other words, the effective length of a robust J-evolution period with central refocusing puls is decreased by approximately $0.6\, t_p$.

As has been shown it is possible to obtain J_{ev}-pulses that acquire J-coupling on top of a 180° rotation. But, as discussed in the beginning, it is necessary to classify whether shorter, conventional 180° shaped pulses, flanked by appropriate delays are equivalent or maybe more efficient compared to the proposed J_{ev}-pulses.

9.4.1 Evaluation of the Time Efficiency of J_{ev}-Pulses

In order to justify the proposed J_{ev}-pulses they must over perform shorter conventional 180° shaped pulses flanked with appropriate delays for J-coupling evolution.

According to Fig. 9.1D, any J_{ev}-pulse can be imagined as a concatenation of free evolution periods τ with a centered, concurrent 180° pulse (so called BUBU pulse). Indeed conventional shaped pulses, flanked with delays τ can be used to result in J_{ev}-building blocks with duration of 1 ms that can be compared with the discussed J_{ev}-pulse.
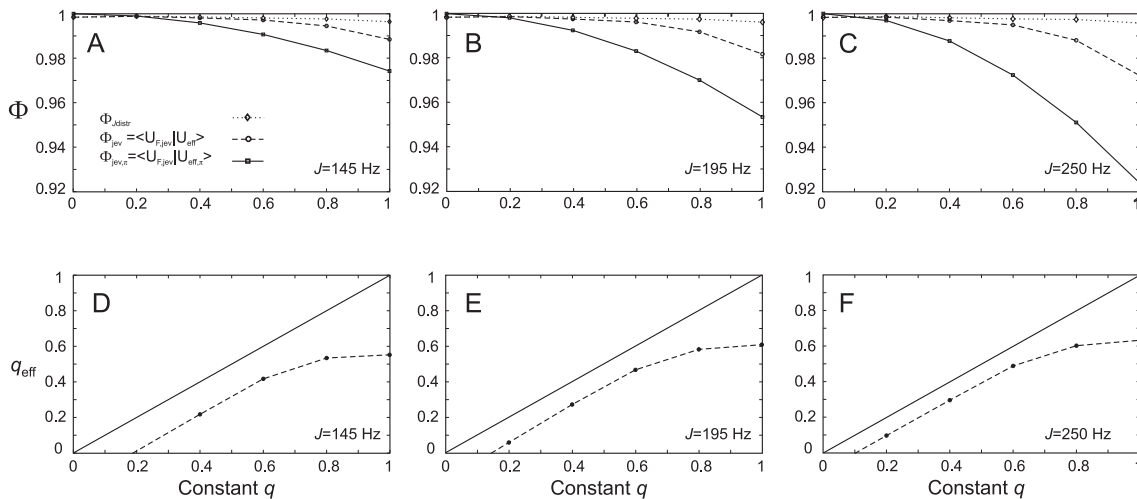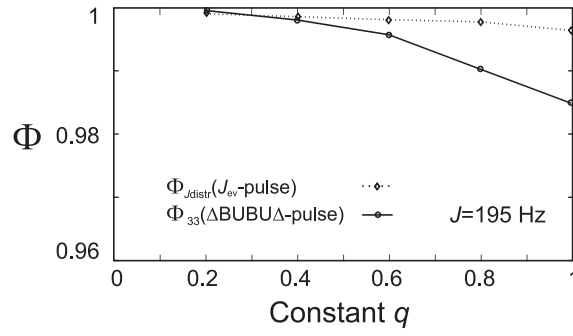
Figure 9.3: Transfer efficiencies for concurrent 180° refocusing pulses, calculated for $J = 195$, Hz and averaged over offsets and B_1 deviations according to Table 9.3. To determine whether J_{ev}-pulses exceed the time efficiency of comparable J_{ev}-building blocks, derived from standard pulses (Fig. 9.1D), they are compared in terms of their 180° fidelity. Six J_{ev}-pulses for $0.001 \leq q \leq 0.999$ are evaluated according to Φ_{Jdistr} (dotted line) and compared to J_{ev}-building blocks derived from shorter BUBU pulses, which are optimized and evaluated according to Φ_{33}. As J_{ev}-pulses exceed the transfer properties of BUBU pulses they are more efficient in terms of time consumption.

The following analysis is done for the case of $J = 195$ Hz (Fig. 9.2B), but the results obtained are comparable for the whole range of J-coupling constants as discussed according to the J-selectivity of the J_{ev}-pulse in the last chapter.

A comparison between J_{ev}-pulse and corresponding J_{ev}-building blocks (composed of two delays τ surrounding a BUBU pulse) is obtained considering the 180° rotation capabilities.

By definition, the J_{ev}-building block acquires the same amount of J-coupling compared to a J_{ev}-pulse with a given q. The analysis starts by finding appropriate delays τ that correspond to the J-evolution that is acquired upon a J_{ev}-pulse. τ is calculated starting from a given q_{eff}. The q_{eff} values from Fig. 9.2E (dashed line) are 0.2/0.058, 0.4/0.272, 0.6/0.466, 0.8/0.581, 0.999/0.608 (q/q_{eff}). For example $q_{eff} = 0.608 = 2\tau$. This results in $t_{p,BUBU} = t_{p,Jev} - 2\tau = 1$ ms -0.608 ms = 0.393 ms. To optimize BUBU pulses, the next even pulse length $t_{p,BUBU} = 0.390$ ms is chosen.

In total four BUBU pulses with duration of 0.730, 0.530, 0.420 and 0.390 ms are optimized corresponding to q_{eff} in the range of $q_{eff} = \{0.2, 0.4, 0.6, 0.8, 0.999\}$. The optimizations are carried out for $J = 195$ Hz. Other parameters are set according to Table 9.3. Because of the decreased duration of pulses they are calculated using x, y-controls with a digitization of 0.5 μs instead of x, y, z-controls.

The fidelity of the BUBU pulses is obtained according to Φ_{33} and plotted in Fig. 9.3 (solid line). This graph determines the physical threshold for concurrent 180° refocusing pulses with respect to the given pulse lengths $t_{p,BUBU}$ and demanded robustness. According to the described setup of the BUBU pulses this graph is suitable to be compared to the 180° rotation capability of the J_{ev}-pulses. In order to do so, the contribution of the 180° rotation and the J-evolution on Φ_{Jev} needs to be distinguished. The effect of the 180° rotation on Φ_{Jev} is obtained, in contrast to the foregoing section, by the definition of a new cost function Φ_{Jdistr}

$$\Phi_{Jdistr} = \max[\Re\langle U_{F,Jev}(J)|U_{eff}\rangle] \quad J = \{0..250\}.$$

Similar to Φ_{jev}, Φ_{Jdistr} relies on the target propagator U_J. But this time J is not set to J_{max} (e.g. $J_{max} = 195$ Hz) but is varied in the range of $J = \{1...J_{max}\}$, with a typical increment of $\Delta_J = 1$ Hz. Φ_{Jdistr} is calculated in that range for every combination of constraints listed in Table 9.3. But only the best transfer efficiency out of the range $J = \{0...J_{max}\}$ is taken for the accumulation of the final te. This procedure is equivalent to allow every possible J-evolution so that only the effect of the 180°rotation is monitored. The resulting graph is given in Fig. 9.2A-C (dotted lines) and Fig. 9.3 (dotted line).

Concerning Fig. 9.3, the 180° rotation capability of the J_{ev}-pulses (dotted line) exceeds the performance of the BUBU pulses (solid line). Since the setup is chosen in order to start from identical amounts of J-evolution, it is concluded that J_{ev}-pulses are more efficient compared to an equivalent J_{ev}-building block made up from BUBU pulses and delays τ. It is found (Fig. 9.3 at $q = 0.999$) that the efficiency of the J_{ev}-pulses increases relatively to the BUBU analogues with increasing q.

9.5 Summary

The J_{ev}-pulses are a non conventional pulses that exceed the class of single spin shaped pulses. They are designed for chemical shift refocusing in heteronuclear coherence transfer elements.

Usually, delays dominate the length of typical coherence transfer elements (e.g. that of the COB-INEPT (Chap. 4)) and thereby also the sequence duration t_s. In order to obtain time optimal coherence transfers, it is not necessary to optimize the sequence as a whole. A fraction of the delay might be located inside the refocusing pulses to reduces the sequence length to an overall duration that is closer to time optimality.

For this reason a concept is derived by so called J_{ev}-pulses that have good refocusing properties and evolve J-coupling on top. With the derivation of a corresponding quality factor Φ_{jev} it is possible to numerically obtain concurrent shaped pulses within approximately 24h of parallel computing using four shared memory nodes.

A strategy to analyze the obtained pulses is described based on the decomposition of the mutual refocusing and J-evolution properties. It is found that the proposed J_{ev}-pulses facilitate J-coupling evolution.

Using a second kind of decomposition strategy and a set of comparable, conventional pulses, it is shown that J_{ev}-pulses not only evolve J-coupling, they also result in sequences with reduced time consumption that are inaccessible with conventional pulses and thereby closer to the physical limit with respect to time consumption. The advantage in time consumption can be given as a fraction of the J_{ev}-pulse length $t_p = 1$ ms and is found to be approximately $q_{\text{eff}} = 0.6$ for the studied set of constraints resulting in a reduced time demand of 0.6 ms for every J_{ev}-pulse that is applied in a sequence.

10. Selective Heteronuclear and Homonuclear Decoupling

Classically described coupling is an effect that is attributed to neighbouring nuclei. They strengthen or weaken the local magnetic field. In the simplest case, a resonance offset is split into two lines and a doublet is obtained.

Decoupling is a technique which prevents the formation of corresponding multiplets. This is accomplished by the rf irradiation of one of the coupling partners. Thus irradiation causes fast interconversion of α and β states so that the local magnetic field seems to be undisturbed by the presence of the coupling partner.

The motivation for using decoupling is usually to avoid signal overlap and to increase the S/N. Decoupling is a crucial step in a variety of experiments, e.g. ^{13}C spectra are recorded with WALTZ-decoupling of protons. Numerous 2D experiments use decoupling in the direct and indirect dimension.

In case of partially aligned samples, e.g. liquid crystals or stretched polymer gels, as well as in the solid state, dipolar couplings add to the scalar couplings. As a function of the distance between the coupled nuclei, dipolar interactions are usually on the order of 100kHz. Quadrupolar couplings can be on the order of MHz. The interactions quite often dominate the other spectral properties like CS and J-couplings. Accordingly, decoupling strategies are crucial to maintain sharp lines.

In partially aligned samples dipolar interactions are approximately three orders of magnitude smaller as compared to the solid state. Couplings between literally all molecular sites are present due to their long-ranged nature $(1/R^3)$. Though these interactions are small, they are manifested in linebroadening.

10.1 Introduction and Motivation

The decoupling obtained by the fast interconversion of α and β states by rf irradiation is mediated by a 180° rotation. A continuous rf irradiation may be considered as an infinite line of 180° pulses. Decoupling is obtained in case the rf amplitude is strong, e.g. dominating the value of the coupling constant.

Beside that, the evolution of coupling needs to be refocused. A single 180° pulse in the center of a delay that affects only the coupling partner will result in a sign inversion of

the involved, shared bilinear operators so that the effect of coupling is cancelled out at the end of the delay.

In the following the observe-spin is denoted as I, while the coupled spin is denoted as S. Various decoupling concepts rely on the referred sign inversion of the bilinear IS term, which is more or less easily accomplished depending on whether the considered spin system is heteronuclear or homonuclear.

Heteronuclear IS spin systems, e.g. $^1H,^{13}C$, are readily decoupled during acquisition. This is because the S spin can be separately addressed by rf controls while the I spin is acquired. Finally, this is a result of the large differences in resonance frequencies of protons compared to heteronuclear spins.

Constitutionally, differences in the offsets of homonuclear IS spin systems are much smaller compared to the case of heteronuclear spin systems. Usually rf controls influence both spins. This complicates the sign inversion of bilinear terms since this relies on the selective inversion of only one spin. Therefore, methods for homonuclear decoupling must exploit some technique to selectively address one spin only. For example BIRD [79] decoupling uses a third, heteronuclear low abundance nucleus, such as ^{13}C, that is coupled to the I spin (see Chap. 5). The heteronuclear coupling is exploited as an additional control-field that mediates the effect of a selective $180°$ pulse to the I spin only. This applies even in homonuclear IS spin systems because of ^{13}C being a dilute natural abundance nucleus.

The Zangger and Sterck method [81] accomplishes essentially the same by using selective pulses during the application of a linear magnetic gradient. Another method includes J-resolved experiments making use of selective $180°$ pulses to decouple spins belonging to different offset-bands. The first two methods, which decouple the full spectrum, have in common that the signal intensity is necessarily decreased significantly. E.g. to the level of the respective natural abundance nuclei. They have in common the requirement of the irradiation of the observe-spin. Classically this is scoped by refocusing the coupling in the indirect dimension of a 2D experiment instead of during the acquisition of the FID in a 1D experiment. As a result experiments are time consuming, for example a 2D HSQC must be acquired as a pseudo-3D experiment in order to apply homonuclear decoupling on top. Only very recently it has been reported that homonuclear decoupling elements are used during the direct detection of the FID [80].

On first glance, it may seem straightforward to directly irradiate the spin under study since there seems to be plenty of time in between two acquired points. However, the opposite is true, since a digital filtering is applied on the continuous data-stream that results in the mentioned data points. A reduction of the sampling time to 50% also reduces the S/N by 50% because the digital filter increasingly fails to avoid the folding of noise into the spectral region. The same is also valid for analogue filters. Therefore, decoupling techniques that make use of short pulses and pulse sequences (e.g. BIRD or Zangger Sterck) may be equally suitable for the direct application during the acquisition of the FID.

In contrast, the selective decoupling sequences that are described in this chapter can be compared to selective J-resolved experiments. Being offset-selective, they share the property of not being short since the selectivity s in Hz is the reciprocal of the time in seconds. A very selective sequence is therefore not suited for the irradiation during the FID because the S/N will reduce significantly. Instead, it is ideally suited for application in heteronuclear experiments. Beside that, the considered sequence can be used for decoupling in the indirect dimension of 2D experiments.

This chapter focuses on an OCT derived selective decoupling sequence for the measurement of ^1J and ^1T couplings. Long range couplings (^nJ and ^nT) with $n > 1$ are decoupled and
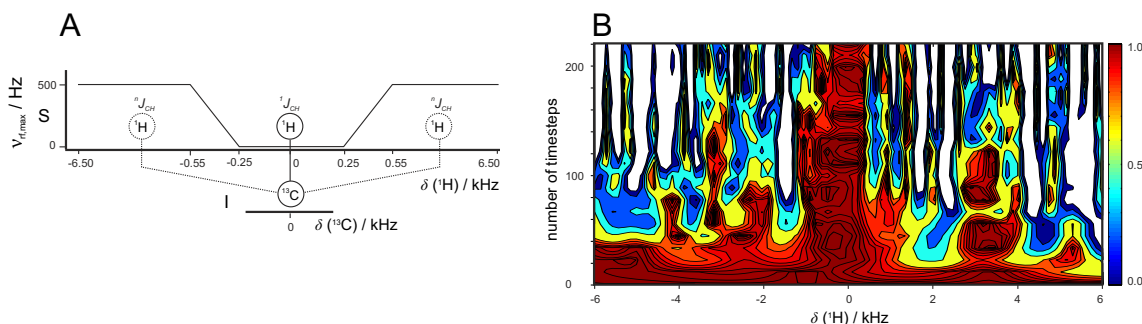
Figure 10.1: Band scheme of the selective proton (S spin) decoupling sequence as a function of the proton offset (A). Carbon (I spin) offset is not considered. The coupling band is set to directly bound protons (via $^1J_{CH}$). $^nJ_{CH}$-coupled protons are decoupled (A). The simulated transfer efficiency of the first 220- out of 4000 steps of an OCT derived selective decoupling sequence is shown in (B). The artwork given in the preamble of this thesis (pages 2 and 3) is adapted from this simulation. The simulated transfer is $S_z \rightarrow S_z$ as a function of the proton offset. Multiple fragments starting from $\rho_0 = S_z$ and ending at the g explicit final operators $C_g = I_z$ within the coupling sequence are simulated and given at the y-axis. The decoupling sequence is constructed of a total of 4000 increments. The simulation shows only transfers according to the first 220 increments. Constant high values in the proton coupling band ($-250 > \nu_{1H} > 250$ Hz) indicate the absence of rf controls and therefore indirectly imply the evolution of couplings in this band. Couplings can be heteronuclear regardless of the ^{13}C offset, or homonuclear, in case the coupled proton spin is also within the coupling range.

relatively narrow lines are acquired. For clarity only ^nJ-couplings are referred to in the following but the considerations also apply for ^nT-couplings.

10.2 Theory

Selective pulses, pulse sequences and decoupling sequences can be obtained from OCT optimizations by stating different target operators as function of the offset, J-coupling or B_1 field. Decoupling sequences in this chapter are offset-selective, e.g. being defined to address only a small band of offsets that can be, for example, in the aromatic or aliphatic band of the proton spectrum.

A heteronuclear two spin system with the observe spin I (^{13}C) and a coupled spin S (^{1}H) is given. The ranges of a selective S pattern (^{1}H) may be illustrated according to Fig. 10.1A. Each I spin can be coupled to a number of S spins. One of the S spins can be the directly coupled S spin that result in the desired $^1J_{CH}$-coupling (if there is more than one directly coupled S spin it is assumed that spins have an identical or at least very similar offset). The other S spins are coupled according to $^nJ_{CH}$-couplings and can have an arbitrary offset within the spectral range. These are wanted to be decoupled from the I spin (Fig. 10.1A).

The idea behind the decoupling sequence is summarized as follows:

- I coherence (inphase or antiphase) is considered.

- If the coupled spin is outside the selective region, rf controls are present that decouple the spin.

- If the coupled spin is inside the coupled region, no rf controls are present and couplings can evolve.

- One carbon can experience more than one coupling: only the coupling within the selective region is selected to evolve, the smaller couplings that contribute to line-broadening are decoupled.

In order to measure the coupling of a certain ^{13}C to its directly attached protons, the offset of the selective decoupling sequence is set to the offset of the directly attached protons. All other protons are decoupled. In theory all other carbons are decoupled from all protons except the ones in the selected region (see Section 10.5).

10.2.1 Heteronuclear Decoupling by Optimal Tracking

An adapted version of the GRAPE algorithm can be used to deduce non-periodic decoupling sequences which can be characterized by several ten thousand independent pulse parameters [141]. In contrast to average Hamiltonian theory, optimal tracking is used to steer an ensemble of spins such that it tracks an optimal trajectory as close as possible. It is given by a number of explicit density operators that must be addressed as a function of time.

A track decoupling sequence can be assumed to be the same as a shaped pulse that accomplishes not only a transfer of initial to final magnetization but has a large number of final operators that are (usually) equally distributed over the duration of the shaped pulse. At each of these final operators the fidelity is evaluated according to the cost function. Often all final operators are identical.

Therefore, a track decoupling pulse can be considered as consisting of a large number of shorter shaped pulses that are concatenated. All of them being ordinary PP pulses, as given by the transfer from one final operator to the next final operator. In contrast, track decoupling sequences avoid the repetitive application of pulse elements that would lead to decoupling sidebands. An optimal track decoupling sequence is therefore characterized by the fact that the inadequateness of a distinct element can be compensated by a successive element.

As indicated above digital acquisition relies on a time-continuous sampling of data-points. Therefore it is not sufficient for a certain state of magnetization to be present at only distinct tracking points in time, e.g. at the points that are addressed by the dwell time. In contrast, the tracking points used for an optimization must be arranged in a density which ascertains the optimal trajectory can not be left, - even in between the tracking points. The density of tracking points must be, therefore, in the range of the cos-function of the property that describes the deviation from the intended trajectory. In the current context, J-coupling is the designated property and the maximum time t between two data points is estimated by $0.9 = \cos(\pi J t)$.

According to the GRAPE optimization of PP pulses (Section 3.1.3) this would require the full time evolution of all possible sets of pulse fragments with increasing length in the interval $\{\rho_0 \ldots \rho_F\}$ as well as the summation over the resulting final matrices to calculate mean cost and gradient information, e.g. a number of G full time evolutions if G tracking points are defined.

$$\sum_g^G U A_g U^\dagger = U \Big(\sum_g^G A_g \Big) U^\dagger \tag{10.1}$$

Instead optimal tracking relies on Eq. 10.1 and expresses that the summation over a number of final matrices $(U A_g U^\dagger)$ equals the running summation of matrices. This means that during the calculation of the time evolution a final state can be added every time a tracking point is passed. By this the need to calculate G full time evolutions is reduced to a single evolution. Accordingly the numerical effort to obtain track decoupling sequences is in principle comparable to the optimization of standard PP pulses.

More information on optimal tracking can be found in [141]. Track decoupling routines are implemented in the optimization program (Section 14.1.2) by Dipl. Chem. T. Reinsperger, Karlsruhe.

10.3 Selective Decoupling Sequences from OCT

A heteronuclear two spin system (I and S) is assumed. The selective decoupling sequence is given by the *decouple* and the *couple* band that is defined as a function of the S spin offset (Fig. 10.1A). The offset of the observe spin I is always set to zero. The transfer properties of the decoupling sequences are discussed separately for the *decouple* and the *couple* band.

- The decoupling band (left and right region in Fig. 10.1A) is defined by the transfer $I_x \rightarrow I_x$. This means that the initial operator $\rho_0 = I_x$ and the target operator and all intermediate tracking operators are $C_j = I_x$. The only property that is of interest for the decoupling band is coupling evolution according to J. This restricts the available density operators to the subgroup $I_x \rightarrow 2I_yS_z \rightarrow -I_x \rightarrow -2I_yS_z \rightarrow I_x$.

- The coupling band (central region in Fig. 10.1A) is given by the transfer $S_z \rightarrow S_z$. A transfer starting from $\rho_0 = S_z$ going to $C_j = S_z$ is accomplished in case no x, y-controls are present in the mentioned region. This implicitly implies the evolution of couplings as they can evolve undisturbed. Again the dense packing of tracking operators is important. It is determined by the cosine function of the maximum rf amplitude ($\pi\nu_{\mathrm{rf,max}}t$) that should result in values close to 1. Accordingly the maximum difference in time between two tracking points is defined in such a way that the trajectory can not significantly deviate from the tracking points - even in between the points. This assures that magnetization always stays along z instead of being only recovered along z at the instance of the tracking points. This is required for implicitly accounting of J-couplings in the coupling band. Furthermore, the offset of carbon is also irrelevant in this region.

For the numerical optimization the pulse length is set to 100 ms. The digitization is 25 μs resulting in 4000 pulse increments. 1000 tracking points are set, digitizing the decoupling sequence in steps of 100 μs. The maximum rf amplitude is set to 500 Hz for the S spin. No controls are considered for the I spin. The product of the track digitization and the rf amplitude is in the small flip angle approximation (10^{-4} s*500 Hz*360° = 18°). The initial random amplitudes are restricted to a maximum of few Hz. B_1 inhomogeneity is not considered. The band widths are set according to Fig. 10.1A and 307 explicit evaluations are considered in the proton dimension for the calculation of cost- and gradient functions. For all spectral regions a J-coupling constant of 200 Hz is considered and a single explicit evaluation is performed. Optimizations typically lasted 24h on a quad core PC.

The optimization process is monitored by simulating the transfer $\rho_0 = I_z \rightarrow C = I_z$ starting always from ρ_0 and propagating G-times forward in time. Therefore the 100 ms decoupling sequence is monitored for the $1 \ldots g \ldots G$ explicit points that are given on the y-axis. The offset of the S spin is given on the x-axis. Fig. 10.1B shows a region out

of the first 220 points of the obtained decoupling sequence. High transfer efficiencies in the central coupling band indicate that no rf controls are present and coupling evolution should take place. Transfer properties in the left and right decoupling band (Fig. 10.1B) differ significantly, as compared to the central region, but can not be entirely judged with respect to the transformation of z-magnetization. A rough estimate off the decoupling field strength, being effectively present over the whole range of the decoupling band, is obtained by the determination of the time that is needed to perform the transfer $I_z \rightarrow I_{x,y}$. This time constant is determined from Fig. 10.1B to be 90 steps*25 μs=2.25 ms. The corresponding rf amplitude is 111 Hz. This is on the order of the $^1J_{\mathrm{CH}}$-coupling (120-250 Hz). Therefore it might be expected that the effective rf amplitude is not sufficient to fully decouple $^1J_{\mathrm{CH}}$-couplings.

Accordingly the decoupling sequence is expected to be sufficient to decouple $^nJ_{\mathrm{CH}}$ couplings which should result in the aspired reduction of the line width and increase the S/N.

10.4 Experimental

The measurement of $^1J_{\mathrm{CH}}$-couplings by means of 1D ^{13}C experiments is complicated by the presence of long range $^nJ_{\mathrm{CH}}$-couplings. Without decoupling lines are usually broad (see Fig. 10.2B), especially if liquid crystalline media are used as co-solvents.

Beside that linebroadening in the isotropic solution is less crucial but also limits the measurement of $^1J_{\mathrm{CH}}$-couplings as will be shown in the following.

A sample containing a 0.5 M solution of menthol in CDCl$_3$ is used. A Bruker 600 MHz Avance III spectrometer (Rheinstetten, Germany) equipped with a cryogenically cooled inverse ^{1}H,^{13}C,^{15}N-triple resonance probehead is used. The rf amplitudes is calibrated to 10 kHz and 500 Hz for ^{13}C and ^{1}H, respectively. Spectra are apodized using exponential decaying functions. The temperature is 300° K. To assure comparability, no decoupling is applied during the relaxation delay.

Using a single scan and WALTZ decoupling with a 90° pulse length of 100 μs, the ^{13}C{^{1}H} spectrum is obtained and used as the reference spectrum (Fig. 10.2A). The line width is determined to be 1.3 Hz.

A single scan ^{13}C spectrum is given Fig. 10.2B. The line width is 24.3 Hz and the S/N is significantly decreased.

A single scan ^{13}C{^{1}H} spectrum using the OCT derived selective decoupling sequence with proton offset set to the directly bound proton is given in Fig. 10.2C. The line width is 2.2 Hz and the S/N is strongly increased compared to the coupled spectrum. In summary the spectral quality and the S/N is significantly enhanced.

10.4.1 Evaluation of Band Selectivity

A systematic experimental evaluation of the decoupling- and the coupling band supplies information that can be compared to the theoretical findings illustrated in Fig. 10.1B.

Therefore the decoupling sequence is evaluated as a function of the proton offset. The carbon signal at approximately 72 ppm is chosen to monitor the response. The resonance frequency of the corresponding proton is assigned to 0 Hz. Starting from this value the proton offset is varied in the range of $-6 < \nu_{\mathrm{H_1}} < 6$ kHz (Fig. 10.3A). The selective coupling band is enlarged in Fig. 10.3B.

The effects of the decoupling sequence seem to be rather chaotic as a function of the proton offset. The coupling range can be recognized though, as it is superimposed by some periodic modulation (see discussion for details).
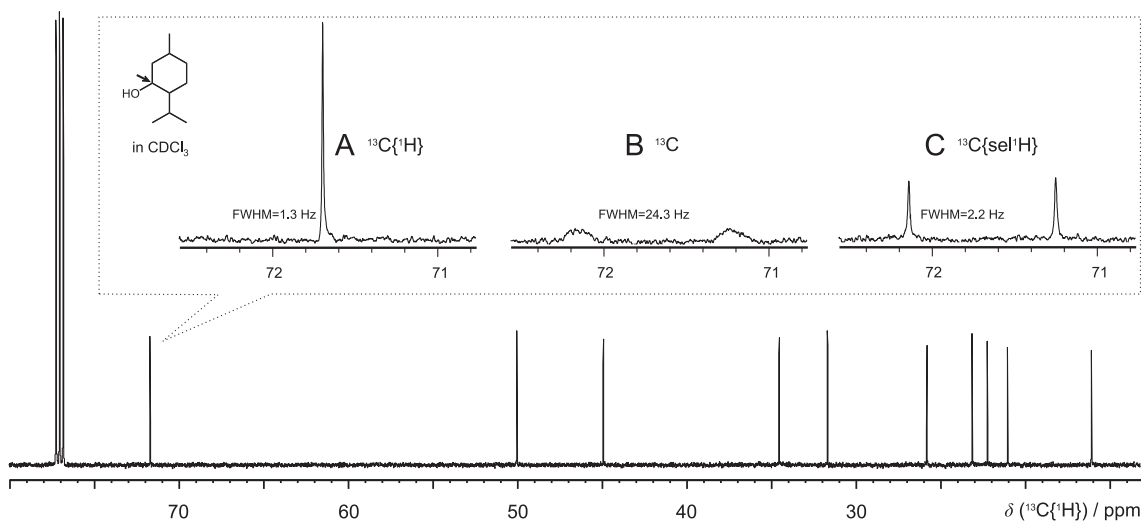
Figure 10.2: ^{13}C spectra of 0.5M menthol in CDCl$_3$. With WALTZ decoupling of protons during acquisition and a respective 90° pulse length of 100 μs (A). Without proton decoupling (B). With the OCT derived selective proton decoupling sequence applied during acquisition and a maximum rf amplitude of 500 Hz (C). $^1J_{CH}$-couplings are retained while linebroadening due to long range couplings ($^nJ_{CH}$) is avoided. The line width (FWHM) is reduced from 24 Hz to 2 Hz, and the S/N is increased. Spectral intensities (A-C) are not scaled and obtained from single scan experiments. Decoupling sequences are not applied during the relaxation delay.

10.5 Discussion

In Fig. 10.3A it is noticeable that the signal intensity outside the selective coupling range has no preferred value. The observed fluctuations in the intensity arise from incompletely decoupled $^1J_{CH}$-couplings and can be seen as a render of the effective decoupling field strength present at a given proton offset. In agreement with the considerations given in Section 10.3, the effective rf strength of the decoupling field is approximately 111 Hz and therefore is smaller compared to the $^1J_{CH}$-coupling of approximately 145 Hz.

A sequence that provides higher decoupling rf strength would be desirable in the optimization of very narrow band decoupling sequences. It could be used for the precise and sensitive determination of long range $^nJ_{CH}$-couplings. This approach would require the full decoupling of the larger $^1J_{CH}$-couplings. However, it is not possible to optimize such sequences since an increased maximum rf reduced the transfer fidelity within the coupling band significantly.

Any rf power that is active in the coupled band partially decouples the evolution of the wanted couplings. Therefore, the coupling constants determined from selective J-decoupled experiments are always smaller than the original coupling constants. In case of the discussed decoupling sequence, $^1J_{CH}$-coupling constants are on average 3% smaller as compared to the coupling constant obtained from the non-decoupled ^{13}C experiment. The mean variation of the individual values to the mean value is 0.55%.

The transfer efficiency in the couple band (Fig. 10.3B) seems to be modulated. The source of this artifact is so far unknown. Dispersive line shape artifacts that superimpose with the main signal may be the reason. As the decoupling sequence is not B$_1$-compensated, this artifacts can be due to a combination of offset and B$_1$-deviations that usually arise at
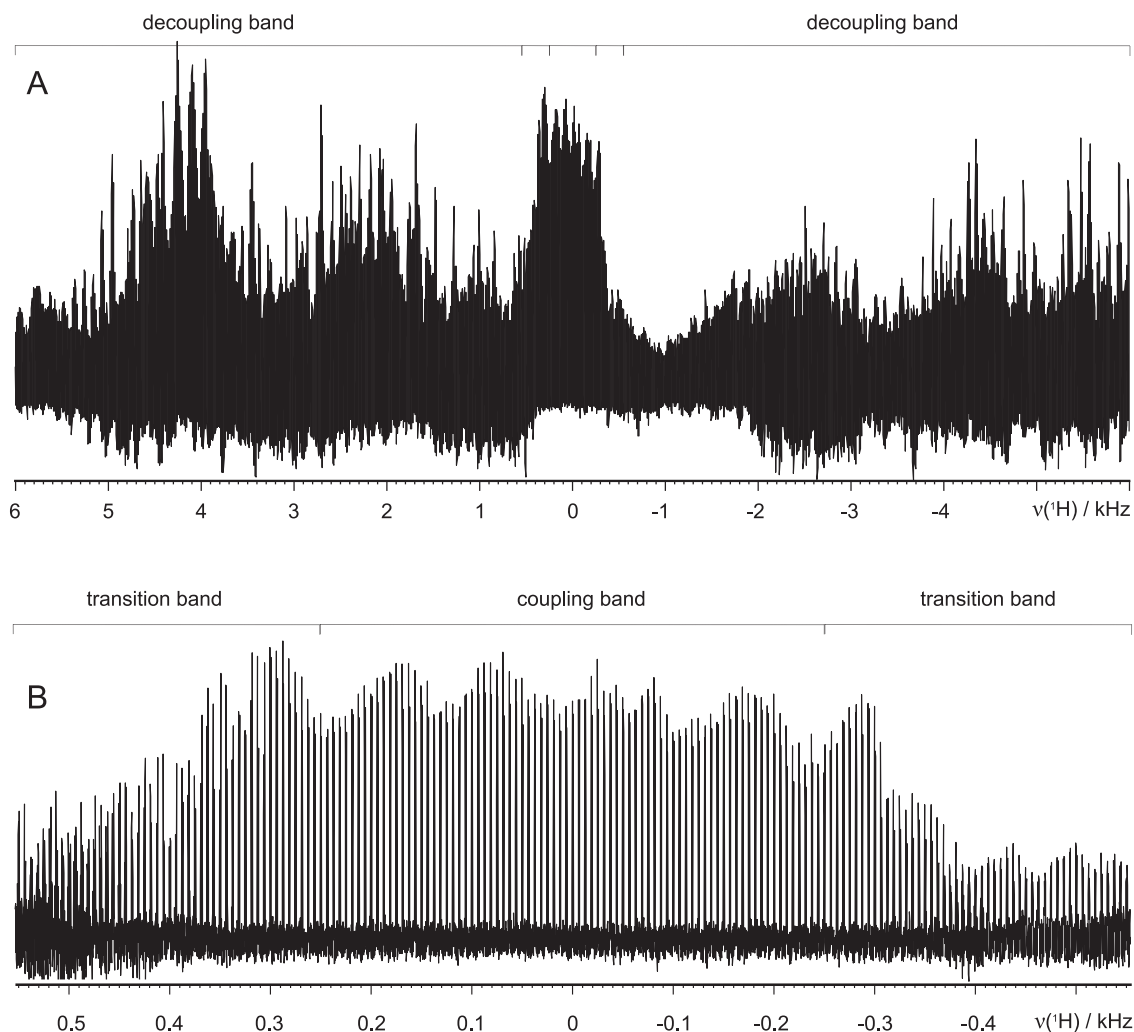
Figure 10.3: Multiple ^{13}C spectra of a 0.5M solution of menthol in CDCl$_3$ recorded with the OCT derived selective decoupling scheme. The proton offset is varied in the range of $-6 > \nu_{1\text{H}} > 6$ kHz. Zero proton offset is defined for the proton directly attached to the signal at $\delta(^{13}C) = 71.7$ ppm (Fig. 10.1). For every experiment only the signal at $\delta(^{13}C) = 71.7$ ppm is shown (A and B). The selective coupling band is illustrated in the enlargement (B). The signal intensity according to the transfer efficiency arises from the coupling- and decoupling properties of the selective decoupling sequence and is compared to the theoretical findings, given in Fig. 10.1B. The comparison reveals that the indirect optimization of coupling properties ($I_x \rightarrow I_x|S_z \rightarrow S_z|I_x \rightarrow I_x$) effectively renders the desired coupling- and decoupling properties to the offset band.

the lower and upper edge of the sample tube.

10.6 Summary

Decoupling sequences are routinely employed to increase the S/N and reduce spectral overlap of NMR data.

In case the coupling constant has to be determined, or an experiment relies on the resolution of coupling information, it is not possible to apply broadband decoupling. In this context, it is assumed that the direct coupling ($^1J_{CH}$) is of interest. It is approximately one order of magnitude larger compared to long-ranged couplings ($^nJ_{CH}$) while the latter are responsible for the linebroadening, the signal overlap and the loss in S/N.

An approach is described to optimize selective decoupling sequences to decouple undesired long-range couplings while wanted $^1J_{CH}$-couplings are retained.

The decoupling sequence is useful for aligned and isotropic samples. ^{13}C-experiments on standard isotropic samples show that the line width can be reduced from 24 Hz down to 2 Hz. Accordingly, the S/N is increased. The sequence is advantageous, in case low concentrated analytes with weak and broad multiplets are studied.

11. Assigning Chiral- and *Meso* Diastereomers using PBLG

Carbon atoms carrying four different substituents induce chirality and the elucidation of the configuration is of high importance as the effect of enantiomers on biological systems may not be identical. But enantiomers have identical physical properties in liquid state NMR and are therefore hard to study. On the other hand, *meso* compounds contain a mirror plane within the molecule, have different physical properties and may be distinguished from the corresponding racemic mixture of the enantiomers (racemic mixtures are abbreviated as *rac* in the following). However, with one exception (see Section 11.1), the patterns observed for *rac* and the equivalent *meso* compounds are qualitatively identical and differ only quantitatively in entities like chemical shift and *J*-couplings.

Therefore, using liquid state NMR, the presence of *meso*, *RR* and *SS* species in a mixture may not be detected easily. If a sample contains only one species (*meso* or *rac*) it is also not possible to assign it to the racemate or the *meso* compound.

The same applies if the mixture of *meso*, *RR* and *SS* species deviate from the statistical distribution. It is not possible to elucidate whether the *meso* or the racemic species is enriched. For illustration, typical molecules of interest are given in Fig. 11.1. The *meso* isomer is also denoted as *unlike*, while the chiral isomers (*RR* and *SS*) are denoted as *like* and mixtures may be denoted with (*u/l*). A survey of methods that are not ideally suited or need chemical modifications for the solution of the problem are listed as follows:

- *ab initio* predictions of solution state chemical shifts could be used to identify the involved molecules. Since experimentally observed differences for (*u/l*) are often on the order of a fraction of a ppm, available quantum chemical calculations are not precise enough since they have an uncertainty of approximately 4-10 ppm.

- Chiroptical methods are not useful. There is no difference to be resolved in the optical sense of rotation for (*u/l*).

- Chiral chromatography may be used to separate enantiomers from each other and also from the *meso* isomer. But in case a sample would contain only the *meso* compound it is not feasible to unambiguously tell whether the *meso* compound is present or the approach failed to separate the enantiomers.
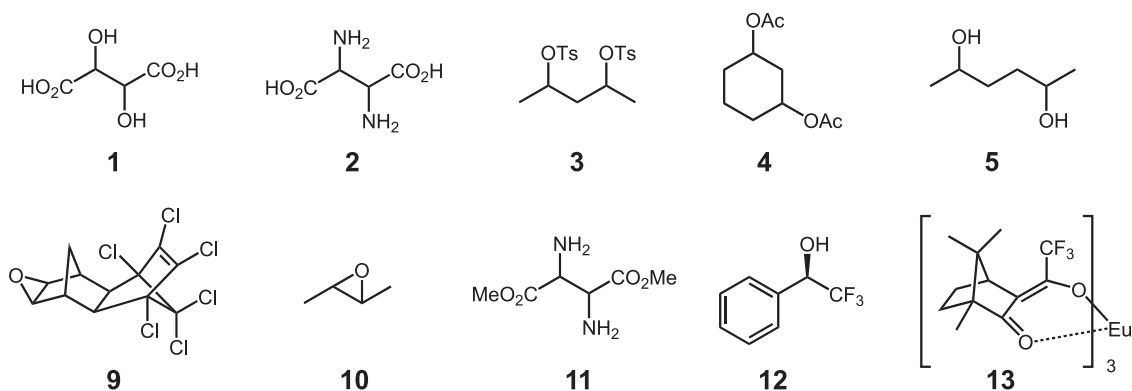
Figure 11.1: List of compounds (**1-5**, **9-11**) that may occur as chiral isomers (RR or SS) or as *meso* isomer. Compound (R)-(-)-α-(Trifluoromethyl)benzyl alcohol serves as chiral solvent **12**. **13** represents tris[3-trifluoromethylhdydroxymethylene-d-camphorato]europium(III) a chiral lanthanide shift reagent.

- A method that employs selectively deuterated analytes is based on the 4-center syn-elimination. Either of ArOH or ArOD in gaseous ions that applies for certain aromatic compounds and is detected using mass spectrometry [142].

Accordingly, this section is concerned about strategies to unambiguously assign racemic mixtures and *meso* isomer in mixtures or independently. Only the internal dependencies of signals, resulting from the present moieties, are used i.e. avoiding the need to chemically derivatize the material under study. Starting from the basic concepts developed in the 1970s [143] it is shown why the discrimination so far is only reported for the easiest model compounds and what can be done to overcome the limitations.

11.1 The Trivial Case

As outlined, there is a special case in which (u/l) mixtures can be unambiguously assigned according to their ^{1}H isotropic spectra. This applies to molecules that share the structural motive of the compound 2,4-ditosyl pentanediol **3** (Fig. 11.1) namely a CH_2 group in the symmetry center that is directly flanked by the stereogenic centers. This should in principal also apply for compound **4**. Because the CH_2 group of interest is overlain by other signals it is so far not shown, whether the expected patterns are also present in this case.

The isotropic proton spectrum of **3** is given in Fig. 11.2 (the signal of the CH_2 group is given in the insert). In the *rac* case, each of the protons in the CH_2 group has one of the neighbouring stereogenic substituents to the same side and one to the opposite side. This results in an identical environment for both protons and accordingly in a single peak (Fig. 11.2, *rac*) with the relative intensity of two.

Whereas the proton positions in the *meso* compound are non equivalent, since one proton is pointing towards the same side as both of the substituents of the stereogenic centers and the other proton points to another direction. Because of the different surroundings they result in two signals. In addition, signals are coupled according to the [2]J_{HH} coupling and result in doublets of triplets (Fig. 11.2 *meso*). Note that the sample composition is not a statistical mixture of the isomers that would be RR:SS:*meso* = 1:1:2 (mol:mol:mol).
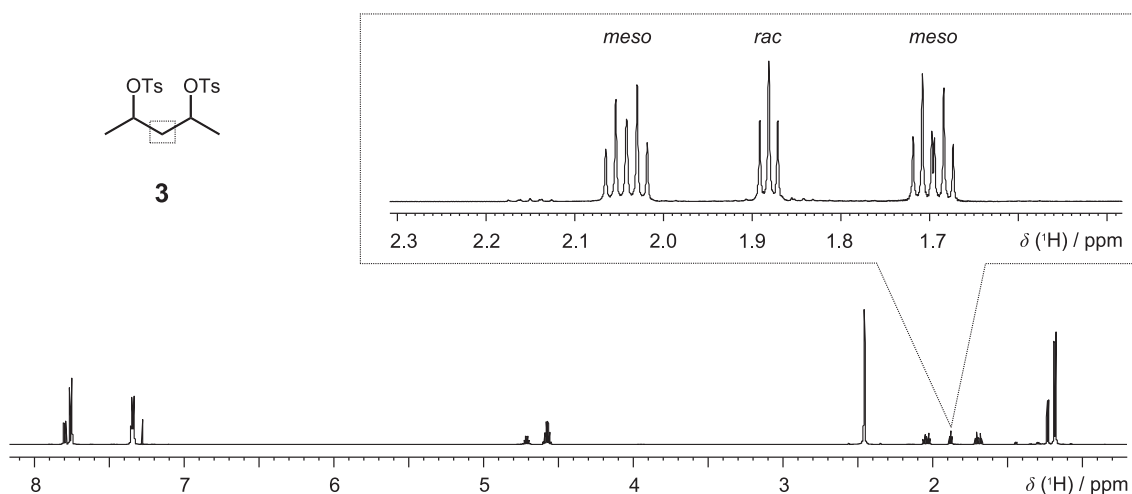
Figure 11.2: Solution proton spectrum of the mixture of isomers of **3** in CDCl$_3$. The CH$_2$ group in the symmetry center (enlarged) can be distinguished for the chiral isomers (denoted as *rac*) and the *meso* isomer. Details are given in the main text.

The described approach is only feasible if the influence of the stereogenic centers towards the chemical environment of the CH$_2$ is of noticeable order. Depending on the substituents, this effect is already too small if the stereogenic centers are separated by three CH$_2$ groups.

It is concluded that there is a need for methods that can discriminate the chiral and the *meso* isomers in case there is no such CH$_2$ group in the symmetry center.

11.2 The Non-Trivial Case

As described by Kainosho et al. in 1972 [143] they successfully obtained the discrimination of the (u/l) isomers **9-11**. The key feature of the proposed method is based on equivalent protons. For the *meso* isomers, these protons are on opposite sides of the mirror plane. Corresponding protons have to be direct neighbours in order to be coupled by the $^3J_{HH}$-coupling. Now, the discrimination of *rac*/*meso* relies on the measure of that $^3J_{HH}$-coupling.

Only very recently Lesot et al. [144] discussed in great detail what can be done if the analyte does not contain $^3J_{HH}$-coupled groups. After considering a number of molecules, spin systems and correlation experiments using different isotopes they concluded that proposed methods based on quadrupolar coupling distinction are so far not feasible.

The mentioned studies [143,144] that are summarized more detailed in the following section rely on the same key concept that is introduced as follows:

In Fig. 11.1 a number of molecules (**1-5**, **9-11**) are given that can form *rac*/*meso* mixtures. For example the three isomers of tartaric acid dimethyl-d_6 ester (the ester of **1**). Using a solution in CDCl$_3$ the spectrum depicted in Fig. 11.3 is obtained. Each of the peaks, corresponding to either the *meso* or the racemic mixtures is schematically given in Fig. 11.4 in the top row.

A chiral anisotropic solution may be obtained by the use of lanthanide shift reagents [145], chiral solvents [146] or liquid crystals, such as PBLG [147]. Equivalent protons become diastereotopic in the chiral environment. In the case of PBLG for example the RCSA gives rise to the diastereotopic discrimination as illustrated in Fig. 11.4 (A, bottom row). Since
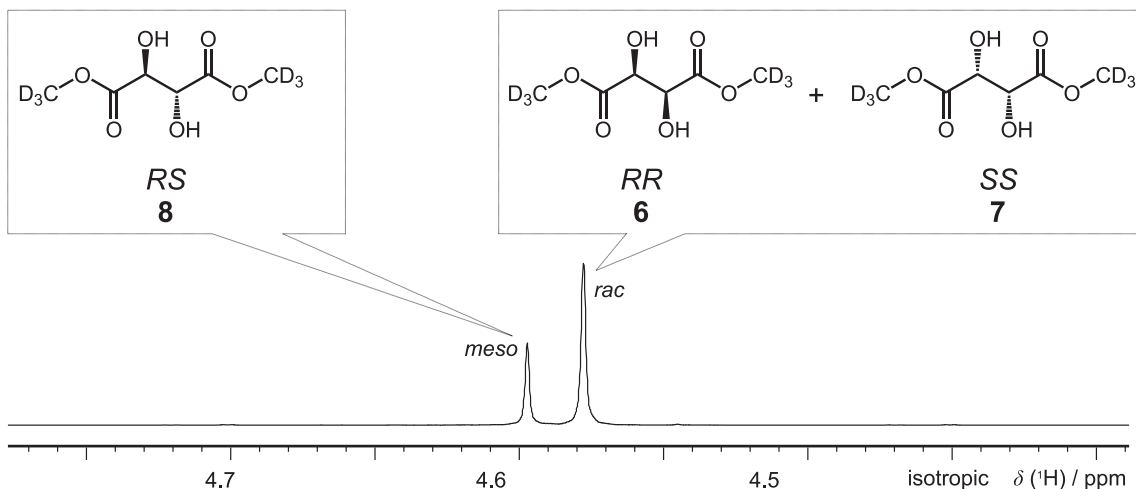
Figure 11.3: Solution proton spectrum of the isomers **6**, **7** and **8** in CDCl$_3$. Qualitatively identical signals (singlets) are obtained for the chiral isomers and the *meso* isomer. The isomers can not be assigned from isotropic data. Here they are assigned since the concentration of the individual species is known.
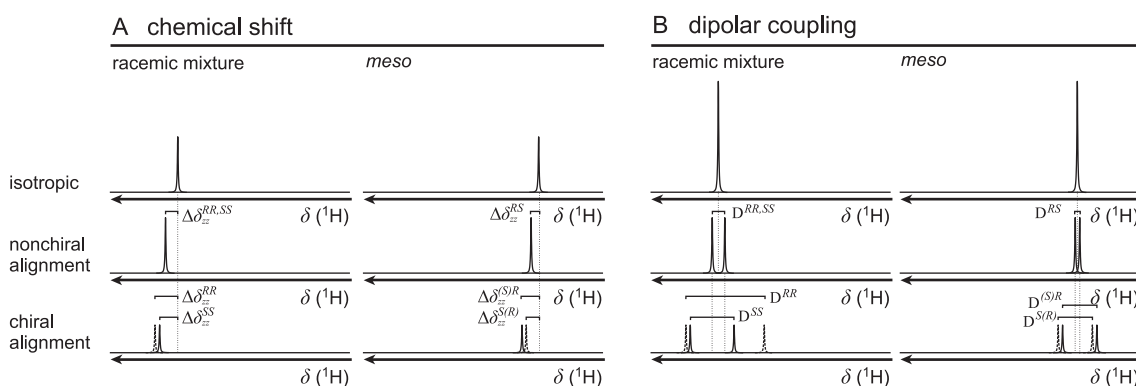
Figure 11.4: Schematic representation of chemical shifts (A) and dipolar couplings (B) in isotropic solution (top row), for non chiral alignment (middle row) and chiral alignment (bottom row) for racemic mixtures and *meso* isomers. Chemical shifts in non chiral alignment are given according to $\Delta\delta_{zz}^{RR,SS}$. The deviation from the isotropic shift is referred to as RCSA. In the chiral alignment media $\Delta\delta_{zz}^{RR}$ and $\Delta\delta_{zz}^{SS}$ may not be identical (A, bottom row). Since the qualitatively identical pattern is also obtained for the *meso* isomer there is no trivial assignment. The same applies for the dipolar coupling (B). Couplings $D^{RR,SS}$ observed for the achiral alignment media are identical and a single coupling D^{RS} is obtained (middle row). In the chiral alignment media couplings D^{RR} and D^{SS} may be not equivalent. The qualitatively identical pattern is obtained for the *meso* isomer (bottom row).

the chemical shift of the R proton is different to the S proton there may be J-coupling within the RS diastereomer (coupling not shown in Fig. 11.4 A), while there can not be any coupling in the RR and SS diastereomers (isochronous signals). Therefore the existence of the scalar coupling unambiguously proves whether the corresponding peaks originate from molecules with RS, RR or SS stereochemistry. (Note that in contrast to the scalar coupling, the absence of dipolar coupling can be also caused by the molecules alignment and therefore is not an unambiguous proof for the racemic mixture).

As this concept relies on the measure of directly coupled diastereotopic protons it might fail if the couplings are too small to be observed or if the sample does not provide the necessary resolution. Furthermore, the application is restricted to $^3J_{\text{HH}}$ couplings.

To principally overcome the restriction, 2D correlation experiments can be employed. The basic idea is the resolution of the signals belonging to the R and S stereogenic centers can be accomplished by any adequate property. For example pseudo contact shifts, chemical shift changes upon chiral solvents, RCSA or RDCs might be used. Once the signals are resolved (Fig. 11.4 bottom line), a transfer step (for example TOCSY) reveals a cross peak between signals resulting from R and S centers. These correlations are only observed for *meso* compounds since the R and the S center must be in the same molecule in order to be correlated.

As there are RR or SS diastereomers in case of the racemic mixture there is the identical transfer, but the cross peak is not resolved as the signals are isochronous. Therefore the absence of a cross peak either indicates the presence of a racemic mixture or the failure of the transfer step. To eliminate this ambiguity additional natural abundance hetero nuclei such as ^{13}C can be used to resolve the cross peak. In this case the cross peak correlates RR or SS moieties (*rac*). By this, a positive, unambiguous determination of *meso* and *rac* is given.

11.3 *Rac/Meso* in Spin Systems Providing a Splitting due to $^3J_{\text{HH}}$ Couplings

Kainosho et al. [143] describes the basic principles of (u/l) recognition. They are able to discriminate (u/l) isomers in *meso*-dimethyl 2,3-diaminosuccinate **11**, the pesticide dieldrin **9** and 2,3-butylene oxid **10** in chiral **12** and the latter two in solution with the chiral shift reagent tris[3-trifluoromethylhdydroxymethylene-d-camphorato]europium(III) **13**. The chiral environment causes anisochronous chemical shifts for the methine protons in **11** and **12** with $\Delta\delta = 0.029$ ppm. On a 600 MHz spectrometer this would correspond to 17.4 Hz that are expected to be resolved. (Note that $\Delta\delta$ values for various isotopes in liquid crystals are approximately one magnitude smaller and can often not be resolved). According to [143], the non-isochronous chemical shift for the *meso* isomer **11** gives rise to a $^3J_{\text{HH}}$-coupling that is measured to be 3.7 Hz, while no such coupling is observed for the RR and SS isomers.

An approach that relies on $^3J_{\text{HH}}$-couplings is reported also for the isomers of **9** and **10** [143]. So far, this approach is limited to the authentication of the *meso* diastereomer since there is no positive response in case of the RR and SS diastereomers. Further, the approach is exclusively limited to $^3J_{\text{HH}}$-coupled moieties since splittings caused by $^nJ_{\text{HH}}$-couplings with $n > 3$ are expected to be too small to be resolved.

The mentioned limitations are addressed in the study presented by Lesot and co-workers [144]. They use a solution of the liquid crystal PBLG in order to discriminate the (u/l) isomers and the enantiomers. They also rely on the use of selectively deuterated analytes since the quadrupolar coupling is a highly sensitive measure for the analytes alignment.

The use of the deuterium spin labels is essential for this approach since differences, introduced upon the alignment, in the *J*-couplings, or the chemical shift are very often too small to be resolved. Having signals resolved due to the *R* and the *S* stereogenic centers one can make use of a more general correlation strategy (as outlined in Section 11.5.2) and by this principally overcome the restriction, which is proven for the $^3J_{HH}$-based approach in the following.

The use of liquid crystals gives rise to RDCs. As dipolar interactions are active through space and are proportional to $1/R^3$ they are long-ranged and are expected to bridge quaternary carbons. Liquid crystalline samples therefore may be beneficial to correlate distant moieties. On the opposite, correlations (e.g. TOCSY) in chiral solvents (that do not induce RDCs) are likely to be hindered by gaps in the spin chain.

The crucial point in the study presented by Lesot et al. [144] is therefore to find experiments/pulse programs that can correlate the signals from the remote deuterium labels. In order to create the desired transfer, they focused on the explicit spin system given by the analyte. For example D-D, D-^{13}C-D and D-^{1}H-D spin systems. For the D-D spin system the coupling is calculated from the distance and the gyromagnetic ratio to be too small to be observed. For the latter two spin systems it is experimentally shown [144] that the correlation is not possible. Though, deuterium is a highly resolving spin label it is concluded that the small gyromagnetic ratio poses severe problems in correlation experiments due to very small dipolar couplings. Other nuclei are investigated to achieve *rac/meso* distinction via different coherence transfer pathways.

11.4 Sample Preparation

Commercially available PBLG with a molecular weight ranging from 150,000 to 350,000 g/-mol is chosen as an alignment media. It is purchased from Sigma-Aldrich, Germany. An amount of 100 mg is transferred in an NMR sample tube. Two samples are prepared. One containing 50 μl of **8** and a second one containing 50 μl of a 2:1 mixture of **7** and **6**. The tube is filled up to a volume of 500 μl with CD_2Cl_2. The samples are sealed and equilibrated for approximately three months. In order to obtain a homogeneous solution, the sample are allowed to flow from the bottom of the sample tube to the top and vice versa. Centrifugation is also used to speed up this process. The samples are stored at 60° C for approximately one month. During this time, sonification at 60° C is applied several times. Nonetheless, broad lines in the deuterium spectrum indicate that a homogeneous solution is not obtained.

According to [147] it is assumed that higher PBLG concentrations may lead to the build up of a stable phase. Therefore the samples are opened and the solvent is evaporated using heat until the samples volume is reduced to approximately 0.5. The solution then is transferred to a 3 mm NMR tube and sealed. The high viscosity and the thin sample tube practically avoids any possibility to move the solution within the tube. The only way of stirring is to heat one end of the sample tube until the solvent boils and thereby pushes away the material.

After applying sonification and heating again the samples become homogeneous as indicated by the deuterium spectrum. The final deuterium splitting for the sample containing **8** and **7** and **6** are 698 and 700 Hz.

11.5 Experimental Strategy

As a result of the discussed studies (Section 11.3) it is decided to choose PBLG to obtain diastereomeric resolution and to rely on ^{1}H^{13}C natural abundance spectroscopy.
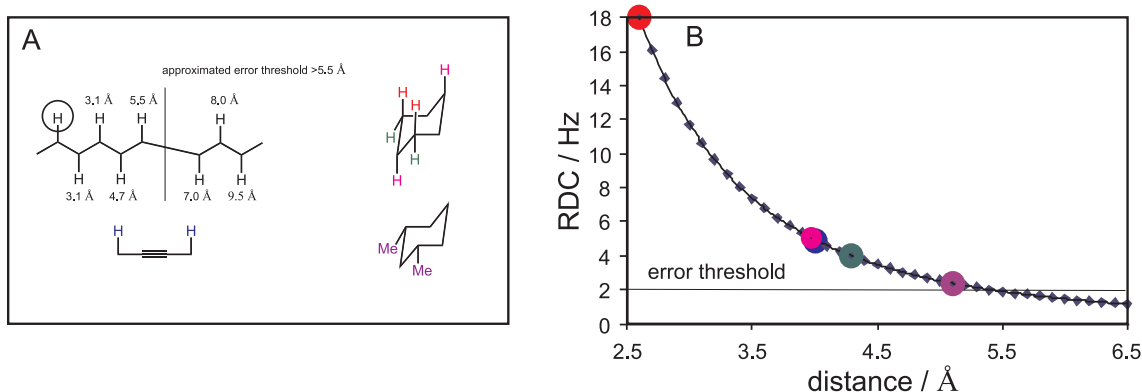
Figure 11.5: Magnitude up to which dipolar couplings may arise for vicinal protons ($^3J_{HH}$) is estimated to be 18 Hz (B). Adequate samples contain approximately 100 mg PBLG in a volume of 500 μl of CDCl$_3$ or CD$_2$Cl$_2$ as a solvent. Couplings for remote protons can be estimated according to the distance dependence of $1/R^3$. Assuming typical line width of 1 Hz couplings may be determined up to a distance of 5.5 Å. A number of moieties that are closer than 5.5 Å are presented in (A). It can be expected that protons within a cyclo hexane ring can be correlated by the dipolar coupling.

PBLG is considered because of the transfer properties through space, which are provided by RDCs. ^{1}H spectroscopy is advantageous because of the vast spin network that can be used to correlate remote centers, e.g. by TOCSY methods.

The protons high gyromagnetic ratio in combination with strong RDCs, on the other hand, can also be exploited to conduct direct correlations between distant centers. This is schematically shown in Fig. 11.5. Assuming vicinal protons ($^3J_{HH}$), the dipolar coupling in a standard PBLG sample (100 mg PBLG, CDCl$_3$, total volume 500 μl) can be roughly estimated to be in the order of 18 Hz (note that the angular dependence on the coupling constant is not considered). Expected dipolar coupling constants are therefore given by the $1/R^3$ dependency according to Fig. 11.5B. Assuming typical natural singlet line widths of 1-2 Hz, the lower threshold to resolve a splitting can be in the order of 5.5 Å. In a favourable situation, protons within a cyclohexane ring (Fig. 11.5A) can be directly correlated by the RDC that evolves through space during the acquisition of the FID without the need to employ further transfer elements. Also the correlation within an aliphatic chain is possible (Fig. 11.5A). The drawback of the strong alignment, on the other hand, is linebroadening due to long range RDCs. Because the molecules under study **6**-**8** have only two protons, additional linebroadening is avoided using deuterium decoupling. For other molecules methods as described in Section 11.5.3, BIRD decoupling (Chap. 5) or selective heteronuclear track decoupling sequences (Chap. 10) can be used to avoid linebroadening.

As 2D spectroscopy is employed to correlate remote centers by the resolution of cross peaks, ^{13}C is used as the nucleus for the second dimension. Fig. 11.6A gives ^{13}C{^{1}H} spectra of the mixture of **6** and **7** and Fig. 11.6C of **8** in PBLG. The observed RCSA values are small. As previously reported [143] the difference in the RCSA values is for the *meso* compound often somewhat higher, while the RR and SS isomers are not resolved within the obtained line width. Accordingly it is concluded that the discrimination of isomers is the bottleneck in the present approach. On the other hand, the correlation step is expected to pretend on some generality since it does not rely on certain spin systems. Note that each center that is equivalent in the isotropic solution and that has anisochronous chemical shifts in the
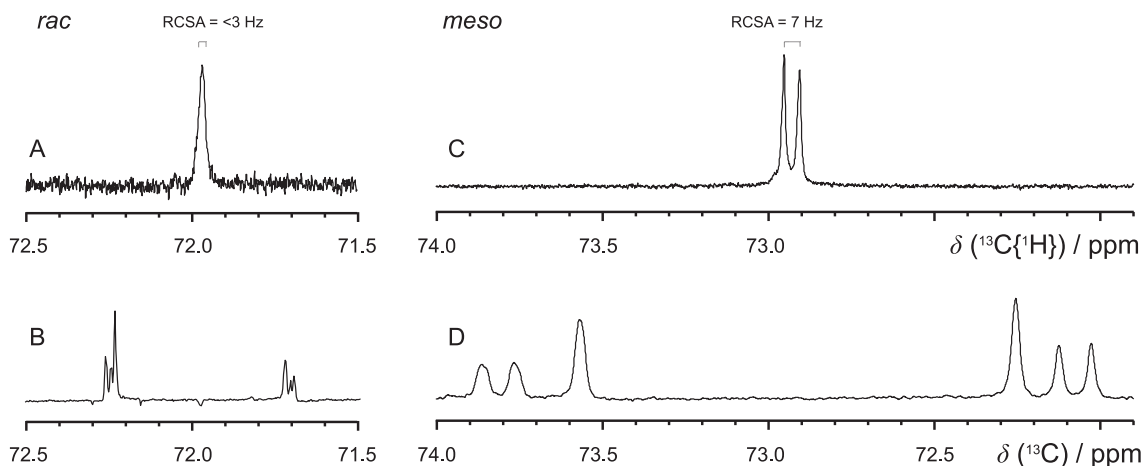
Figure 11.6: $^{13}C\{^1H\}$ spectra (A, C) and ^{13}C spectra of **6** and **7** (B, D) and **8** (C, D) in PBLG CD_2Cl_2. RCSA is not sufficient to resolve the enantiomers within the line width of 3 Hz (A). Differences in RCSA of 7 Hz are observed for the *meso* isomer (C). Non decoupled spectra (B, D) are modulated according to the $^1T_{CH}$ and $^2T_{CH}$ coupling.

chiral environment can be used to accomplish the (u/l) discrimination. Centers therefore do not necessarily need to be the stereogenic center.

11.5.1 HSQC Experiments

Pulse schemes used are represented in Fig. 11.7. A t_1 and t_2 coupled HSQC are acquired. Additionally, deuterium decoupling using the WALTZ64 sequence and a 90° pulse length of 1000 μs is applied. The pulse sequence is shown in Fig. 11.7A.

For the experimental setup, rf amplitudes are calibrated to be 20 and 10 kHz for ^1H and ^{13}C, respectively. A Bruker 600 MHz Avance III spectrometer (Rheinstetten, Germany) equipped with an inverse $^1H,^{13}C,^{15}N$-triple resonance probehead is used. 16k complex data points are acquired in the directly detected dimension with 512 t_1-increments for the indirect dimension in corresponding HSQC experiments. For each of the increments, two scans are recorded. Spectra are apodized using 90° phase shifted squared sine bell functions in both dimensions.

Spectral data for the mixture of the enantiomers is shown in Fig. 11.8. Each molecule detected in the HSQC contains a ^{13}C atom. Due to the low abundance of ^{13}C most of the considered molecules contain a single ^{13}C atom and the spin system under study is therefore a ^1H-^{13}C-^{12}C-^1H spin system (Fig. 11.8).

The resulting spectra show several couplings. These are the homonuclear $^3T_{HH}$ coupling in the direct dimension, the large heteronuclear $^1T_{CH}$ coupling in the direct and the indirect dimension and the small $^2T_{CH}$ coupling in the indirect dimension for both: the RR and the SS diastereomer.

A dipolar coupling depends on the average orientation of the axis between the coupled nuclei in correlation to the magnetic field. For the sample containing the mixture of enantiomers, $^3T_{HH}$-couplings (Fig. 11.9) of 55 Hz and 19 Hz are obtained for the SS and the RR diastereomer. Therefore two HH-vectors with different average orientation must exist. This is only possible if two species are present that align differently as is the case for the mixture of the enantiomers. Therefore the sample containing **6** and **7** is an example for
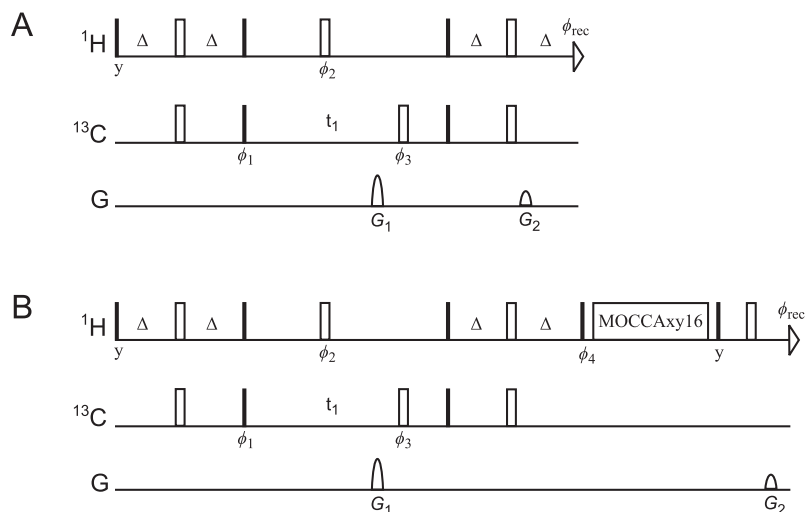
Figure 11.7: Pulse sequences of a standard HSQC (A) and an HSQC-TOCSY (B). The phase cycle is $\phi_1 = x, -x$, $\phi_2 = 4(x), 4(-x)$, $\phi_3 = x, x, -x, -x$, $\phi_4 = -y, y$, $\phi_{\text{rec}} = x, -x, -x, x$,. Gradients G_1 and G_2 are applied with the ratio 80:20.1 for coherence order selection. The phase-sensitive echo/antiecho recording scheme is achieved via changing the sign of G_1 every other increment. $\Delta = 1/4J$. MOCCA-xy16 is used as a TOCSY mixing sequence [148] with a 180° pulse length of 40 μs. If the molecule under study contains deuterium, WALTZ decoupling on the deuterium channel is applied.

the situation where the direct coupling (according to the concept illustrated in Fig. 11.5) through space is sufficient for a discrimination. In this case the assignment of a racemic mixture would be also possible without the possibility to resolve differences in the RCSA.

In the case that two multiplets with identical direct $^nT_{\text{HH}}$ through space are obtained, an additional correlation step is employed to assign the data.

11.5.2 HSQC-TOCSY Experiments

Although the spectrum shown in Fig. 11.8 is already unambiguously assigned to the racemic mixture of **6** and **7**, the HSQC-TOCSY spectrum is considered as follows.

For the experimental setup, rf amplitudes are calibrated to be 20 and 10 kHz for ^{1}H and ^{13}C, respectively. The duration of the TOCSY mixing pulse is set to 40 μs and the mixing time is 100 ms. As a TOCSY sequence the MOCCAxy16 sequence [148] is advantageously chosen to accomplishes maximum transfer as it constructively adds up all contributions that arise from scalar J-couplings, RDCs and NOEs. 16k complex data points are acquired in the directly detected dimension with 512 t_1-increments for the indirect dimension in corresponding HSQC experiments. For each of the increments, two scans are recorded. Spectra are apodized using 90° phase shifted squared sine bell functions in both dimensions.

Fig. 11.9A and B show the lower half of the interesting region of the HSQC spectra for the racemic mixture and the *meso* compound. The corresponding HSQC-TOCSY spectral regions are presented in Fig. 11.9C and D.

Assuming the ^{1}H-^{13}C-^{12}C-^{1}H spin system (Fig. 11.8), signals resulting from directly ^{13}C bound protons are selected by the HSQC. According to this transfer an attenuated $^1T_{\text{CH}}$ doublet is obtained that resembles the one that is already observed in the HSQC (Fig.
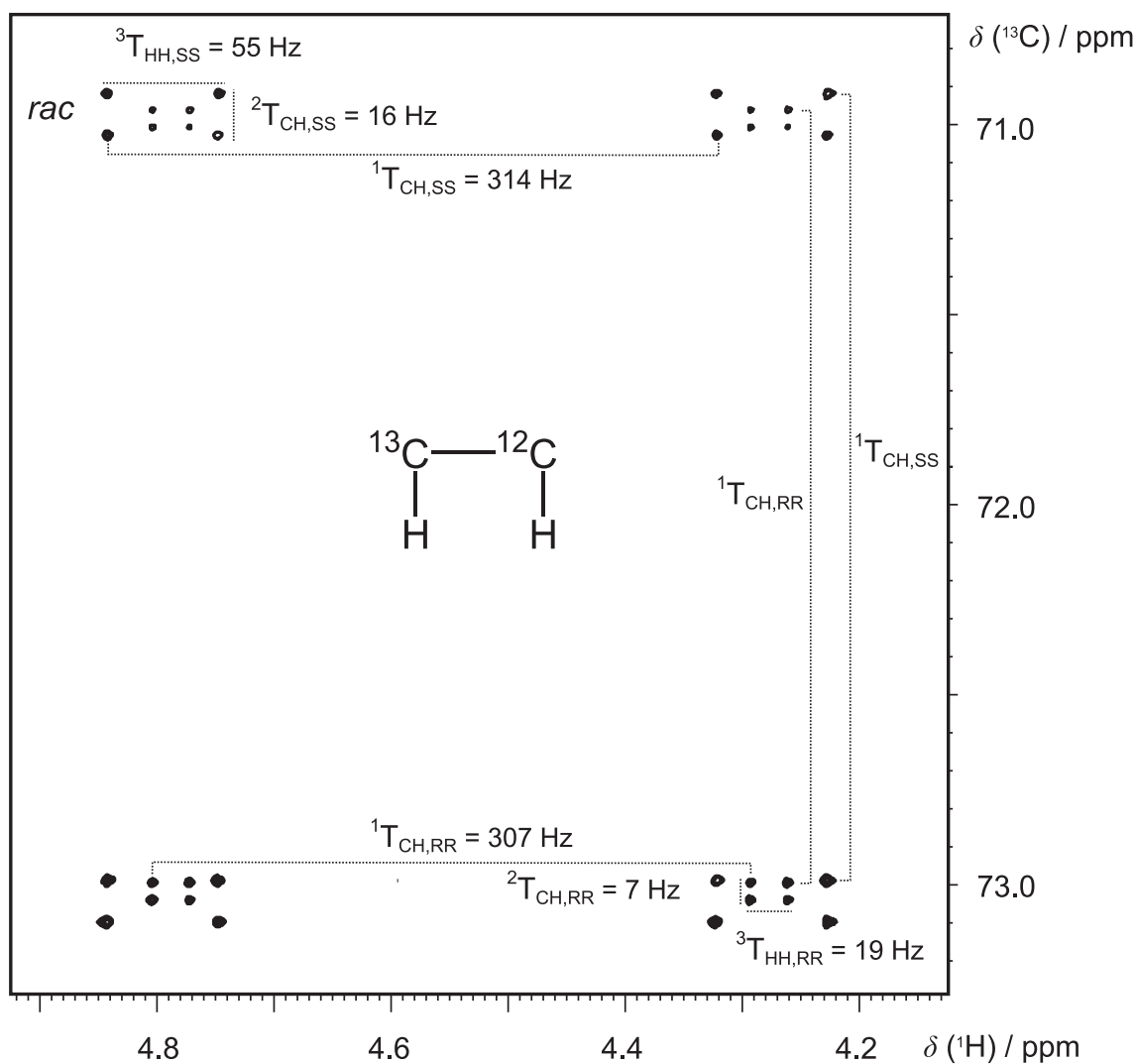
Figure 11.8: t_1, t_2 coupled $^1\text{H}^{13}\text{C}\{^2H\}$-HSQC spectrum of **6** and **7** in PBLG, CD_2Cl_2. According to the ^1H-^{13}C-^{12}C-^1H spin system various couplings are observed in the direct and indirect dimension. Two different $^3T_{\text{HH}}$ couplings are observed that can only result from two HH-vectors that are differently oriented in space and therefore originate from different molecules and are assigned to the mixture of enantiomers.
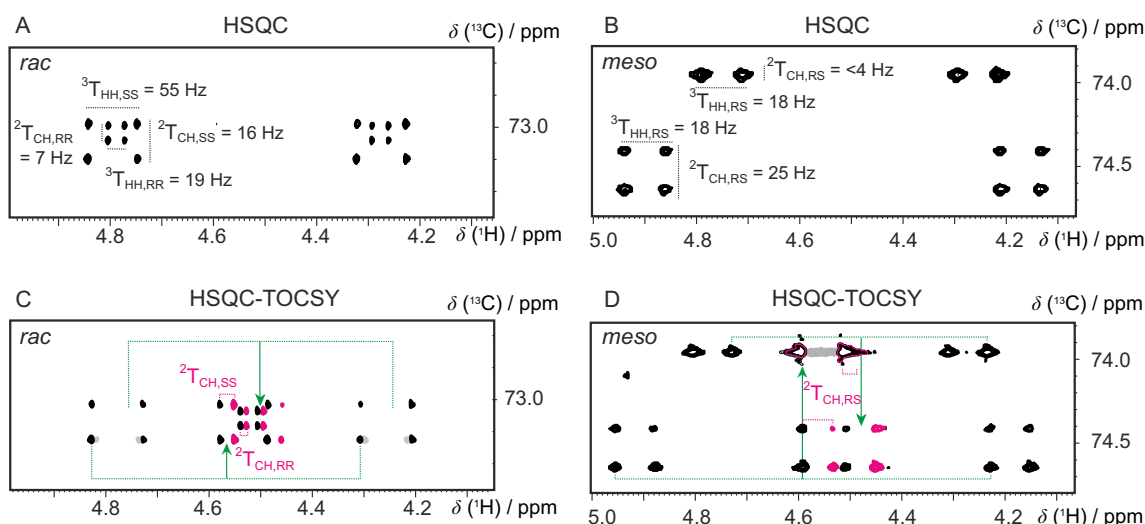
Figure 11.9: Regions of HSQC (A, B) and HSQC-TOCSY (C, D) spectra as presented in Fig. 11.8. HSQC spectra (A, B) show qualitatively identical patterns for the mixture of the enantiomers **6** and **7** (A) and the *meso* isomer **8** (B). A TOCSY transfer is now used to correlate either correspondent (R with R) centers in the enantiomers or in equivalent center (R and S) in the *meso* isomer. In the first case cross peaks in the center of the original signals are expected (C). In the latter case the cross peak is shifted to the center of the opposite stereogenic center (D). Accordingly the mixture of chiral isomers and the *meso* isomer can be unambiguously assigned.

11.9A and C). Upon the TOCSY sequence additional cross peaks are created in the center of the $^1T_{CH}$ doublet (Fig. 11.9C and D). Because of the considered spin systems this signals must result from magnetization that is transferred to the ^{12}C bound protons. Since molecules containing a single ^{13}C are selected by the HSQC, each of the ^{12}C bound protons is neighboured by a ^{13}C. Accordingly, cross peaks are split by the $^2T_{CH}$ coupling in the direct dimension (Fig. 11.9C,D, red).

Up to here, the actual situation is qualitatively identical for RR and SS (Fig. 11.9C) and *meso* (Fig. 11.9D). Note that for the *meso* isomer one of the $^2T_{CH}$ couplings is 25 Hz, while the other one is smaller than the line width and therefore is not observed. Quantitative differences in the chemical shift of the cross peaks are observed. Each of the enantiomers, RR or SS, contains two molecular sites with an identical chemical environment in the chiral solvent. Therefore the cross peak occurs in the center of the $^1T_{CH}$ doublet (indicated by the green arrows, Fig. 11.9C).

The chemical environment in the *meso* isomer (RS) is not identical. Cross peaks therefore are not centered according to the $^1T_{CH}$ doublet. To illustrate this, magnetization is assumed that gives rise to the well resolved signal at 4.92 ppm (proton dimension, Fig. 11.9D). This signal results from one stereogenic center that is arbitrarily assigned to S. After the magnetization is encoded in the carbon dimension at approximately 74.7 ppm it is transferred to the other stereogenic center. During the FID it evolves under the chemical surrounding of the R center and is therefore centered according to the $^1T_{CH}$ doublet at approximately 74.0 ppm in the carbon dimension. The green arrows (Fig. 11.9D) indicate that the cross peaks adopt the chemical shift of the opposite signal. Since the discussed transfer can only occur within a single molecule, the data is unambiguously assigned to the *meso* isomer.
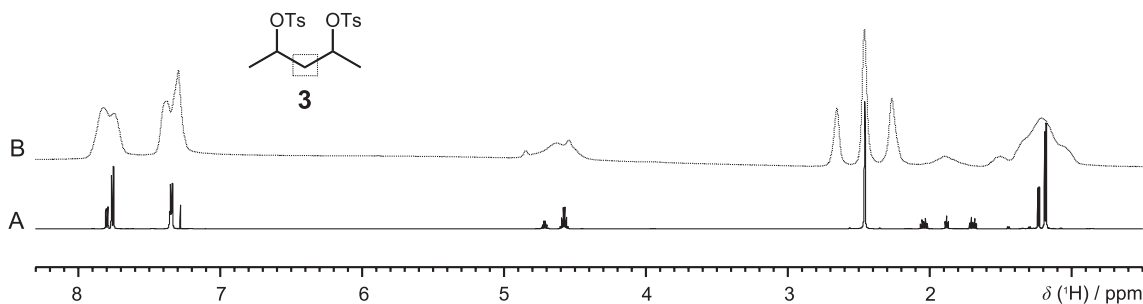
Figure 11.10: Solution proton NMR spectra of the mixture of isomers of **3** in CDCl$_3$ (A). The same analyte dissolved in a liquid crystalline solvent prepared from PBLG results in broad lines (B). To do a (u/l) discrimination, experiments must contain a decoupling element to avoid linebroadening by long range couplings.

11.5.3 Larger Natural Abundance Molecules

According to Fig. 11.1 the compounds **3** and **4** may also occur as a mixture of (u/l) isomers. Two samples containing PBLG are prepared similarly to the description given in Section 11.4. CDCl$_3$ is used as the solvent.

After obtaining homogeneous alignment with quadrupolar splittings of 821 and 692 Hz, a proton spectrum is recorded using the sample containing **3** (Fig. 11.10). Because of the strong alignment and the larger number of protons all signals are broadened due to long-range couplings.

The same applies for the sample containing the isomers of **4** (spectra not shown). Instead of the HSQC-TOCSY, a J-resolved approach is applied in order to avoid the dipolar linebroadening. The J-resolved proton experiment selectively irradiates a certain group to decouple it from the rest of the spin system. According to Fig. 11.10 the stereogenic centers containing the oxygen are ideally suited since they are separated from the aromatic and the aliphatic region.

Fig. 11.11 shows the pulse sequence of the selective J-resolved experiment. It starts with the excitation of carbon coherence that is dephased. Proton coherence is excited, during t_1 a J-resolved spectrum is recorded in the indirect dimension. An INEPT step with $\Delta = 1/(4J)$ follows. Antiphase is refocused on carbon and inphase magnetization is acquired while protons are decoupled using WALTZ64. The resulting spectrum is shown in Fig. 11.12.

Clearly, the decoupling procedure is effective. The peak width (full width half maximum (FWHM)) in the carbon dimension is only limited by the samples homogeneity and the shim and is measured to be 5 Hz. This is an acceptable value but narrow lines would be desirable but are often limited by the sample. In comparison, the line width in the indirect dimension is 8 Hz and proves the decoupling performance of the selective J-resolved experiment.

Nonetheless, Fig. 11.12 shows none of the desired quantities. Only the large $^1T_{\text{CH}}$-couplings are resolved. First of all, differences in the RCSA in the carbon dimension would be needed to resolve RR, SS and the two different moieties of the RS diastereomer. None of them are resolved. This might be due to the broad lines and because RCSA is very small for sp^3 hybridized centers since the electron distribution has spherical symmetry (note that the hybridization of the methine groups in the tartaric acid ester is effectively sp^2 (Section 11.5.2).
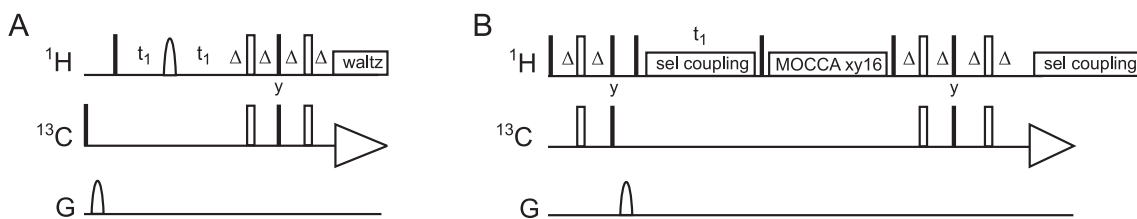
Figure 11.11: Pulse sequences for the acquisition on carbon that employ decoupling on hydrogen in the indirect dimension. (A) A *J*-resolved experiment for the detection of $^3T_{HH}$ couplings in the indirect dimension. A selective 180° pulse is used to decouple the signal of interest from the rest of the spectral region. (B) A carbon-detected HSQC-TOCSY experiment. Magnetization of directly ^{13}C bound protons is dephased while ^{12}C bound protons are excited. Selective decoupling is applied for the group of interest during t_1. A TOCSY transfer is applied to spread the magnetization over the whole molecule. Magnetization is transferred via $^1T_{CH}$ to carbon and is refocused to inphase. Inphase magnetization is detected while selective heteronuclear track decoupling is applied (B). Note that selective coupling can also be applied to antiphase signals. The desired spectrum should contain proton chemical shift, RCSA and long range HH couplings between equivalent groups in the indirect dimension and carbon chemical shift, RCSA and $^1T_{CH}$ couplings in the direct dimension. The indirect dimension is processed in magnitude mode and the direct dimension phase sensitive.

The second possibility to assign the enantiomers would have been the occurrence of the direct $^4T_{HH}$ couplings through space. For each of the enantiomers a distinct coupling should have been observed in the indirect dimension. Actually, no splitting is observed (Fig. 11.12) so that the coupling must be smaller than 8 Hz.

It is therefore concluded that the *J*-resolved experiment is not useful for the application to arbitrary (*u*/*l*) mixtures and an experiment that exploits the RCSA on protons could be more suitable. An HSQC-TOCSY-like experiment that is sensitive to proton chemical shift and RCSA in the indirect dimension is depicted in Fig. 11.11B. It uses a decoupling sequences (heteronuclear selective track (Chap. 10)) that is also supposed to provide selective homonuclear decoupling. So far this experiment has not been acquired.

11.6 Discussion

Using the isomers of the tartaric acid ester (**6**, **7** and **8**) it is easily possible to assign the stereo isomers to the enantiomers and the *meso* isomer. Useful information is obtained from both:

- direct HH-couplings that are sufficient for the assignment of the racemic mixture and

- the correlation of the RCSA resolved proton signals that gives evidence about both: the enantiomers and the *meso* isomer.

The favourable situation may be owed to the electronic structure of the tartaric acid. More details about the electronic structure can be obtained from the ^{13}C satellites. Therefore the solution proton spectrum of the isomers of **1** in D_2O is recorded (Fig. 11.13A). Since the ^{12}C bound methine protons are anisochronous, no $^3J_{HH}$-coupling is observed for the central
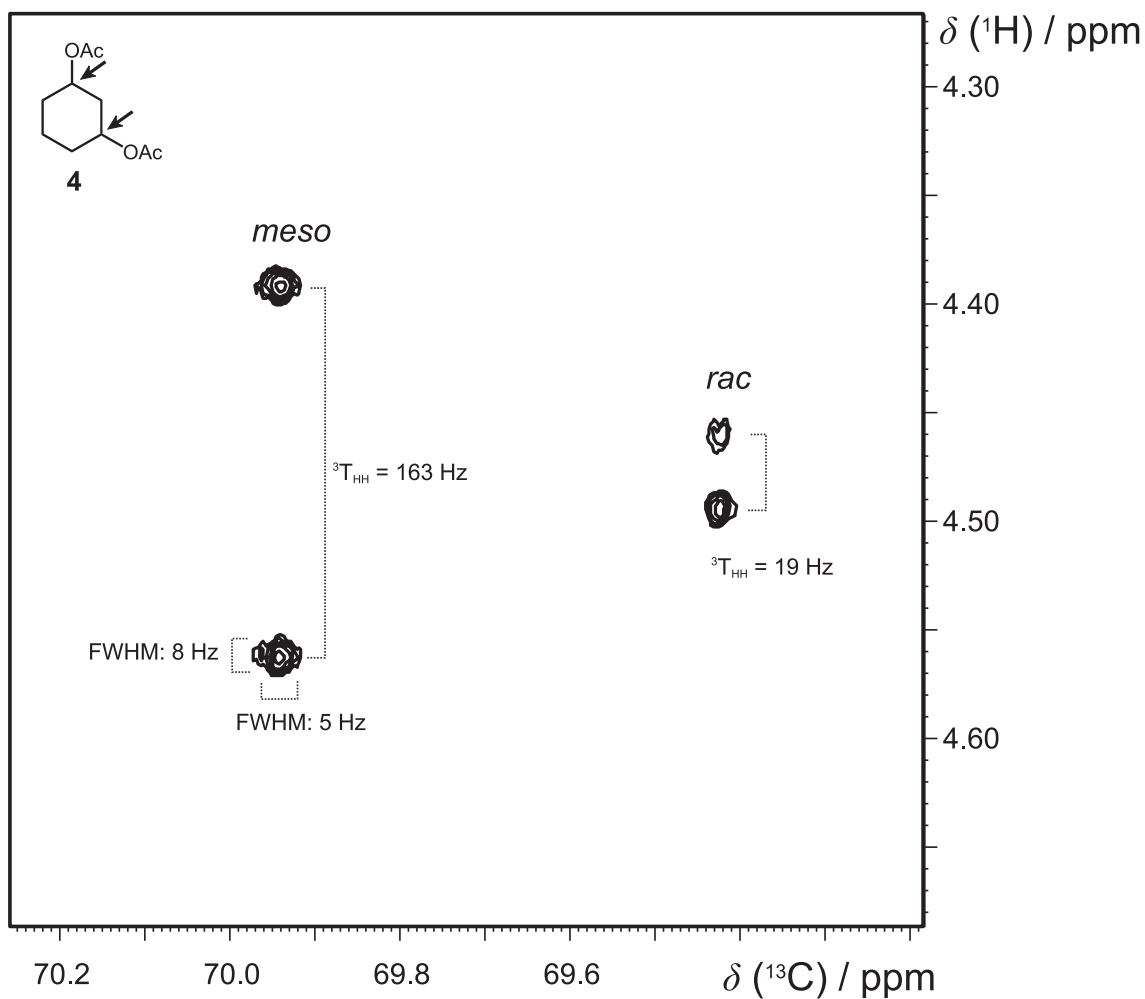
Figure 11.12: Proton J-resolved carbon detected experiment (pulse sequence shown in Fig. 11.11) applied to a sample containing a mixture of the isomers of **4**. $^1T_{CH}$ couplings are resolved in the indirect dimension. Desired discrepancies in carbon RCSA are not resolved as well as $^4T_{HH}$-couplings. Peaks are assigned to rac and $meso$ according the known intensities of the used substances.
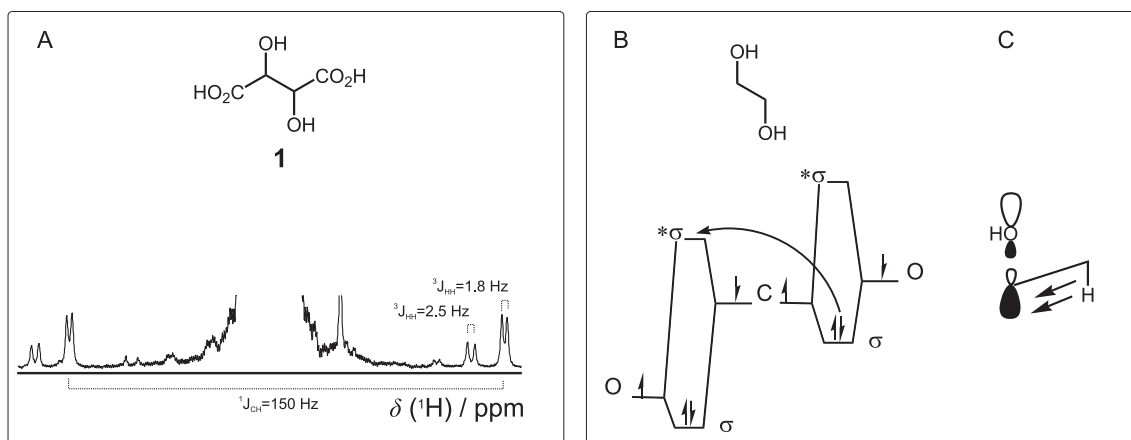
Figure 11.13: The solution proton spectrum of of the mixture of isomers of tartaric acid **1** in D_2O (A) reveals ^{13}C satellites that allow conclusions on the hybridization of the methine groups (B). Hyperconjugation (C) induces the Gauche effect that result in quasi sp^2 hybridization of the methine groups, the hindered rotation around the sigma bond and the small $^3J_{HH}$-couplings. The less spherical distribution of electrons in sp^2 hybridized moieties (compared to sp^3) can results in stronger RCSA values.

signal, while the ^{13}C satellites reveal a $^3J_{HH}$-coupling of approximately 2 Hz. According to the Karplus relation small $^3J_{HH}$ values are obtained for cis protons if there is no fast rotation around the sigma bond. Tartaric acid has no bulky groups that could avoid fast rotation.

Further, the large $^1J_{CH} = 150$ Hz coupling is a sign that the contribution of the s-orbital is significantly reduced. Typical values for sp^3 hybridized moieties are found within the range of 120-145 Hz and for sp^2 within a range of 160-180 Hz. It may be therefore concluded that the CH-groups are partially sp^2 hybridized and form a double bond that restricts the rotation.

This effect is known as *gauche effect* and it is reported for a number of compounds carrying vicinal electronegative substituents such as 1,2-ethylene glycol and 1,2-difluor ethane. It is caused by hyper conjugation (Fig. 11.13C) that gives stabilization according to the partial overlap of a σ^* and a σ orbital. Finally it causes the syn position of the discussed protons and the rehybridization. Since the electron distribution in sp^2 carbons is not of spherical symmetry, corresponding RCSA values are larger. This might be the reason why the HSQC-TOCSY experiments (Fig. 11.8) afforded sufficient RCSA values.

The failure of the *J*-resolved experiments to assign the isomers of **4** may be owing to the carbons hybridization. This experiment also relied on proton couplings, while it is not sensitive to proton chemical shifts and RCSA. Future experiments that evolve chemical shifts and RCSA on protons may be advantageous. In this case, a suitable decoupling strategy may be given by selective track decoupling (Chap. 10).

Another approach would be the use of chiral solvents such as **12** or lanthanide shift reagents **13** since the change in chemical shifts is reported to be large [143]. In this case the correlation between remote centers is assumed to be challenging. Furthermore, it is noted that lanthanide shift reagents at the present 600 MHz spectrometer can perform significantly different to what is observed on the early 40 MHz machines. Finally, a combination of chiral solvents, lanthanide shift reagents and liquid crystals could be considered.

11.7 Summary

Although a mixture of enantiomers gives rise to different signals compared to the corresponding *meso* isomer, it is not generally possible to tell which signal corresponds to which species (without one exception (Chap. 11.1).

A study from the 1970s [143] and a recent one [144] have shown that chiral solvents and lanthanide shifts reagents can be used to identify the racemic mixture. Examples are given for substances that allow the measurement of $^3J_{HH}$-couplings. This coupling must connect the parts to the right and the left of the symmetry center. Therefore the substance must contain an H-C-C-H spin system in the center. The approach is not possible if protons are separated by more atoms. The approach gives no unambiguous assignment for the chiral isomers since it relies on the absence of a coupling that could be also caused by an insufficient resolution, e.g. if the coupling is to small to be detected.

In the current study PBLG is used as a chiral alignment medium. The analyte is the tartaric acid dimethyl-d_6 ester. Using a t_1 and t_2 coupled HSQC spectrum, dipolar HH couplings are measured that unambiguously identify the presence of the chiral isomers.

In addition HSQC-TOCSY experiments are acquired. This experiment is intended to also correlate distant groups as they may be found in other analytes. Using the differences in proton RCSAs, it is possible to correlate the centers within all isomers in order to unambiguously assign them to either the chiral isomers or the *meso* isomer.

Unfortunately, studies employing a selective *J*-resolved experiment in order to decouple long range RDCs and obtain narrow lines in standard small molecule samples fail to resolve the signals.

12. Assigning Chiral- and *Meso* Diastereomers using Chiral Solvents

12.1 Motivation

Pursuing essentially the same objective as discussed in Chap. 11, the scope of this chapter is to enable the assignment of (u/l) diastereomers for larger molecules, e.g. standard synthetic products. As it is shown in the Section 11.5.2, the assignment of tartaric acid methyl ester to either the mixture of enantiomers or the meso isomer is possible. But it is also recognized that the approach critically relies on the special electronic structure (Section 11.6) of tartaric acid. Accordingly, it is not possible to assign other substances to their (u/l) isomers.

The philosophy of how the chiral isomers are discriminated from the meso isomer is based on the resolution of signals originating from R and S stereogenic centers in a chiral environment. Using 2D NMR spectroscopy, the resolved signals are then correlated. Since the crosspeak signals are different for the chiral isomers and the meso isomer, signals can be assigned (see. Chap. 11.2).

The approach therefore relies on the (i) resolution of signals in a chiral environment and (ii) their correlation.

- Using PBLG as a chiral liquid crystal, it is found (Section 11.5.2) that the resolution is the bottleneck since RCSA values are usually very small and obtained line widths are limited by the samples homogeneity and are additionally broadened due to long range RDCs. On the other hand the correlation step can be expected less problematic since RDCs are long-ranged.

- Chiral solvents are described [143] to change the chemical shift according to the present stereogenic centers while retaining the line width of the signals. Differences observed for equivalent centers can be up to approximately 0.016 ppm (approx. 10 Hz at a field strength of 600 MHz). On the other hand, due to the absence of RDCs, the correlation of distant groups is assumed to be more challenging.

Prior to any correlation experiment the necessary precondition is the resolution of signals, therefore the focuse of this chapter is on the use of chiral solvents, such as R-TFB [149].

12.2 2,4-Ditosyl Pentanediol 3

12.2.1 Sample Preparation and 1D Experiments

R-TFB (**3**) is purchased from Sigma-Aldrich, Germany. 21 mg of the isomers of **3** (Fig. 12.1) are dissolved in 160 μl of *R*-TFB. The solution is filled in a 3 mm sample tube and the tube is sealed.

A Bruker 600 MHz Avance III spectrometer (Rheinstetten, Germany) equipped with an inverse ^{1}H,^{13}C,^{15}N-triple resonance cryogenically cooled probehead is used. The temperature is set to 298° K. HSQC-TOCSY experiments are performed with 500 complex data points in the directly detected dimension and with 256 t_1-increments for the indirect dimension. Spectra are not apodized. The majority of signals resulting from the analyte are not overlaid by the solvent and the signals are strong enough to be detected beside the solvent. No presaturation of solvent signals is needed.

Changes introduced upon the usage of *R*-TFB as a solvent are obtained by the comparison to spectral data that is recorded from an isotropic solution using CDCl$_3$ as a solvent. Fig. 12.1 reports the proton spectrum of **3** in CDCl$_3$ and *R*-TFB. Impurities and solvent signals are labelled with "x". Various signals are shifted upon the interaction to the chiral solvent and isochronous signals from equivalent groups become anisochronous. This is observed in the aromatic region (Fig. 12.1,B) and the aliphatic region (Fig. 12.1,C). Signals of the groups *1*, *2* and *3* are changed. For example the isolated methyl group *3* reports an inequivalence of 5.8 Hz. But the correlation of the two methyl groups (*3*) is expected to be difficult since they are the most separated moieties in the molecule.

The proton decoupled carbon spectrum is given in Fig. 12.2A. The larger range of chemical shifts effectively avoids spectral overlap and a number of molecular sites can be therefore discussed in detail (Fig. 12.2B-E). Each of the regions out of the main spectrum shows a set of equivalent groups obtained from either the chiral isomers or the meso isomer. In the aromatic region one of the quarternary carbon (*6*) reports an inequivalence of 2.3 Hz, while no difference is observed for the other species (Fig. 12.2B). The same applies for the other quarternary carbon (*5*) making them futile for the correlation experiments. In the aliphatic region there is no discrimination for the group (*4*) and (*3*) (Fig. 12.2D,E). Anisochronous chemical shifts for the methyl groups (*1*) are found (Fig. 12.2E).

Accordingly, the signals of the methyl groups (*1*) are chosen for the following correlation experiments.

12.2.2 HSQC-TOCSY Correlation Experiment

An HSQC-TOCSY experiment with pulse sequence given in Fig. 11.7 is considered. The duration of the 180° TOCSY mixing pulse is set to 40 μs and the mixing time is 200 ms. The resulting spectrum is shown in Fig. 12.3A. Doublets are obtained in the direct dimension according to the $^1J_{CH}$- and the $^3J_{HH}$-coupling with 128 Hz and 6.3 Hz, respectively.

The peaks are multiplied in the indirect dimension and they appear tilted according to the inequivalence of chemical shifts that are also found in the proton and carbon spectra (Figs. 12.1 and 12.2). As a consequences the inequivalence must be just large enough to result in a noticeable tilt, while it is not necessary to fully resolve the signals. Values as small as 1.5 Hz (Fig. 12.3A) are large enough.

The TOCSY correlation peak occurs in the center of the $^1J_{CH}$ doublet. Since the ^{13}C atom of the equivalent group is far apart, no additional heteronuclear coupling is acquired for the correlation peaks. The mixture of chiral isomers (*RR* and *SS*) is assigned to the multiplet at $\delta(^{13}$C)=21.0 ppm since the chemical surrounding for either *R* in *RR* or *S* in
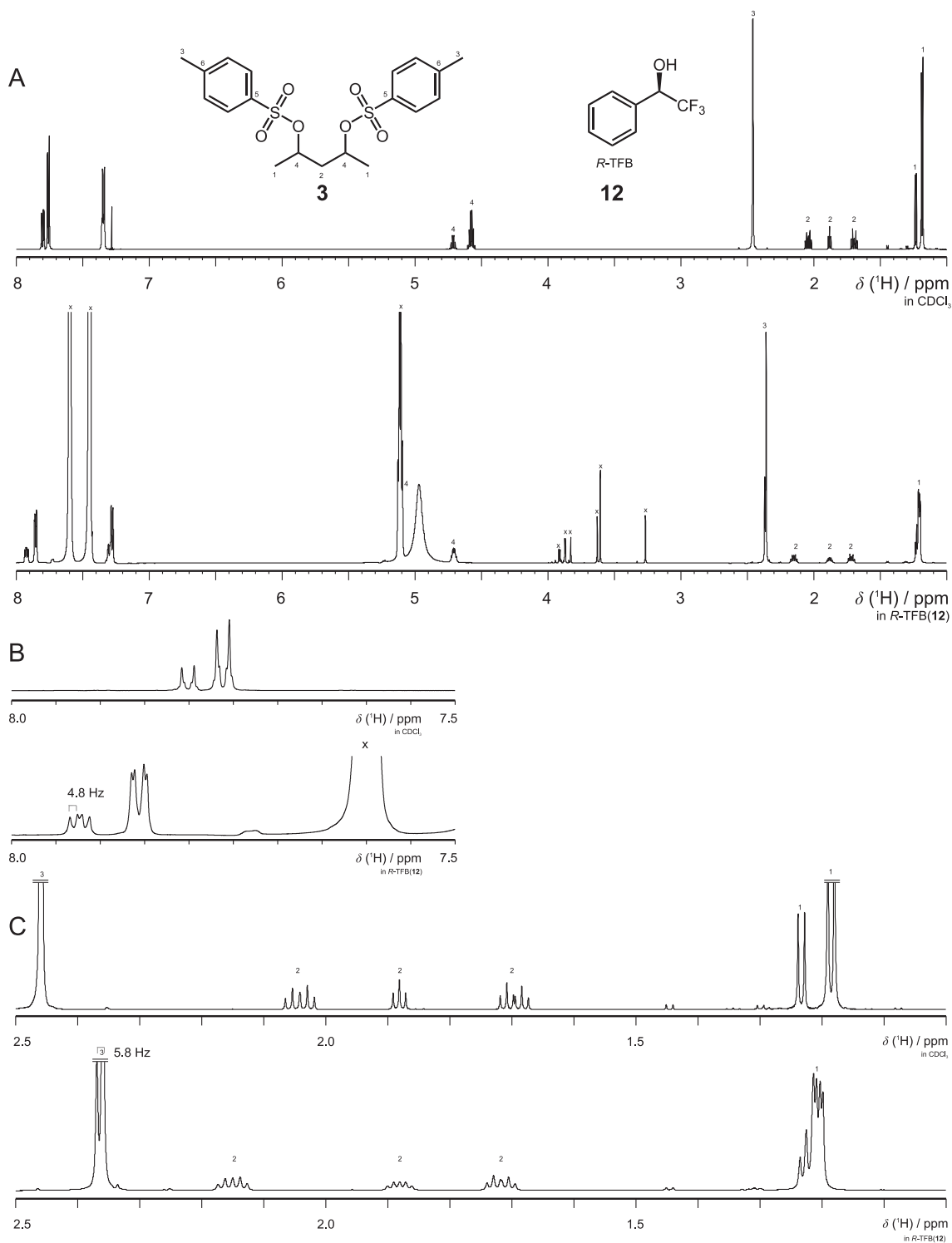
Figure 12.1: Proton spectra of **3** in CDCl₃ and *R*-TFB (A). Details given in (B) and (C) show a comparison for a number of signals. Some of the signal sets are doubled due to the interaction with the chiral solvent (B and C). A corresponding difference in the chemical shift is given in (B) for one of the aromatic signals. Signals originating from the solvent and impurities are labelled with "x".
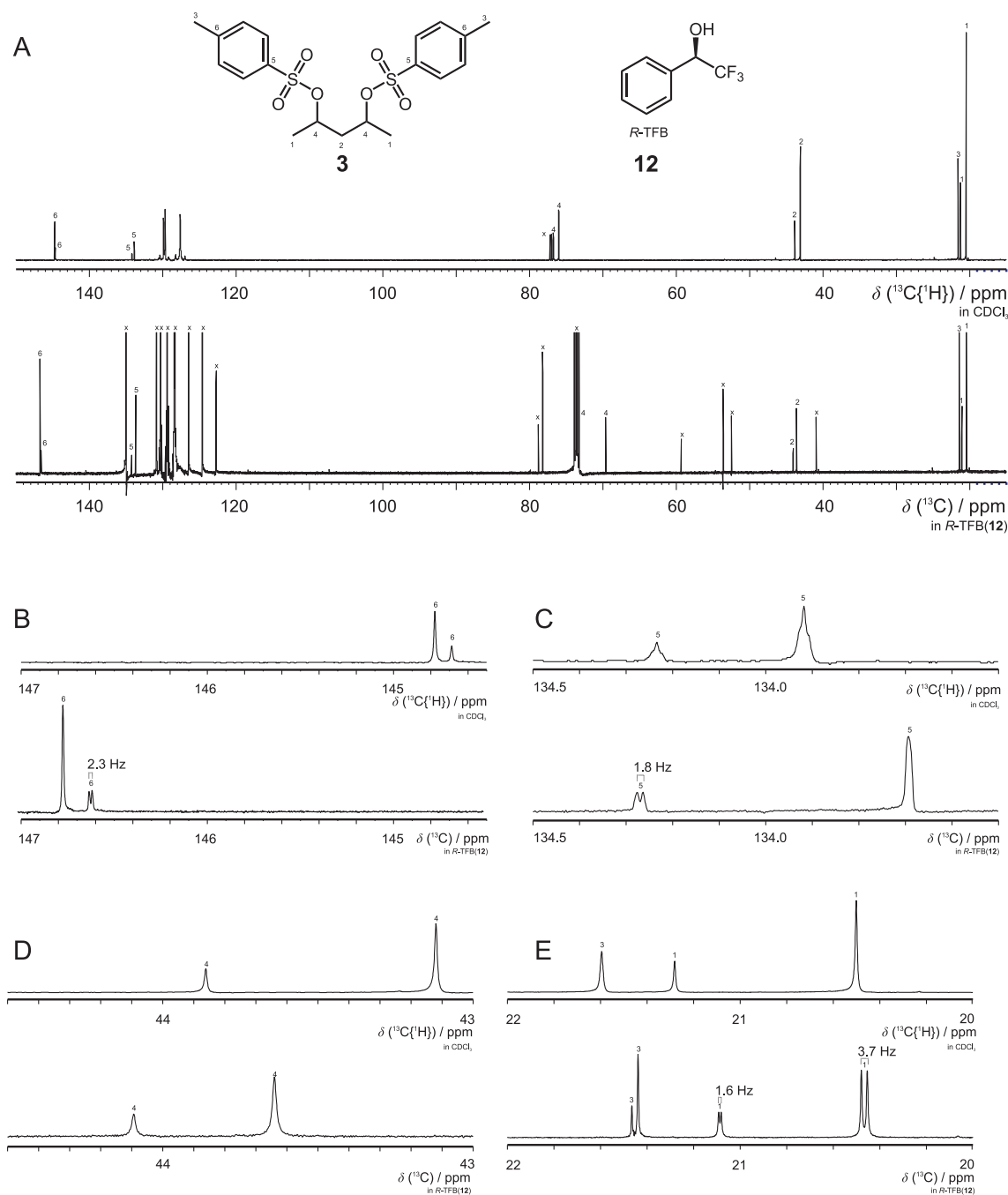
Figure 12.2: Carbon spectrum of **3** in CDCl$_3$ and *R*-TFB (A). Details given in (B-E) are shown for better comparison. Some of the signal sets are broadened or doubled due to the interaction between the analyte with the chiral solvent (B-E). Differences in the chemical shifts are given in Hz. The carbon signal of the methyl group *1* shows the highest difference (E). Signals originating from the solvent and impurities are labelled with "x".
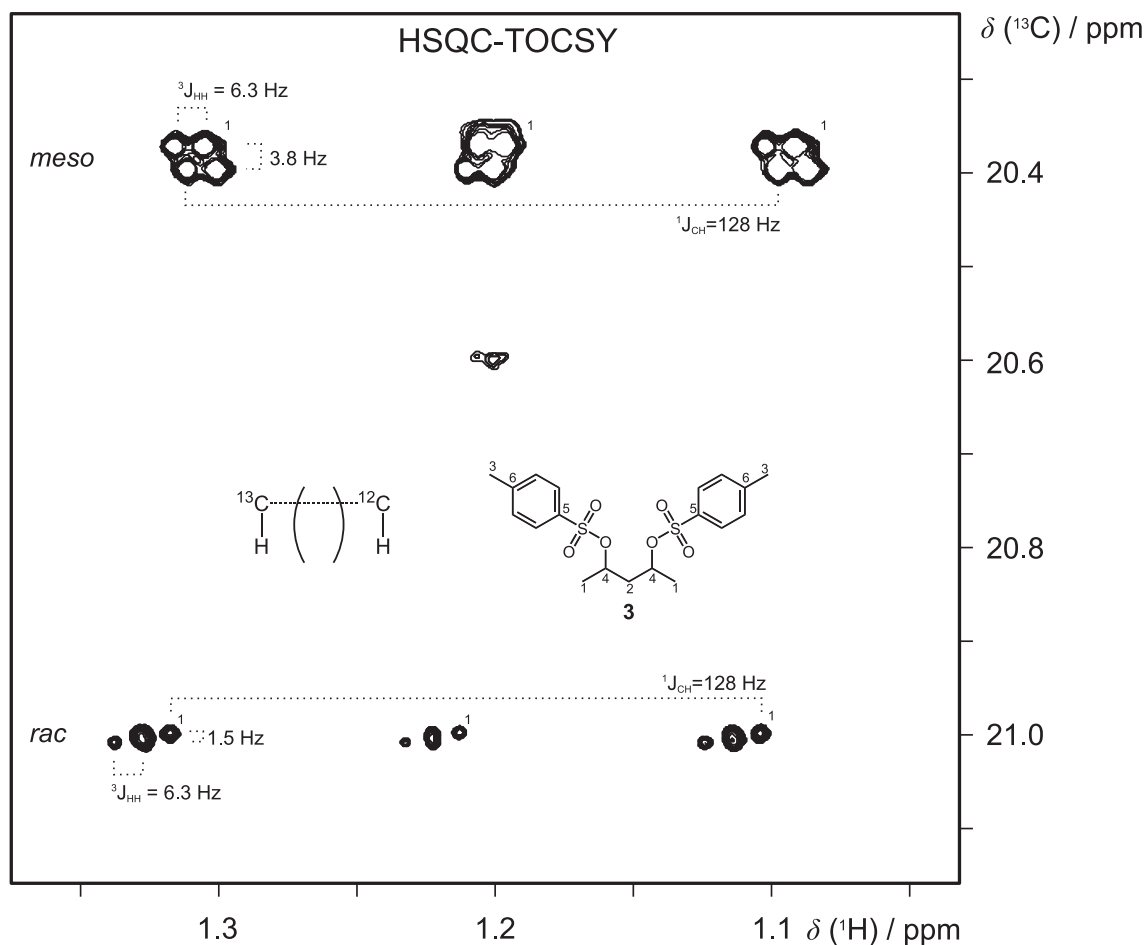
Figure 12.3: HSQC-TOCSY spectrum of **3** in *R*-TFB recorded using the pulse sequence given in Fig. 11.7B. TOCSY correlations between equivalent methyl groups *1* are obtained in the center of the $^1J_{CH}$ doublets as the correlation involves a ^{13}C and a ^{12}C bound proton. The tilt of the cross peak reveals whether the molecule contains identical or opposite stereogenic centers. The $^1J_{CH}$ doublets close to $\delta(^{13}C)$=20.4 ppm have an opposite tilt compared to the central TOCSY peak and are assigned to the *RS* isomer (*meso*). All peaks at $\delta(^{13}C)$=21.0 ppm have an identical tilt and are assigned to the *RR* and *SS* isomers (racemic mixture).

SS is identical. This is assigned because the initial group gives rise to the $^1J_{\text{CH}}$-coupled doublet that has the same tilt as the correlated TOCSY signal.

In the same way, the *meso* isomer (RS) is assigned to the signals at $\delta(^{13}\text{C})$=20.4 ppm. Magnetization that starts from the initial center (the $^1J_{\text{CH}}$ doublet) results in a TOCSY correlation peak with inverse tilt.

12.2.3 Discussion

Though it is expected that anisochronous chemical shifts are readily obtained for equivalent groups in the chiral solvent R-TFB **3**, the ^{13}C spectrum (Fig. 12.2) reveals only small effects. For most of the equivalent groups, only the u or the l species reported inequivalent chemical shifts. For the considered analyte **3** all isomers give inequivalent shifts for the methyl group *1* and the assignment is based on this signals. But in principle any other signal with inequivalent chemical shifts could be used as long as TOCSY correlations can be acquired.

Analyte **3** being a typical small molecule with not directly neighboured stereogenic centers and rotational flexibility around the σ-bonds, the assignment of (u/l) isomers may pretend on some generality for other natural products or synthetic compounds.

Sharp lines are obtained in the chiral liquid solvent R-TFB **3** enabling the possibility to resolve various molecular sites that can potentially be used for the assignment procedure. If low intensity peaks are obtained due to the limited availability or solubility of the analyte, presaturation techniques can be employed on the solvent signals.

Finally, it is concluded that in most cases the use of chiral solvents is better suited than the use of the liquid crystal PBLG for the assignment of (u/l) isomers because of the higher homogeneity of the samples and because of larger changes in the chemical shifts.

12.3 2,5-Hexanediol 14

12.3.1 Sample Preparation and 1D Experiments

R-TFB **3** and 2,5-hexanediol **14** (mixture of the isomers) is purchased from Sigma-Aldrich, Germany. Using a 3 mm tube, a sample containing 5 μl 2,5-hexanediol **14**, 5 μl benzene-d_6 and 140 μl R-TFB is prepared.

A Bruker 600 MHz Avance III spectrometer (Rheinstetten, Germany) equipped with an inverse ^{1}H,^{13}C,^{15}N-triple resonance cryogenically cooled probehead is used. The temperature is set to 320° K. HSQC and HSQC-TOCSY experiments with 4k complex data points in the directly detected dimension and with 256 t_1-increments for the indirect dimension is acquired. The number of scans for each t_1 increment is two (HSQC) or 8 (HSQC-TOCSY). TOCSY experiments with 200 ms MOCCA-xy16 [148] mixing and a corresponding 180° pulse length of 40 μs is applied. Spectra are apodized using 90° phase shifted squared sine bell functions with line width coefficient of zero Hz in both dimensions. No presaturation of the solvent signals is employed.

It is observed that carbon lines belonging to 2,5-hexandiol **14** are approximately 0.4 Hz broader compared to other signals originating from various impurities found in the solvent. By changing the temperature from 280°K to 340°K in increments of 10° K it is observed that the sharpest lines and highest signal-to-noise-ratio is obtained for 320° K. A stable and homogeneous magnetic field is found to be crucial for the experimental setup. The sample is locked to benzene-d_6 and is equilibrated for approximately 1h at 320° K and the sample is shimmed using Brukers 1D topshim-routine. Off-axis shims are further shimmed manually according to the lock signal. Finally, the sample is shimmed using a continuous
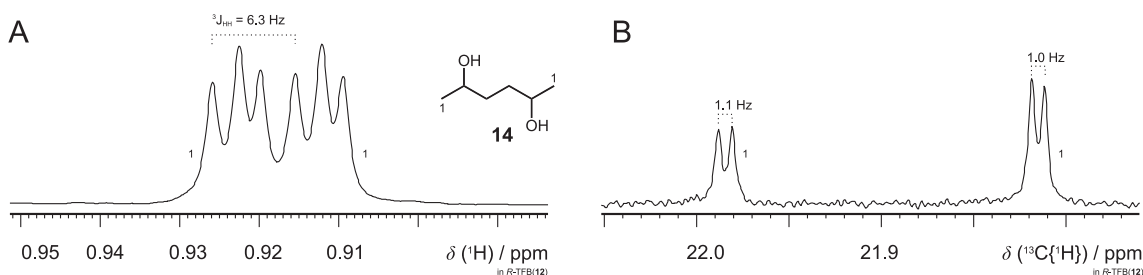
Figure 12.4: ^{1}H (A) and ^{13}C{^{1}H} (B) signals of the methyl group of 2,5-hexanediol **14** measured at 320° K in *R*-TFB **3**. The proton spectrum shows several superimposed signals that are split to doublets due to $^3J_{HH}$-couplings. The carbon spectrum (B) reveals distinct signals for the (*u/l*) isomers. Upon the interaction to the chiral solvent, signals for each distinct stereogenic center are obtained that are separated by approximately one Hz for both species. Differences observed are important for the correlation and assignment of (*u/l*) isomers.

train of ^{1}H experiments with an acquisition time of approximately 1.2 s and a relaxation delay of 10 ms.

A part of the aliphatic region is enlarged in Fig. 12.4A,B and shows the signals which are assigned to the methyl groups *1* of 2,5-hexandiol **14**. A number of superimposed doublets with $^3J_{HH} = 6.3$ Hz is obtained in the proton spectrum indicating fast rotation of the methyl group. The carbon spectrum is more resolved and reveals distinct signals for the *meso* isomer and the chiral isomers. The signals further derivatize upon the interaction to the chiral solvent so that for each species (*u/l*) two signals are obtained that are separated by approximately one Hz. Apart from that, signal patterns obtained are very similar to the pattern of the methyl groups in 2,4-ditosyl pentanediol **3** (Section 12.2.2). The methyl group is found to be most suitable for the assignment of the isomers (see Section 12.3.4 for details).

12.3.2 HSQC Experiment

Using the HSQC experiment given in Fig. 11.7 the signals that are separated by approximately one Hz in the carbon dimension (Fig. 12.4B) are not resolved in the indirect dimension (data not shown). And it is observed that the FID in the indirect dimension is decayed after approximately 1/3 of the coherence lifetime that is observed in the 1D ^{13}C{^{1}H} experiment. Accordingly it is assumed that the decay of antiphase (2D experiment, indirect dimension) and inphase carbon coherence (1D experiment) can not be assumed to be equivalent.

To avoid that, additional refocusing delays with centered 180° pulses are added after the first and before the second INEPT element to obtain inphase magnetization that evolves in the indirect dimension. Waltz64 decoupling is used for decoupling during t_1. (Note that synchronous decoupling is needed in order to not annul artifact cancellation by phase cycling). The resulting HSQC spectrum is shown in Fig. 12.5A. Signals in the indirect dimension are resolved as they are in the 1D experiment. The sum of the projection of the columns is superimposed with the 1D ^{13}C{^{1}H} and similar line widths are found (data not shown). This suggest that HSQC experiments work well, if they rely on the t1 encoding of inphase magnetization, as the 1D ^{13}C experiment does.

In the direct dimension, the HSQC experiment effectively avoids the overlap that is observed in the proton spectrum (Fig. 12.4A). The differences in the proton chemical shifts

for equivalent signals are determined to be 3.8 Hz and 0.1 Hz, respectively. As a result, both sets of signals are tilted to the right.

12.3.3 HSQC-TOCSY Experiment

Also the HSQC-TOCSY experiment given in Fig. 11.7 is extended by additional spin-echo elements to obtain inphase evolution of ^{13}C signals in the indirect dimension (see Chap. 12.3.2) to assure line widths that are comparable to the 1D ^{13}C$\{^1$H$\}$ signals.

The resulting spectrum is shown in 12.5B. TOCSY correlation peaks are obtained in the centers of the $^1J_{\text{CH}}$-doublets. The mixture of the chiral isomers (RR and SS) is assigned to the multiplets at $\delta(^{13}$C$)$=21.98 ppm since the chemical surrounding for either R in RR or S in SS is identical. The tilt of the correlation peak must be equal to the tilt of the originating $^1J_{\text{CH}}$-doublet.

The *meso* isomer (RS) is assigned to the signals at $\delta(^{13}$C$)$=21.81 ppm. Magnetization originating from the initial $^1J_{\text{CH}}$-doublet is transfered across the symmetry center to the equivalent group at the other side of the molecule and the magnetization evolves under a differente chemical surrounding, which results in an inverse tilt of the peak.

In both cases, the signals can be unambiguously assigned to either the u or the l isomer.

12.3.4 Discussion

As described in the foregoing Section, a homogeneous sample, good shims and long coherence lifetimes are needed to resolve small differences in chemical shifts that are obtained due to the analytes interaction with the chiral solvent. Differences in chemical shifts are always small, and usually <5 Hz (for both, ^{13}C and ^{1}H).

Also HSQC signals resulting from the $^2J_{\text{CH}}$ signals are observed and can in principle be used for the analysis. Since the magnitude of the $^2J_{\text{CH}}$ coupling is on the order of the $^3J_{\text{HH}}$ couplings they may superimpose and obscure the weaker TOCSY signals. In this case an additional INEPT element, which transfers $^2J_{\text{CH}}$ magnetization into non-detectable double/zero quantum coherence, can be added after the TOCSY mixing time.

Small differences observed in the chemical shifts of the different stereogenic centers limit the usability of available groups as well. Practically, methyl groups are found to be best suited. Moieties that are split into broad multiplets due to $^nJ_{\text{HH}}$ couplings result in broad multiplets. Acquisition of inphase carbon coherence while WALTZ64 decoupling is enabled is essential. If the proton multiplets are broad (e.g. filling the whole $^1J_{\text{CH}}$ doublet) decoupling in the proton dimension may be required. In such a case a ^{13}C detected HSQC-like experiment can be considered. Such an experiment would start with proton magnetization on the remote, ^{12}C bound, proton. This magnetization evolves during t_1 on protons while selective decoupling (Chap. 10) is applied to carbon. Using TOCSY, the magnetization is transferred to the equivalent, ^{13}C containing moiety and carbon antiphase is created which is refocused to inphase and acquired while protons are decoupled using WALTZ64.

Beside that, the TOCSY correlation step is found to be uncritical for the present analyte. The same may be assumed for other analytes that share the motive of a connected proton spin chain. Problems in the TOCSY correlation are expected if the spin chain is interrupted. This is observed for molecules containing quarternary carbons, e.g. triple bonds.

Methyl groups in isopropyl moieties are problematic for the discussed approach, since the dominant signal that is obtained after the TOCSY transfer is due to the correlation within
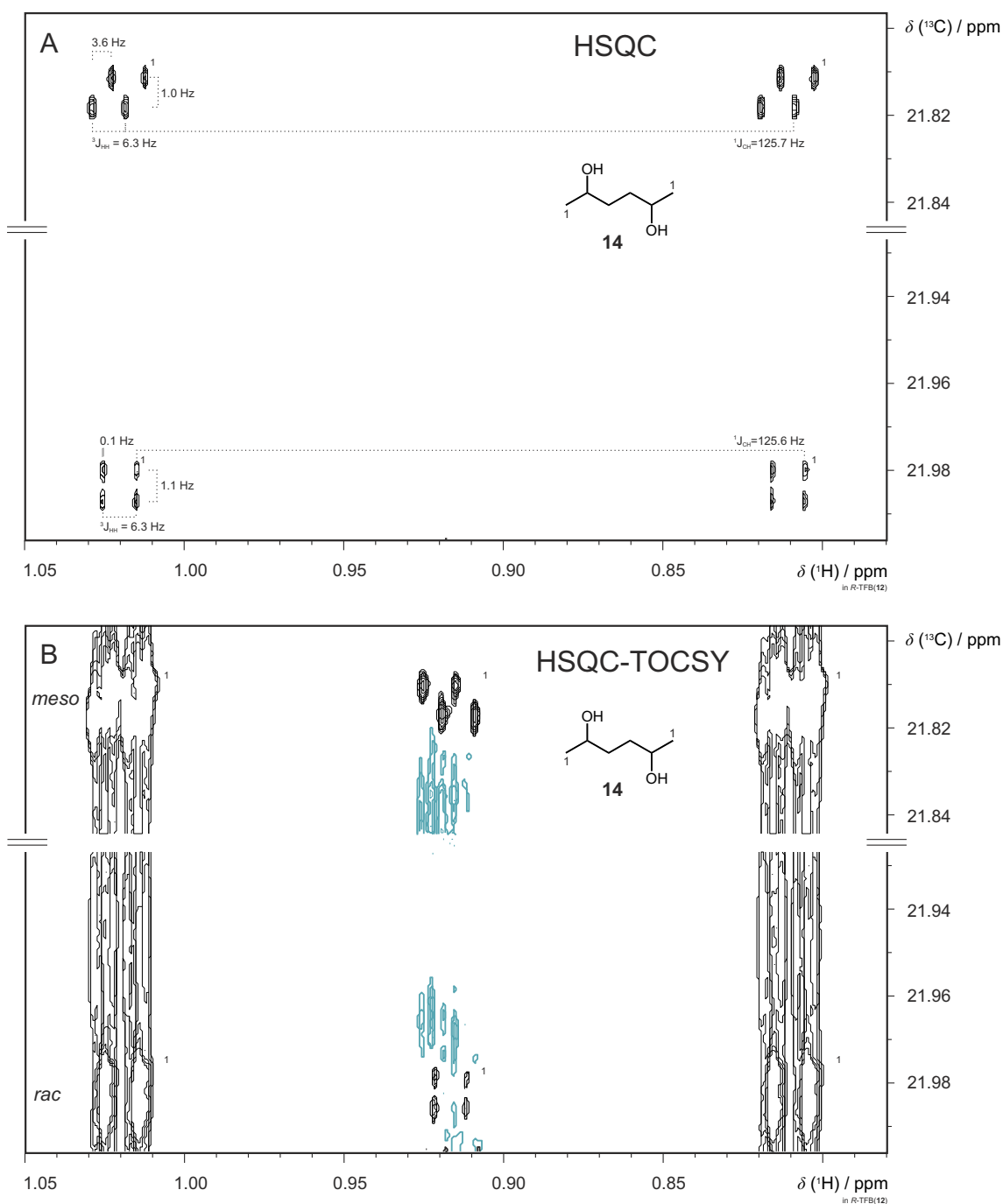
Figure 12.5: HSQC (A) and HSQC-TOCSY (B) spectra of 2,5-hexanediol **14** measured at 320° K in *R*-TFB **3**. Pulse sequences used are similar to the ones presented in Fig. 11.7, except that additional spin echo elements, with $\Delta = 1/(4^1 J_{\mathrm{CH}})$, are added after the first and before the second INEPT element to assure inphase evolution in the indirect dimension, while WALTZ64 decoupling is applied on protons. This is found to be required in order to resolve the signals of the carbon dimension (Fig. 12.4B). In the chiral solvent, the two methyl groups in **14** are not equivalent and give rise to distinct signals. Differences in the chemical shift of 0.1-3.8 Hz are resolved in the HSQC experiment (A). A tilt of the TOCSY peak (B) that is identical to the $^1 J_{\mathrm{CH}}$ peaks indicates the chiral isomers, while an inverse tilt assigns the *meso* isomer.

the isopropyl group. The tilt of that correlation peak equals the tilt of the $^1J_{CH}$ signals. Surprisingly, this TOCSY correlation peak appeared to be additionally split into a doublet in the direct dimension. The value is approximately 6 Hz. This signal is extinguished by using an additional INEPT element (calibrated to 6 Hz) after the TOCSY to create heteronuclear double/zero quantum coherences (data not shown). It may be concluded that the discussed artifact is due to a $^nJ_{CH}$-coupling (with $n < 5$). Because of this, isopropyl groups can be assumed to be useful in the process of assigning (u/l) isomers.

12.4 Summary

The unambiguous assignment of the *meso* isomer and the chiral isomers is inaccessible by achiral solution NMR methods.

In chapter 11 it is shown that NMR spectroscopy in chiral liquid crystalline media is only of limited usefulness in the context of the problem statement since a special electronic structure, present in tartaric acid derivatives, is exploited to accomplish the analysis. The approach is not possible for other analytes.

As an alternative, the current chapter describes the use of chiral solvents. It is shown that equivalent groups to the right and the left of the symmetry center give rise to distinct signals that can be resolved in ^{1}H,^{13}C-correlation experiments. Differences are larger compared to data obtained from liquid crystalline samples. Another importent property found for chiral solvents is the narrow line width that is found throughout all experiments.

Signals, which are obtained from the mixture of the isomers are successfully assigned to either the *meso* or the chiral isomers.

13. Synthesis of Poly(γ-benzyl-L-glutamate) (PBLG)

13.1 Motivation and Introduction

The discrimination of enantiomers by analytical means is an interesting challenge and of high importance since the biological effects of enantiomers may not be identical. Frequently, it is observed that biological active natural products consist of one enantiomer only. Any synthesis that facilitates this product relies on information about the absolute stereochemical configuartion.

Conventional methods to assign the absolute configuration of chiral substances include ECD, X-ray diffraction and NMR analysis using Mosher esters and similar chemical derivatives. In achiral solution and without chemical ligation the absolute configuration of substances is unattainable with NMR spectroscopy.

Only in the past 10 years the *ab initio* calculation of chiroptical spectral information afforded the determination of the absolute configuration without the need to chemically ligate the substance under study [150]. Most common methods include electronic circular dichroism (ECD), optical rotation dispersion (ORD), Raman optical activity (ROA) and vibrational circular dichroism (VCD) [151]. Chiroptical methods are currently the method of choice concerning the determination of chiral substances.

In this context, the nevertheless not less important role of NMR spectroscopy is, so far, the relative assignment of stereoisomers to reduce the number of possibilities in order to facilitate a reliable chiroptical prediction of spectral data.

As outlined in Chap. 11, NMR spectroscopy is capable of resolving enantiomers if a chiral dissolvent or orientation media is used. For example differences in RDCs measured upon the analytes interaction with PBLG are in most cases highly significant and easy to obtain. Only the *ab initio* calculation of experimental data (e.g. RDCs) is so far not reported.

Actually, the calculational methods are the sticking point that restricts the application of NMR spectroscopy in the analysis of chiral substances. For example the *ab initio* calculation of RDCs would probably require MD simulations of the liquid crystal PBLG and its interaction with the analyte for a time that is long enough to ensure the proper average of the dipolar parameters. This conceptually simple plan critically relies on the correct behaviour of the force field and the setup of the MD. The approach can only be
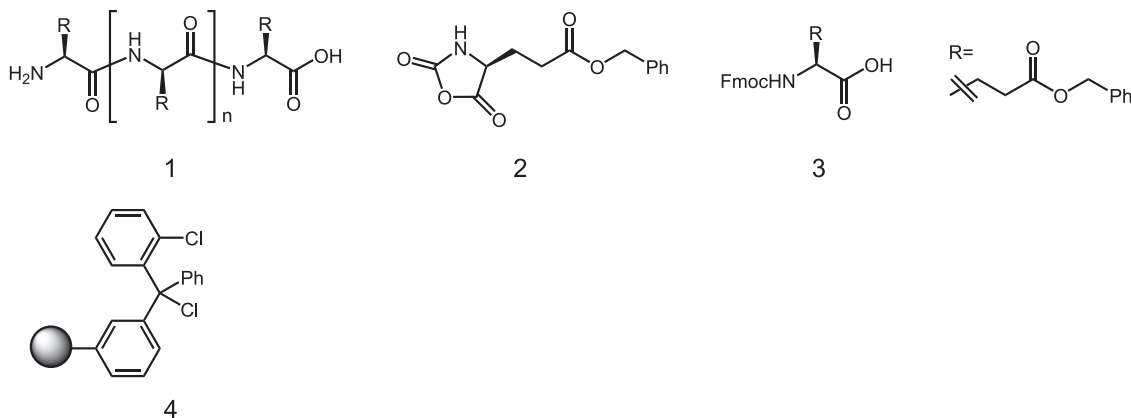
Figure 13.1: Poly(γ-benzyl-L-glutamate) (PBLG) **1**. The synthesis of **1** for $n = 29$ is aspired. N-carboxyanhydrides (NCAs) **2** are used for the ring opening synthesis of **1**. The Fmoc protected and benzyl protected glutamic acid **3** is used for solid phase peptide synthesis using 2-chlorotrityl-chlorid-resin **4** as the solid support.

successful if the simulation provides a realistic scenario for all aspects of steric, electronic and dynamic interactions between the analyte and the chiral dissolvent.

Accordingly, any information about the kind of interaction between the PBLG and the analyte can help to constrain the MD simulation in a way to drastically reduce the amount of complexity. Unfortunately, nothing is known to the best of the present knowledge, about the characterization of analyte-PBLG-interactions. This might also be due to PBLG being a polypeptide that is used with a molecular weight of 150,000-350,000 g/mol. Polymers often complicate NMR measurements due to their molecular weight which reduces the molecular tumbeling and increases the dephasing of NMR signals.

To study the discussed interactions short PBLG oligomers are synthesized that can be characterized by solution state NMR methods.

13.2 Synthesis

PBLG **1** is usually synthesized from N-carboxyanhydrides (NCAs) **2** using a ring opening polimerizations (ROP) [152].

Also the synthesis based on solid phase peptide synthesis is reported [152]. Since a polypeptide with 20-30 residues is aspired and the incorporation of isotopically labelled amino acids may be needed at a later point of time to address a certain position within the polymer by means of NMR spectroscopy it is decided to pursue a solid phase peptide synthesis.

Special care is taken to choose an appropriate solid support since the benzyl ester in the side chain should be stable under the conditions that are used to cleave the final product from the resin. Benzyl esters are reported to be stable for ph>1.0 [153]. A solid support suitable for mild cleavage (approximately 1% TFA in CH_2Cl_2) is the 2-chlorotrityl-chlorid-resin **4** (purchased from Sigma-Aldrich, Germany)

Loading the amino acid on the solid support
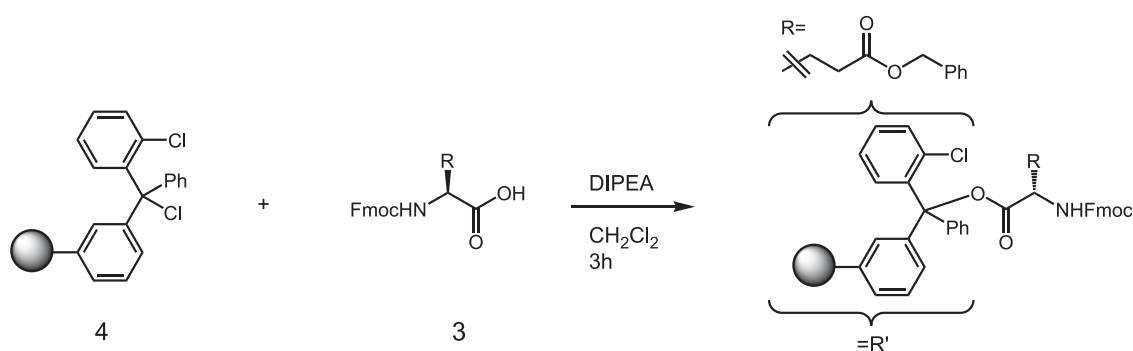
Figure 13.2: The solid support **1** is loaded with the protected amino acid **3**.

193 mg of the resin containing approximately 250 μMol active chloride functionalities are balanced and swollen in dry CH_2Cl_2. Three equivalents (344 mg, 750 μMol) of the Fmoc protected amino acid **3** (purchased from Sigma-Aldrich, Germany) and three equivalents (193 mg, 750 μMol) of DIPEA are added. The mixture is shaken at room temperature for 3h.

Fmoc cleavage
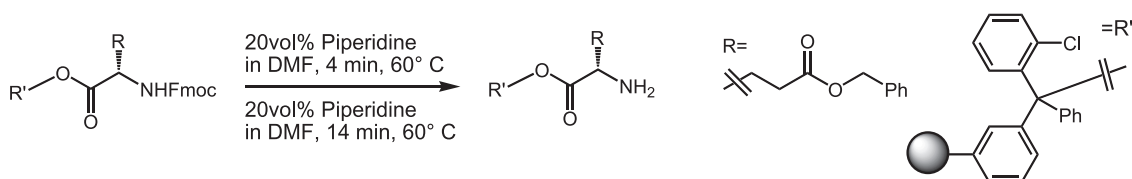
Figure 13.3: The Fmoc protection group is removed using a solution of piperidine in DMF.

The resin is washed three times with DMF. To remove the Fmoc protection group, a solution of 20vol% piperdine (purchased from Roth GmbH, Germany) in DMF is added. The resin is shaken for 4 min. at 60° C for all following deprotection and coupling steps since PBLG is known to form a white, insoluble precipitate in DMF at room temperature. The deprotection mixture is replaced by a fresh solution and the resin is shaken for additional 14 min. at 60° C. The resin is washed five times with approximately 3.0 ml of DMF.

Coupling of the amino acid
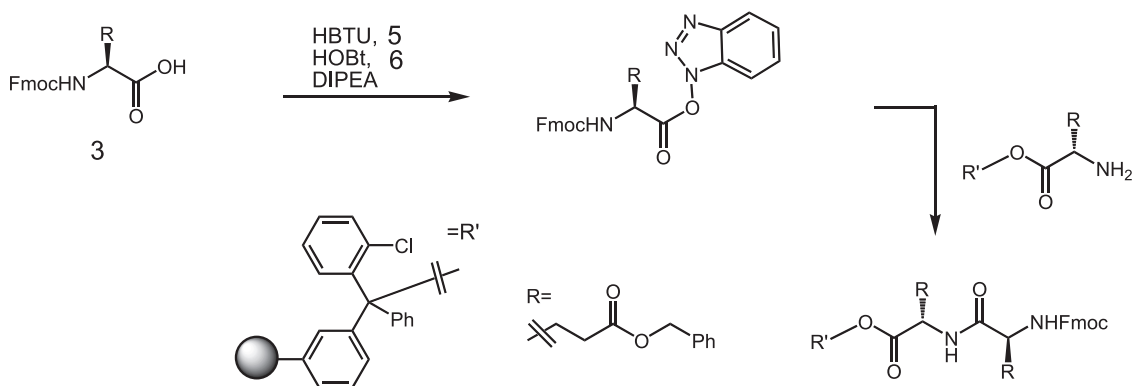
Figure 13.4: The protected amino acid **3** is activated using the coupling reagent HBTU **5**. An active ester is formed with **6**. The activated amino acid is used for the elongation of the polymer chain.

Three equivalents (344 mg, 750 μMol) of the Fmoc protected amino acid **3** are mixed with a solution of three equivalents (285 mg, 750 μMol) of HBTU **5** (purchased from Iris Biotech GmbH), three equivalents (101.3 mg, 750 μMol) of HOBt **6** (purchased from Iris Biotech GmbH) and 6 equivalents (193 mg) of DIPEA (purchased from Iris Biotech GmbH). The resin is shaken with the solution for 30 min at 60° C. The resin is washed five times with approximately 3 ml of DMF.

Cleavage

The resin is washed with CH_2Cl_2 and MeOH and dried under reduced pressure. The cleavage mixture is prepared from CH_2Cl_2 containing 1vol % of TFA (purchased from VWR) and 0.5 vol% H_2O. The cleavage mixture is shaken with the resin at room temperature for approximately 1 hour. The filtrate is evaporated in a nitrogen stream and the oily residue is precipitated with cold Et_2O. The precipitate is centrifuged, washed with Et_2O and dried using a nitrogen stream.

In total 31 residues are coupled. The molecular weight of the resulting polymer is calculated to be 31*219.236+18.015=6,814.331 g/mol and the exact mass expected in the mass spectrum is 31*219.089+18.011=6,809.786 g/mol.

Yield

Before cleavage, the dry resin is balanced and the weight is compared to the weight of resin that is used for the synthesis. After the synthesis the weight is icreased by 57 mg. This is considerably less than the expected increase of 1.7 g (250 μMol*6,814 g/mol). After cleavage a dry substance with approximately 50 mg is obtained.

13.3 Analysis and Discussion

The obtained substance forms a jelly liquid on contact with $CHCl_3$. Because of the apolarity and the high weight, characterization by LCMS is not successful. Earlier stages are analysed after removal of the side chain protective groups with LCMS.

The exact mass is not found in the MALDI spectra.

Either the number of growing polymer chains on the resin is much lower than expected or the elongation process does not happen as planned. The used resin could be deactivated by

moisture. To exclude that, the synthesis is repeated with resin that had glycine preloaded by the supplier as the first amino acid. Also this synthesis does not afford more product.

Reasons for the abortion of the chain growth may be due to the formation of an α-helical structure. It is reported [154] that PBLG forms an α-helix in DMF. This is usually accompanied with the formation of hydrogen bonds that can prevent the chain from growing and is a well known problem in solid phase peptide synthesis. In such a situation a microwave assisted synthesis and the application of double coupling steps might improve the result.

13.3.1 NMR Measurements on Low Weight PBLG

Two samples of PBLG are prepared. One containing 40 mg of a mixture of short chain PBLG and the other containing 40 mg of commercially available PBLG with a molecular weight of 30,000-70,000 g/mol. 500 μl of CDCl$_3$ are added and the tubes are sealed. Both samples provide an immobile gel.

A Bruker 600 MHz Avance III spectrometer (Rheinstetten, Germany) equipped with an inverse ^{1}H,^{13}C,^{15}N-triple resonance cryogenically cooled probehead is used. 4k complex data points are acquired in the directly detected dimension with 512 t_1-increments for the indirect dimension in the HSQC experiments. Spectra are apodized using 90° phase shifted squared sine bell functions in both dimensions. The temperature is 298° K.

Results for the ^{1}H,^{13}C-HSQC experiments are shown in Fig. 13.5. The spectrum obtained from the short chain PBLG (Fig. 13.5, black) shows a large number of impurities in the aliphatic and aromatic region. Although only very little material is obtained signals are found that overlay with signals obtained from the commercial product (shown in red).

Because of the small quantity of received material, it is concluded that the desired 31-mer is not obtained. Nonetheless, shorter equivalents may be present that result in signals also found in the spectra of the commercially available PBLG. The signals can be attributed to the molecular sites of PBLG (Fig. 13.5, green numbers).

Beside that, the line widths of the spectra of the discussed samples are very similar. This is surprising when considering the differences in size of the used polymers and may be due to the low viscosity and apolarity of the solvent CDCl$_3$ as well as the intrinsic flexibility of the side chains. The backbone might be stiffer and corresponding signals can be broad.

13.4 Summary

Future studies concerning the assignment of the absolute configuration of enantiomers by means of NMR spectroscopy rely on a chiral solvent, e.g. the liquid crystal PBLG. The acquisition of experimental parameters (e.g. RDCs) to distinct the enantiomers is steadily performed.

Beside this, the *ab initio* computation of the spectral properties is so far not described. Accordingly, enantiomers can be discriminated by the experimental data but not assigned to the absolute configuration.

More information about the analyte-PBLG-interaction is desired for a better prediction of spectral data in order to assign the absolute configuartion. Commercially available PBLG has a molecular weight of 30,000-70,000 g/mol. The question whether this polymer is suitable to study the analyte-PBLG-interactions or whether lighter PBLG-analogues are preferable is the motivation on the synthesis of a PBLG chain with 31 residues.

Though the intended 31-mer is not obtained, the synthesis yields a mixture of shorter analogues. The obtained material is studied using a ^{1}H,^{13}C-HSQC experiment. Despite
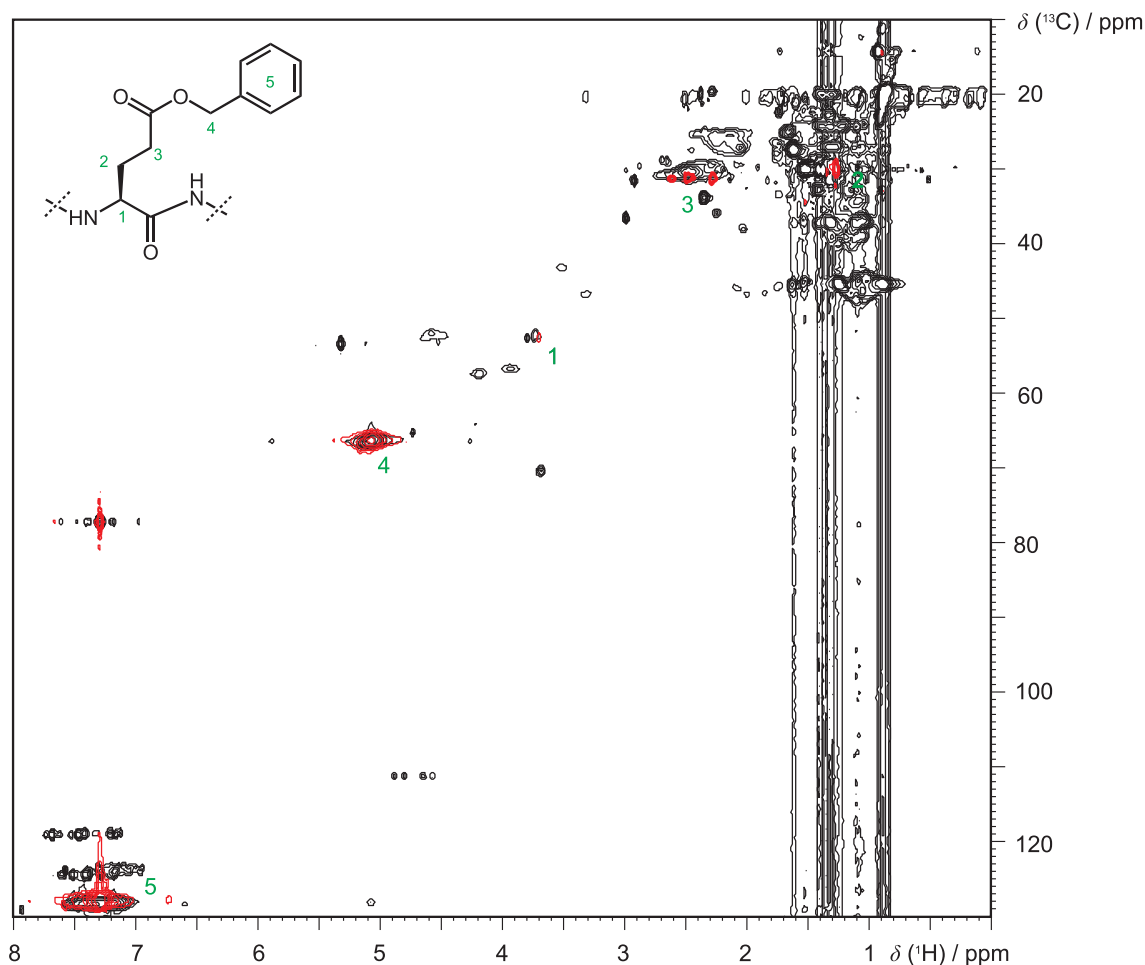
Figure 13.5: t_1, t_2 decoupled ^{1}H,^{13}C-HSQC spectra of the short chain PBLG (40 mg in 500 μl CDCl$_3$) obtained by the described synthesis (black). Signals resulting from various impurities are detected. Corresponding spectrum of 15 mg of commercially available (Sigma-Aldrich, Germany) PBLG with a molecular weight of 30,000-70,000 g/mol in 600 μl CDCl$_3$ (red). Though it is expected that the synthesis did not yield the desired 31-PBLG-mer, but instead a distribution of shorter equivalents, signals obtained are similar to the ones from the commercial sample. Because of the high molecular weight it is assumed that shorter analogues are preferrable. The synthesis of a lighter analogue is carried out. Surprisingly, line shapes in the present HSQC spectra are quite comparable so that the commercially available PBLG might be suitable for future NMR studies.

the enormous difference in size between the short chain PBLG and the commercially available PBLG (30,000-70,000 g/mol), it is found that NMR properties are very similar. The reason for this might be attributed to the intrinsic flexibility of the side chains, which causes comparable relaxation rates.

Bibliography

[1] http://de.wikipedia.org/wiki/Lagrange-Multiplikator .

[2] L. S. Pontryagin, V. G. Boltyanskii, R. V. Gamkrelidze, E. Mischenko, The Mathematical Theory of Optimal processes, *Interscience Publishers* **1962**.

[3] N. Khaneja, T. Reiss, C. Kehlet, T. Schulte-Herbrüggen, S. J. Glaser, Optimal control of coupled spin dynamics: design of NMR pulse sequences by gradient ascent algorithms, *J. Magn. Reson.* **2005**, *172*, 296–305.

[4] M. H. Levitt, Spin Dynamics, Basics of Nuclear Magnetic Resonance, *John Wiley and Sons, Ltd.* **2008**.

[5] M. A. Janich, R. F. Schulte, M. Schwaiger, S. J. Glaser, Robust slice-selective broadband refocusing pulses, *J. Magn. Reson.* **2011**, *213*, 126–135.

[6] T. E. Skinner, N. I. Gershenzon, M. Nimbalkar, W. Bermel, B. Luy, S. J. Glaser, New Strategies for Designing Robust Universal Rotation Pulses: Application to Broadband Refocusing at Low Power, *J. Magn. Reson.* **2012**, *216*, 78–87.

[7] K. Kobzar, T. E. Skinner, N. Khaneja, S. J. Glaser, B. Luy, Exploring the limits of broadband excitation and inversion, *J. Magn. Reson.* **2004**, *170*, 236–243.

[8] K. Kobzar, T. E. Skinner, N. Khaneja, S. J. Glaser, B. Luy, Exploring the limits of broadband excitation and inversion: II. Rf-power optimized pulses, *J. Magn. Reson.* **2008**, *194*, 58–66.

[9] K. Kobzar, S. Ehni, T. E. Skinner, S. J. Glaser, B. Luy, Exploring the limits of broadband 90° and 180° universal rotation pulses, *J. Magn. Reson.* **2012**, *225*, 142–160.

[10] S. Machnes, U. Sander, S. J. Glaser, P. de Fouquières, A. Gruslys, S. Schirmer, T. Schulte-Herbrüggen, Comparing, Optimising and Benchmarking Quantum Control Algorithms in a Unifying Programming Framework, *Phys. Rev. A* **2011**, *84*, 022305.

[11] P. de Fouquières, S. G. Schirmer, S. J. Glaser, I. Kuprov, Second Order Gradient Ascent Pulse Engineering, *J. Magn. Reson.* **2011**, *212*, 412–417.

[12] I. Kuprov, C. T. Rodgers, Derivatives of spin dynamics simulations, *J. Chem. Phys.* **2009**, *131*, 234108.

[13] M. Koos, Pulssequenzoptimierung mittels Optimal Control Theory, *diploma thesis, KIT* **2011**.

[14] T. O. Levante, T. Bremi, R. R. Ernst, Pulse-Sequence Optimization with Analytical Derivatives. Application to Deuterium Decoupling in Oriented Phases, *J. Magn. Reson. Series A* **1996**, *121*, 167–177.

[15] U. Sander, Numerical and Algebraic Studies for the Control of Finite-Dimensional Quantum Systems, *Ph.D. thesis, TU München* **2010**.

[16] S. W. J. Nocedal, Numerical optimization, *New York: Springer* **1999**.

[17] A. Wächter, L. T. Biegler, On the Implementation of a Primal-Dual Interior Point Filter Line Search Algorithm for Large-Scale Nonlinear Programming, *Mathematical Programming* **2006**, *106(1)*, 25–57.

[18] M. R. Hestenes, E. Stiefel, Methods of conjugate gradients for solving linear systems, *J. Res. natl. Bur. Stand.* **1952**, *49(6)*, 409–436.

[19] R. Tycko, H. M. Cho, E. Schneider, A. Pines, Composite pulses without phase distortion, *J. Magn. Reson.* **1986**, *61*, 90–101.

[20] H. Cho, A. Pines, Iterative maps for broadband excitation of transverse coherence in two level systems, *J. Chem. Phys.* **1987**, *86*, 6591–6601.

[21] L. Emsley, G. Bodenhausen, Optimization of Shaped Selective Pulses for NMR Using a Quaternion Description of Their Overall Propagators, *J. Magn. Reson* **1992**, *97*, 135–148.

[22] A. J. Shaka, A. Pines, Symmetric phase-alternating composite pulses, *J. Magn. Reson.* **1987**, *71*, 495–503.

[23] D. Brown, Constant amplitude broadband refocusing pulses from numerical optimization, *Magn. Reson. Chem.* **2011**, *49*, 705–709.

[24] C. K. Anand, A. D. Bain, A. T. Curtis, Z. Nie, Designing optimal universal pulses using second-order, large-scale, non-linear optimization, *J. Magn. Reson.* **2012**, *219*, 61–74.

[25] H. Geen, R. Freeman, Band-Selective Radiofrequency Pulses, *J. Magn. Reson* **1991**, *93*, 93–141.

[26] S. Odedra, S. Wimperis, Use of composite refocusing pulses to form spin echoes, *J. Magn. Reson.* **2012**, *214*, 86–75.

[27] T. W. Borneman, M. D. Hürlimann, D. G. Cory, Application of optimal control to CPMG refocusing pulse design, *J. Magn. Reson.* **2010**, *207*, 220–233.

[28] M. Garwood, M. Y. Ke, Symmetrical Pulses to Induce Arbitrary Flip Angles with Compensation for Rf Inhomogeneity and Resonance Offsets, *J. Magn. Reson.* **1991**, *94*, 511–525.

[29] N. Khaneja, S. J. Glaser, R. Brockett, Sub-Riemannian Geometry and Time Optimal Control of Three Spin Systems: Quantum Gates and Coherence Transfer, *Phys. Rev. A* **2002**, *65*, 032301.

[30] T. O. Reiss, N. Khaneja, S. J. Glaser, Time-optimal coherence-order-selective transfer of in-phase coherence in heteronuclear IS spin systems, *J. Magn. Reson.* **2002**, *154*, 192–195.

[31] N. Khaneja, S. J. Glaser, Efficient transfer of coherence through Ising spin chains, *Phys. Rev. A* **2002**, *66*.

[32] T. O. Reiss, N. Khaneja, S. J. Glaser, Broadband geodesic pulses for three spin systems: time-optimal realization of effective trilinear coupling terms and indirect SWAP gates, *J. Magn. Reson.* **2003**, *165*, 95–101.

[33] N. Khaneja, T. Reiss, B. Luy, S. J. Glaser, Optimal control of spin dynamics in the presence of relaxation, *J. Magn. Reson.* **2003**, *162*, 311–319.

[34] N. Khaneja, B. Luy, S. J. Glaser, Boundary of quantum evolution under decoherence, *Proc. Natl. Acad. Sci. USA* **2003**, *100*, 13162–13166.

[35] D. Stefanatos, N. Khaneja, S. J. Glaser, Optimal control of coupled spins in the presence of longitudinal and transverse relaxation, *Phys. Rev. A* **2004**, *69*, 022319.

[36] C. Kehlet, Design of optimum liquid-state NMR experiments in the presence of relaxation, *master thesis, TU München* **2003**.

[37] T. O. Reiss, Anwendung der Steuerungstheorie auf die kernmagnetische Resonanzspektroskopie - von der Entwicklung computergestützer Optimierungsmethoden bis zur experimentellen Umsetzung, *Ph.D. thesis, TU München* **2002**.

[38] K. Kobzar, Optimal Control, Partial Alignment and More: The Design Of Novel Tools for NMR Spectroscopy of Small Molecules, *Ph.D. thesis, TU München* **2002**.

[39] G. A. Morris, R. Freeman, Enhancement of nuclear magnetic-resonance signals by polarization transfer, *J. Am. Chem. Soc.* **1979**, *101*, 760.

[40] D. R. Burum, R. R. Ernst, Net Polarization Transfer Via a J-Ordered State for Signal Enhancement of Low-Sensitivity Nuclei, *J. Magn. Reson.* **1980**, *39*, 163.

[41] G. Bodenhausen, D. J. Ruben, Natural abundance nitrogen-15 NMR by enhanced heteronuclear spectroscopy, *Chem. Phys. Lett.* **1980**, *69*, 185.

[42] M. Sattler, J. Schleucher, C. Griesinger, Heteronuclear multidimensional NMR experiments for the structure determination of proteins in solution employing pulsed field gradients, *Progr. NMR Spectrosc.* **1999**, *34*, 93.

[43] K. Hallenga, G. M. Lippens, A Constant-Time ^{13}C,^{1}H HSQC with Uniform Excitation over the Complete ^{13}C Chemical-Shift Range, *J. Biomol. NMR* **1995**, *5*, 59.

[44] F. C.-. refocused multidimensional C-13-edited pulse schemes using broadband shaped inversion, refocusing pulses, *J. Magn. Reson. B* **1996**, *112*, 63.

[45] P. Tzvetkova, S. Simova, B. Luy, PEHSQC: A simple experiment for simultaneous and sign-sensitive measurement of ((1)J(CH)+D-CH) and ((2)J(HH)+D-HH) couplings, *J. Magn. Reson.* **2007**, *186*, 193.

[46] A. Enthart, J. C. Freudenberger, J. Furrer, H. Kessler, B. Luy, The CLIP/CLAP-HSQC: pure absorptive spectra for the measurement of one-bond couplings, *J. Magn. Reson.* **2008**, *192*, 314–322.

[47] S. Wimperis, G. Bodenhausen, Heteronuclear coherence transfer over a range of coupling constants. A broadband-INEPT experiment, *J. Magn. Reson.* **1986**, *69*, 264–282.

[48] G. Bodenhausen, R. R. Ernst, Direct Determination of Rate Constants of Slow Dynamic Processes by Two-Dimensional Accordion Spectroscopy in Nuclear Magnetic-Resonance, *J. Am. Chem. Soc.* **1982**, *104*, 1304.

[49] M. for measurement of intermolecular NOEs by multinuclear NMR spectroscopy: Application to a bacteriophage lambda N-peptide/boxB RNA complex, Zwahlen, C. and Legault, P. and Vincent, S. J. F. and Greenblatt, J. and Konrat, R. and Kay, L. E., *J. Am. Chem. Soc.* **1997**, *119*, 6711.

[50] E. Kupče, R. Freeman, Compensation for spin-spin coupling effects during adiabatic pulses, *J. Magn. Reson.* **1997**, *127*, 36.

[51] W. Krishnan, M. Rance, Influence of Chemical-Exchange among Homonuclear Spins in Heteronuclear Coherence-Transfer Experiments in Liquids, *J. Magn. Reson. A* **1995**, *116*, 97.

[52] S. Meiboom, D. Gill, Modified Spin-Echo Method for Measuring Nuclear Relaxation Times, *J. Magn. Reson.* **1958**, *29*, 688.

[53] H. Y. Carr, E. M. Purcell, Effects of Diffusion on Free Precession in Nuclear Magnetic Resonance Experiments, *Phys. Rev.* **1954**, *94*, 630.

[54] F. A. A. Mulder, C. A. E. M. Spronk, M. Slijper, R. Kaptein, R. Boelens, Improved HSQC experiments for the observation of exchange broadened signals, *J. Biomol. NMR* **1996**, *8*, 223.

[55] R. Riek, G. Wider, K. Pervushin, K. Wüthrich, Polarization transfer by cross-correlated relaxation in solution NMR with very large molecules, *Proc. Natl. Acad. Sci. USA* **1999**, *96*, 4918.

[56] N. Khaneja, J. S. Li, C. Kehlet, B. Luy, S. J. Glaser, Broadband relaxation-optimized polarization transfer in magnetic resonance, *Proc. Natl. Acad. Sci. USA* **2004**, *101*, 14742.

[57] D. P. Frueh, T. Ito, J. S. Li, G. Wagner, S. J. Glaser, N. Khaneja, Sensitivity enhancement in NMR of macromolecules by application of optimal control theory, *J. Biomol. NMR* **2005**, *32*, 23.

[58] N. Khaneja, F. Kramer, S. J. Glaser, Optimal experiments for maximizing coherence transfer between coupled spins, *J. Magn. Reson.* **2005**, *173*, 116.

[59] J. P. Palao, R. Kosloff, C. P. Koch, Protecting coherence in optimal control theory: State-dependent constraint approach, *Phys. Rev. A* **2008**, *77*, 63412.

[60] P. E. Spindler, Y. Zhang, B. Endeward, N. Gershenzon, T. E. Skinner, S. J. Glaser, T. F. Prisner, Shaped optimal control pulses for increased excitation bandwidth in EPR, *J. Magn. Reson.* **2012**, *218*, 49.

[61] U. Hohenester, G. Stadler, Optimal quantum control of electron-phonon scatterings in artificial atoms, *Physica E* **2005**, *29*, 320.

[62] M. Ndong, C. P. Koch, Vibrational stabilization of ultracold KRb molecules: A comparative study, *Phys. Rev. A* **2010**, *82*, 43437.

[63] T. M. Barbara, R. Tycko, D. P. Weitekamp, Composite Sequences for Efficient Double-Quantum Excitation over a Range of Spin Coupling Strengths, *J. Magn. Reson.* **1985**, *62*, 54.

[64] A. M. Torres, T. T. Nakashima, R. E. D. McClung, J-Compensated Proton-Detected Heteronuclear Shift-Correlation Experiments, *J. Magn. Reson.* **1993**, *102*, 219.

[65] A. M. Torres, W. A. Bubb, D. J. Philp, P. W. Kuchel, Improved *J*-compensated sequences based on short composite pulses, *J. Magn. Reson.* **2008**, *194*, 81–88.

[66] A. M. Torres, R. E. D. McClung, *J*-Compensated DEPT Sequences, *J. Magn. Reson.* **1991**, *92*, 45–63.

[67] E. L. Hahn, Spin Echos, *Phys. Rev.* **1950**, *94*, 580.

[68] B. Luy, K. Kobzar, T. E. Skinner, N. Khaneja, S. J. Glaser, Construction of Universal Rotations from Point to Point Transformations, *J. Magn. Reson.* **2005**, *176*, 179–186.

[69] B. Ehni, S. Luy, BEBE^{tr} and BUBI: J-compensated concurrent shaped pulses for ^{1}H-^{13}Cexperiments, *in press, J. Magn. Reson.* **2012**.

[70] G. Kummerlöwe, F. Halbach, B. Laufer, B. Luy, Precise measurement of RDCs in water and DMSO based gels using a silicone rubber tube for tunable stretching, *The Open Spectrosc. J.* **2008**, *2*, 29.

[71] G. Kummerlöwe, E. F. McCord, S. F. Cheatham, S. Niss, R. W. Schnell, B. Luy, Tunable alignment for all polymer gel/solvent combinations for the measurement of anisotropic NMR parameters, *Chem. Eur. J.* **2010**, *16*, 7087.

[72] J. L. Yan, A. D. Kline, H. P. Mo, M. J. Shapiro, E. R. Zartler, A novel method for the determination of stereochemistry in six-membered chairlike rings using residual dipolar couplings, *J. Org. Chem.* **2003**, *68*, 1786.

[73] K. Kobzar, H. Kessler, B. Luy, Stretched gelatin gels as chiral alignment media for the discrimination of enantiomers by NMR spectroscopy, *Angew. Chem. Int. Ed.* **2005**, *44*, 3509.

[74] N. I. Gershenzon, T. E. Skinner, B. Brutscher, N. Khaneja, M. Nimbalkar, B. Luy, S. J. Glaser, Linear phase slope in pulse design: application to coherence transfer, *J. Magn. Reson.* **2008**, *192*, 235–243.

[75] B. Luy, J. P. Marino, ^{1}H-^{31}P CPMG-correlated experiments for the assignment of nucleic acids, *J. Am. Chem. Soc.* **2001**, *123*, 11306–11307.

[76] K. Kobzar, B. Luy, Analyses, extensions and comparison of three experimental schemes for measuring ($^n J_{CH} + D_{CH}$)-couplings at natural abundance, *J. Magn. Reson.* **2007**, *186*, 131–141.

[77] A. M. Souza, G. A. Alvarez, D. Suter, Experimental protection of quantum gates against decoherence and control errors, *Phys. Rev. A* **2012**, *85*, 032306.

[78] J. A. Aguilar, M. Nilsson, g. A. Morris, Simple Proton Spectra from Complex Spin Systems: Pure Shift NMR Spectroscopy Using BIRD, *Angew. Chem. Int. Ed.* **2011**, *50*, 9716–9717.

[79] J. R. Garbow, D. P. Weitekamp, A. Pines, Bilinear Rotation Decoupling of Homonuclear Scalar Interactions, *Chem. Phys. Lett.* **1982**, *93*, 504–509.

[80] P. Sakhaii, B. Haase, W. Bermel, Experimental access to HSQC spectra decoupled in all frequency dimensions, *J. Magn. Reson.* **2009**, *199*, 192–198.

[81] K. Zangger, H. Sterk, Homonuclear broadband-decoupled NMR spectra, *J. Magn. Reson.* **1997**, *124*, 486–489.

[82] O. W. Sørensen, J. C. Madsen, N. C. Nielsen, H. Bildsøe, H. J. Jakobsen, An Improved Refocused INEPT Experiment. Application for Sensitivity Enhancement and Spectral Editing in ^{13}C NMR, *J. Magn. Reson.* **1988**, *77*, 170–174.

[83] J. Stoustrup, O. Schedletzky, S. J. Glaser, C. Griesinger, N. C. Nielsen, O. W. Sørensen, Generalized Bound on Quantum Dynamics: Efficiency of Unitary Transformations between Non-Hermitian States, *Phys. Rev. Let.* **1995**, *74*, 2921–2924.

[84] A. Bax, R. Freeman, S. P. Kempsell, Natural abundance carbon-13-carbon-13 coupling observed via double quantum coherence, *J. Am. Chem. Soc.* **1980**, *102*, 4849–4851.

[85] A. M. Torres, T. T. Nakashima, R. E. D. McClung, Improvement of INADEQUATE Using Compensated Delays and Pulses, *J. Magn. Reson.* **1992**, *99*, 99–117.

[86] J. Bunkenborg, N. C. Nielsen, O. W. Sørensen, Doubling the sensitivity of natural abundance ^{13}C-^{13}C INADEQUATE with off-resonance compensation, *Magn. Reson. Chem.* **2000**, *38*, 58–61.

[87] N. C. Nielsen, H. Thøgersen, O. W. Sørensen, Doubling the Sensitivity of INADEQUATE for Tracing Out the Carbon Skeleton of Molecules by NMR, *J. Am. Chem. Soc.* **1995**, *117*, 11365–11366.

[88] N. C. Nielsen, O. W. Sørensen, The Tolerance to *J* Mismatch and the Symmetry Properties of INADEQUATE CR, *J. Magn. Reson. Series A* **1996**, *123*, 135–139.

[89] M. H. Levitt, *Magn. Reson. Chem.* **1982**, *48*, 234.

[90] A. D. Bain, D. W. Hughes, C. K. Anand, Z. Nie, R. V. J., Problems, artifacts and solutions in the INADEQUATE NMR experiment, *Magn. Reson. Chem.* **2010**, *48*, 630–641.

[91] M. H. Levitt, Symmetrical composite pulse sequences for NMR population inversion., *J. Magn. Reson.* **1982**, *48*, 234–264.

[92] A. J. Shaka, R. Freeman, Composite pulses with dual compensation, *J. Magn. Reson.* **1983**, *55*, 487–493.

[93] W. S. Warren, Effects of arbitrary laser of NMR pulse shapes on population-inversion and coherence, *J. Chem. Phys.* **1984**, *81*, 5437–5448.

[94] M. H. Levitt, Composite pulses, *Prog. NMR Spectrosc.* **1986**, *18*, 61–122.

[95] R. Freeman, J. Friedrich, X. L. Wu, Fourier-transform spectra without a phase gradient, *J. Magn. Reson.* **1988**, *79*, 561–567.

[96] D. J. Lurie, Numerical design of composite radiofrequency pulses, *J. Magn. Reson.* **1986**, *70*, 11–20.

[97] L. Emsley, G. Bodenhausen, Gaussian pulse cascades - new analytical functions for rectangula selective inversion and in-phase excitation in NMR, *J. Magn. Reson.* **1990**, *165*, 469–476.

[98] B. Ewing, S. J. Glaser, G. P. Drobny, Development and optimization of shaped NMR pulses for the study of coupled spin systems, *Chem. Phys.* **1990**, *147*, 121–129.

[99] T. E. Skinner, M. Braun, K. Woelk, N. I. Gershenzon, S. J. Glaser, Design and Application of Robust RF Pulses for Toroid Cavity NMR Spectroscopy, *J. Magn. Reson.* **2011**, *209*, 282–290.

[100] K. Kobzar, B. Luy, N. Khaneja, S. J. Glaser, Pattern pulses: design of arbitrary excitation profiles as a function of pulse amplitude and offset, *J. Magn. Reson.* **2005**, *173*, 229–235.

[101] D. Abramovich, S. Vega, Derivation of broadband and narrowband excitation pulses using the Floquet Formalism, *J. Magn. Reson. A* **1993**, *105*, 30–48.

[102] V. L. Ermakov, G. Bodenhausen, Broadband excitation in magnetic resonance by self-refocusing doubly frequency-modulated pulses, *Chem. Phys. Lett.* **1993**, *204*, 375–380.

[103] E. Kupče, R. Freeman, Wideband excitation with polychromatic pulses, *J. Magn. Reson. A* **1994**, *108*, 268–273.

[104] K. E. Cano, M. A. Smith, A. J. Shaka, Adjustable, broadband, selective excitation with uniform phase, *J. Magn. Reson.* **2002**, *155*, 131–139.

[105] T. E. Skinner, T. O. Reiss, B. Luy, N. Khaneja, S. J. Glaser, Application of optimal control theory to the desing of broadband excitation pulses for hight resolution NMR, *J. Magn. Reson.* **2003**, *163*, 8–15.

[106] T. E. Skinner, T. O. Reiss, B. Luy, N. Khaneja, S. J. Glaser, Reducing the duration of broadband excitation pulses using optimal control with limited RF amplitude, *J. Magn. Reson.* **2004**, *167*, 68–74.

[107] T. E. Skinner, T. O. Reiss, B. Luy, N. Khaneja, S. J. Glaser, Tailoring the optimal control cost function to enable shorter broadband excitation pulses, *J. Magn. Reson.* **2005**, *172*, 17–23.

[108] T. E. Skinner, K. Kobzar, R. bendall, W. Bermel, B. Luy, N. Khaneja, S. J. Glaser, Optimal control design of constant amplitude phase-modulated pulses: application to calibration-free broadband excitation, *J. Magn. Reson.* **2006**, *179*, 241–249.

[109] N. I. Gershenzon, K. Kobzar, B. Luy, S. J. Glaser, T. E. Skinner, Optimal control design of excitation pulses that accomodate relaxation, *J. Magn. Reson.* **2007**, *188*, 330–336.

[110] M. A. Keniry, B. C. Sanctuary, Experimental verification of composite inversion pulses obtained by series expansion of the offset angle, *J. Magn. Reson.* **1992**, *97*, 382–384.

[111] A. J. Shaka, Composite pulses for ultra-broadband spin inversion, *Chem. Phys. Lett.* **1985**, *120*, 201–205.

[112] M. A. Smith, H. Hu, A. J. Shaka, Improved broadband inversion performance for NMR in liquids, *J. Magn. Reson.* **2001**, *151*, 269–283.

[113] M. H. Levitt, R. Freeman, Compensation for pulse imperfections in NMR spin-echo experiments, *J. Magn. Reson.* **1980**, *43*, 65–80.

[114] S. Wimperis, Iterative schemes for phase-distortionless composite 180° pulses, *J. Magn. Reson.* **1991**, *93*, 199–206.

[115] C. S. Poon, R. M. Henkelman, 180° Refocusing pulses which are insensitive to static and radiofrequency field inhomogeneity, *J. Magn. Reson.* **1992**, *99*, 45–55.

[116] S. Wimperis, Broadband, narrowband and passband composite pulses for use in advanced NMR experiments, *J. Magn. Reson. A* **1994**, *109*, 221–231.

[117] C. S. Poon, R. M. Henkelman, Robust refocusing pulses of limited power, *J. Magn. Reson.* **1995**, *116*, 161–180.

[118] J. Moore, M. Jankiewicz, A. W. Anderson, J. C. Gore, Evaluation of non-selective refocusing pulses for 7 T MRI, *J. Magn. Reson.* **2012**, *214*, 212–220.

[119] Y. A. Tesiram, M. R. Bendall, Universal equations for linear adiabatic pulses and characterization of partial adiabaticity, *J. Magn. Reson.* **2002**, *156*, 1–15.

[120] M. A. Janich, R. F. Schulte, M. Schwaiger, S. J. Glaser, Robust slice-selective broadband refocusing pulses, *J. Magn. Reson.* **2011**, *213*, 126–135.

[121] A. J. Bryson, Y. C. Ho, Applied Optimal Control, *Hemisphere Publ., Washington DC* **1975**.

[122] V. F. Krotov, Global Methods in Optimal Control, *Marcel Decker Publ, New York* **1996**.

[123] J. P. Palao, R. Kosloff, Optimal control theory for unitary transformations, *Phys. Rev. A* **2003**, *68*, 062308.

[124] M. Ndong, H. Tal-Ezer, R. Kosloff, C. P. Koch, A Chebychev propagator for inhomogeneous Schrödinger equations, *J. Chem. Phys.* **2009**, *130*, 124108.

[125] S. Conolly, D. Nishimura, A. Macovski, Oprimal control to the magnetic resonance selective excitation problem, *IEEE Trans. Med. Imaging MI-5* **1986**, 106–115.

[126] J. Mao, T. H. Mareci, K. N. Scott, E. R. Andrew, Selective inversion radiofrequency pulses by optimal control, *J. Magn. Reson.* **1986**, *70*, 310–318.

[127] D. Rosenfeld, Y. Zur, Design of adiabatic selective pulses using optimal control theory, *Magn. Reson. Med.* **1996**, *36*, 401–409.

[128] T. Schulte-Herbrüggen, A. Spörl, N. Khaneja, S. J. Glaser, Optimal Control for Generating Quantum Gates in Open Dissipative Systems, *Phys. Rev. B* **2011**, *44*, 154013.

[129] C. Kehlet, T. Vosegaard, N. Khaneja, S. J. Glaser, N. C. Nielsen, Low-power homonuclear dipolar recoupling in solid-state NMR developed using optimal control theory, *Chem. Phys. Lett.* **2005**, *414*, 204–209.

[130] C. Kehlet, J. T. Nielsen, Z. Tosner, N. C. Nielsen, Resolution-Enhanced Solid-State NMR ^{13}C-^{13}C Correlation Spectroscopy by Optimal Control Dipolar-Driven Spin-State-Selective Coherence Transfer, *J. Phys. Chem. Lett.* **2011**, *2*, 543–547.

[131] S. Ehni, B. Luy, A systematic approch for optimizing the robustness of pulse sequence elements with respect to couplings, offsets and B$_1$-field inhomogeneities (COB), *Magn. Reson. Chem.* **2012**, *50*, 63–S72.

[132] S. R. Hartmann, E. L. Hahn, Nuclear double resonance in the rotating frame, *Phys. Rev.* **1962**, *128*, 2042.

[133] J. Hilgert, K. H. Neeb, Lie-Gruppen und Lie-Algebren, *Springer-Verlag, Berlin* **1991**, 213.

[134] R. Otten, J. Villali, D. Kern, F. A. A. Mulder, Probing Microsecond Time Scale Dynamcis in Proteins by Methyl ^{1}H Carr-Purcell-Meiboom-Gill Relaxation Dispersion NMR Measurements, *J. Am. Chem. Soc.* **2010**, *132*, 17004–17014.

[135] D. Hansen, P. Neudecker, P. Vallurupalli, L. E. Mulder, Kay, Determination of Leu Side-Chain Conformations in Excited Protein States by NMR Relaxation Dispersion, *J. Am. Chem. Soc.* **2010**, *132*, 42–43.

[136] H. Koskela, I. Kilpelainen, S. Heikkinen, CAGEBIRD: improving the GBIRD filter with a CPMG sequence, *J. Magn. Reson.* **2004**, *170*, 121–126.

[137] H. Koskela, I. Kilpelainen, S. Heikkinen, LR-CAHSQC. An application of a Carr-Purcell-Meiboom-Gill-type sequence to heteronuclear multiple bond correlation spectroscopy, *J. Magn. Reson.* **2003**, *164*, 228–232.

[138] M. Nimbalkar, B. Luy, T. E. Skinner, J. L. Neves, N. I. Gershenzon, K. Kobzar, W. Bermel, S. J. Glaser, The Fantastic Four: A plug 'n' play set of optimal control pulses for enhancing NMR spectroscopy, *J. Magn. Reson.* **2013**, *228*, 16–31.

[139] A. M. Torres, W. A. Bubb, P. W. Kuchel, Experiments to Detect Long-Range Heteronuclear Shift Correlations: LR-*J*-HSMQC, *J. Magn. Reson.* **2002**, *156*, 249–257.

[140] N. Khaneja, S. J. Glaser, R. Brockett, Sub-Riemannian geometry and time optimal control of three spin systems: Quantum gates and coherence transfer, *Phys. Rev. A* **2002**, *65*.

[141] J. L. Neves, B. Heitmann, N. Khaneja, S. J. Glaser, Heteronuclear decoupling by optimal tracking, *J. Magn. Reson.* **2009**, *201*, 7–17.

[142] T. Cao, M. K. Nguyen, S. V. Serafin, T. H. Morton, Stereochemical Preferences in 4-Center Syn-Eliminations from Gaseous Ions, *J. Org. Chem.* **2008**, *73*, 6099–6107.

[143] M. Kainosho, K. Ajisaka, Use of Chiral Solvents or Lanthanide Shift Reagents to Distinguish meso from d or l Diastereomers, *J. A. Chem. Soc.* **1972**, *94*, 9524–9526.

[144] K. B. Ali, O. Lafon, H. Zimmermann, E. Guittet, P. Lesot, Homo- and heteronuclear 2D NMR approaches to analyse a mixture of deuterated unlike/like stereoisomers using weakly ordering chiral liquid crystals, *J. Magn. Reson.* **2007**, *187*, 205–215.

[145] G. M. Whitesides, D. W. Lewis, The Determination of Enantiomeric Purity Using Chiral Lanthanide Shift Reagents, *J. Am. Chem. Soc.* **1971**, *93*, 5914–5916.

[146] W. H. Pirkle, S. D. Beare, Optically Active Solvents in Nuclear Magnetic Resonance Spectroscopy. VII. Direct Determination of Purities and Correlations of Absolute Configurations of Sulfoxides, *J. Am. Chem. Soc.* **1968**, *90*, 6250–6251.

[147] E. L. Wee, W. G. Miller, Liquid Crystal-Isotropic Phase Equilibria in the System Poly-γ-benzyl-α,L-glutamate-Dimethylformamide, *J. Phys. Chem.* **1971**, *75*, 1446–1452.

[148] I. Felli, R. Pierratelli, S. J. Glaser, B. Luy, Relaxation-optimised Hartmann-Hahn transfer using a specifically tailored MOCCA-XY16 mixing sequence for carbonyl-carbonyl correlation spectroscopy in 13C direct detection NMR experiments, *J. Biomol. NMR* **2009**, *43*, 187–196.

[149] W. H. Pirkle, R. L. Muntz, I. C. Paul, Chiral Nuclear Magnetic Resonance Solvents. XI. A Method for Determining the Absolute Configuration of Chiral N,N-Dialkylarylamine Oxides, *J. Am. Chem. Soc.* **1971**, *93*, 2817–2819.

[150] R. K. Kondru, P. Wipf, D. N. Beratan, Theory-assisted determination of absolute stereochemistry for complex natural products via computation of molar rotation angles, *J. Am. Chem. Soc.* **1998**, *120*, 2204–2205.

[151] P. Wipf, D. N. Beratan, Optical signatures of molecular dissymmetry: Combining theory with experiments to address stereochemical puzzles, *Acc. Chem. Res.* **2009**, *42(6)*, 809–819.

[152] H. R. Marsden, J. W. Handgraaf, F. Nudelman, N. A. J. M. Sommerdijk, A. Kros, Uniting Polypeptides with Sequence-Designed Peptides: Synthesis and Assembly of Poly(γ-benzyl L-glutamate)-b-Coiled-Coil Peptide Copolymers, *J. Am. Chem. Soc.* **2010**, *132*, 2370–2377.

[153] http://www.organic-chemistry.org/protectivegroups/hydroxyl.shtm .

[154] P. Gallot, Comb-like and block liquid crystalline polymers for biological applications, *Prog. Polym. Sci.* **1996**, *21*, 1035–1088.

14. Appendix

14.1 Optimization Program OCTOPUSSI

14.1.1 The Executable

OCTOPUSSI is a program that is developed throughout the work of this thesis to deduce the described shaped pulses and coherence transfer elements. It is the successor of OCTOPUS that is written by Kyryl Kobzar [38]. It bases on the theory outlined in Chap. 3. While OCTOPUS is based on the Bloch space that is suitable for single spin optimizations, OCTOPUSSI operates in the Liouville von Neumann space and can consider higher spin systems.

OCTOPUSSI is written in Fortran and is compiled with the Intel compiler. A dynamically linked version that can run under 32 and 64bit linux is obtained using Intel compiler 9.1.036. A statically linked version that can operate on every 64bit linux system is obtained using Intel compiler 12.1.13.

OCTOPUSSI must be compiled for the spin system it is intended to be used for. The variable *nspins* is set to the number of spins and the variable *nctrl* is set to the desired number of controls (e.g. 4, if x and y controls are considered for the first and second spin) in the file octopussi.cmn.

The program is executed with

./octopussi input

input specifies the input file. The program starts with a random pulse or reads an existing pulse (as given in the *input* file). A convenient way to resume an optimization is to call the program with an arbitrary, additional argument, e.g.

./octopussi input a

will continue the last pulse optimization starting from temporary pulse data (usually *temp_0001*, *temp_0002*...) that have been written to disk but considering changed optimization parameters that might have been written to the *input* file.

14.1.2 The Input File

The optimization program does not use any arguments except the two outlined above. Everything else is specified in the input file. The input file contains the following:

Listing 14.1: Input File

```
 1 #************************************************************************
 2 #               Optimization parameters
 3 #************************************************************************
 4 # pulse files for read in must not contain empty lines at the end
 5 # start with ./octopussi input, or ./octopussi input a to read the latest temp-file
 6 # setup optimization by choosing (and compiling):
 7 # - octopussi.cmn-> nspins, nctrl=total number of controls
 8 # sctrl1=type of control for spin 1. Considers same control type on all spins
 9 # 0 = no control          supported read format
10 # 1 = x                   -
11 # 2 = xy                  3 column (x y time)
12 # 3 = xyz                 4 column (x y time z)
13 # 4 = phase               -
14 # 5 = time                3 column (x y time)
15
16 # costtype=numerical code for the kind of cost- and gradient function that is used
17 costtype = 74
18 # showtype: 0=off, 1=show all implemented optimization methods, 2=only show optimization methods that fit to the curr
19 showtype = 0
20
21 ####### Initial and Final States #######################################
22 # Define Initial- and Final State, and Unitary, or special Unitary. Uf=expm(-i*2pi*uniangle/360*unitary)
23 # Ix.., Sx.., Iy Sz..(normalization factors aren't needed), expl=explicit (write it into the code),
24 # example: -1 Iz, 2 Iy Sz
25 # showstate: 0=off, 1=show intialrho and targetrho, 2= show unitary and uni_inversion
26 initialrho = Iz
27 targetrho = Iy
28 unitary = Ix
29 uniangle = 180
30 showstate = 0
31
```

```
32 ######## Optimization Method ################################################
33 # 1= Constant Epsilon
34 # 2= Conjugated Gradients (CG)
35 Method = 2
36
37 ######## Parameters Offset spin 1 (offs), spin 2 (offs2), J-coupling (J)#
38 # n=number of points, c=central value, r=range of valuesm
39 # noffs=1 switches offset optimization off
40 noffs = 40
41 coffs , Hz = 0
42 roffs , Hz = 30000
43 noffs2 = 1
44 coffs2 , Hz = 0
45 roffs2 , Hz = 37500
46 nJ = 1
47 #cJ , Hz = 0
48 cJ , Hz = 0
49 rJ , Hz = 630
50
51 ######## B1-inhomogeneity ################################################
52 # nB1 must be <=51. and odd. nB1=1 dissables B1-field compensation 53.8
53 nB1 = 2
54 MaxB1 deviation , +/- % = 5
55 nB2 = 1
56 MaxB2 deviation , +/- % = 10
57
58 ######## Pulse initialization (0 => random pulse ,1 => file) #############
59 #if homonuclear Read_File2 must contain zeros. if heteronuclear only duration from Read_File is considered.
60 Readpulse_Flag = 0
61 Read_File = out_pulse0001
62 Read_File = out_pulse0001
63
64 ######## Pulse Parameters ################################################
65 #if read pulse, pulse length and timestep must match the read-pulse-files. npulses is always calculated by the follow
66 Pulse length , us = 500
67 Timestep , us = 0.5
68
69 ######## Truncation , Termination , Update ###############################
70 Ampl_Max , Hz = 12000
71 Ampl_Max2 , Hz = 20000
72
73 Rnd_Ampl_Max , Hz = 100
74 Seed = 24
75 nopt = 1
76
77 # maxiter.   gives the max iteration# of const E, CG and Ipopt. Upper limit of iterations also determined by 'Toleran
78 # Tolerance: is the abortion limit. it refers to convergence in cost (and Error (Ipopt))
79 # ForceIt:   0=off , 1= forces 'Max. Iterations'-iterations despite negative cost or toler-termination
80 # Kamikaze   0=off , 1=termination by tolerance is disabled (constE ,CG, Ipopt). Note that this also disables the emerg
81 # pardon:    0=off , n=number of convergence criteria that doesn't terminate optimization
82 # Update:    Determines in which interval cost is printed, temppulse is written and abortion criteria is checked (co
83 # Epsilon:   Epsilon for Method 'constant epsilon'
84 maxiter = 100000
85 Tolerance = 0.00001
86 ForceIt = 1
87 Kamikaze = 1
88 pardon = 0
89 Update = 10
90 epsilon = 1000000000
91
92 ######## Parallelization (OpenMP) ########################################
93 # Performs the parallel computation of Cost and Grad (on a shared memory System with multiple CPUs. (Not suited for p
94 # DANGER: Parallelization is implemented in such a way that just the offset-loop of CS_I is parallelized. Therefore t
95 # 'parallelization ': 0=off , >0= # of Threads.
96 # 'race_err_detect ': 0=off , 1=check cost and gradient (to perform the check 'parallelization ' must be turned on. Cho
97 parallelization = 4
98 race_err_detect = 0
99
100
101
102 ######## Decoupling by Tracking ##########################################
103 dwell , us = 50
104 n_FID = 100
105 #Ppdwell = int(npulses/n_FID). im abstand von 'Ppdwell' incrementen wird targetrho auf rho addiert
106 lwidth / Hz = 6
107 #parameters for homonuclear decoupling
108 # CS scaling: 0=1/sqrt(3) , 1=custom by scalecs
109 CSscaling = 1
110 scalecs = 1.0
111 #duty cycle: must be <1! only CG
112 dutycycle = 1.0
113 # tony: bitte den dutycycle in service.f beim costtype so definieren, dass er
114 #bei anderen optimierungsarten automatisch so gesetzt wird, dass dieser parameter
115 #nicht in rflimit auftaucht!
116
117 ######## COOP ############################################################
118 # pulse length must be sum of all pulse lengths!
119 # number of COOP pulses
120 ncoop = 0
121 # penalty operators: 1 = Ix   2 = Iy   3 = Iz   4 = Sx   5 = Sy   6 = Sz
122 # 7 = 2IySz   8 = 2IySy   9 = 2IySx
123 penaltyop = 3
124
125 ######## Composite-Pulse #################################################
126 # 0=disable , 1=enabl4es composite pulse with standard 1 spin xy-ctrl and resets ctrl and writes a file if 'converge_s
127 # only constE , set 'epsilon ' carefully
128 compositepulse = 0
129 nrot = 2.5
130
131 ######## Homonuclear UR ##################################################
```

```
132 # omits combinations of offs1, off2 that are in the range of 'omitDeltaOff'. (Because in this reagon strong coupling
133 # needs 'homonuclear'= 1
134 omitDeltaOff / Hz = 0
135 # 'constantPhase': 0=disable, 1= constant phase with max rf
136 constantPhase = 0
137
138 ######## Delay−Hardpulse−Sequence #########################################
139 # hardpulse: 0=disable, 1=single optimization with random pulse according to ScaleRandDelay and ScaleRandhardP or rea
140 # homonuclear: 0=nspins(as defined in octopussi.cmn), 1=homonuclear 2spin system (define nspins=2, nctrl=4 and sctrl(
141 hardpulse = 0
142 homonuclear = 0
143 # blankS: defined for Delay−Hardpulse and all other opt. methods
144 blankS = 1
145 # 'xonly': 0=off, 1=Ix−ctrls only
146 xonly = 0
147 #'setincrlength': 0=off, x=time/s. sets the duration of the first and/or last delay of a hp−sequence. is deactivized
148 setincrlength_first = 0.000000001
149 setincrlength_last  = 0.000000001
150 #npulses='nincrm'. npulses is in hardpulse case not calculated by plength/timestep.
151 nincrm = 3
152 localmax = 0.0
153 maxsuccess = 3
154 epsilon_delay = 0.0000001
155 epsilon_pulse = 100000000000
156 converg_success = 0.0001
157 #'ScaleRandDelay': equivalent to 'Rnd_Ampl_Max'. scales down the random delays of a starting hp−sequence
158 ScaleRandDelay = 100.0
159 #'ScaleRandHardP': equivalent to 'maxrf': scales down the random delays of a starting hp−sequence
160 ScaleRandHardP = 100.0
161 #epsilon_pulse<1e8, otherwise instability! near optimum according to gradoutput maybe larger
162 #nincrm=number of delay and pulses, blankS: 0=no blank, 1=blank control spin 2, lengthmax=overall delay duration, loc
163 #solution that is interpreted as success, maxsuccess=determins how much successful optimizations are done, epsilon_de
164 #converg_success=for cost>localmax this determines the convergences for termination
165
166 ######## 1 Spin phi0 Relaxation−pulse for saturation cost&grad ##########
167 # 0=disable, 1=t1, t2 relaxation according to t1, t2
168 relaxation = 0
169 t2 = 01
170
171 ########  Selective Pulses ################################################
172 #pattern: 0=no pattern
173 #pattern: 1= 1spinXY _offset_ selective pulse. according to the cost/grad (with same date) you can choose between
174 # (i)   selective−saturation−pulse (Iz−>xy|Iz−>Iz|Iz−>xy)=(sat|p2p|sat)   (2011.02.22). needs initialrho = Iz, targetrh
175 # (ii) selective−UR−pulse          (Ueff=1|Ueff=expm(−i*pi*Ix)|Ueff=1)   (2011.06.26). Set 'unitary' and 'uniangle' fo
176 # (iii)
177 # (iv) replaces the pmB1 by a explicit B1 range (2011.07.21)
178 # (v)   selective−UR−pulse          (UR|UR|UR)=(Ueff=exp(−i*2pi*w*Iz)|Ueff=exp(−i*pi*Ix)|(Ueff=exp(−i*2pi*w*Iz))   2011
179 # (vi) replaces coffs & roffs by explicit offset range (2012.03.30)
180 plotwdistr = 1
181 pcenter, Hz = 000
182 prange, Hz = 700
183 scaleCenterChecks = 10.0
184 scaletransition = 3.0
185 # transition: 0=defined by 1/pulselength, #=transition/Hz
186 transition = 1000
187 ########pattern: 3=1spinXY _B1_ selective Pulse (sat|p2p|sat),          (2011.06.01), SE.'nB1outer' determins the # o
188 B1min = 0.2
189 B1max = 1.2
190 transitionB1 = 0.2
191 nB1outer = 4
192 ########pattern: 4=do ordinary B−setup for both spins defined by 'B1min' 'B1max' 'B2min' 'B2max' 'nB1' 'nB2'
193 B2min = 0.3
194 B2max = 1.0
195 ########pattern: 6=do ordinary offset setup for both spins defined by
196 # "off1min","off1max", "off2min", "off2max", "noffs" & "noffs2"
197 off1min = −750
198 off1max = 4300
199 off2min = −750
200 off2max = 4300
201 ########j−selective: activated by 'costtype' automatically. Define Passband with
202 #'cJ', 'rJ' and stopband with 'pcJ', 'prJ' and 'scaleJstopChecks'. use 'plotwdistr' to show explicitly how checks are
203 pcJ, Hz = 15
204 prJ, Hz = 30
205 scaleJstopChecks = 5
206
207 ######## Stepsize Optimization (CG) ######################################
208 # CG (critical for performance): tolerated deviation between Epsilon and EpsilonOpt, within the algorithm is allowed
209 Convergence = 0.1
210
211 ######### Ipopt ##########################################################
212 # default=4
213 Printlevel = 0
214 # 0=Understand=default 'Tolerance' as Tol. in Overall NLP error. 1=Understand Tol. as Tol. in cost (similar to const
215 # 0 terminates Ipopt with Success message (save option). 1 terminates Ipopt with Error 1 Message
216 Termination Method = 0
217
218 # default=1=disable
219 Dual infeasibility tolerance = 1
220 # default=−1=maximization
221 Objective Scaling Factor = −1
222 # default=yes
223 Accept every trial step = yes
224 # lBFGS=1...+inf, default=30, limited Memory Maximal History Hessian−Approximation. Danger: lBFGS>30 my slowdown each
225 lBFGS = 30
226
227
228
229
230 ######## Pre Optimization Method: ########################################
231 # if 'Premeth' .ne. 0 a Pre Optimization with 'Presteps' is ran, followed by Optimization with standard 'Method'
```

```
232 # i.e. Premeth my be useful in multiple optimizations to ensure that Ipopt will start to converge with every starting
233 # Premeth: 1=constE, 2=CG, 3=Ipopt
234 Premeth = 0
235 Presteps = 1
236
237 ######### Exploring The Limits ######################################### #
238 # (Perform 'Number Increments'+1 Optm. increasing plength by 'pincr')
239 # 'pincr' must be a multiple of 'timestep'
240 # nincr: 0=disable expl, n=number of pulse enlongations
241 # creates separate folders for each pulselength (containing the temp_0001)
242 nincr = 0
243 # pincr: pulse increment for enlarging pulse length
244 pincr, us = 500
245
246 ######### Derivative Check #################################################
247 # (checks the Gradient by calculating the finite differentiation to the I, S or IS−ctrl. for the number of timesteps
248 # DANGER: The derivcheck is not meant to be used in combination with offset −, b1− or j−compensation since an averaged
249 # DANGER: The file derivcheck.f must contain the actual cost functions for I and S−Spin. If you adapt the cost for a
250 # DANGER: Do not trust derivcheck, if finiteDiv−Grad<1E−12. (since real*8 is just precise til the 13th digit)
251 # DANGER: Derivcheck doesn't check parallel derivatives
252 # derivch: 0=off, 1=Ictrl, 2=Sctrl, 3=I+Sctrl. dPhi/dCtrl= (phi(CtrlNtimesteps+deltactrl)−phi(CtrlNtimesteps))/deltac
253 derivch = 0
254 ntimesteps = 3
255 # default deltactrl = 0.1. consider Machine precision: including 13th digit precise
256 deltactrl = 0.1
257
258 ######### Spaghetti−Plot #################################################
259 # (writes file 'logfile' containing the convergence of the problem as a function of time and #of iterations)
260 # spaghetti: 1=enables spaghetti−output, 2=skips optimization, if cost<icost
261 spaghetti = 0
262 # spaghettitime = time[s] when spaghetti−optimization is aborted. If another termination criteria is chosen, set here
263 spaghettitime = 2700
264 #scales the cost so that costscale*displayedCost −>1
265 costscale = 1
266 #icost is the initial cost. sometimes ipopt doesn't start to converge if the initial cost is small. Therefore an opti
267 icost = 0.11
268
269 ######### Phasesweep #########################################################
270 # optimzes a pulse with the constraint, that the phase is piecewise constante swept by the following parameters. with
271 # 'psweepp': 0=off, intg=#of timesteps within the same phase cutoff
272 psweepp = 20
273 # 'phaseincr': increments psweepp by this real number 0
274 phaseincr = 74.1
275 # 'phasecut': cuts phase if it exceeds +− 'phasecut' 0
276 phasecut = 38
277
278 ######### Universal Rotation with axis(offset??) #########################
279 # quadratic phase pulse 2010.07.22
280 # the phase of the rotation axis (of a UR−pulse) between Ix,Iy as a function of the current offset??
281 #urspuenglicher wert = 0.00001
282 Offset constant = 0.00001
283
284 ######### unitary rotation with j−evolution: ### cost phi3 J−evolution ###
285 # Upi=expm(−i*2pi*uniangle/360(Ix +Sx)), Uj=expm(−2i*pi*jevconst*J*plength/2*IzSz)
286 # Uf = Uj*Upi*Uj, tries to let some j evolution happen during universal rotation
287 # 0 no evolution ... 1 full evolution
288 jevoconst = 0.0
289 ### cost phi3 J−evolution with j distribution # nJdistr: 1=disables jdistribution, 201=maximum # rjdistr[Hz]: varies
290 nJdistr = 1
291 rJdistr = 249
292 # cJdistr: 0= take the actual hcp(1) (according to cJ, rJ, nJ) as center and allow the distribution specified with n
293 cJdistr = 0
294
295 # plotjdistr: 0=off, 1=plots skalar product onto all target Ufs defined within 'rjdistr' if 'njdistr' isn't equal 1
296 plotjdistr = 0
297 #zerjHevo: 0=multiplies the J−term in the Hamiltonian of the propagation with 0. 1=multiplies it with 1.
298 zerojHevo = 1
```

14.1.2.1 Available Cost Functions: *costtype*

Currently, the optimization program knows a number of optimization problems that are
specified by a cost function. The gradient is the derivative of the cost function and each
cost function has a dedicated gradient that is automatically chosen by the program and
can not be reassigned at runtime by the user. The combination of a certain cost function
and a gradient defines an optimization method that is addressed by the *costtype* integer.

A list of supported *costtypes* with description of the problem statement is printed by setting
showtype=1. Running

        ./octopussi input

will output the information:

Listing 14.2: Available Optimization Methods

```
1
2    List of implemented optimization methods according to costtype
3    ===================================================================================
4
5    ———————— Hard Coded Cost Functions ——————————————————————————————————
6    01: explicit cost function, hard coded.
7
8    ———————— Phi0 Cost Functions ————————————————————————————————————————
9    11: 1,2 spins xy, first order grad, Phi0, 2010.08.12 SE
10   12: 1 spin xyz, Phi0, first order grad, 2010.09.29 SE
11   13: 2 spin xyz, first order grad, Phi0, 2010.09.29 SE
12   14: 1 spin xy, exact grad, Phi0, 2010.09.30 SE
13   15: 2 spin xy, exact grad, Phi0, 2010.06.19 SE
14   16: 2 spin xyz, exact grad, Phi0, 2010.09.27 SE
15
16   ———————— Phi3 Cost Functions ————————————————————————————————————————
17   31: 1,2 spins xy, first order grad, Phi3, 2010.07.15 SE
18   32: 1 spins xyz, first order grad, Phi3, 2010.07.15 SE
19   33: 1 spins xyz, exact grad, Phi3, 2010.06.25 SE
20   34: 2 spins xy, exact grad, Phi3, 2010.06.24 SE
21        Homonuclear Jcomp UR, for INADEQUATE, Uf=e(−i*pi*(Ix+Sx)) hard coded
22   35: 1 spin xy, exact grad, Phi3, 2012.04.03 TR
23        grad defined by evolution of 3 density operators, partially hard coded!
24        also known as Phi rot, proof given in URLimits
25   36: 2 spins xy, exact grad, Phi3, 2012.11.25 SE
26        2 spin Hweak
27
28   ———————— Decoupling, COOP Cost Functions ————————————————————————————
29   51: 2 spin xy, exact grad, Phi0, 2011.06.07 TR
30        heteronuclearTRACK: Ix−>Ix, {S}
31        because paralleliz set: initr=Sx targetr=Sx noffs=#, noffs2=1, nj=1, cj=145
32   52: 2 spin xy, exact grad, Phi3, 2011.08.16 TR
33        dipolar magic angle homodec no Tracking
34        define chemical shift scaling via scalecs
35   61: 1,2 spin xy, exact grad, Phi0, 2011.11.14 TR
36        BEBOP for COOP multiscan (defined by ncoop)
37        resulting pulses written in single file
38   62: 2 spin xy, TRACK, 2012.05.09 TR,SE
39        offset selective heteronucleare decoupling
40   63: 2 spin xy, TRACK, 2012.10.19 SE
41        offset selective homonucleare decoupling
42        Spin1: in pass band, decoupled to spin 2in stop band
43
44   ———————— Selective, Composite, Time Cost Functions ——————————————————
45   71: 1 spin xy, exact grad, Phi0, 2011.06.01 SE
46        B1 selective: pattern=3
47        p2p|p2p|p2p = min(Iz)|Iz−>−Iz|min(Iz)
48   72: 1 spin xy, exact grad, Phi3, 2011.06.26 SE
49        offset selective: pattern=1
50        UR|UR|UR = Ueff=1|Ueff=exp(−i*pi*Ix)|Ueff=1
51   73: 1 spin xy, exact grad, Phi3, 2011.10.04 SE,
52        offset selective: equivalent to Brukers Q3
53        UR|UR|UR = Ueff=exp(−i*2pi*w*Iz)|Ueff=exp(−i*pi*Ix)|(Ueff=exp(−i*2pi*w*Iz)
54   74: 1 spin xy, exact grad, Phi0, 2012.05.08 TR
55        offset selective: pattern=1
56        p2p|p2p|p2p = Iz−>Iz|BEBOP/BIBOP|Iz−>Iz
57   75: 2 spin xy, exact grad, Phi0/dt, 2011.03.20 SE
58        hard pulse delay sequence: set hardpulse=1
59        constE only. set nopt=2000
60   76: 2 spin xy, exact grad, Phi3/dt, 2011.02.29 SE
61        hard pulse delay sequence: set hardpulse=1
62   77: 2 spin xy, exact grad, Phi0, 2012.08.14 SE
63        j−selective (BIRD): stop|pass (i_rho−>i_rho)|(i_rho−>finalrho)
64   78: 2 spin xy, Phi0/dt hp−delay, exact grad, 2012.09.23 SE
65        j−selective (BIRD): stop|pass (i_rho−>i_rho)|(i_rho−>finalrho)
66        constE only. set nopt=2000
67
68   ———————— Special Cost Functions —————————————————————————————————————
69   81: 1 spin xy, exact grad, min(Iz), 2011.02.22 SE
70        xyBEBOP, saturation
71   82: 2 spin xy, exact grad, Phi3b BUBI, 2010.06.19 SE
72        spin1: UR, spin2: p2p, Phi3b = R<U_F U_Seff|U_eff> + R<rho_F|rho_end>
73   83: 2 spin xyz, exact grad, Phi3b BUBI, 2010.06.19 SE
74        spin1: UR, spin2: p2p, Phi3b = R<U_F U_Seff|U_eff> + R<rho_F|rho_end>
75   84: 1 spin xy, exact grad, Phi3 quadratic phase, 2010.07.22 SE MK
76        UR around an axis that has an angl to the Ix−axis that is quadratic
77        as a function of the offset
78   85: 2 spin xy, exact grad, Phi3 Jevolution, 2010.07.22 SE MK, <Uj*Upi*Uj|Ueff>
79        Concurrent UR180 pulses, that accomplish a amount of heteronuclear coupling
80        Uj=e^(−2ipi*jevconst*J*plength/2*IzSz), Upi=e^(−i2pi*uniangle/360(Ix+Sx))
81   86: 2 spin xyz, exact grad, Phi3 Jevolution, 2010.07.22 SE MK, <Uj*Upi*Uj|Ueff>
82        With J−distribution.(to account for every J coupling in the defined range)
83   87: 2 spin xyz, exact grad, Phi3 BUBU, 2010.10.22 SE
84        Concurrent heteronuclear UR180 for comparison with Jevolution
85   88: 2 spin xy, exact grad, Phi3 Homodecoupling, 2010.01.25 TR,SE
86        Pure shift: Khaneja, explicitinitial and final states: rhoI=Ix+Sx,
87        rhoF=Uf*rhoI*Uf^, Uf=expm(−iHtp), H=wiIz+wsSz + scalecs*piJ*2IxSx
```

- Each available described method starts with the *costtype*-integer followed by the spin system. Pulses or pulse sequences are considered to operate in a respective spin system and the spin-system-information informs whether the chosen cost function is suitable for that spin system (e.g. 1,2spins means that this cost function can be used for one or two spin systems).

- "first order grad" or "exact grad" gives information about the implementation of the gradient (see Chap. 3.2).

- The name of the cost function is given (e.g. Phi0, Phi3...)

- The date when the method was implemented and the abbreviation of the responsible person is given.

- More advanced optimization protocols that exceed the domain of Phi0/Phi3-pulses often provide additional information of how they are defined. For example which transformation is aspired. Also information about required parameters is given.

Available optimization protocols are grouped according to their *costtype*.

- $11<costtype<31$: Φ_0. Optimizations will yield p2p pulses that accomplish a transfer defined by an initial and final operator.

- $31<costtype<51$: Φ_3. UR pulses. These pulses do not need magnetization with a defined initial state but can be used equivalent to hard pulses.

- $51<costtype<71$: TRACK decoupling and COOP optimizations.

- $71<costtype<81$: Selective pulses (offset selective, B_1 selective, J-selective), pulses with the time as optimization variable, pulse sequences with time as variable and intersecting hard pulses with fixed phase and fixed rf amplitude, pulse sequences with time as variable and intersecting hard pulses with variable phase and variable rf amplitude.

- $81<costtype$: Special cost functions. Currently: xyBEBOP, BUBI, quadratic phase as function of the offset Phi3 UR180 pulses, J-evolution and Khaneja homonuclear decoupling.

14.1.2.2 Initial and Final States

In case a Φ_0 based cost function is used, initial and final states are given by setting the variables *initialrho* and *finalrho* to the spin operators according to the examples given in the input file. For Φ_3 cost functions the rotation axis is defined by *unitary* and the rotation angle in degree is set by *uniangle*. *initialrho*, *finalrho* and *unitary* can also be set to *expl* to use an explicit matrix that has to be specified in the source code (file: ham.f). If the *showstate* variable is $\neq 0$ the used states are displayed in matrix representation.

14.1.2.3 Optimization Method

Method sets the optimization method to constant epsilon, conjugated gradients or Ipopt. The stepsize for constant epsilon is defined by *epsilon*. If the cost function shows chaotic jumps and does not increase monotonically, *epsilon* is too large. Also the precision of conjugated gradients is defined by *Convergence* that will indirectly influence how many evaluations of the cost function are needed for each iteration. Note that Ipopt must be compiled for the used system and the dynamically linked executable must be used.

14.1.2.4 Pulse Specifications

Properties to be compensated in a shaped pulse are set by a center-, a range and a number of evaluation steps (*coffs*, *roffs* and *noffs*) for the first and second spin. J-coupling between that nuclei is defined by *cJ*, *rJ* and *nJ*. B_1 deviations are defined by *MaxB1 deviation +/-* % and *nB1* evaluations are performed.

14.1.2.5 Pulse Initialization

If *Readpulse_Flag = 0* an optimization is started with a random pulse. The random number generator is initiated with the seed value *Seed* and the random amplitude is scaled to *Rnd_Ampl_Max, Hz*. If *Readpulse_Flag = 1* a pulse is read from the file set by *Read_File*. For heteronuclear spin systems a pulse may be read for every spin by defining more than one *Read_File* statements.

14.1.2.6 Pulse Length and Digitization

The pulse length is given by *Pulse length, us*. Digitization is given by *Timestep, us*

14.1.2.7 Maximum rf

The maximum amplitude of the pulse is set for the first spin by *Ampl_Max, Hz* and for the second spin by *Ampl_Max2, Hz*.

14.1.2.8 Termination, Update, Tempfiles, Number of Optimizations

Every *Update* steps, temporary pulse files are written to disk (filename e.g. temp_0001). Also every *update* steps the optimization can be terminated. Either if *maxiter* iterations are performed for each of the *nopt* started optimizations. Or if the *tolerance* criterion is fulfilled. The *tolerance* termination can be delayed by defining *pardon > 0*. In this case *pardon tolerance*-events are needed for termination. Termination can be avoided by setting *ForceIt* and *Kamikaze* equal 1.

14.1.2.9 Parallelization

On program start, the number of shared memory cores available on the current system is determined and displayed. It is recommended to set the number of cores that should be used in parallel by the variable *parallelization*. If only one core should be used *parallelization* is set to 1. If new gradient functions are implemented they can be tested whether race-errors are present by setting *race_err_detec* $\neq 0$.

14.1.2.10 Composite Pulses

Composite pulses, being pulses consisting of several consecutive hard pulses, may be obtained by setting *composite = 1*. This pulses are not truncated to a maximum rf amplitude but restricted to a maximal number of rotations of the corresponding magnetization by setting *nrot*, which is the number of full rotations.

14.1.2.11 Pulse Delay Sequences

Pulse delay sequences are obtained by choosing an appropriate cost function and setting *hardpulse = 1*. Homonuclear sequences are obtained by setting *homonuclear = 1*. In a two spin system, controls on the second spin can be set to zero by *blanks = 1*. Sequences using only *x*-controls can be obtained by setting *xonly = 1*.

Hard pulse delay sequences are defined by the number of increments *nincrm*. For example *nincrm = 3* yields a sequence starting with a pulse, followed by a delay and ending with a pulse. For most optimization procedures the length of the odd pulse increments is fixed to 0.5 μs, while the even numbered delays are time-variable. Accordingly, the sequences are updated with amplitude information for odd increments and time information for even increments.

Sequences always start and end with a pulse. If sequences are not wanted to start and end with a certain pulse the *setincrlength_first* and *setincrlength_last* variables can be set to a coefficient that scales the first and last pulse in length.

Most of the hard pulse delay optimizations are very likely to converge towards a local optimum. The dominant local optimum is often characterized by a transfer graph (as function of J) that is the sine function. To obtain sequences that exceed this local maximum, a large number of optimizations must be performed. Either by setting a large number of optimization by *nopt* or by using *localmax*. *localmax* is set to the numerical value that is approached by the cost function. The optimization method must be constant epsilon in this case. If the cost function now again approaches *localmax* a random reset of the pulse sequence is triggered. This is done until *maxsuccess* sequences are obtained that exceed *localmax*. The convergence termination criteria for successful pulses is *converg_success*.

14.1.2.12 Relaxation

xyBEBOP pulses (*costtype = 81*) can consider exponentially decaying magnetization. To enable the exponential decay, *relaxation* is set to 1 and *t2* is the corresponding time coefficient in seconds.

14.1.2.13 Selective Pulses

Selective pulses are used to define a certain transfer within a certain range of a property (offset, B_1 or J-coupling) and a second kind of transfer within another range of the same property. Transfers can be Φ_0 or Φ_3 or several combinations of both with any combination of *initialrho*, *finalrho* and *unitary*. Because of the multitude of possible combinations most selective pulses that can be addressed by *costtype* have predefined transfer properties to serve a certain appointment. Details about that are given in the *costtype* descriptions. Therefore, the definition of the transfer can not be changed by the user without recompiling the code.

Concerning offset selective pulses the outer range of standard selective pulses of the form stop|pass|stop or pass|stop|pass are defined by *coffs, Hz, roffs, Hz, noffs* and the inner range is defined by *pcenter, Hz, prange, Hz*. The program automatically assigns the number of points for all regions and displays it. The number of points for the central region is changed by setting the coefficient *scaleCenterChecks*. The transition region is automatically set by the reciprocal of the pulse length but can be adjusted by the coefficient *scaletransition*. No points are set within the transition region. Alternatively the transition region can be explicitly defined by setting *transition* to a value $\neq 0$. This value is given in Hz and specifies the range of the transition region. The list of offsets that is created by adjusting the mentioned parameters is plotted by setting *plotwdistr = 1*.

B_1 selective pulses are available in combination with xyBEBOP pulses (denoted here as "sat", standing for saturation). The pulse will do a sat|p2p|sat transformation as a function of the B_1 field. Parameters are specified according to *B1min* and *B1max*.

J-selective pulses are obtained by selecting the corresponding *costtype* and setting *pcJ, Hz, prJ, Hz* and *scaleJstopChecks* in accordance to the procedure described for offset selective pulses.

14.1.2.14 Derivative Check

The numerical values of the derivative of the cost function can be compared to finite difference gradients (see Chap. 3.2.5). This is done by setting *derivch*>0. 0=off, 1=first spin, 2=second spin, 3=first and second spin. The comparison is done for *ntimesteps* time steps. For the calculation of finite difference gradients, controls are changed by a small number *deltactrl* in Hz.

14.1.2.15 Exploring the Limits

To examine the effect of the pulse length on the pulse performance, the program can optimize multiple pulses and then successively increase the pulse length until the desired maximum pulse length is reached. This is enabled by setting $nincr \neq 0$. The pulse length is elongated by the value *pincr, us*. This is done *nincr* times until the final duration is reached. *pincr, us* must be a multiple of *Timestep, us*.

14.1.2.16 Phasesweep

This option allows to optimize pulses that fulfil the criteria that the discretized pulse phase has to change continuously. This class of pulses evolves less heteronuclear coupling when applied concurrently with other shaped pulses. Pulses therefore do not need to be compensated against *J*-coupling in a two spin system. *psweepp*Timestep, us* defines a phase increment. During this increment the optimization is free to change the phase to deviate from the given mean value. The next phase increment deviates by *phaseincr* from the phase of the previous increment.

14.1.3 Information Given by the Program

The program writes optimization parameters in the header of temporary- and final pulse files. Apart from that the program gives information on start-up. For example the output for optimizing a selective pulse according to *costtype = 74* is:

Listing 14.3: Program Output

```
 1
 2   *******************************************************************************
 3   *************** Octopussi -  Liouville von Neumann Space ******************
 4      compiled for: 1 spin, nctrl I:     2, input file: input
 5   *******************************************************************************
 6      costtype:          74
 7   1spin xy, exact grad, Phi0, 2012.05.08 TR
 8   offset selective: pattern=1
 9   p2p|p2p|p2p = Iz->Iz|BEBOP/BIBOP|Iz->Iz
10   *******************************************************************************
11   Parallelization=04, autothread=00.      Running 04 threads on 08 processors
12   *******************************************************************************
13
14   Start P. stored in ./input_oct/in_pulse0001
15   optimization #           1
16   rhoI -> rhoF: 01 Iz  ->01 Iy       unitary:      01 Ix
17   blankS is set to 0 because there is no second spin to blank.
18
19   Checks for Pattern Pulse:       17 | 1| 10  | 1 | 17    min: 30    noffs:  40 -> 44
20   ................|:::::::::::|................
21
22    1   -15000.00   0
23    2   -14146.88   0
24    3   -13293.75   0
25    4   -12440.62   0
26    5   -11587.50   0
27    6   -10734.38   0
28    7    -9881.25   0
29    8    -9028.12   0
30    9    -8175.00   0
31   10    -7321.88   0
32   11    -6468.75   0
33   12    -5615.62   0
34   13    -4762.50   0
35   14    -3909.38   0
36   15    -3056.25   0
37   16    -2203.12   0
38   17    -1350.00   0
39   18     -350.00   1
40   19     -272.22   1
41   20     -194.44   1
42   21     -116.67   1
43   22      -38.89   1
44   23       38.89   1
45   24      116.67   1
46   25      194.44   1
47   26      272.22   1
48   27      350.00   1
49   28     1350.00   0
50   29     2203.12   0
51   30     3056.25   0
52   31     3909.38   0
53   32     4762.50   0
54   33     5615.62   0
55   34     6468.75   0
```

```
56   35      7321.88    0
57   36      8175.00    0
58   37      9028.12    0
59   38      9881.25    0
60   39     10734.38    0
61   40     11587.50    0
62   41     12440.62    0
63   42     13293.75    0
64   43     14146.88    0
65   44     15000.00    0
66
67                        Pattern−Pulse−Mode
68   ***************************************************************************
69   Starting Conjugated Gradient (CG) Optimization. Initial Cost   0.7719383083
```

In line 4 the program reports that it is compiled for a single spin optimization and is using two controls (x and y).

In line 6 the cost type is given, followed by a description of the optimization procedure. In this case an offset-selective pulse will be optimized that has three transfer regions. Each of this transfer regions are defined by a p2p transfer (line 9, p2p|p2p|p2p). The left and the right transfer region are predefined to be $I_z \rightarrow I_z$. The transfer in the central region can be chosen by setting *initialrho* and *targetrho*.

In line 11 the program states that 4 processors are used.

The initial (random) pulse is saved and the path is given in line 14.

Line 15 indicates that a single optimization is performed.

Line 16 indicates the initial and final state according to *initialrho* and *targetrho*.

Details about the selective pulse are given in line 19. The number of points in the respective regions are given. By this, the automatic procedure changed the user defined number of points (40) to (44).

Starting from line 22, the 44 explicit offsets are listed followed by an integer that indicates the stop (0) or the pass (1) band.

14.1.4 Format of Supported Pulse Files

The program can read and write pulses and pulse sequences that are given in the $x,y,time$ or $x,y,time,z$ format.

x,y,z denote real values that give the rf amplitude in Hz. *time* denotes a real valued number that gives the time in seconds.

A typical output file in the $x,y,time$-format is given by:

Listing 14.4: Data Format

```
 1
 2  #   costtype =              81
 3  #   1spin xy, exact grad, min(Iz), 2011.02.22 SE
 4  #   xyBEBOP, saturation
 5  #   ——————————————————————————————————
 6  #     Cost              0.99798769819 ( 1 − abs(Iz−>Iz))
 7  #     Date, Time     2013.04.20, 21:03:23
 8  #     Parallelization=04, autothread=00.       Running 04 threads on 04 processors
 9  #     rhoI −> rhoF: 01 Iz   −>01 Iy
10  #      unitary:       01 Ix
11  #     uniangle =       180.000
12  #     npulses=      1000
13  #     timestep, us=    0.500
14  #     plength, us=      500.000
15  #     blankS =          0
16  #     xonly =            0
17  #   ——————————————————————————————————
18  #     BW_I, Hz=          30000.0
19  #     Number OffsI=      40
20  #     maxrf_I, Hz=      12000.0
21  #     Number B1=      2
22  #     B1 dev +−%=      5.000
23  #     Center J, Hz=       0.0000
24  #     Number J, Hz=      1
25  #     Range J, Hz=        630.0
26  #     Method=           Constant Epsilon
```

```
27  #       Amplitude=              truncation to MaxRf
28  #       #iterations=                8950
29  #       Seed=           24
30  #
31  #    Ampl X/Hz,  Ampl Y/Hz,    Duration/s
32              584.756            −7127.457   0.0000005000
33             −892.168            −6884.322   0.0000005000
34            −2367.134            −6545.964   0.0000005000
35            −3728.424            −6136.257   0.0000005000
36            −5064.280            −5625.976   0.0000005000
37            −6389.753            −5006.463   0.0000005000
38              ...
```

Files to be read do not necessarily need to have a header.

14.2 Abbreviations

Å	Ångström 10^{-10} m
B_0	static magnetic field
B_1	magnetic field of the rf
BEBE	broadband excitation broadband excitation
BIRD	bilinear rotation decoupling
BUBI	broadband universal broadband inversion
CLIP-HSQC	clean-inphase-HSQC
COB	couplings, offsets, B_1-deviation
COS	coherence order selection
CPMG	Carr-Purcell-Meiboom-Gill
CS	chemical shift
CTE	coherence transfer elements
D	dipolar coupling
DIPEA	Diisopropylethylamin
DMF	Dimethylformamid
DQ	double-quantum
EPR	electron paramagnetic resonance
FID	free induction decay
Fmoc	9-Fluorenylmethoxycarbonyl
FWHM	full width half maximum
GRAPE	gradient ascent pulse engineering
HBTU	2-(1H-benzotriazol-1-yl)-1,1,3,3tetramethyluronimhexyfluorophosphat
HOBT	1-Hydroxybenzotriazol
HSQC	heteronuclear single quantum coherence
INADEQUATE	incredible natural abundance double quantum transfer experiment
J	scalar coupling
LCMS	liquid chromatography mass spectroscopy
MALDI	matrix-assisted laser desorption ionization
MD	molecular dynamics
MRI	magnetic resonance imaging
NMR	nuclear magnetic resonance
OCT	optimal control theory
p2p	point to point
PBLG	poly-γ-benzyl-L-glutamate
PFG	pulsed field gradient
PP	point to point
ppm	parts per million
RCSA	residual chemical shift anisotropy
RDC	residual dipolar coupling
rf	radio frequency
rt	room temperature
S/A	signal to artifact
S/N	signal to noise
sp	shaped pulse
SQ	single-quantum
te	transfer efficiency
T	$J + D$
TOCSY	total correlation spectroscopy
TOP	time optimal
UR	universal rotation

14.3 Danksagung

Diese Arbeit wäre nicht möglich gewesen ohne den Kontakt zu einer Vielzahl von Menschen. Im Arbeitskreis, zu anderen Arbeitskreisen und darüber hinaus.

Mein tiefster Dank gebührt Prof. Dr. Burkhard Luy für die Aufnahme in seinen Arbeitskreis, die exzellenten Ideen und Projekte, die nimmer endende Geduld bei der Lehre der NMR Spektroskopie, die Bereitstellung der herausragenden apparativen Ausstattung und die außergewöhnlichen Einsichten in dieses faszinierende Feld der modernen NMR Spektroskopie und Pulsoptimierung mittels Optimal Control Theory.

Mein Dank gilt dem gesamten Arbeitskreis. Für die unzähligen, spannenden, fachlichen Diskussionen. Insbesondere für die inspirierende Atmosphäre und die schöne Zeit.